EPFL

Development of a Transient Neural Interface for Minimally Invasive Recording and Stimulation

Adele FANELLI

■ École
polytechnique
fédérale
de Lausanne

2022

Abstract

Transient electronics enabling devices to safely disappear in the environment can be applied not only in green electronics, but also in bioelectronic medicine. Neural implants able to degrade harmlessly inside the body eliminate the need for removal surgery and potentially reduce inflammation responses and the chronic adverse reactions hindering device functionality and putting patients' health at risk. On the contrary, the degradation of the device allows for safe tissue remodelling around the implant over time and even migration of cells inside the device, as in the case of scaffolds applied in tissue engineering. Non-degradable implants instead cannot offer such opportunity and most often induce the creation of an unwanted glial scar, insulating the device, distancing it from the source of information (i.e., neurons) until they become useless. Removal of such devices could be complicated and represent an additional risk for the patient, if not also a good reason to oppose the therapy in the first place. The latest effort in limiting these unwanted effects is to minimize the invasiveness of the implant by reducing its size and promising results of this strategy have been obtained. However, if hardware failures, loss of therapy efficacy or infection development were to occur, retrieval of the implant might be necessary. Transient interfaces enter this scene of minimally invasive devices by addressing the chronic complications with degradable materials. Unfortunately, at the moment transient neurotechnology can be used only for very short-term applications, such as monitoring of intracranial pressure, temperature, or neural activity around cerebral interventions. If applied to the peripheral nervous systems, they could also take part in the enhancement of motor recovery after injury or stroke. The main reason why only this type of applications is possible for now is the short lifetime of the materials used to build these interfaces: fast degrading metals allow for operations rarely longer than a few days, strongly limiting the available time window for collecting information or for a therapy to be finished.

To solve this problem, we propose a transient, all-polymeric neural interface able to work for longer time scales. In this way, longer operational time could be allowed while also maintaining the transiency of the device and of the therapy. This would enable new applications of transient neurotechnology, such as recording of brain activity for a prolonged and more useful period of time before resection of epilepsy foci or tumours. The device consists of a polycaprolactone (PCL) scaffold with patterned poly 3,4-ethylene dioxythiophene : polystyrene sulfonate (PEDOT:PSS) traces and electrodes. PCL offers one of the slowest degradation rates among biodegradable polyesters, and the biocompatible PEDOT:PSS, mixed with ethylene glycol (EG), grants high electrochemical properties. In vivo testing of the platform was performed by inserting it inside the visual cortex of mice and recording epileptic seizures, local field potentials and visually evoked responses up to twelve weeks. Results showed low noise levels for the entire test duration and histological analysis highlighted the cellular infiltration inside the penetrating PCL scaffold over time, hinting to potential tissue remodelling processes, which would not occur with a non-degradable device.

To increase the device potential for a clinical translation and further reduce inflammatory responses caused by penetrating interfaces, a minimally invasive procedure for its implantation has been proposed. The blood vasculature supplying the brain and nerves can be used as an access route to the

neural tissue, offering a close enough location without direct damage to the tissue. This strategy has already been successfully employed by the company Synchron and their Stentrode™ device. By re-shaping the all-polymeric transient neural probe using a stent-inspired design, the new interface can be navigated through a 5Fr (approximately 1.67 mm) catheter and deployed inside 2 mm-diameter channels. Characterization specific to the new working environment showed promising electrodes endurance to pulsatile flow and prolonged stimulation, together with a good safety profile. This device could be used for neural recording or stimulation from within a blood vessel, for either central or peripheral nervous system thanks to the extension of the vasculature network. By simplifying the implantation procedure of the neural interface and maintaining transiency, physicians and patients could feel more confident in applying innovative neurotechnology-based treatments, widening for example the access to deep brain stimulation therapy.

In an attempt to reach even sub-millimetre sized vessels and enable crossing of complex vasculature, a new navigation paradigm combined with micro-engineered probes has been designed. A thin, ultra-flexible polyimide strip can move without manual push, propelled by only the hydrodynamic dragging forces of a pulsatile flow at physiologically relevant velocity. The device is able to cross even 3D knot-like structures with curvatures as high as 0.25 mm^{-1}. By attaching a small cylindrical magnetic head at its extremity, it is possible to control the direction of the probe in front of bifurcations using low magnitude magnetic fields, without manual push-based strategies of current guidewires, and thus reducing the risk of vessel walls perforation. By exploiting standard microfabrication procedures, electrodes and sensors for temperature and flow can be embedded onto these micro-probes, for unprecedented local interrogation of deep vasculature regions. The magnetic fields of this system can also induce bending and thrusts of the magnetic head to start a crawling-like forward pace of the probe in absence of blood flow. This allows for investigation of areas where flow is impaired, such as in obstructed arteries due to embolism, thrombosis, or traumatic injury.

In conclusion, this thesis introduces new neural interfaces in the field of minimally invasive neurotechnology, with the goal of reducing adverse effects and complications related to non-degradable implants and open surgery. These devices and the ideas behind them have the potential one day to be new tools of the bioelectronic medicine toolbox, contributing to the advancement of innovative treatments for neurodegenerative disorders.

Keywords

Sommario

L'elettronica «transiente» che consente ai dispositivi di scomparire in sicurezza nell'ambiente può essere applicata non solo nell'elettronica sostenibile, ma anche nella medicina bioelettronica. Gli impianti neurali in grado di degradarsi in modo innocuo all'interno del corpo eliminano la necessità di un intervento chirurgico di rimozione e potenzialmente riducono le risposte infiammatorie e le reazioni avverse croniche che ostacolano la funzionalità del dispositivo e mettono a rischio la salute dei pazienti. Al contrario, la lenta degradazione del dispositivo consente un rimodellamento sicuro dei tessuti attorno all'impianto e persino la migrazione delle cellule all'interno del dispositivo, come nel caso degli «scaffold» applicati nell'ingegneria dei tessuti. Gli impianti non degradabili invece non possono offrire tale opportunità e il più delle volte inducono lo sviluppo di un'importante capsula fibrotica, isolando elettricamente il dispositivo, allontanandolo dalla fonte di informazione (cioè i neuroni) fino a renderli inutilizzabili. La rimozione di tali dispositivi potrebbe essere complicata e rappresentare un rischio aggiuntivo per il paziente, se non anche un buon motivo per opporsi in primo luogo alla terapia. La strategia più recentemente impiegata per limitare questi effetti indesiderati è quella di ridurre al minimo l'invasività dell'impianto riducendone le dimensioni e in questo modo sono stati ottenuti risultati promettenti. Tuttavia, se dovessero verificarsi guasti hardware, perdita di efficacia della terapia o sviluppo di infezioni, potrebbe essere necessaria ancora la rimozione dell'impianto. Le interfacce «transienti» entrano quindi in questa scena di dispositivi minimamente invasivi affrontando le complicazioni croniche con materiali degradabili. Sfortunatamente, al momento la neurotecnologia «transiente» può essere utilizzata solo per applicazioni a brevissimo termine, come il monitoraggio della pressione o temperatura intracranica, o dell'attività neurale intorno agli interventi cerebrali. Se applicati al sistema nervoso periferico, potrebbero anche partecipare al miglioramento del recupero motorio dopo un infortunio o un ictus. Il motivo principale per cui per ora solo questo tipo di applicazioni è possibile è la breve durata dei materiali utilizzati per costruire queste interfacce: i metalli a rapido degrado consentono operatività raramente più lunghe di pochi giorni. Ciò limita fortemente la finestra di tempo disponibile per la raccolta di informazioni utili o per una terapia di essere portata a termine.

Per risolvere questo problema, proponiamo un'interfaccia neurale «transiente» interamente polimerica in grado di funzionare su scale temporali più lunghe. In questo modo si potrebbero consentire tempi operativi più lunghi mantenendo allo stesso tempo la temporaneità del dispositivo e della terapia. Ciò consentirebbe anche nuove applicazioni della neurotecnologia «transiente», come la registrazione dell'attività cerebrale per un periodo di tempo prolungato e maggiormente utile prima della resezione di focolai epilettici o di tumori. Il dispositivo è costituito da un substrato e chiusura in policaprolattone (PCL) con tracce ed elettrodi di poli 3,4-etilene diossitiofene: polistirene sulfonato (PEDOT:PSS). Il PCL offre una delle velocità di degradazione più lente tra i poliesteri biodegradabili e il PEDOT:PSS, biocompatibile, miscelato con glicole etilenico (EG), garantisce elevate proprietà elettrochimiche. I test in vivo dell'interfaccia sono stati eseguiti inserendola all'interno della corteccia visiva di topi e registrando crisi epilettiche, potenziali di campo locale e risposte visivamente evocate fino a dodici settimane. I risultati hanno mostrato bassi livelli di rumore per l'intera durata del test e l'analisi istologica ha evi-

denziato l'infiltrazione cellulare all'interno dello scaffold in PCL, suggerendo potenziali processi di rimodellamento dei tessuti, che non si verificherebbero con un dispositivo non degradabile.

Per aumentare il potenziale del dispositivo per una traslazione clinica e ridurre ulteriormente le risposte infiammatorie causate dalle interfacce penetranti, è stata proposta una procedura minimamente invasiva per il suo impianto. La vascolatura che irrora il cervello e i nervi può essere utilizzata come via alternativa per l'accesso al tessuto neurale, offrendo una posizione sufficientemente vicina ma senza causare danni diretti al tessuto. Questa strategia è già stata adottata con successo dall'azienda Synchron e dal suo dispositivo Stentrode™. Rimodellando il dispositivo «transiente» interamente polimerico basandosi su un design ispirato a quello di uno stent, la nuova interfaccia può essere navigata attraverso un catetere da 5Fr (circa 1.67 mm) e distribuita all'interno di canali di 2 mm di diametro. La caratterizzazione, specifica per il nuovo ambiente di lavoro, ha mostrato una promettente resistenza delle proprietà degli elettrodi ad un flusso pulsatile e ad una stimolazione prolungata, insieme a un buon profilo di sicurezza. Questo dispositivo potrebbe essere utilizzato per la registrazione di segnali nervosi o per la stimolazione neurale effettuata dall'interno di un vaso sanguigno, sia in riferimento al sistema nervoso centrale sia a quello periferico, grazie all'estensione della rete vascolare. Semplificando la procedura di impianto dell'interfaccia neurale e mantenendo la sua transitorietà, medici e pazienti potrebbero sentirsi più sicuri nell'applicare trattamenti innovativi basati sulla neurotecnologia, ampliando ad esempio l'accesso alla terapia di stimolazione cerebrale profonda.

Nel tentativo di raggiungere anche vasi di dimensioni sub-millimetriche e consentire l'attraversamento di tortuosità vascolari, è stato progettato un nuovo paradigma di navigazione combinato con interfacce micro-ingegnerizzate. Una sottile striscia di poliammide ultraflessibile può muoversi senza spinta manuale, ma spinta soltanto dalle forze di trascinamento idrodinamico di un flusso pulsatile a velocità fisiologicamente rilevanti. Il dispositivo è in grado di attraversare anche strutture 3D simili a nodi con curvature fino a 0.25 mm^{-1}. Attaccando una piccola testa magnetica di forma cilindrica alla sua estremità, è possibile controllare la direzione della sonda davanti a biforcazioni utilizzando campi magnetici di bassa intensità, senza strategie basate sulla spinta manuale di fili guida, riducendo così il rischio di perforazione delle pareti dei vasi. Sfruttando le procedure di micro-fabbricazione standard, elettrodi e sensori per la temperatura e il flusso possono essere incorporati in queste micro-sonde, per interrogazioni locali senza precedenti di regioni vascolari profonde. I campi magnetici di questo sistema possono anche indurre delle flessioni ripetute e le spinte conseguentemente generate della testa magnetica per avviare un'andatura strisciante in avanti della sonda in assenza di flusso sanguigno. Ciò consente di indagare le aree in cui il flusso è compromesso, come le arterie ostruite a causa di embolia, trombosi o lesioni traumatiche.

In conclusione, questa tesi introduce nuove interfacce neurali nel campo della neurotecnologia mininvasiva, con l'obiettivo di ridurre gli effetti avversi e le complicanze legate agli impianti non degradabili e alla chirurgia a cielo aperto. Questi dispositivi e le idee che stanno loro dietro hanno il potenziale per essere un giorno nuovi strumenti della cassetta degli attrezzi della medicina bioelettronica, contribuendo al progresso di trattamenti innovativi per i disturbi neurodegenerativi.

Parole chiave

Interfaccia neurale, elettronica transiente, biomateriali, polimero conduttivo, matrice di elettrodi su stent, minima invasività, controllo attraverso campi elettromagnetici, navigazione guidata dal flusso, attuazione magnetica, medicina bioelettronica

Contents

List of Figures

List of Tables

List of Equations

Chapter 1   Introduction

In this introductory chapter, pertinent concepts in the fields of biomaterials, neurotechnology and implantable devices will be presented. These are key elements to understand all facets of the proposed thesis. Starting from the concept of transient and biodegradable electronics, the focus will then be on devices at the interface with the neural tissue. Once the main limitations of current devices both in the academic and commercial worlds are defined, the strategies to overcome them and the consequent goal of the thesis will be described.

1.1 Transient electronics

The field of transient electronics include all electrically active devices that are able to fully or partially degrade in a harmless way in aqueous environments[1]. The most straightforward application of such devices is green electronics: reducing electronic waste (e-waste) by using degradable materials for its components could strongly compensate for the 50 million tons of electronic and electrical hardware produced in the world every year[2,3]. Another interesting application of transient electronics is the creation of sophisticated protection systems for sensitive data storage. These devices would for example need a trigger-induced degradation, to dissolve when needed[4].

Most relevant to this thesis is the application of transient electronics to the biomedical field. Degradable bioelectronics could open the doors to new implantable devices for therapeutics and diagnostics that, after completing their task, could safely be resorbed or eliminated by the body, without the need of a specific surgery for device removal. Moreover, given the degradation of the device within the body, this mechanism would allow the tissue around the implant to grow back with time and potentially reduce chronic inflammations that commonly occur with permanent implants. By triggering a strong inflammatory reaction, non-degradable devices could be more prone to operational failures than transient electronic devices. When a permanent implant ceases to work or becomes therapeutically ineffective, it could be difficult to retrieve it and dangerous to the patient. For this, degradable active implants could represent a more acceptable alternative, with potentially lower risks for the recipient.

Staying within the healthcare context, it would be possible to fabricate single-use medical devices that could replace current technologies with more eco-friendly counter parts. On the same line, degradable e-skins and wearable devices, used for the detection of biomarkers (i.e., pH, temperature) and motion would help reduce environmental pollution[5].

Before 2012 the degradability concept was mainly applied to polymers for passive biomedical implants, such as scaffold for tissue engineering. However, when the team led by John Rogers at University of Illinois reported in 2012 the first degradable form of silicon (**Figure 1.1**A), the possibility to make degradable active implants with embedded sophisticated electronic circuitry could be finally envisioned[6]. This technological advancement enabled the rise of transient electronics, that is in fact a materials-driven field of research.
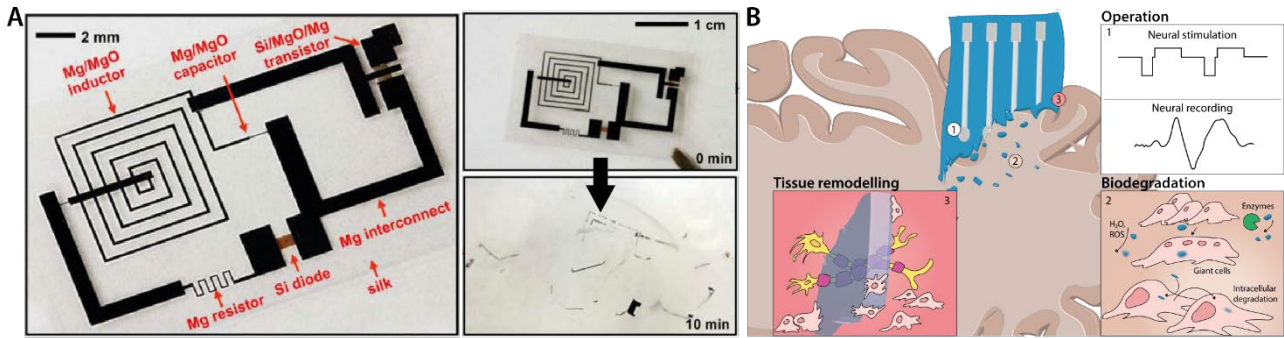
Figure 1.1 Transient electronics. A) First device prototype introduced by Hwang et al. in 2012 (left) and its degradation in water after 10 minutes (right). Adapted from Hwang et al.[6] **B**) Schematic representation of a degradable neural interface implanted in a brain, with insets showing: 1) possibility for neuromodulation or neural recording, 2) biodegradation mechanisms and 3) tissue remodelling through the degrading device by cells penetration.

1.1.1 Materials

Researchers can draw useful materials for transient electronics from several different pools. Natural and synthetic polymers offer tuneable mechanical properties and good insulation capability. For this reason, they are typically employed for the substrate and the encapsulation of transient electronic devices ('Carrier materials' in **Figure 1.2**). Conversely, degradable and non-toxic conductors, semi-conductors or dielectrics are typically used in the device operational elements ('Active materials' in **Figure 1.2**).
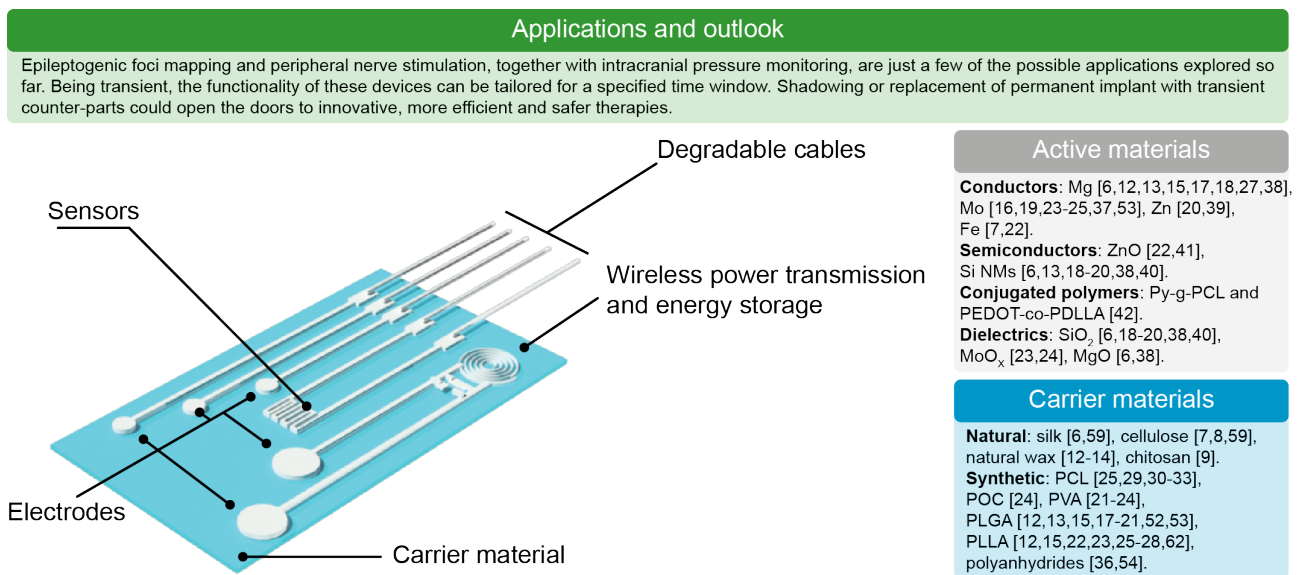
Figure 1.2 Transient neurotechnology. The green box highlights current applications and future outlooks of transient neurotechnology. A set of representative devices is shown in the sketch, with identified components. Materials used and suggested for active components (sensors, electrodes, traces and connections) and insulating carriers are listed in the grey and light blue boxes, respectively.

1.1.1.1 Carrier materials

Natural polymers such as silk[6], cellulose[7,8] and chitosan[9] provide soft and flexible scaffolds for transient implants with a low inflammation response. Also, their processability has been improved, together with their compatibility with electronics. Current challenges for this class of materials lie in their porous structure, potentially leading to premature leakage[8], poor lot-to-lot reproducibility and critical immunogenicity of animal-derived samples. So far, silk represents the best trade-off in this category[9–

[11]. Finally, natural waxes could be exploited as an insulating material or, when mixed with conductive micro and nanoparticles, as electrical components[12–14].

Synthetic polymers and their combinations offer highly tailorable degradation rates allowing transient devices to adapt to a wide range of applications requiring functionality for different periods. Common synthetic polymers in this field are: poly-l-lactide-co-glycolide (PLGA) [12,13,15–21], polyvinyl alcohol (PVA) [21–24], poly-l-lactide (PLLA) [12,15,22,23,25–28] and poly-ε-caprolactone (PCL) [25,29–33]. The interest in these materials is understandable as they all have Food and Drug Administration approval for certain medical applications[11,34,35]. Their main degradation route in the body is via hydrolysis, with their by-products becoming water-soluble and then excreted or entering the tricarboxylic acid cycle and being eventually cleared in the form of carbon dioxide and water[11]. As an alternative, polyanhydrides have also been proposed as encapsulation components of transient electronics, offering a hydrophobic barrier to biofluids[36]. For devices that need to sustain high strains, degradable and stretchable elastomers have been developed. Poly (1,8-octanediol-co-citrate) (POC) can endure strains as high as 50% while maintaining the electrochemical performances of stretchable supercapacitors built on its surface[24]. PCL-derived polyurethanes with Young's modulus lower than 3.8 MPa can ensure efficient insulation for 30 days[37].

1.1.1.2 Active materials

Conductive materials are crucial components of neurotechnology. Transient devices typically use metallic-based conductors, such as magnesium (Mg) [6,12,13,15,17,18,27,38], zinc (Zn) [20,39] and molybdenum (Mo) [19,23–25], which are also conveniently involved in biological functions[9]. One of the advantages of these metals is their complete solubility, by hydrolysis as electrochemical reaction with water (their standard electrode potential is lower than the one of oxygen)[1]. However, it also represents their main weakness since their fast dissolution reduces the device lifetime to a few days or weeks, maximum.

Semiconductors is another relevant category of materials used in transient devices. A standard Si-based integrated circuit of a few hundred microns in thickness will require several hundred years to dissolve by hydrolysis. On the other hand, thin monocrystalline silicon nanomembranes (Si NMs) and nanoribbons of tens of nanometres in thickness can disappear in less than a few weeks, degrading into $Si(OH)_4$ well below solubility limits and toxicity levels[6]. The degradation kinetics of Si NMs can vary mostly according to dimension, solution content and silicon doping[1]. Biologically friendly silicon opens the doors to more sophisticated electronics patterning on transient substrates[6,13,18–20,38,40]. Zinc oxide (ZnO) is also used as a biodegradable semiconductor in transient thin-film transistors[41] and energy storage units[22].

Conjugated polymers represent an attractive alternative as active materials for transient neurotechnology. Degradable conductive or semiconducting polymers are obtained generally by mixing pristine or doped conjugated polymers, such as polyaniline (PANI), polypyrrole (PPy) or poly(3,4-ethylenedioxythiophene) (PEDOT), with degradable polyesters, polyurethanes or natural polymers[42]. The advantage of this solution is tailoring the degradation rate of the conductive components of transient devices, thus overcoming the fast dissolution rate of some metals. Nevertheless, this advantage comes at the cost of a substantial reduction in conductivity[42]. For this reason, their use in transient electronics has been delayed.

Last, films of silicon oxides (SiO_2) [6,18–20,38,40], magnesium oxides (MgO) [6,38] or molybdenum oxides (MoOx) [23,24] can be used as degradable dielectrics.

1.2 Transient neurotechnology

Transient electronics also becomes appealing for medical applications like neurotechnology, where electrically active devices are employed at the interface of the neural tissue for either status monitoring or stimulation of excitable cells. As mentioned before, transient, biodegradable and implantable devices are attractive because they eliminate the risks related to surgical retrieval[25] and reduce the chronic inflammation and foreign body reaction (recruitment of monocytes and lymphocytes, followed by fibroblasts migration, macrophages fusion and formation of fibrotic capsule around the implant)[43,44]. Permanent implants might be subjected to bacteria and biofilms development leading to infections and the consequent need for their removal[45–50]. Since the first pioneering work[6], transient bioelectronics have grown fast, opening possibilities never thought of before. Among others, the portfolio of devices presented so far includes biodegradable sensors for monitoring neural activity, pressure, pH, biomarkers, temperature, motion and blood flow[12,13,26,27,30,38,51,52], remotely controllable on-demand drug delivery systems[15], smart stents[31], power supplies[17,22,23,32,53,54] and neural stimulators[18,37,55].

In neurotechnology, transient electronics is still in its infancy, but it represents an exciting direction towards innovative solutions to alleviate the burden of neurological and mental disorders.

1.2.1 Recent transient devices in neurotechnology

Multiple and multifunctional bioresorbable devices have been manufactured, addressing several medical needs, from transient monitoring of biological parameters to transient neurostimulation.

Continuous monitoring of the intracranial pressure (ICP) in patients that underwent a traumatic brain injury or invasive surgical procedure (e.g. decompressive craniectomy) is crucial to understand the clinical condition, improve the treatment and avoid possible adverse effects[56]. Kang et al. developed a wireless and fully degradable ICP sensor able to work for three days and degrade entirely within eight weeks in vivo (**Figure 1.3**A). A temperature sensor (**Figure 1.3**B,C), a pH sensor and accelerometers were added on the same degradable platform for a more comprehensive clinical status[38]. In another study, a temperature-sensitive capacitor, consisting of polyethylene glycol (PEG), monitored the rat's intracranial temperature for four days[12]. Yang et al. extended the device lifetime by adding natural wax to the encapsulation[13]. Moreover, additional sensors were integrated to warn of leakage due to biofluids penetration. The device remained functional for three weeks in vivo. Lu et al. implemented an LC-resonance system coupled with a pressure-sensitive capacitor to bypass the percutaneous wires connected to the external device and eliminate the need for a battery[52]. The device monitored the ICP and temperature in rats for four days before degradation.
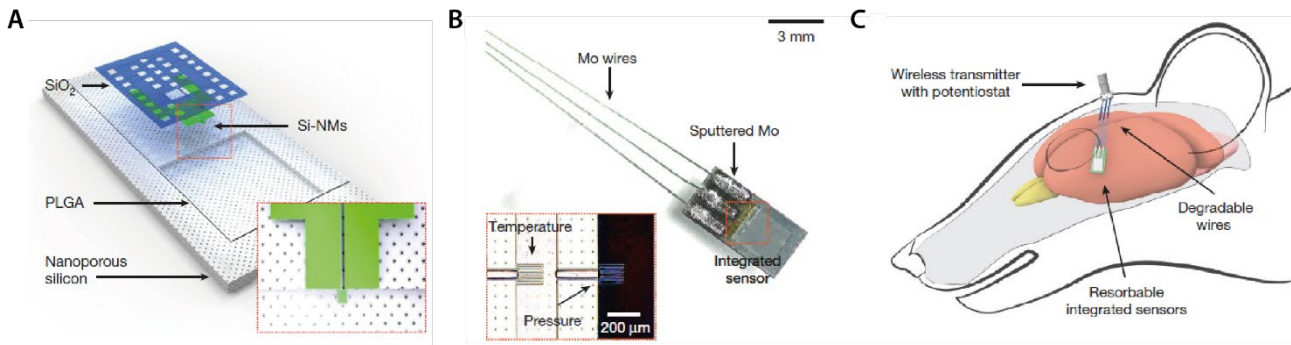
Figure 1.3 Biodegradable sensors for the brain. A) Schematics of the intracranial pressure sensor designed by Kang et al., with inset showing the sensing Si NMs. B) Biodegradable multisensory platform with detectors for intracranial pressure and temperature designed by Kang et al. C) Schematics of the implantation of the device in B in mice, with wireless data transmitter. Figure adapted from Kang et al. [38].

Neural interfaces take advantage of transient neurotechnology by connecting the brain and nerves within a predetermined temporal window. The electrocorticography signal is typically used for foci mapping in drug-resistant epileptic patients before and after surgical sectioning of epileptogenic areas. Monitoring the neural activity depends on the surgery frequency and can last for several days[57]. Transient neural interfaces perfectly fit this application. Yu et al. developed a transient neural interface (**Figure 1.4**A) able to capture interictal and seizure-like spiking activity in mice for a month before degrading, as well as smaller amplitude signals such as somatosensory evoked potentials (**Figure 1.4**B) [19]. Xu et al. added a degradable pressure sensor on the same platform to monitor cortex swelling during neural recording[25]. Neural signals monitoring was also demonstrated by Bai et al. using bioresorbable photonic devices able, as spectrometers, to sense the cerebral temperature and its oxygen saturation[20]. Similarly, Fu et al. fabricated a biodegradable fibre for optical neural interfaces capable of deep brain fluorescence sensing and optogenetic interrogation in vivo for up to three days[28].

Neurostimulation is crucial to address neurological and mental disorders. Transient neurotechnology offers exciting answers also in this direction. Koo et al. reported regeneration and functional recovery of injured nerves by electrical stimulation using a fully biodegradable cuff electrode wirelessly controlled through an Mg-based antenna (**Figure 1.4**C-E) [18]. Radiofrequency power transfer generates enough voltage from the electrodes for nerve activation at a depth of 80 mm. This transient neurostimulator overcomes the limits of intraoperative stimulation used to enhance neural recovery, allowing extra-operational and on-demand wireless stimulation for six days. The lifetime of this device was then extended by Choi et al. by using materials with slower degradation rates (i.e. PCL-derived polyurethane for encapsulation and Mo for electrodes) [1,37].
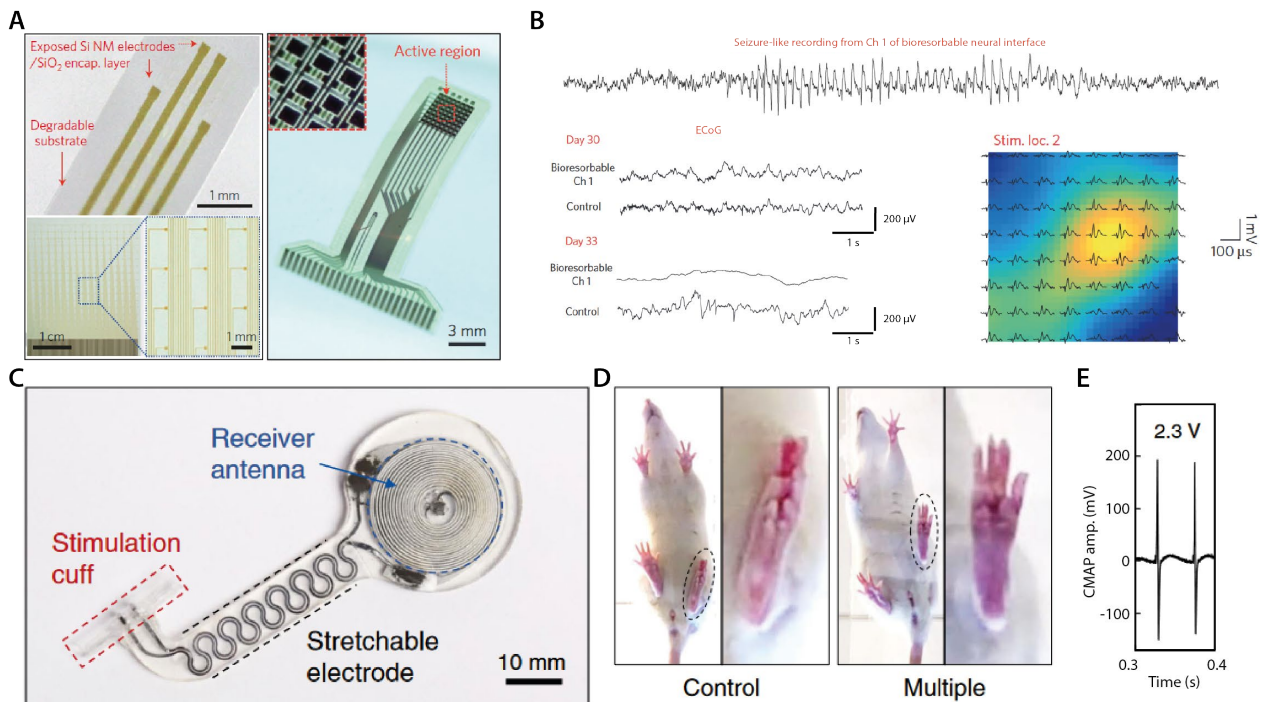
Figure 1.4 Neurostimulation and neural recording with biodegradable electronics. **A)** Different configurations of a biodegradable electrode array for neural recording, with 4-electrode configuration (top left) and 16 x 16 configuration (bottom left), with 128 field-effect transistors (bottom right) with source, drain and gate electrodes in Mo (300 nm thick) and channel in SiO_2 (300 nm thick). Encapsulation is in $SiO_2/Si_3N_4/SiO_2$ and substrate is in PLGA. The traces and electrodes, in Si NMs (300 nm thick), are encapsulated in 100 nm of SiO_2 and 30 μm of PLGA. **B)** Top, seizure-like recordings from the device in A implanted in rat; bottom left, electrocorticography (ECoG) recordings from the device in A, at day 30, when the device is still operational, and at day 33, when the device stops working. Control electrode is a non-degradable stainless-steel microelectrode; bottom right, cortical recordings from the 64 sensing channels of the device in A after stimulation of a whisker. Pictures and graphs of A,B are adapted from Yu et al.[19]. **C)** Stretchable cuff-electrode for non-pharmacological neuromuscular regeneration. Substrate (100 μm thick), encapsulation (100 μm thick) and inter-layer (50 μm thick) are in b-DCPU; the stimulation cuff is in PLGA, 30 μm thick; electrodes and traces are in Mo, 15 μm thick and 200 μm wide; the diode is in Si NMs, 1.2 μm thick; the stacked coils are in Mo, 50 μm thick. **D)** Functional recovery of injured left hindlimb showed by increased toe spread after multiple neurostimulation with the device in A. **E)** Compound muscle action potentials (CMAPs) measured from the gastrocnemius muscle and generated by stimulation at 2.3 V of the sciatic nerve by the cuff-electrode in C. Pictures and graphs in C-E) are adapted from the work of Choi et al.[37].

Implantable and biodegradable energy providers represent an alternative to wireless power transfer. One of the first biodegradable batteries was developed by Yin et al., who compared single-cell batteries with an Mg anode, phosphate-buffered saline as electrolyte and a cathode material varied among iron, tungsten and molybdenum, all encased in polyanhydride (**Figure 1.5**A) [58]. Huang et al. developed a fully biodegradable and self-electrified device for neuroregenerative medicine with a battery composed of an Mg anode, a sodium alginate electrolyte and a $Mo-MoO_3$ cathode, all encapsulated by a PLGA-polyanhydride layer[54]. Similarly, Sheng et al. developed a fully biodegradable supercapacitor made out of in situ grown flakes of amorphous MoO_X electrodes and a sodium alginate electrolyte gel. Experiments in mice demonstrated device integrity for approximately a month before packaging rupture, followed by complete resorption in six month[23]. Another bioresorbable capacitor was introduced by Li et al. PLLA, ZnO, Fe and PVA/phosphate-buffered solution hydrogel were the main components of their device (**Figure 1.5**B,C) [22]. The operational lifetime in vivo was fifty days, and complete degradation occurred within six months. In the future, it would be interesting to apply piezoelectric and triboelectric energy transducers in neurotechnology. Degradable materials with such properties have been recently tested for biomedical applications[21,53,59–62]. Jiang et al. reported several bioabsorbable triboelectric nanogenerators based on natural materials, reaching open-circuit voltages between 8 and 55 V (**Figure 1.5**D-F) [60]. Curry et al., instead, optimised the crystallinity and alignment of PLLA nanofibers to create a piezoelectric transducer, sandwiched between Mo electrodes, to convert electrical input into ultrasound waves for the transient opening of the blood-brain barrier in mice[61].
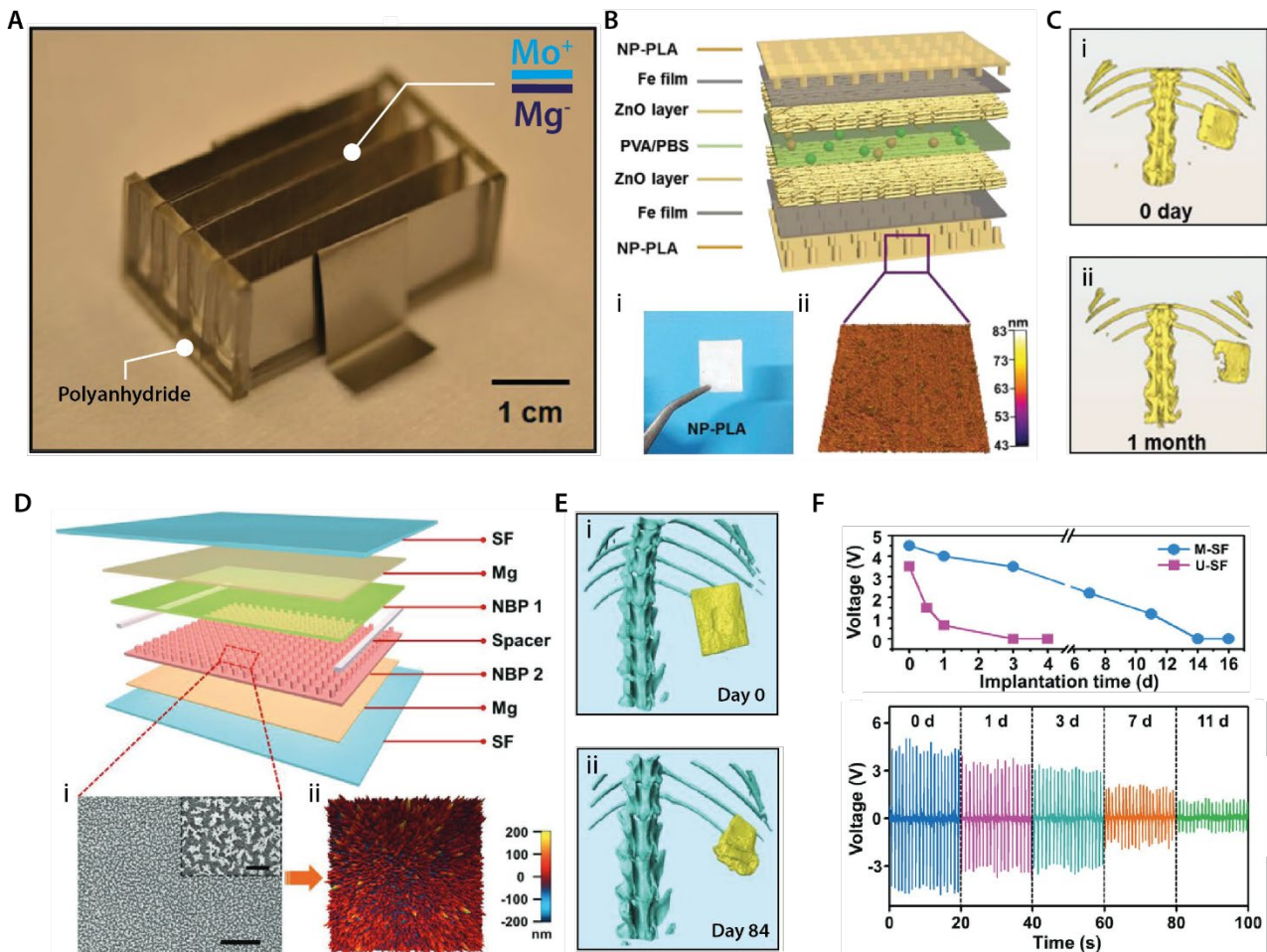
Figure 1.5 Degradable batteries and bioabsorbable triboelectric nanogenerators (TENG). A) Image of a biodegradable battery with Mg-Mo cells stacked in series, with phosphate-buffered saline as electrolyte and encapsulated in polyanhydride. Adapted from Yin et al.[58] **B**) Exploded structure of a bioabsorbable capacitor built with PLA nanopillars, Fe, self-assembled nanoporous ZnO and PVA/PBS hydrogel (electrolyte). The red and green spheres in the electrolyte represent cations and anions. The inset **i**) shows a picture of the NP-PLA film; the inset **ii**) shows the atomic force microscopy morphology of the NP-PLA film. **C**) Micro-computed tomography of the device implanted in rat **i**) at day 0 and **ii**) after one month. B and C are adapted from Li et al.[22] **D**) Exploded structure of a general biodegradable triboelectric nanogenerator comprised of silk fibroin (SF) and Mg. NBP 1 and 2 stand for natural bioresorbable polymer 1 and 2, which could be any among chitin, cellulose, SF, rice paper and egg white, and work as friction layers. Inset **i**) is a scanning microscopy picture and **ii**) an atomic force microscopy picture of an NBP (not specified in the original manuscript). Scale bar in **i**) is 5 μm; 1 μm in the magnification. **E**) Micro-computed tomography image of in vivo degradation of a silk fibroin-TENG in rats. The image in **i**) is taken on day 0 and the image in **ii**) is taken on day 84. **F**) Top: output voltage monitored in vivo of a methanol treated silk fibroin-TENG (M-SF) compared to a non-treated one (U-SF); bottom: 20-s electrical output recording of M-SF TENG in vivo. D-F are adapted from Jian et al.[60].

1.2.2   New research directions and challenges in transient neurotechnology

There are multiple possibilities introduced by transient electronics in the biomedical field. Advancement in chemistry, materials science and engineering allowed the definition of a new class of devices with a bright future in medicine. However, new research directions can be explored to expand the potential of these devices.

Transient devices can find application in several clinical cases like temporary brain mapping or preliminary trials of neurostimulators. By degrading harmlessly over time inside the body, no complicated removal surgery is required when the device is not needed anymore or if it malfunctions. Also, transient neurotechnology reduces the waste of non-degradable disposable neural interfaces. Moreover, the absence of a permanent implant potentially allows the tissue to safely remodel around the site of implantation, decreasing the risk of chronic infections and inflammation. Biocompatible temporary implants could offer an invaluable instrument for research as well. Despite the invasiveness of the im-

plantation procedure, transient neural interfaces might provide a more attractive alternative to standard devices for patients undergoing innovative treatments allowing neuroscience research to advance.

The challenges in the field include the limited compatibility of standard microfabrication processes with biodegradable materials and the limited range in the degradation rate of the active components. In the past years, implantable neurotechnology has largely improved thanks to materials and fabrication strategies enabling soft [63], stretchable [64], conformable [65] and injectable [66] devices for compliant and minimally invasive neurotechnology. Some biodegradable polymers have appropriate mechanical properties, such as, among others, low elastic modulus, high strain at break and low hysteresis. However, their limitation often arises from the low compatibility with standard fabrication processes. Low temperature and solvent-free fabrication techniques are necessary for building biodegradable neurotechnology. However, the reproducibility and reliability of these manufacturing methods still need improvement compared to standard cleanroom processes.

Another challenging research direction is the alignment of the materials degradation rate with the required device lifetime. Some applications might be short-term (e.g., a few days or a couple of weeks), and available transient neurotechnology can match this timeline already. For example, intraoperative brain mapping of epileptogenic areas lasts hours before resection, while two weeks are sufficient for intracranial pressure monitoring after surgery[67]. Other applications might require longer durations, and the device degradation rate must be tailored accordingly. This material-related issue is currently faced by developers of bioresorbable stents, for which mechanical support is vital within the first 3–6 months after deployment[68]. In neurotechnology, a longer device lifetime (i.e., > two months) might be beneficial in neurostimulation for regeneration and functional recovery after nerve injury, surgery and stroke events[69,70]. Successful pain relief at 12 months has been obtained after a peripheral nerve stimulation therapy of 60 days[71]. A longer therapeutic application might further improve recovery. The short-term functional life of devices is associated with the fast degradation of metals used in the active elements (e.g., Mg, Zn and Mo). Conductive or semiconductive materials with a slower degradation rate are necessary to extend the lifetime of transient devices. Degradable conductive polymers are advantageous for researchers to tailor the degradation rate. However, today this improvement is at the expense of their conductivity. The search for highly performant conductive and semiconductive biodegradable polymers is needed in transient neurotechnology.

Achieving a slower degradation rate and longer lifetime might also enable transient neurotechnology for long-term applications. Whereas the transient electronics concept is intrinsically founded on temporary applications, chronic use of such devices could also be investigated. Permanent implants such as deep brain stimulators, cardiac defibrillators and pacemakers, are often subjected to infections[45–48], loss of efficacy or appearance of adverse effects[49]. These problems can lead to complete or partial removal, substitution or repositioning of the device even within just the first year of implantation[48,49]. Thus, transient devices able to sustain active functioning for longer periods before degrading offer the opportunity to mitigate these issues. Similarly, biodegradable power supplies with a slow degradation rate could substitute current non-degradable batteries, which need replacement every 2–5 years[50].

Regardless of the device duration, the disposal of the implant within the body might require a different timeline. Slow degradation is an appealing feature for transient neurotechnology since it might also allow for better tissue remodelling and reduced chronic postsurgical wound complications[1,30,39]. On the other hand, trauma upon implantation is unavoidable; therefore, making transient neurotechnology combined with drug delivery and regenerative medicine is an exciting pathway to lower acute reac-

tions. While degrading, the transient neurotechnology might in fact release compounds to mitigate the inflammatory response or embed cells to promote tissue remodelling and regeneration.

1.3   A minimally invasive approach in neurotechnology

The ultimate goal of developing a transient neural interface is to minimize patients' discomfort for the best therapeutic outcome. In fact, as mentioned before, using degradable materials and embedded drug delivery systems could reduce inflammation, so that these body-compliant materials do not cause counterproductive reactions of the tissue hindering device functionality and thus necessitate further intervention on the patient. Moreover, removing the need for device retrieval eliminates additional surgeries for the patient. It could be said then that such a device design is in line with the "minimally invasive approach"[72,73]. There is no universal definition of what is "minimally invasive" but Paul S. Larson, MD suggested a few guidelines in the field of deep-brain stimulation (DBS): "decrease patient's discomfort, reduce operative time, and/or minimize penetration of the brain"[73]. When designing a minimally invasive neural interface, all these aspects should be addressed.

Besides the choice of materials, the device size deeply impacts the surgical footprint left after implantation, in terms of lesion size, blood vessels avoidance and consequent inflammatory reaction to the implant. Multiple efforts have been recently put in place to reduce the size of implantable microelectrode arrays and therefore, the penetrated volume in the brain[74–76]; some relevant examples of devices that are minimally invasive in this sense are reported in the next paragraphs.

Zhao et al. successfully developed a 1 µm-thick flexible neural electrode array, called nanoelectronic thread, NET (**Figure 1.6**A,B) [77], that can be implanted using 12 µm diameter tungsten microwires as a temporary shuttle, leaving a minimal surgical footprint of less than 200 µm^2. Histology after two months from implantation in mice revealed normal neural and astrocyte density (**Figure 1.6**E). This result is in line with a previous report by the same group, where no glial scar formation occurred with the same device after five months from implantation, astrocytes surrounded only capillaries in a physiological way, microglia was not activated, and neuronal distribution was not preferential with respect to device location (**Figure 1.6**C,D). Moreover, the recording performance of the electrodes was stable in the long-term: noise level decreased and the number of active electrodes and the signal-to-noise ratio (SNR) value increased in the first month and remained stable up to four months[78]. However, a cranial opening of 3 mm by 3 mm was necessary to access the brain and implant the device with the shuttle[79].

Guan et al. proposed instead a degradable shuttle for their Neurotassels[80]: 12 x 3 µm probes were assembled by capillary forces inside a pure PEG shank that dissolves when implanted in the wet biological tissue. Compared to the NET, each thread is clearly thicker and larger, but it can allow for a valuable trade-off between higher channel counts and minimal footprint. In fact, immunohistochemistry after five weeks from implantation showed a minimal neuronal cell loss around the implant, which was less than the one induced by a silicon probe with a similar cross-section. Also in terms of signal quality, the Neurotassels obtained an SNR of approximately seven, which was stable for six weeks, and they were able to isolate multiple sortable neurons at all time points (10 µm diameter electrodes). Moreover, the cranial opening needed to implant the device was only 2 mm^2. Compared to the NET, Neurotassels can be scaled-up to 1024 channels and still assembled in a PEG fibre of approximately 100 µm diameter, by reducing the thread cross-section to 3 x 1.5 µm^2, similar to neurites size. In a follow-up work[81], they pushed the dimensions of the probes even further to approach mechanical characteristics of neurons: the new electrodes consist in free-standing films of 50 or 100 nm of gold, 25 µm

long and 3 μm wide. The traces of these electrodes are insulated between two layers of 1 μm thick polyimide. Additional holes in between traces were cut out of the polyimide. After twelve weeks from implantation of the device (120 channels) in mice brains, with the same method based on the PEG shuttle, it is possible to notice tissue penetration inside the holes of the device and neuron continuity across it. This allowed for identification and tracking of neuron populations during a behavioural task and identification of 71 single units at twelve weeks post-implantation.

As an alternative strategy to avoid completely the use of a temporary/degradable shuttle for device implantation and further reduce the surgical footprint, Vitale et al. developed a microactuation system that exploits tension forces to insert their microfibers inside a mice brain. These carbon nanotubes fibres (CNTf, **Figure 1.6**H), with diameters ranging from 12 to 25 μm, do not buckle and are smoothly inserted by this system (**Figure 1.6**F)[82]. Computational simulations showed that applying force on a single point on them, such as when insertion is manual, is more inefficient than distributing the applied load along the probe. Their system consists in a polydimethylsiloxane (PDMS) microfluidic device where the flow of a phosphate-buffered saline (PBS) and dextran solution pushes a microwire inside a mouse brain, without bending or rupture, nor excessive fluid injection in the brain that could affect its pressure levels. Even though this delivery system is attractive, unfortunately they didn't report data concerning the tissue response to it, nor the size of the skull opening needed for insertion (**Figure 1.6**G).
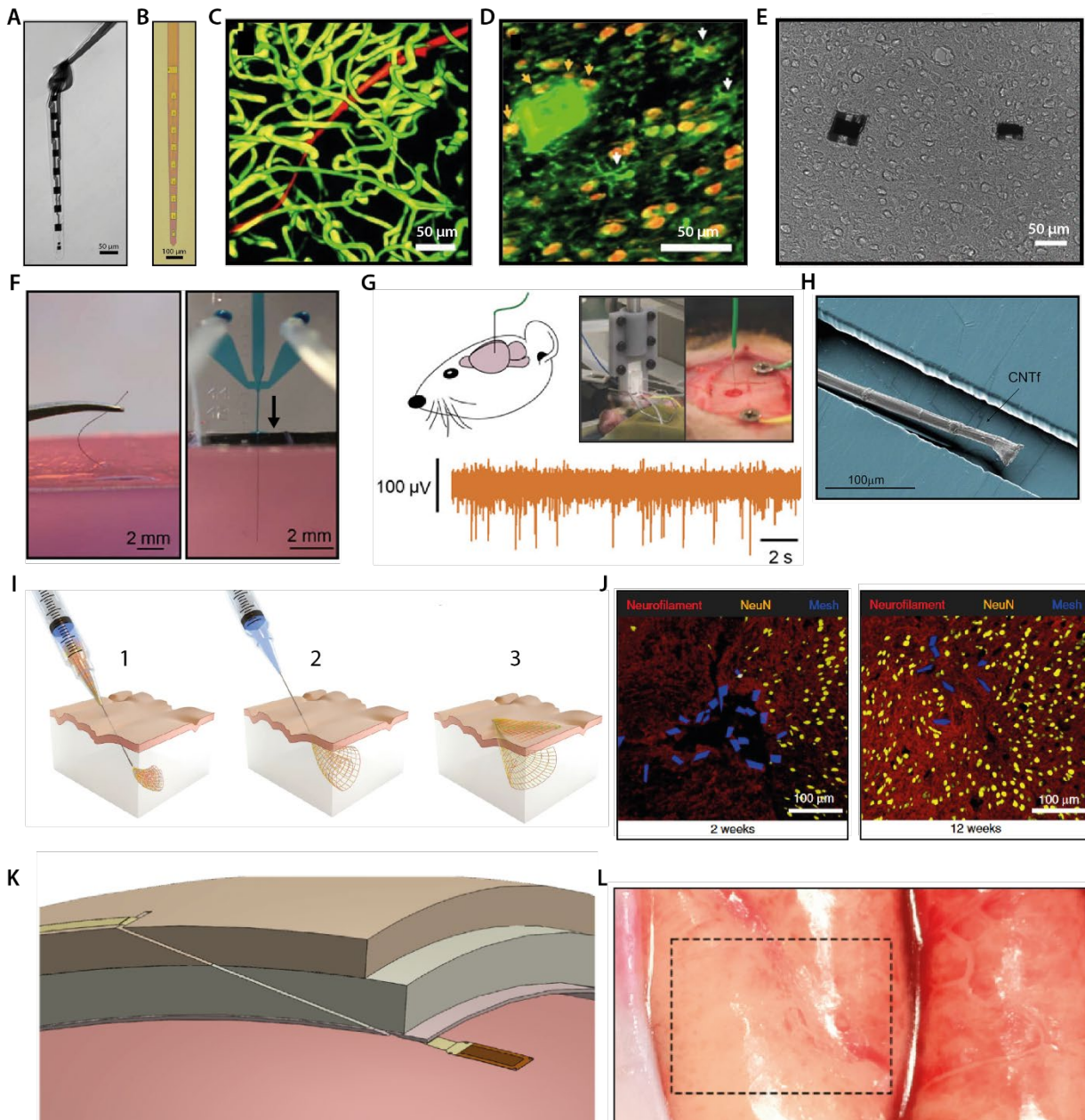
Figure 1.6 Minimally invasive implants and implantation procedures. **A**) Picture of a NET device suspended in water and knotted at the tweezer tip. Scale bar is 50 μm. **B**) Microscopy picture of a NET after fabrication. Scale bar is 100 μm. **C**) Reconstruction of blood vasculature around the implant via 2-photon microscopy after 2 months from implantation. **D**) Projections of confocal micrographs showing nuclei somata in orange (NeuN) and microglia in green (Iba-1), around the NET implant after 5 months from surgery. White arrows indicate microglia soma and the orange arrows the neuron in contact with the device. A-D are adapted from Luan et al.[78]. **E**) Normal distribution of neurons and tissue morphology around the NET implant after 2 months. Adapted from Zhao et al.[77]. **F**) Failed attempt of manual insertion of a CNTf microelectrode in agarose (left) and successful insertion using a microfluidic propulsion (right). **G**) Sketch of in vivo testing in rat (top left) and actual setup of implantation of CNTfs using the microfluidic device in D (top right). In orange a representative trace of neural recording by the CNTf microelectrode in acute experiment). **H**) SEM image with false colours showing the 12 μm microelectrode inside the microfluidic channel. D-F are adapted from Vitale et al.[82]. **I**) Schematics of the delivery of the mesh electrodes proposed by Fu et al. and Liu et al. Injection can be done using a capillary needle. Adapted from Liu et al.[83]. **J**) Horizontal brain slices stained for neurofilaments (red, neural axons), NeuN (yellow, neural somata) and implanted mesh (blue) at different time points (2 and 12 weeks) in the hippocampus (left) and cortex (right). Adapted from Fu et al.[84]. **K**) Schematics of the cranial micro-slits through which a subdural polyimide electrocorticography (ECoG) array is inserted. The dark orange rectangle is the polyimide pocket at the back of the device, inside which the stylet is inserted to pull the device. The stylet is already removed in the schematics. **L**) Microscopy picture of the undamaged cortical surface post-mortem, after removal of the device in K (location indicated by the dashed rectangle). K and L are adapted from Ho et al.[85].

Another "minimally invasive" device is the mesh electrode-array presented by Fu et al.[79,84]. Not only did they aim at minimizing the size of the implant and the impact of the implantation procedure, but they also chose materials and geometries that would give their electrode-array mechanical properties

similar to those of the neural tissue (0.1 nN m bending stiffness of the device) to further reduce inflammatory reactions. The mesh is 800 nm thick, and each strand is 20 μm wide. It can be folded inside a glass capillary needle with an outer diameter of 650 μm, for which a 1 mm-burr hole is opened through the dura. By connecting this needle to a loaded syringe, it is possible to deliver the mesh inside the brain by controlling the syringe flow (20-50 ml h^{-1}, total injected volume 10-100 μl, **Figure 1.6**I). After delivery the external connections of the electrodes are handled. Due to the injury caused by the insertion needle, at two weeks post implantation cell density around the implant is low; however, at six- and twelve-weeks astrocytes, microglia and neurons are present at a normal density through and around the mesh, suggesting low chance of chronic inflammation (**Figure 1.6**J). This was confirmed by histology data after 1 year post implantation. In a following work the authors further miniaturized the mesh to fit inside a 170 μm outer diameter needle and delivered it inside mice brains leaving a footprint diameter of 185 μm, but no histological data has been reported yet[86].

Similarly, Ho et al. recently reported a polyimide-based microelectrode array that can be implanted in a minimally invasive procedure[85]. The procedure consists in cutting cranial oblique micro-slits, of 5.5 mm length and 400 μm width, and, under endoscopic and fluoroscopic guidance, the device is led through them using a stylet. The stylet is inserted in a PI pocket attached to the back of the MEA and from there it pulls the device inside the cranial slit. Once the electrodes are in contact subdurally with the brain, the stylet is retrieved, leaving the electrocorticography (ECoG) array inside (**Figure 1.6**K). This delivery procedure didn't cause tissue damage or pia rupture in Göttingen minipigs, even after removal of the device (**Figure 1.6**L). It must be noted that for this test the authors did not mention at what time point the device was removed. In this particular case, the device size was not minimized as in the previous examples, although the total thickness is still low (20 μm), the electrode density high (529 electrodes per 0.48 cm^2 cortical area) and the skull incision small (approximately 5.5 mm x 400 μm).

Finally, on the road of miniaturization of neural interfaces, it's worth to mention the novel approach to neuromodulation represented by the use of smart nanoparticles (NPs) [76,87]. For example, piezoelectric NPs can be targeted by ultrasound waves to locally generate a voltage stimulating the surrounding neurons; similarly gold NPs can be excited using light and locally produce heat (photothermal effect), causing capacitive currents depolarizing neurons membranes. Conjugated polymer NPs can also be used as nano-photovoltaic cells that, once illuminated with a proper wavelength, generate enough voltage to stimulate cells. However promising NPs are, thanks to their dimension and injectability through micro-syringes, the main challenges faced by this technology are the poor control over biodistribution, unclear biosafety and the lack of cellular target specificity without appropriate gene therapy.

These works support the hypothesis that a smaller device can be considered as "minimally invasive" in terms of minimizing the skull opening and reducing the inflammatory response by minimizing the lesion size created in the tissue by a miniaturized implant.

However, in all the cases described in the last paragraphs, a burr hole in the skull was always indeed necessary to deploy the devices inside or onto the brain. Compared to complete craniotomy, as of today there is not sufficient data to strongly define burr hole drilling less risky, but rather with comparable outcomes[88–90]. For this, not all neurosurgeons prefer these innovative procedures. In terms of terminology, these surgeries fall within the minimally invasive neurosurgeries procedures[73,91,92]. The International Society on Minimally Invasive Neurosurgery (ISMIN) affirms however that a level I or II recommendation for a minimally invasive procedure, such as the key-/burr- hole surgery, cannot be provided[92]. To clarify, the Congress of Neurological Surgeons (CNS) defines as level I recommendation

one that is supported by evidence from randomized clinical trials, and level II recommendation one whose evidence is given by comparative clinical studies, such as non-randomized, case-control and other comparable studies. More information about these guidelines can be found at: https://www.cns.org/guidelines/guideline-procedures-policies/guideline-development-methodology. The absence of these trials nowadays defines the impossibility for a level I or II recommendation of such procedures compared to well-established full craniotomies. In fact, it would not be possible to expect from a patient the availability for an unnecessary larger incision, with a consequent larger scar leftover, when a smaller option is available[92]. If on one hand the patient's choice might justify the need for small-scar procedures, on the other hand this makes it difficult to establish that smaller incisions unequivocally imply less risks and leaves the choice to the discretion, opinion and experience of the surgeon.

A strongly promising approach that bypasses completely any cranial opening for the implantation of a neural interface is the one recently proposed by Oxley et al. and sporadically used in the past[93]. This strategy exploits the blood vessels as an access route to the brain, using wire electrodes or electrodes mounted on a stent to perform neural recording and stimulation from within a vascular channel. This approach allows access to the neural tissue avoiding potential damage caused by direct contact to it. Given the anatomical distribution of the vasculature, an endovascular electrode array might be implanted not only in the brain, but also in limbs for example for neuromodulation of the neuromuscular system in a motor rehabilitation context.

Concerning terminology, this approach might also be considered "minimally invasive" as it even eliminates penetration of the neural tissue, avoiding possible fibrotic scar formation and consequent loss of information, and with minimal surgical incisions. However, according to this terminology there shouldn't be any difference between the endovascular devices and penetrating probes described above. In fact, even the stimulator of DBS therapy is considered minimally invasive. On the other hand, the risks associated with endovascular implantation of devices might be less compared to those of keyhole craniotomies, but the terminology nowadays would be the same. There is a need for new terminology that, rather than describing invasiveness, defines a risk level. As a matter of fact, what is commonly defined as "minimally invasive" is what is actually thought of as "minimally risky". In an attempt to clarify this, Leuthardt et al. suggested a more risk-specific terminology to be used as a standard in the field of Brain Computer Interfaces (BCIs)[94]. When describing a BCI system, according to the authors, one could classify devices as: "non-invasive" (i.e., no skin penetration), "embedded" (i.e., penetrating until the inner table of the cortical bones) and "intracranial" (i.e., penetrating the intracranial space). Implantation procedures of "embedded" devices do not carry life-threatening risks or high morbidity probability. "Embedded" devices can be "minimally invasive" if the surgical incision is less than 1 cm long. "Intracranial" devices instead might cause life-threatening risks, brain injury, infection, and haemorrhage. Additionally, "intracranial" devices can be "minimally invasive" if the surgical incision is less than 1 cm long. According to the authors then, a "minimally invasive" device is not necessarily one with less risks. Nonetheless, endovascular and tissue penetrating probes would still fall within the same category of "minimally invasive intracranial" devices. A more in-depth analysis of the risks of different implantation procedures could further discriminate among the safety of different devices, especially of the endovascular ones. However, given the early stage of these technologies, it is difficult to reach a fair comparison today.

As of today, common risks associated with DBS system implantations and use are infection (4.2-10%), confusion (5.98%), hematoma (3.3%) and intracerebral haemorrhage (1.3%)[95–97]. However, confusion and haemorrhage occurrence can decrease with increasing surgeon experience[96]. In comparison, im-

plantation of endovascular devices such as cardiovascular implantable electronic devices (CIED) showed 0.9% of infection rate at 1-year follow up in 2 separate studies[98,99]. One of which details that 75% of the infections occurred at the pocket site and the remaining 25% was bacteraemia or endocarditis[99]. Another work analysed longer follow up periods and reported a 6.2% rate of infection at 15 years from implantation and 11.7% at 25[100]. Overall, 66.1% were at the pocket site and 33.9% were blood stream infections. These results suggest that for CIED, most infections occur at the pocket site, and not at the endovascular electrodes. For this, a degradable envelope with an antibacterial drug might reduce this risk locally[99]. In the case of electrodes mounted on a stent, instead of floating wires, the risks of infection could potentially be even less. Stent infections are in fact rare. Reddy et al. in 2019 reviewed cases since their first report in 1993 and found only 77 cases reported of stent infections, with a rate of more than 2 million stent implantations per year[101,102].

However, it must be noted that there are other risks concerning stent implantation, the most relevant among them is thrombus formation (1-3%), followed by re-stenosis (3.4%); stent adjacent stenosis is quite common as well (10-15%)[103]. In-stent stenosis might be reduced by using device coatings that release drugs inhibiting neointimal hyperplasia, such as those of drug-eluting stents (DES)[104–106]. Raza et al. reported a preliminary safety profile of endovascular neural interfaces, by analysing lessons learnt from venous sinus stenting and implantable cardiac devices[103]. Regarding the former, their conclusion is that in-stent thrombosis could be the main threat to patients and its probability of occurrence could be reduced by perioperative antiplatelets and anticoagulants therapy[103]. Regarding the latter, useful information could be collected concerning the leads: high-risk events related to their presence in the blood stream could be stenosis, thrombosis, infection, and rupture/malfunction. Lead-induced stenosis might be related to the ratio between lead diameter and vessel size; however, a definitive correlation hasn't been found yet. Instead, a stronger influence was given by the history of intravenous catheterization. Lead-induced thrombosis could be potentially prevented by anticoagulation therapies, as for in-stent thrombosis. Infection development could be affected by multiple factors: comorbidities in patients, longer and more complex surgical procedures increasing the handling time of the device, and the overall size of the implant. A possible strategy to reduce risk of infection could be perioperative administration of antibiotics and use of lead with special antibacterial coatings. Overall, only more specific data about endovascular neural interfaces collected in the future will be able to set the ground for a scientific and objective analysis of the risks implicated in the use of these devices. This preliminary analysis might suggest that risk of infection could be less with stent-electrode arrays compared to DBS system, however thrombosis and stenosis represent new threats that need to be accounted for.

1.4 Endovascular neurotechnology

Using the blood vessels to deliver electrodes is a minimally invasive strategy for neural recording and neuromodulation. By removing the need of a craniotomy, avoiding possible damage to the neural tissue and potentially decreasing perioperative risks, as discussed in the previous section, this approach might make neurotechnology available to a pool of patients larger than that of today[97].

1.4.1 Brief history

The first reported use of endovascular electrodes for neural recording was published in 1973: Penn et al. used a catheter with a platinum-cobalt magnet at the tip and they implanted it in the middle cerebral artery using magnetically-guided navigation and used the electrode to record epileptic activity of the patient's brain[107,108]. Although upon insertion of the device in the vessel an electrocardiographic

artefact was detected, it attenuated when reaching the cerebral target. No neurological damage to the patient was reported and only a minimal sedation was required (such as the one used for a routine angiography). Comparing the obtained signal with one recorded via standard scalp leads, higher frequency rhythms (14-16 Hz instead of 8-9 Hz) were detected with the endovascular electrode[108]. Only after 1995 did new studies come out on the use of endovascular wires for neural recording of intracranial EEG, interictal signals and evoked potentials, demonstrating the feasibility of this approach [107,108]. To increase the number of recording sites, a catheter with 16 electrodes mounted on it was used by Thomke et al. in 1998 to record intracranial epileptic seizures from the temporal lobe of a patient [108]. Although the article reports the recorded traces, the authors did not analyse the quality of the obtained signals.

1.4.2 Recent advances

In 2005, Llinás et al. envisioned the application of nanotechnology to reach the capillary bed of the brain and perform neural recording from there[109]. Nanoprobes could be collected within a catheter and then spread along the target area, allowing high specificity recording without damaging the brain parenchyma. Firstly, they demonstrated recording of stimulated activity of the sciatic nerve from the sciatic artery using 20 μm Pt/Ir wires. The endovascular signals were compared to those obtained using a 300-μm silver ball electrode placed on the surface of the nerve. The noise level and frequency characteristics of the endovascular approach are comparable to those of the direct-contact electrode. A difference in the power was noted but attributed to the difference in electrode size. In a second set of experiments, the authors used 1 μm-diameter Pt wires with a cup-like enlargement at the tip, given by the deposition of Pt Black to reduce electrode impedance; this enlargement worked also as a "sail", to help move the electrode navigation within the vessel by being carried by the blood flow. Using these electrodes, the authors demonstrated neural recording of the spinal cord signals from capillaries following nerve stimulation, with results larger in amplitude than surface electrodes. Finally, they propose to substitute metallic electrodes with polymeric, flexible, non-reactive, anisotropic conductors. For this, they used polypyrrole films with a thickness of 15 x 15 μm to record stimulated neural activity of the sciatic nerve from the sciatic artery. The amplitude of the intravascular signal is higher than the one obtained by the surface electrode and similar to those obtained by intravascular metallic electrodes.

In the same collaboration group, Watanabe et al. worked in 2009 on the optimization of the microwire size and navigation inside sub-millimetre channels[110]. They used a microcatheter to deliver a 1 μm-diameter Pt wire inside 400 μm-diameter blood vessels and reached a curvature radius of 700 μm with a flow velocity of 5 mm s^{-1} (saline). With this electrode they were able to detect ex vivo neural responses (although not action potentials) from the anterior spinal artery close to the stimulated spinal cord of *Xenopus laevis*, that were comparable to signals measured via surface electrodes.

In 2014, Bower et al. demonstrated endovascular neural recording from the superior sagittal sinus (SSS) of pigs[111]. The signal was compared to that obtained by a subdural grid with both 40 μm-diameter microelectrodes and standard clinical contacts of 1 mm-diameter. The intravascular device was a standard, clinical-depth electrode with both macro and micro-contacts; it was inserted after craniotomy via an incision in the SSS (**Figure 1.7**A,B). Recording was tested after seizure induction: the amplitude of epileptiform spikes recorded from the two devices was similar and microelectrodes on the two of them were able to detect high-frequency signals missed by the macro electrodes (**Figure 1.7**C). To evaluate the possible attenuation of the neural signal given by the endothelial vessel walls, a sinusoidal signal with different frequencies was applied between defined subdural electrodes and its

recording by the intravenous device was monitored. Results showed that the signal was detected with high fidelity until 1 kHz, suggesting the possibility for endovascular electrodes to reliably sense high-frequency oscillation. This is valuable for example in epilepsy foci mapping.

Along the same line, He et al. in 2016 investigated the signal quality of endovascular electroencephalography in rabbits for brain mapping[112]. Specifically, they studied visually evoked potentials (VEPs), steady state auditory evoked potentials (SSAEPs) and steady state visually evoked potentials (SSVEPs) and compared results to dead animal controls and scalp electrodes signals (**Figure 1.7**D). Cardiac contamination was removed. The authors implanted guidewire electrodes in the basilar artery and moved them while recording. The obtained signals and their signal-to-noise ratio (SNR) changed in amplitude depending on the electrode position within the vessel and proximity to the signal source. Overall, the SNR was better than scalp electrodes and for a wider range of frequency for SSAEPs than SSVEPs. Dead animal controls ensured the absence of non-biological artefacts.
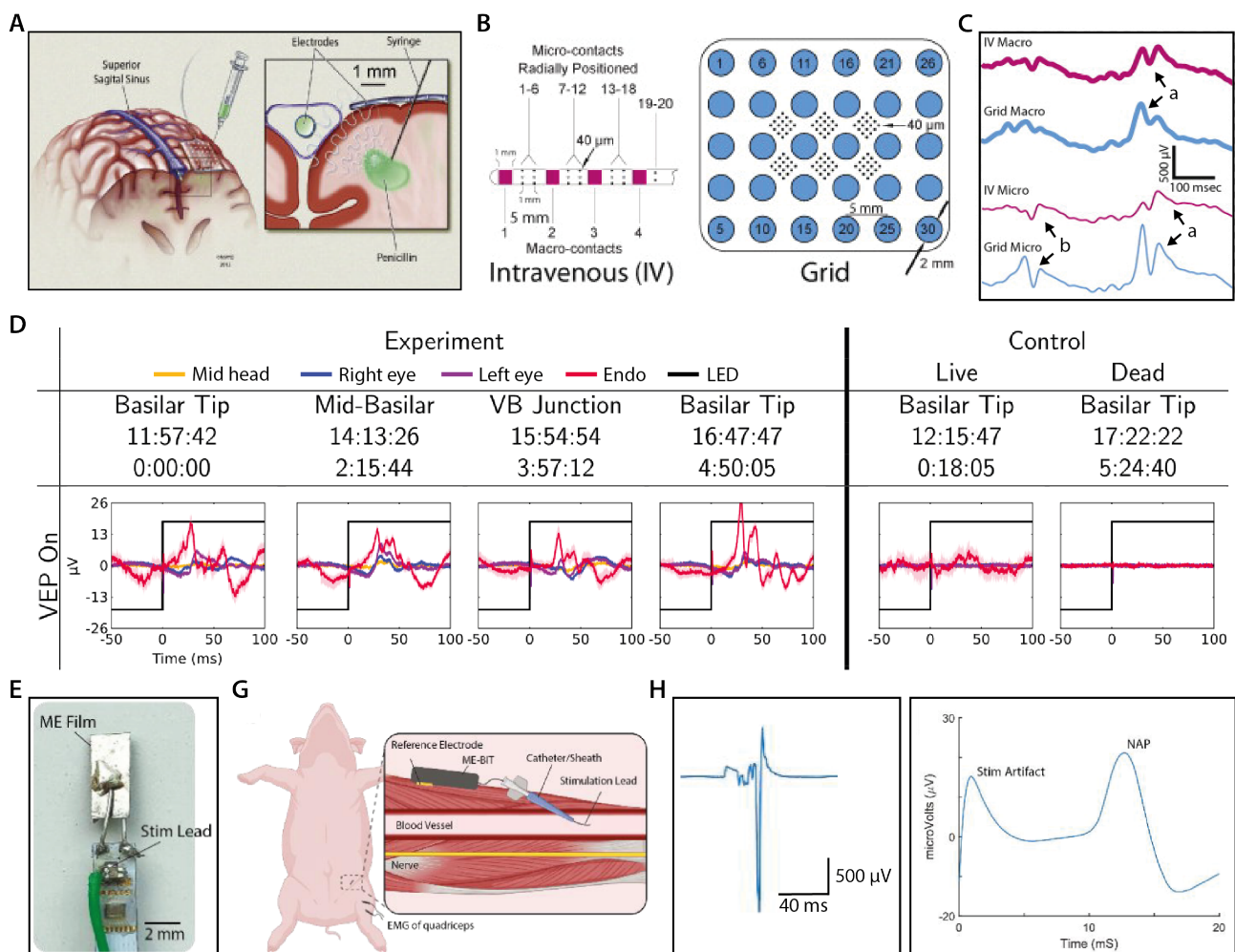
Figure 1.7 Recent endovascular neural interfaces. **A**) Experimental set-up of Bower et al. Standard subdural grids are compared to endovascular electrodes after injection of penicillin inducing epileptic seizures in pig. **B**) Schematics of the electrodes used in A. **C**) Neural recording of epileptic seizure by intravenous (IV, magenta) and subdural grid (blue) macro (thick lines) and micro (thin lines) electrodes. Large epileptiforms (a) are detected by all systems, while smaller spikes (b) are detected only by microelectrodes. A-C are adapted from Bower et al.[111]. **D**) Visually evoked potentials (VEPs) stimulated via LED and recorded by endovascular guidewire electrodes in different locations of the rabbit brain and vasculature (left). A control is reported using measurement in dead animal (right). Adapted from He et al.[112]. **E**) Magnetoelectric (ME) film connected to an integrated circuit and stimulating leads. **G**) Schematics of the implantation of the ME bioimplant (ME-BIT) inside the femoral artery to stimulate the femoral nerve. **H**) Electromyographic signal recorded from the bicep femoris during stimulation with the ME-BIT (left) and neural action potential (NAP) of the femoral nerve recorded by hook electrodes during endovascular stimulation with the ME-BIT (right). E-H are adapted from Chen et al.[113].

Recently, Cheng et al. proposed a novel endovascular wire powered wirelessly by a magnetoelectric (ME) system[113] (**Figure 1.7**E). By applying a magnetic field to a magnetostrictive material (Metglas), a deformation is induced on a piezoelectric film producing a consequent voltage. The generated voltage is then used to power the endovascular wire and stimulate the peripheral nerve adjacent to the blood vessel. While the wire stays in the vessel, the powering system is located between muscular fascicles outside the vessel, working as an anchoring point for the wire. This is also due to its size: 1.75 mm wide, 5 mm long and 0.3 mm thick. By controlling the frequency of the applied magnetic fields, the value of the generated voltage can be controlled. In this way it is possible to transmit information to the device and an application-specific integrated circuit (ASIC) connected to the ME system can transform that information into specific stimulation parameters. However, this increases the overall size of the device to 3 x 2.15 x 14.8 mm, with encapsulation. When the device is inserted in an ex-vivo model of porcine tissue, operational voltages > 1.8 V were reached even at device depth down to 25 mm in the tissue with a 3 mm air gap between the transmitter and the tissue. Moreover, the wireless link was also maintained with a 25 mm misalignment between the transmitter and receiver. An in-vivo experiment in a pig attempted femoral nerve stimulation from within the femoral artery with the transmitter 1.5 cm far from the receiver (**Figure 1.7**G). Generated compound muscle action potentials (CMAPs) were recorded, and downstream nerve action potentials were used to control that the muscle activation was actually induced by the activation of the sciatic nerve and not by direct muscle stimulation (**Figure 1.7**H). Overall, this approach allows for wireless stimulation actuated by an endovascular electrode. However, the current size of the receiver might represent a thrombus source and an obstacle to blood flow, if chronically implanted, although the authors proved its delivery even inside the femoral artery. Moreover, accurate control of the electrode position might be needed to ensure its proximity to the target nerve.

The main limitation of the endovascular electrodes seen so far is the unsuitability for chronic applications: both catheters and wires cannot be placed inside blood vessels for long periods of time due to the high risks of thrombus formation through disruption of the blood flow[109,111]. Moreover, position stability is critical, and, because of this, selectivity might be lost. To overcome these difficulties, in 2016, Opie et al. introduced the possibility to use a metallic stent as an endovascular support of Pt electrodes for neural recording from within a blood vessel[93]. In this way, the placement of electrodes is fixed, high proximity to the neural tissue is promoted by the expansion of the stent inside the vasculature, and chronic recordings might be performed given the compatibility of the stent primary function with the blood flow. The next section will describe more in detail their findings.

1.4.3   The Stentrode™

The Stentrode™ is built over a commercially available, self-expanding, intracranial Nitinol stent of 3 mm diameter, normally used for clot retrieval. Pt disks of 750 µm diameter are glued to the stent strut cross-links and their cable connections are wrapped around the main shaft to which the stent is attached (**Figure 1.8**A). The device can be inserted inside catheters with diameters down to 0.89 mm, at which electrodes start to detach due to friction[93]. In a first proof of concept the device is implanted in the SSS of a sheep (2 mm diameter) using a 4Fr catheter (1.1 mm internal diameter) and minimally invasive catheter angiography (**Figure 1.8**A). Upon implantation, 7 out of 35 electrodes appeared short-circuited to the stent. In another similar study, besides short-circuiting of the electrodes, the authors report methods used to identify and exclude from further analysis electrodes with wire fractures, both after implantation and due to mechanical fatigues induced by the repetitive neck movements of the sheep (**Figure 1.8**B) [114]. Vessel wall incorporation was obtained in approximately 6 days and was monitored by imaging and electrodes impedance study. The characteristics of the latter in fact

changed greatly during the first 6 days but stabilized afterwards: fitting the data to an equivalent circuit model, a capacitive increase occurring in that time window suggested protein absorption to the electrode surface (**Figure 1.8**C-E). To test the recording ability of the device, somatosensory evoked potentials (SSEPs) were induced by stimulation of the median nerve. The signal amplitude was stable over 28 days but the percentage of the viable electrodes that effectively detected the SSEPs increased in the first 4 days after implantation. Supporting a good incorporation of the device within the vessel walls, the recording sensitivity also increased over time. The signal morphology significantly changed among 2.4 mm-distanced electrodes, suggesting discrimination of different neuronal populations. When compared to recordings of ECoG by subdural and surface electrode arrays, the Stentrode™ showed a performance comparable to that of the epidural array and slightly inferior to that of the subdural. Specifically, ECoG amplitude and maximum bandwidth was significantly higher in subdural than epidural and endovascular electrodes at frequencies below 200 Hz; sheep chewing artefacts were similar with all devices. Chronic EEG recordings were achieved up to 190 days in a freely moving sheep (**Figure 1.8**F). Lumen patency was maintained up to 12 weeks, with average strut-to-lumen distance of 339 μm at the end and electrodes inclusion in the vessel walls occurring mostly in the first month and stabilizing after that[115]. A few occlusions of adjacent veins were reported but no adverse effects occurred.
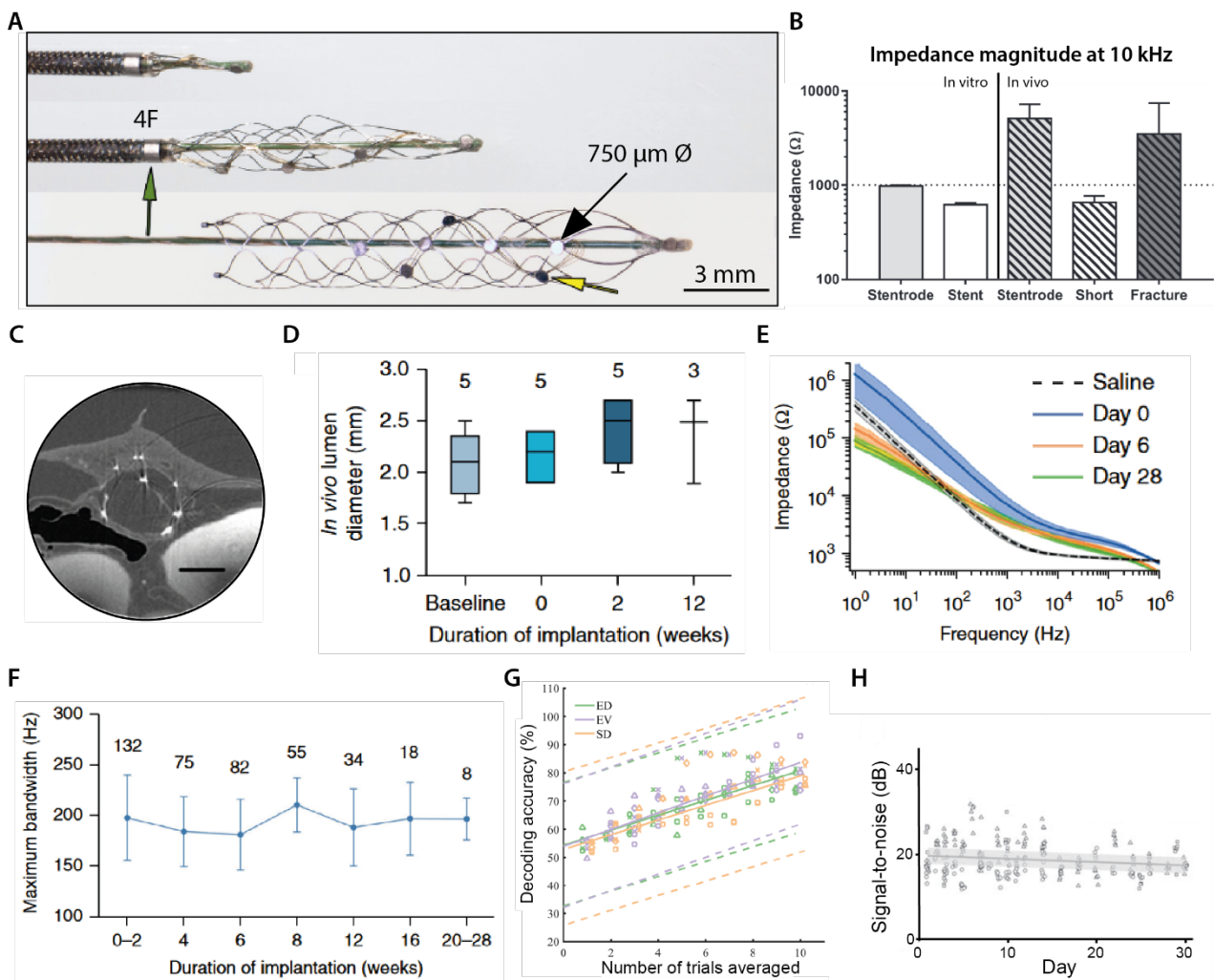
Figure 1.8 Stentrode™ development and characterization. A) The Stentrode™ with Pt electrodes (yellow arrow) mounted on the Solitaire (Covidien) stent and deployed through a 4F catheter (green arrow). **B**) Impedance module at 10 kHz of electrodes mounted on the stent (Stentrode) and of bare stents in vitro (left). On the right, impedance module values at 10 kHz of functional electrodes mounted on stent (Stentrode), short-circuited to the stent (Short) and fractured cable (Fracture). Short-circuited electrodes in vivo have similar values to bare

stents in vitro and can be easily excluded. To determine fractured cable-electrodes, analysis of the phase angle of the impedance can be used (not reported in this work). **C)** Synchrotron X-ray image of vessel wall incorporation of Stentrode™ at day 0 ex vivo in SSS of sheep. Scale bar is 2 mm. **D)** Sheep SSS internal lumen measurements via cerebral angiography at different time points after Stentrode™ implantation. **E)** Impedance spectroscopy measurements of Stentrode™ in vivo at different time points, compared to in vitro measurements in saline. The minimal difference between day 6 and day 28 suggests stabilization of the electrode-tissue interface. **F)** Maximum bandwidth from signals recorded by Stentrode™ implanted in sheep for 190 days. The number above each point represents the number of channels, cumulative of multiple sheep used in the study. **G)** Accuracy of decoding evoked potentials by median nerve stimulation in sheep and recorded from within the SSS by the Stentrode™ (EV, purple), epidurally (ED, green) and subdurally (SD, orange). **H)** Visually evoked potentials signal-to-noise ratios over 30 days of the Stentrode™ implanted in the SSS of sheep. Error bar is the root mean square error for the fit. A, C-F are adapted from Oxley et al.[93]. B is adapted from Opie et al.[114], G from Gerboni et al.[116] and H from John et al.[117].

Going further in evaluating the potential of the Stentrode™ as a possible Brain Computer Interface (BCI), the authors analysed the ability of the device to detect somatosensory evoked potentials and compared its performance to subdural and epidural electrodes[117]. The detection accuracy of the endovascular electrodes was comparable to those of epidural and subdural devices in sheep, with no significant effect of the presence of either the dura or the vascular endothelium (**Figure 1.8**G). Analysing the signal-to-noise ratio (SNR), all devices showed similar SNR, that would similarly increase when signal was increased. A chronic evaluation of the ability of the device to detect evoked signals in time was carried out by monitoring SNR and peak-to-peak (PP) amplitude of visually evoked potentials (VEPs) in sheep over 30 days (**Figure 1.8**H)[116]. Large VEPs could also easily be used to calibrate the signal of a BCI interface and quickly assess electrodes viability. Results showed that variations in time of SNR and PP decreased in the last 10 days, suggesting that the device properties stabilized. Overall, both SNR and PP only slightly decreased over time, with a more pronounced negative slope for the latter. Other studies focused on the development of a signal classifier to accompany the Stentrode™ in a complete BCI interface[118].

After investigating through 7T functional magnetic resonance imaging (fMRI) the ideal locations in human for decoding the motor intention[119], a first early-feasibility study in men has been carried out in 2020 using customised thin-film monolithic stent-electrode arrays, with mechanical characteristics comparable to commercial stents[120,121]. Two patients with upper limb paralysis related to amyotrophic lateral sclerosis (ALS) underwent a venography neurointervention surgery where the Stentrode BCI was implanted in the superior sagittal sinus close to the motor cortex. Transvascular leads were connected to an inductively powered internal telemetry unit (ITU) placed subdermally in the patients' chest. Infrared light was used to wirelessly transmit the signal to an external telemetry unit (ETU), that would again send the signal to a tablet. The training started approximately 2 months after implantation and required a different number of sessions for the two patients. While using an eye-tracker to navigate a mouse on a screen, clicking was defined by the motor neuroprosthesis detecting muscular contraction from the motor cortex. The system was able to identify "no click", "short click" and "long click" conditions. Performance testing sessions required typing of specific words for standardized assessment and, inspired by the instrumental activities of daily living (IADL), they included also texting, emailing, online payment and shopping tasks. Unsupervised use of the system was allowed after 86 and 71 days from surgery for patient 1 and 2 respectively. Importantly, the caregiver involvement for the use of the system is minimal, as only tablet turn-on and ETU connection are required. On the same line, stent delivery being a common interventional procedure, the training required for medical doctors to implant the device would be relatively easy.

Besides BCI uses of such neural interface, endovascular neuromodulation applications have also been investigated[122]. The device has been implanted at the intersection of the cruciate sulcal veins (CSVs) with the superior sagittal sinus of 8 awake and freely moving sheep. Testing started after complete endothelialisation of the device, approximately a month after implantation. Depending on the location of the electrodes, responses in different muscle groups were achieved. Some examples of elicited

movements include lip, jaw, or neck movements. Approximately 5.6 mA were required to achieve detectable responses. The authors compared the Stentrode™ to subdural and penetrating electrodes: effective stimulation was achieved by a similar percentage of available electrodes in the different devices (91%, 86% and 91% for endovascular, subdural and penetrating respectively). A possible use of neuromodulation directed by an endovascular neural interface could be to either replace or work alongside deep brain stimulating leads. In this context, Teplitzky et al. identified different key locations in the brain vasculature where vessels of at least 1 mm diameter are found adjacent to deep brain stimulation (DBS) therapy targets[123]. Specifically, they used the MRI and MR angiography scans of a single subject to create a 3D model of the human brain and vasculature. They found 5 areas close to large (> 1 mm) vessels:

- the anterior nucleus of the thalamus, usually stimulated in epileptic patients, adjacent to the internal cerebral vein
- the fornix, usually stimulated in Alzheimer's disease patients, adjacent to the internal cerebral vein
- the nucleus succubens, usually stimulated in patients with treatment resistant depression, obsessive-compulsive disorders, addiction, obesity or anorexia mentosa, adjacent to the A1 segment of the anterior communicating artery
- the subgenual cingulate white matter, usually stimulated in treatment resistant depression patients, adjacent to the segment 2 of the anterior communicating artery
- the ventral capsule, usually stimulated in patients with obsessive-compulsive disorders, adjacent to the segment 2 of the anterior communicating artery

As an example, they modelled the stimulation efficiency in terms of neuronal activation probability in the fornix and in the subgenual cingulate white matter, generated by guidewire electrodes and ring electrodes, the latter with adhesion to the vessel walls similar to the one of stents. Their results suggested better performances of the ring electrodes compared to the guidewires, although suboptimal placement showed high variability in neural activation. Ring-electrodes conveyed neuronal activation similar to the one induced by standard stereotactic DBS leads.

1.4.4   Current limitations

The main limitation of the Stentrode™ is the presence of the stent shaft, due to the use of stentriever technology, which is not optimized for long-term applications[103]. This might be the source of thrombus and might be prone to mechanical failure, such as what occurred with the repetitive neck movements of the sheep in the presented studies. More studies investigating the appropriate lead diameter and material are required: cardiac devices (i.e., pacemakers, defibrillators) taught us that a thinner lead does not always ensure a lower risk of thrombosis; careful material choice and lead placement avoiding highly mechanically solicited areas should be used to increase durability against mechanical fatigue[103]. At the same time, being an endovascular device, dual antiplatelet therapy is necessary[103]. Given the preliminary animal studies of the Stentrode™ endothelialisation, the therapy should be carried out at least for the first month after implantation. However, it is still too early to understand what the long-term complications of this device are.

Surgery duration and overall size of the implant leads and receiver should be minimized to reduce the risk of infection[103]. The latter can be strongly reduced by antibiotic treatment prior to surgery and for a period afterwards. However, if an infection was to take place, then removal of the device could potentially be considered. Removal of an endotehlialised stent, whether it is because of an infection or de-

vice failure, is challenging, although technological advances reduced its adverse risks[124,125]. However, information regarding such procedure was only found for cardiovascular stents and not cerebrovascular devices.

Moreover, the use of a commercial stent, designed for applications in stenosis conditions, could cause unnecessary vessel over-expansions and additional stresses to the surrounding tissues[103]. Not only this, but the metallic substrate could also cause shortcuts of the electrodes and might not be suitable for other applications in the peripheral systems (the current Stentrode™ design is inspired by brain stents, i.e., Solitaire SAB by Covidien and TrevoPro by Stryker Neurovascular).

Anatomical variations in the blood vasculature might be an obstacle limiting the pool of available patients[103]. For example, there might be risks of occluding unilateral dominant vessels encountered during navigation. In the absence of appropriate collateral and compensatory drainage, there might be neurological complications and consequent obligation in excluding a patient. Moreover, in the presence of tortuous vascular structures, current catheter technologies might not be able to reach peripheral targets due to their limited manoeuvrability and the increased risk of damaging the vessel walls or the carried device. State-of-the-art catheter navigation systems rely on the ability of the interventional radiologist to manoeuvre and navigate the guidewire inside the vasculature. Once the guidewire is advanced, the catheter is tracked over and faithfully follows the path imposed by the guidewire. In correspondence of turns and intersections, the guidewire is gently pushed against the vessel wall and rotated to change its direction. The latest technological advancements, including tip deformation by cable-driven mechanisms or shape-memory properties of materials, showed promising results in increasing manoeuvrability, and improving speed and efficacy of interventions. However, the stiffness of the catheter, required to sustain sufficient pushability and torqueability, might still limit accessibility. A new design for an endovascular neural interface could allow to overcome these problems by taking advantage of new materials, advanced microfabrication techniques, and novel technological paradigms in catheters navigation, guidewire-less, such as magnetically guided endovascular interventions[126,127].

1.5 Thesis strategy

1.5.1 Motivation and open challenges

The Stentrode™ has definitely opened a significant door in the field of minimally invasive neurotechnology: it offers a novel neural interface, able to chronically record neural signals and successfully work as a Brain Computer Interface, without needing a craniotomy for its implantation and avoiding possible damage to the neural tissue. Still, if on one hand it offers a minimally invasive implantation procedure, on the other hand the core device could be improved by addressing a few of the limitations described in the previous section. Among these, the difficulty in device removal in case of failure, loss of efficacy, patient's preference or safety, also shared by other minimally invasive electrode arrays, might be solved by replacing the permanent implant with degradable electronic devices. However, their short lifetime (< two weeks) is not able yet to cover chronic applications.

The goal of this thesis is to develop a new neural interface that combines the advantages of endovascular devices and transient electronics and overcomes their current limitations. This device, with a stent-inspired design, can be implanted in a blood vessel, thus without needing a craniotomy, and is able to record and stimulate the surrounding neural tissue, avoiding possibly damaging direct contact with it and subsequent strong inflammatory reactions. At the same time, using a degradable scaffold for electrodes support eliminates the need for further removal surgeries. If a device replacement is needed,

after degradation, a new device can be implanted in the same location, without the complexity possibly induced by removal of the old one (i.e., obstructing fibrotic scar, adhered tissue). Moreover, long-term complications related to permanent implantations of foreign bodies would be avoided. Choosing a degradable material with a slow degradation rate allows for tissue remodelling around the implant and better integration in the vessel walls, compared to metallic, permanent stents and non-degradable neural interfaces. In order to avoid the high dissolution rate of degradable metals commonly used in transient electronics, biocompatible and more durable conductive polymers can be used to fabricate the electrodes and traces of the envisioned neural interface, making it an overall all-polymeric device for durable use.

The overall motivation behind this project is to build a durable neural interface that can ideally reduce to the minimum the inflammatory reaction without heavily affecting the performance. Possible applications that this device could cover include: temporary mapping of electrical activity of specific brain structures (such as the ones described by Teplitzky et al.[123], **Section 1.4.3**) before, during or after interventions; preliminary trials of neurostimulation therapies for both central and peripheral nervous system; recovery of injured nerves by neurostimulation; enhancement of motor recovery by precise neuromuscular stimulation. Moreover, the safe transiency of the device and its simple and minimally invasive implantation procedure could favour patients' predisposition to undergo the surgery and increase the pool of targetable patients. If this is true, the amount of collectable data would also increase, enriching scientists with precious information for improving therapeutic strategies fighting neurodegenerative disorders.

The challenges around this device are multiple. First of all, the choice of materials should be in line with transient electronics and demonstrate sufficient performance and operational lifetime. Secondly, its design needs to be compliant with a delivery via small calibre catheters to reach the target locations in the vasculature. Third, its fabrication should be tailored to delicate transient materials, poorly compatible with standard microfabrication processes. Finally, the characterization should take into consideration the endovascular environment to which the device will be exposed. The present thesis addresses these challenges and explores further improvements.

A major limitation of the endovascular approach for neurotechnology is the vasculature curvature complexity, impossible to overcome with current catheter steering technologies. A potential solution introduced in this thesis is the development of a flow driven, magnetically steered, robotic navigation system of specifically microengineered endovascular probes. This not only would allow to enlarge the pool of available therapeutic targets in the body, especially targeting the microvasculature, but also would reduce the risk of vessel wall perforation. Moreover, the autonomous capabilities of flow driven navigation may assist the physicians and reduce their prior lengthy training requirements. By using blood flow as an energetic source and magnetic fields for steering, pushability and torquability requirements are no longer needed, thus allowing further miniaturization of the endovascular devices. Via cleanroom-based microfabrication techniques such devices could be equipped with microscopic electronic circuits, which could be used to monitor temperature, blood flow and perform electrical stimulation or recording.

Combined together, strategies and devices presented in this work could provide a new toolkit in the field of bioelectronic medicine that could expand our knowledge of the human body and pave the way for innovative therapies.

1.5.2   Objective and thesis structure

The general objective of this thesis is to develop a minimally invasive and transient neural interface, able to work from within a blood vessel, and propose a novel navigation system for endovascular probes. The next chapter (**Chapter 2**) will describe the development of a transient all-polymeric neural probe for prolonged neural recording, addressing fabrication techniques, electrochemical characterization and in vivo testing, with the collaboration of the Laboratory of Professor Rosa Chiara Paolicelli from the University of Lausanne. In **Chapter 3**, the device design is revisited to allow an endovascular implantation, followed by specific characterization. A possible delivery system is developed and preliminarily validated, thanks to the collaboration with the research team of Paolo Machi, MD of the Neuroradiology Division of Geneva Hospital. The following **Chapter 4** focuses on overcoming a common challenge of the delivery of endovascular devices: complex vasculature structures preventing target access due to low flexibility and manual control of catheters. The proposed strategy, applicable to the device in **Chapter 3** or similar others (e.g., the Stentrode™), was developed in collaboration with the Microbiorobotic systems laboratory of EPFL and explores the development of a flow-driven, magnetically directed, navigation system for microengineered endovascular probes. This system can potentially reduce intraoperative risks during catheterization procedures and overcome complex vasculature ramifications, blocking current catheter technology. In this context, an alternative system is then proposed in **Chapter 5,** for when the device navigation cannot be propelled by perfusion flow, such as in obstructed arteries. A magnetic actuation can compensate for the absence of flow and allows for navigation of sophisticated probes inside sub-millimetre vessels. The devices described in **Chapter 4** and **Chapter 5** host circuitry for neural recording or stimulation, thermal sensing and flow analysis, opening the door for high-proximity study of conditions in deep vascular segments. Finally, the last chapter (**Chapter 6**) of the thesis will wrap up the obtained outcomes, highlight current limitations, and suggest future directions.

Chapter 2 All-polymeric transient neural probe for pro-longed in vivo electrophysiolog-ical recordings

The goal addressed in this chapter is the development and testing of an implantable, transient neural interface able to record neural signals for longer than current transient devices (i.e., one month).

This chapter is adapted from the following article:

Authors: L. Ferlauto*, P. Vagni*, A. Fanelli, E. G. Zollinger, K. Monsorno, R. C. Paolicelli, D. Ghezzi (*equal contribution)

Affiliations:

- L. Ferlauto[†], P. Vagni[‡], A. Fanelli, E. G. Zollinger and D. Ghezzi: Medtronic Chair in Neuroengineering, Center for Neuroprosthetics and Institute of Bioengineering, School of Engineering, École polytechnique fédérale de Lausanne, Switzerland
- K. Monsorno and R. C. Paolicelli: Department of Biomedical Sciences, Faculty of Biology and Medicine, University of Lausanne, Switzerland

Contributions: **A. Fanelli** worked on the manufacturing resolution (fabrication, tests, data analysis), performed the accelerated degradation study in vitro, and contributed to the discussion about the electrodes' degradation. L. Ferlauto: designed the study, fabricated the devices, performed electrochemical characterization and analysed data, performed surgeries, performed immunohistochemistry, collected confocal images, and wrote the manuscript. P. Vagni: designed the study, performed surgeries, performed electrophysiology and analysed data, performed immunohistochemistry, collected and analysed confocal images, and wrote the manuscript. E. G. Zollinger: performed the surgeries and immunohistochemistry, collected confocal images, and performed cytotoxicity assay. K. Monsorno and R. C. Paolicelli: supplied genetically modified mice and participated in the histological tests. D. Ghezzi: supervised the entire study and wrote the manuscript. All the authors read and accepted the manuscript.

[†]Now at University of Bologna, Italy.

[‡]Now at New York University, US.

2.1 Introduction

Building devices able to disappear in the surrounding environment after a programmed lifetime, leaving minimal and harmless traces after their disposal, is a fascinating idea for the development of green electronics to preserve the environment by reducing waste production and recycling processes [58,128–131]. The same concept is also appealing for medical devices [6,18,27], such as localised drug release systems [132], power units [133], external sensors [134] and implantable recording systems [38], to eliminate the risks related to surgical retrieval [25] and reduce the chronic foreign body reaction [43].

In medical applications, the durability of transient devices is highly dependent on the degradation time and process of the materials used for the substrate and encapsulation layers and, most importantly, of the functional components exposed to the body. While several biodegradable natural or synthetic polymers, such as cellulose [128], silk [135] and poly(lactic-co-glycolic acid) [19,136], are often used as substrate and encapsulation materials, so far the choice for the functional elements has always landed on transient inorganic materials. These materials, such as magnesium, zinc, molybdenum, or iron, dissolve within minutes, hours, or maximum days, once in contact with body fluids [134,137]. This short functional window still limits the list of potential medical applications for transient devices.

To extend the lifetime of transient medical devices, and consequently increase their possible applications, such as for example mid-term monitoring of the brain activity, our strategy is to switch from degradable metals to entirely polymer-based devices. Poly-ε-caprolactone (PCL), one of the biodegradable polyesters with the slowest degradation rate[35], offers a prolonged stability of substrate and encapsulating components of the device, protecting the conductive traces and electrodes. Fastly dissolving metals can be replaced by low-quantities of poly(3,4-ethylenedioxythiophene) (PEDOT), doped with polystyrene sulfonate (PSS). This material allows for low impedance, high charge injection capabilities[138] and can be easily patterned on sensitive materials, such as PCL (low melting temperature, high susceptibility to solvent). The results show the fabrication and the in-vitro characterization of all-polymeric transient neural probes (TNPs) allowing prolonged electrophysiological in-vivo recordings up to three months post-implantation. Histological studies revealed minimal foreign body reaction both in the short- and long-term.

2.2 Results

2.2.1 Probe fabrication and characterization

We fabricated TNPs based on PCL as substrate and encapsulation layers, and PEDOT:PSS doped with EG as a conductive element, by using soft lithographic techniques (**Figure 2.1** and **Figure 2.3**a,b). PCL is a commercial biodegradable polyester widely used in biomedical applications [35,139–141]. It is easy to process and has a longer degradation time (several months or years[35]) compared to most biodegradable polymers. PEDOT:PSS dispersed in water is commercially available, has excellent biocompatibility, has the ability to support cells viability [142,143], and can be integrated into softer systems like elastomers [144,145] and hydrogels [146,147]. EG doping of PEDOT:PSS is known to improve its conductivity [148,149]. The micro-structured PCL-based substrate (thickness 60–70 μm) and encapsulation (thickness 60–70 μm) layers have been obtained by replica moulding. The hollow regions of the substrate layer have been manually filled with PEDOT:PSS:EG to create electrodes, traces and contact pads (**Figure 2.1**a-c).
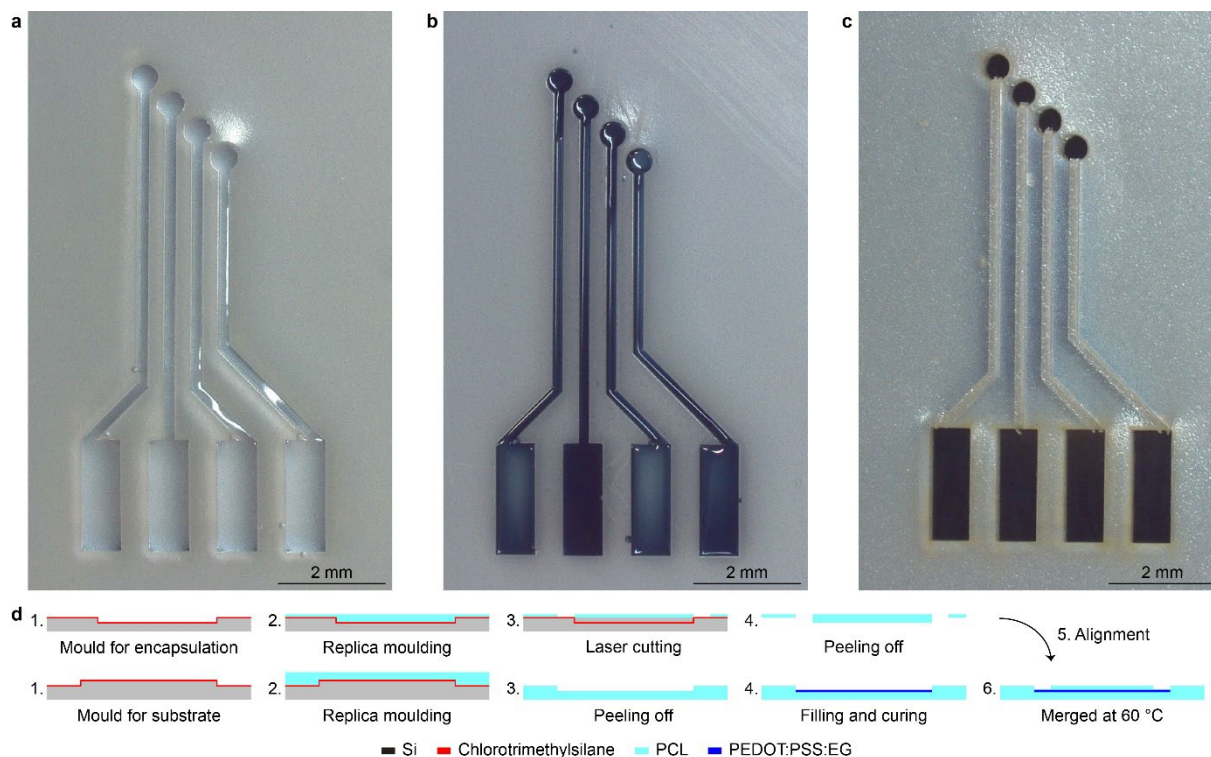
Figure 2.1 Fabrication of all-polymeric transient neural probes. (**a**) PCL substrate obtained via replica moulding. (**b**) PCL substrate with PEDOT:PSS:EG deposited in the hollow regions (50-µm depth) corresponding to the electrodes, traces, and pads. (**c**) Probe encapsulated with a matching PCL layer with protruding traces (60 µm thick) and openings to expose the recording sites and the pads. (**d**) Process flow of the main fabrication steps (dimensions are not in scale).

Electrodes are 500 µm in diameter (**Figure 2.3**c,d) and traces are 200 µm wide (**Figure 2.3**e). At the electrode level, the PEDOT:PSS:EG layer is approximately 3 µm thick, while at the trace level, it is approximately 1 µm thick (**Figure 2.2**). After curing of the PEDOT:PSS:EG, the PCL encapsulation layer has been manually flip-bonded to the substrate layer via a low-temperature process (total probe thickness ranging from 120 to 140 µm). This procedure ensured a complete filling of the trenches for the conductive traces (**Figure 2.3**e).
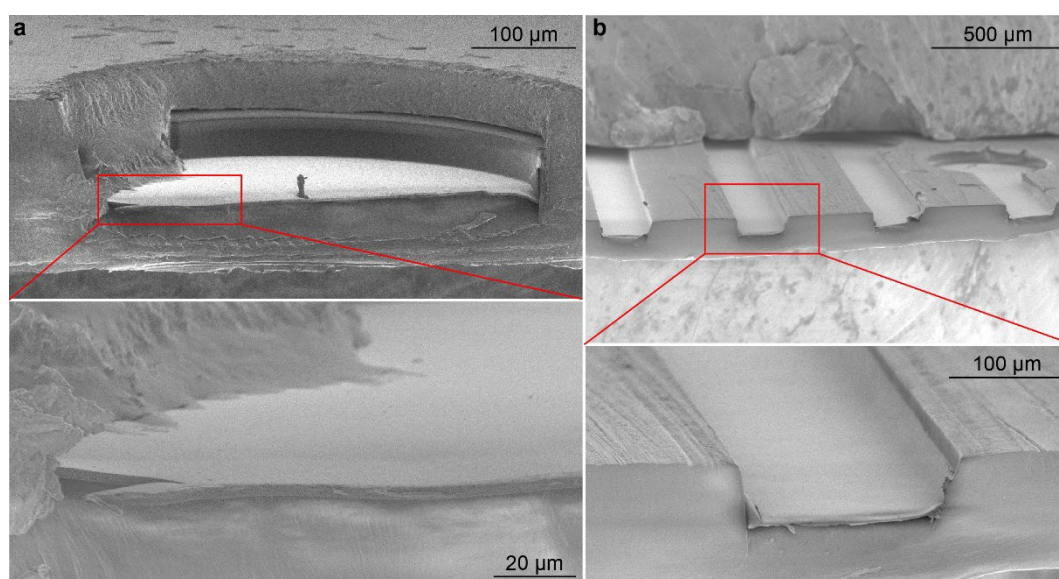
Figure 2.2 SEM characterization of the all-polymeric transient neural probe. (**a**) Cross-section of one electrode after cutting (image tilt 10°). The insert shows a magnification. (**b**) Cross-section at the level of the traces after cutting without the encapsulation layer (image tilt 10°). The insert shows a magnification.

IS showed remarkable performances of all-polymeric TNPs based on PEDOT:PSS:EG, characterised by low impedance magnitude (**Figure 2.3**f) and low impedance phase angle (**Figure 2.3**g) over a wide range of frequency (from 10 Hz to 100 kHz), which makes them appropriate for the recording of both low- and high-frequency neuronal signals, such as LFPs and neural spiking activities respectively. The comparison of multiple probes showed very low intra-probe variability. On the other hand, the inter-probe variability might be explained by the manual deposition process of PEDOT:PSS:EG resulting in a variable thickness of the conductive layer.
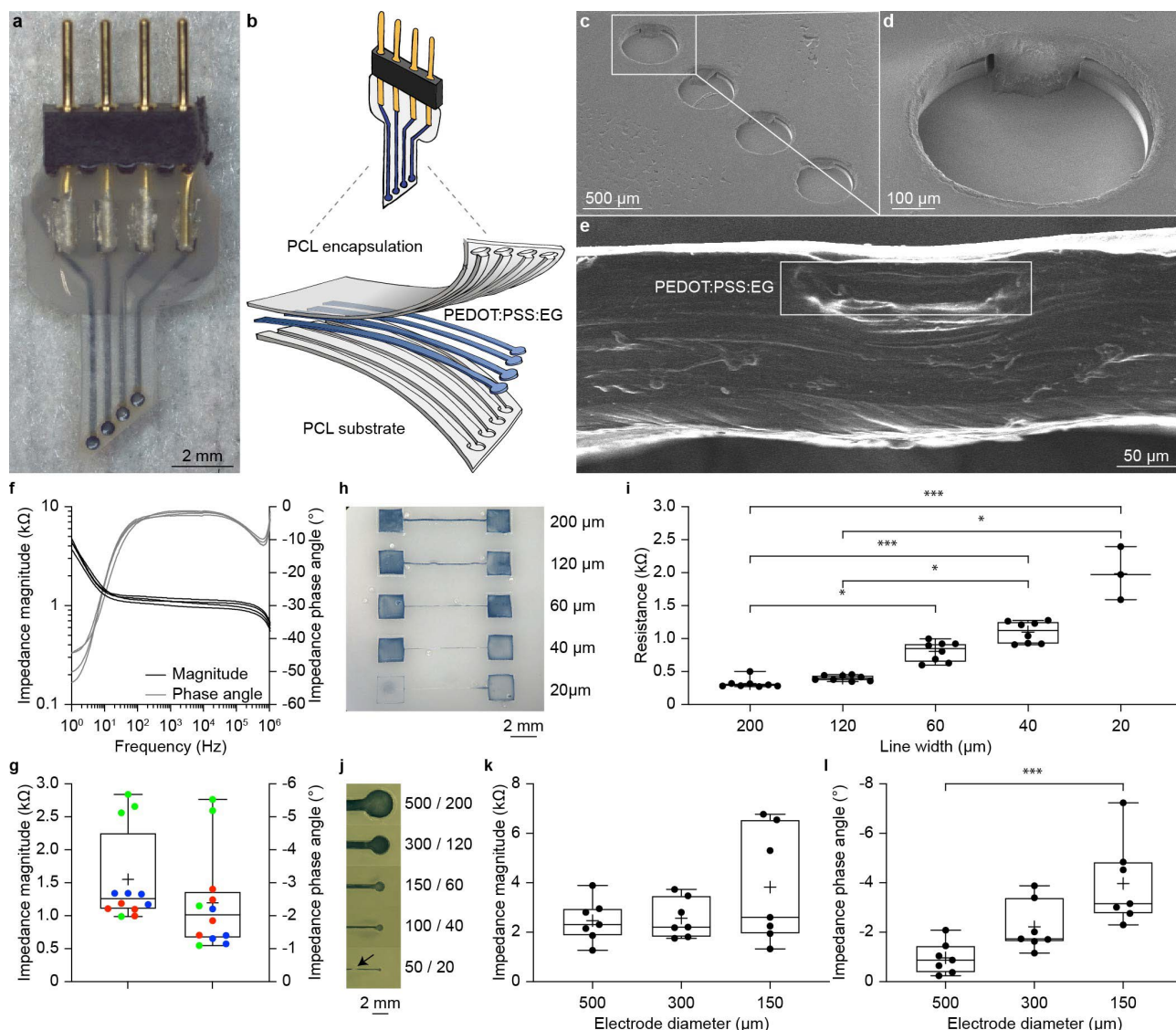
Figure 2.3 All-polymeric transient neural probes. (**a**) Picture of a fully assembled TNP with four PEDOT:PSS:EG electrodes. (**b**) Sketch of the TNP highlighting the three layers: PCL encapsulation, PEDOT:PSS:EG electrodes and PCL substrate. (**c**) Scanning electron microscopy image of the four electrodes encapsulated in PCL (image tilt 45°). (**d**) Magnification of one electrode (image tilt 45°). (**e**) Scanning electron microscopy image of the cross-section of one encapsulated trace (image tilt 10°). (**f**) Plots of the impedance magnitude (black) and impedance phase angle (grey) of 4 electrodes from a representative TNP. (g) Quantification of the impedance magnitude (left) and impedance phase angle (right) at 1 kHz for all the 4 electrodes from 3 TNPs (respectively in red, blue, and green). (**h**) Picture of traces with decreasing width: 200 µm, 120 µm, 60 µm, 40 µm and 20 µm. Traces are 6.3 mm long and pads are 2 × 2 mm². (**i**) Quantification of the trace resistance as a function of the trace width. Kruskal-Wallis: p < 0.0001. Dunn's multiple comparisons test: 200 µm vs. 120 µm p > 0.9999; 200 µm vs. 60 µm p = 0.0202; 200 µm vs. 40 µm p = 0.0001; 200 µm vs. 20 µm p > 0.0004; 120 µm vs. 60 µm p = 0.5545; 120 µm vs. 40 µm p = 0.0158; 120 µm vs. 20 µm p = 0.0118; 60 µm vs. 40 µm p > 0.9999; 60 µm vs. 20 µm p = 0.6738; 40 µm vs. 20 µm p > 0.9999. (**j**) Picture of electrodes not encapsulated with decreasing electrode diameter and trace width: 500/200 µm, 300/120 µm, 150/60 µm, 100/40 µm and 50/20 µm (electrode diameter/trace width). (**k**) Quantification of the impedance magnitude at 1 kHz as a function of the electrode diameter. Kruskal-Wallis: p = 0.6462. (**l**) Quantification of impedance phase angle at 1 kHz as a function of the electrode diameter. Kruskal-Wallis: p = 0.0002. Dunn's multiple comparisons test: 500 µm vs. 300 µm p = 0.1578; 500 µm vs. 150 µm p = 0.0009; 300 µm vs. 150 µm p = 0.2790.

To verify that the excellent electrochemical characteristics of the TNPs were not related to shortcuts between electrodes caused by the porosity of the PCL scaffold, we took advantage of an all-polymeric TNP with a modified design embedding 17 electrodes (**Figure 2.4**). In this specific device, four traces were interrupted, due to a gap in the PEDOT:PSS:EG layer (**Figure 2.4**a-c). As expected, only the corresponding electrodes were rightfully not functional (**Figure 2.4**d,e), thus confirming that shortcuts between electrodes are not present. Besides electrochemistry, we also measured the averaged line resistance of the traces, which was 319.5 ± 75.01 Ω (±s.d., n = 8 traces; **Figure 2.3**h,i) for 200 μm wide and 6.3 mm long traces.
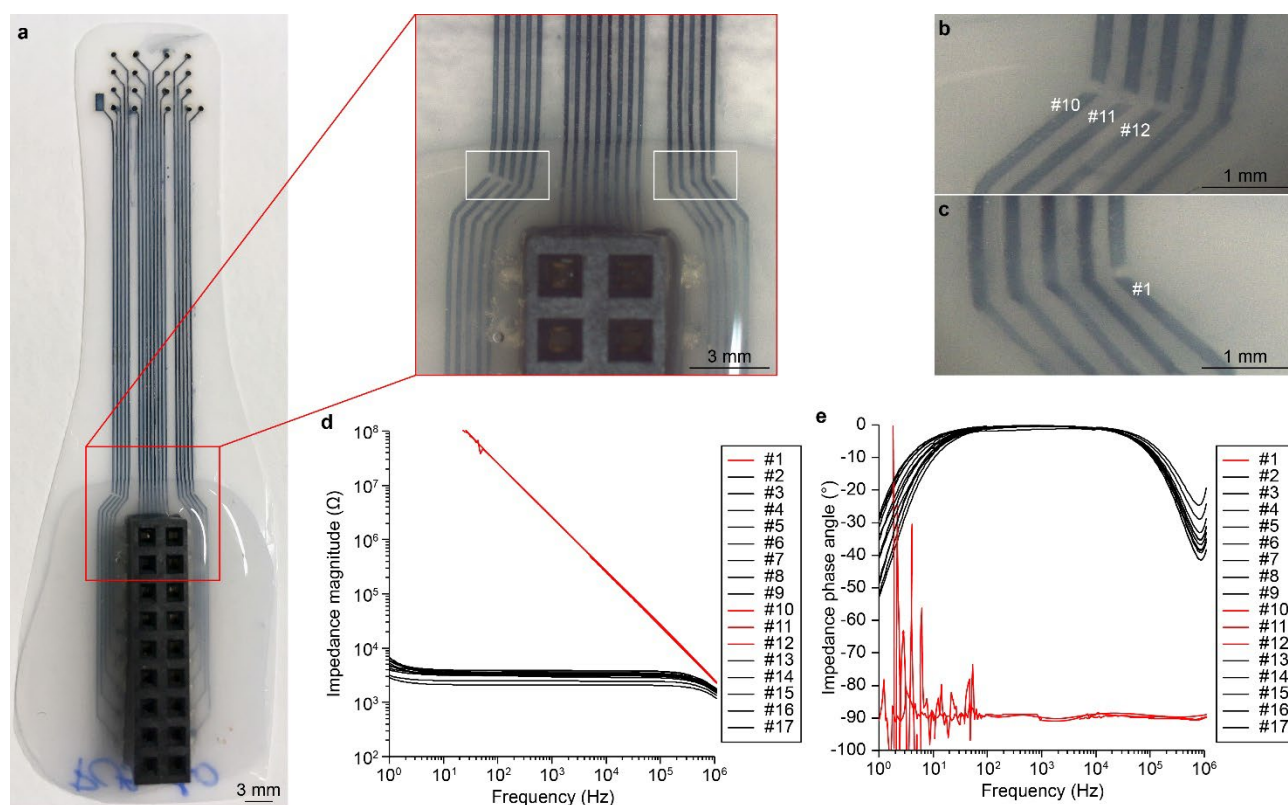
Figure 2.4 Independence of the electrodes. (**a**) Picture of an all-polymeric TNP with higher channel count (17 electrodes, 700 μm in diameter) and its connector. The red box shows a magnified view of a portion of the neural probe where traces appear to be disconnected. (**b,c**) Magnification of the disconnected traces and corresponding electrode numbers. The images correspond to the white boxes in (a). (**d**) Plot of the impedance magnitude of all 17 electrodes as a function of frequency. In red are highlighted the measurements from the electrodes with disconnected traces. (**e**) Plot of the impedance phase of all 17 electrodes as a function of frequency. In red are highlighted the measurements from the electrodes with disconnected traces.

Then, we investigated the minimum dimensions for electrodes and traces that could be reached using these materials and fabrication methods. First, we fabricated narrow traces and measured the average line resistance (n = 8 traces for each dimension; **Figure 2.3**h,i). As expected, the line resistance significantly increased with the decrease of the width. It must be noted that for 20 μm wide traces, only 3 out of 8 traces appeared to be connected. Therefore, the resolution limit for traces is 40 μm. Next, we fabricated TNPs with smaller electrodes and traces (**Figure 2.3**j) and tested IS (n = 7 electrodes for each dimension). As expected, the impedance magnitude (**Figure 2.3**k) and the impedance phase angle (**Figure 2.3**l) increased with the reduction of the electrode diameter. Among the dimensions tested, the smallest electrode (50-μm electrode diameter and 20-μm trace width) resulted not connected (**Figure 2.3**j, black arrow), as expected due to the narrow trace. Electrodes with 100 μm dimeter (40 μm trace width) resulted not working because the electrode openings in the PCL encapsulation layer closed during the bonding to the PCL substrate. Hence, the minimum dimensions reached for the electrode diameter was 150 μm (60 μm trace width).

Pure PEDOT:PSS electrodes have been previously described for in-vitro applications to record cardiac and neural signals and in-vivo neuromodulation. A flexible all-polymer microelectrode array reported impedance magnitude value (1.5 MΩ) at 1 kHz for 120-µm electrodes substantially higher than the ones reported here [150]. The higher impedance magnitude was caused by the deposition method of PEDOT:PSS in a polymeric channel, which led to surface coating only and not to the complete filling of the channel, thus reducing the electrode surface area. A second device exploring inkjet-printed PEDOT:PSS reported an impedance magnitude value (19.5 kΩ) at 1 kHz for an electrode area corresponding approximately to the area of a round electrode with a diameter of 300 µm comparable to the TNP [151]. In a third report, PEDOT:PSS/glycerol electrodes showed an average impedance magnitude at 1 kHz of 6.3 kΩ for an electrode area of 0.5 mm² (corresponding to the area of a round electrode with a diameter of 800 µm) which is similar to the TNP [152].

Last, cytotoxicity tests performed in-vitro showed a cell viability of 96.9 ± 7.2% (mean ± s.d., 2 probes, 6 replicas per probe) and opened the way for the in vivo validation of the devices (**Figure 2.5**).
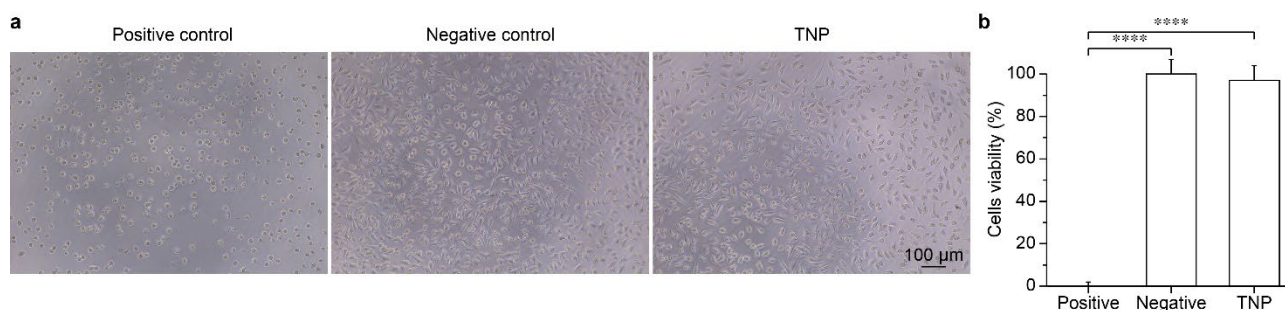
Figure 2.5 Cytotoxicity in-vitro. (**a**) Representative optical images for each condition tested: positive control (left), negative control (middle) and TNP (right). (**b**) Quantification of the mean (±s.d.) cells viability in the three conditions tested. Positive control 0 ± 1.8% (9 replicas); negative control 100 ± 6.8% (9 replicas); all-polymeric TNPs 96.9 ± 7.2% (2 probes, 6 replicas per probe). One-way ANOVA: F = 853.4 and p < 0.0001. Tukey's multiple comparisons test: positive control vs. negative control p < 0.0001; positive control vs. neural probes p < 0.0001; negative control vs. neural probes p = 0.4852.

2.2.2 Functional validation in vivo

To assess the capability of all-polymeric TNPs in recording neural activity, we performed in-vivo acute brain recordings in mice upon induction of epileptic seizures. All-polymeric TNPs were implanted in the visual cortex area of anaesthetised mice (**Figure 2.6**a), and the neural activity was recorded both before and after intraperitoneal injection of the convulsant PTZ, which is routinely used to test anti-convulsants in animals [153–155]. The transition between resting state and epileptic activity after PTZ injection was clearly detected by the TNPs with an excellent signal to noise ratio (**Figure 2.6**b), thus demonstrating the potential of these all-polymeric TNPs for monitoring epileptic activity.
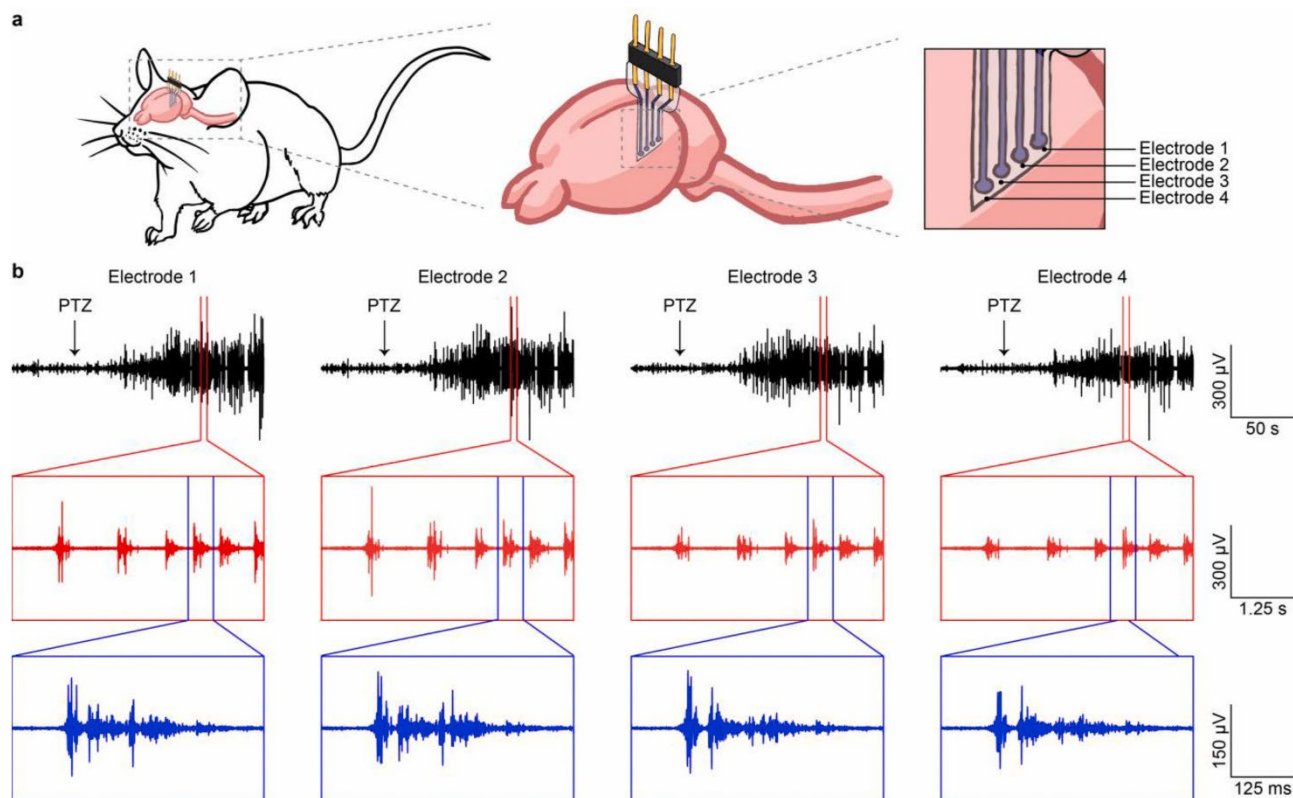
Figure 2.6 Acute recordings with all-polymeric transient neural probes. (**a**) Sketch of the TNP implanted in a mouse brain for in vivo recordings. (**b**) Detection of epileptic activity after injection of PTZ (black arrow) from the four electrodes of an all-polymeric TNP. The red and blue boxes show an enlargement of the recorded activity.

Next, we performed chronic in vivo recordings of baseline activity, LFPs at rest and visually evoked potentials (VEPs) to assess the longevity of the device. All-polymeric TNPs were implanted in the visual cortex area of mice, and their functionality was evaluated through periodic recordings up to 3 months post-implantation (**Figure 2.7**). The broad-band noise of recordings was computed from baseline recordings (2.5 min, bandpass filter 0.1–2000 Hz and sampling frequency 8192 Hz). The noise plot (**Figure 2.7**a) shows the evolution of the noise level for each working electrode over time (filled circles). Once an electrode was found not properly functional (empty circles), it was excluded from further analysis. The applied criteria of exclusion were the following: i) appearance of periodic artefacts not linked to any biological function (red arrow in **Figure 2.7**a); ii) noise level higher than the average plus twice the standard deviation of the noise at each time point; iii) lack of VEPs. The number of excluded electrodes progressively increased over time (**Figure 2.7**b), with 3 out of 16 electrodes still properly functional after three months. LFPs (2.5 min, bandpass filter 0.1–100 Hz and sampling frequency 819.2 Hz) are not strongly affected by broad-band noise because of the low pass filter at 100 Hz. On the other hand, LFPs are characterised by a strong delta rhythm (0.5–4 Hz) due to the animal anaesthesia (**Figure 2.7**c). Early after implantation, electrodes showed a narrow power spectral density (PSD) in the range of delta rhythm (black traces in Fig. 4c and black lines in **Figure 2.7**d). Over time, because of the electrode deterioration, the normalised PSD shows activity at higher frequency in electrodes that were previously considered not properly functional because of high broad-band noise (grey line in **Figure 2.7**d). Conversely, electrodes still considered functional showed a narrow PSD (red line in **Figure 2.7**d). As a consequence, the relative power of the delta band decreases with the deterioration of the electrodes (**Figure 2.7**e). For each electrode, early after implantation, a low noise correlates with a high relative power of the delta band. However, at the exclusion point, there is a reduction of the relative delta power which is globally proportional to the increase of noise (linear re-

gression: slope = −1.369, R square = 0.527). Overall, all-polymeric TNPs retain good in-vivo recording capabilities for months after implantation, even if they progressively lose functionality and only a few electrodes are still properly functional after three months.
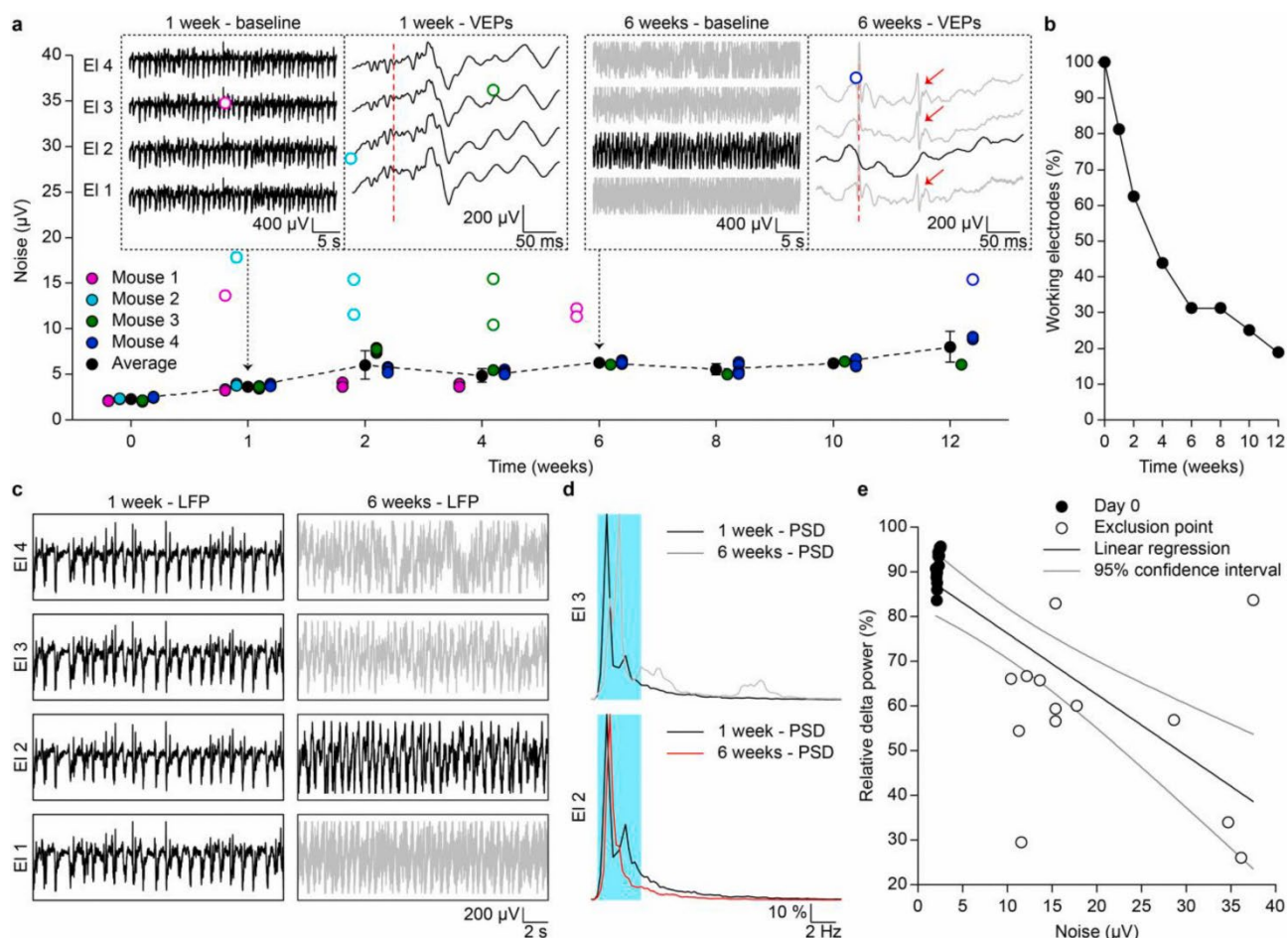
Figure 2.7 Long-term functioning in-vivo. (**a**) Noise evaluation as a function of time during in-vivo chronic recordings at fixed time points. Different colours correspond to different mice; filled circles correspond to the electrodes considered functional and thus included in the calculation of the average (±s.d.) noise values (black circles and dashed line), while empty circles correspond to the electrodes considered not correctly working and thus excluded from the calculation of the average noise. The two insets show single baseline recordings (left) and VEPs (right) from all the four electrodes of the TNP implanted in mouse 3 at week 1 and week 6 post-implantation; the red dashed line indicates the light stimulus for VEPs (10 cd s m^{-2}). The traces in grey are from electrodes considered not functional. The red arrows show periodic artefacts not linked to any biological function. (**b**) Plot of the percentage of working electrodes as a function of time during in-vivo chronic experiments. (**c**) Representative example of LFPs recorded from all the electrodes of the TNP implanted in mouse 3 at week 1 and week 6 post-implantation. The traces in grey are from electrodes considered not functional. (**d**) Representative examples of normalised power spectral densities obtained from the recordings from two electrodes (numbers 2 and 3) of the probe implanted in mouse 3 at week 1 (black traces) and week 6 (black, grey and red) after implantation. The trace in grey is from the electrode considered not functional, while the trace in red is from the electrode considered still functional. (**e**) Correlation between the relative power of the delta band and the noise of the electrodes immediately after implantation (16 electrodes, black circles) or at the time point of exclusion (13 electrodes, empty circles). The black line is the linear regression, while the grey lines the 95% confidence interval.

At this stage, the cause of electrode deterioration is not easy to determine. So far, only a few studies have investigated the chronic performances of PEDOT:PSS in-vivo [156–159], and the results indicated a reduction in performance after a few months of implantation. Many factors could contribute to the deterioration of PEDOT:PSS in-vivo, related to both materials properties and interaction with the biological environment. A commonly reported problem is the adhesion of PEDOT:PSS to the substrate[160]. The weak adhesion between PEDOT:PSS and polyesters[161], like PCL, plays a crucial role since PEDOT:PSS might be subjected to water-induced swelling and delamination during the degradation of the PCL scaffold. PEDOT has also been reported to undergo degradation by hydrolysis when exposed to salt aqueous solutions[162] or by high concentration of hydrogen peroxide, which is a physiological

oxidant[163,164]. Macrophages cultured with PEDOT:PSS generated a significant amount of hydrogen peroxide, that is a significant factor involved in cellular phagocytosis[165]. PEDOT:PSS could possibly be degraded by the combination of hydrolysis and presence of hydrogen peroxide following device implantation[160].

2.2.3 Evaluation of the foreign body reaction

To investigate the acute phase of the foreign body reaction induced by TNPs, we performed a histological paired comparison between all-polymeric TNPs and polyimide (PI) implants, surgically placed in the two hemispheres of the brain of the same mice (**Figure 2.8**a). The PI implants were chosen as a reference for non-degradable flexible implants. Also, the implants have been manufactured with similar dimensions to be more comparable (TNP: ~130 μm thick and 1.3 mm wide; PI: 125 μm thick and 0.7 mm wide). Evaluations have been made at 1- and 2-months post-implantation, 6 mice for the first time point and 5 mice for the second.
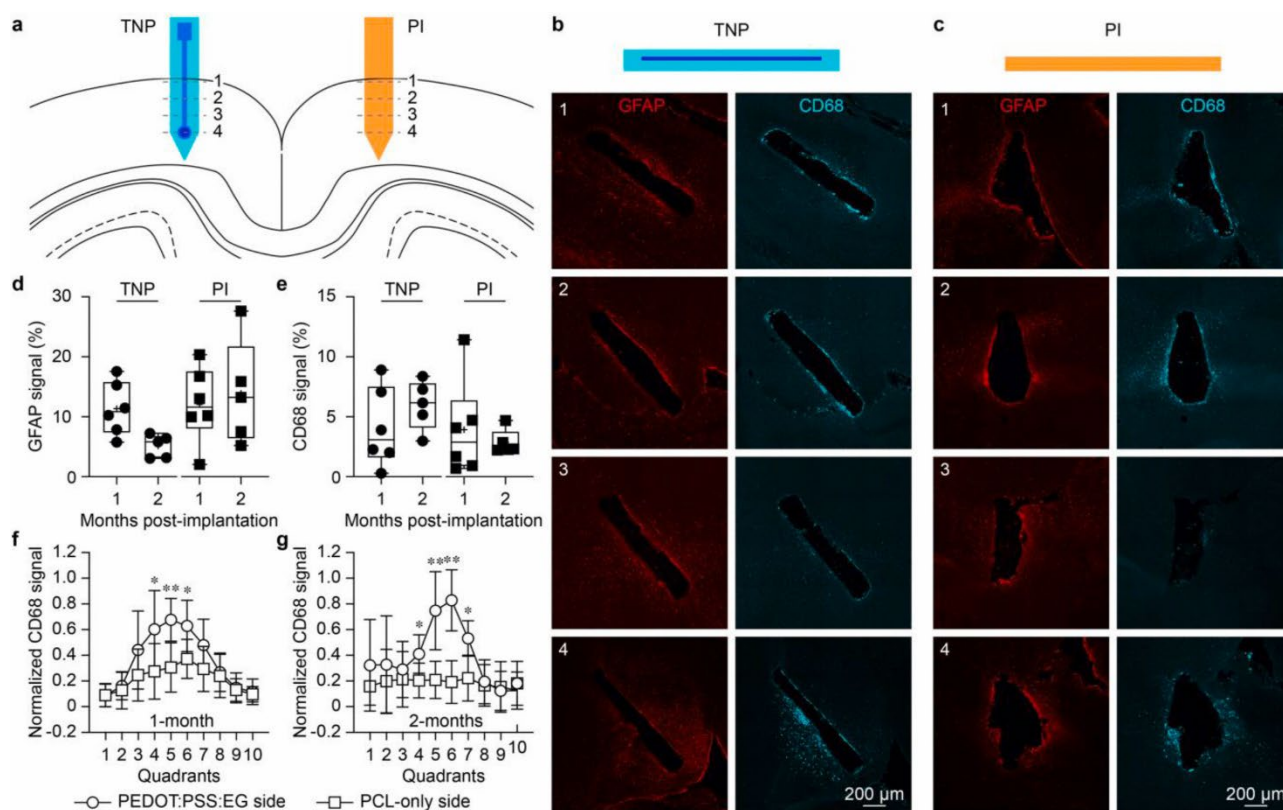
Figure 2.8 Foreign body reaction induced by all-polymeric transient neural probes. (**a**) Sketch of the TNP and PI probe implanted in both visual cortices of a mouse. For each probe, four slices were taken at four depths into the cortical layers. (**b,c**) Example of GFAP (in red) and CD68 (in cyan) expression in horizontal slices (four depths into the cortical layers indicated by the numbers) obtained from the hemisphere implanted with the TNP (**b**) and with the PI probe (**c**) 1-month post-implantation. (**d,e**) Quantification of the area occupied by GFAP signal (**d**) and CD68 signal (**e**) at 1-month and 2-month post-implantation for TNPs and PI probes. Results from all the images at each depth were averaged together: 3 images per depth. (**f,g**) Quantification of the normalised area occupied by the CD68 signal above (PEDOT:PSS:EG side) and below (PCL-only side) TNPs at the level of the electrode at 1-month (**f**) and 2-month (**g**) post-implantation.

For each mouse, horizontal brain slices were sampled at different cortical depths (**Figure 2.8**a from 1 to 4) and analysed after image segmentation (**Figure 2.9**). Images were rotated to align the probe horizontally (**Figure 2.9**a) and converted to binary using a local threshold algorithm: all pixels which intensity was above the threshold were assigned the value of 1, while to the rest of the pixels were assigned the value of 0 (**Figure 2.9**b). A group of adjacent pixels with value 1 was defined as a blob, and the area of each blob was calculated, along with the coordinates of its centroid. The image was divided

into 10 × 10 quadrants (**Figure 2.9**c), for each of which the total area of blobs (with their centroid included in that quadrant) was computed. Then, the total area occupied by blobs in the zone adjacent to the probe (**Figure 2.9**d) was calculated as the cumulative area of all the quadrants included in a rectangle defined by the extremities of the probe (manually specified for each of the images), minus the area of the probe itself.
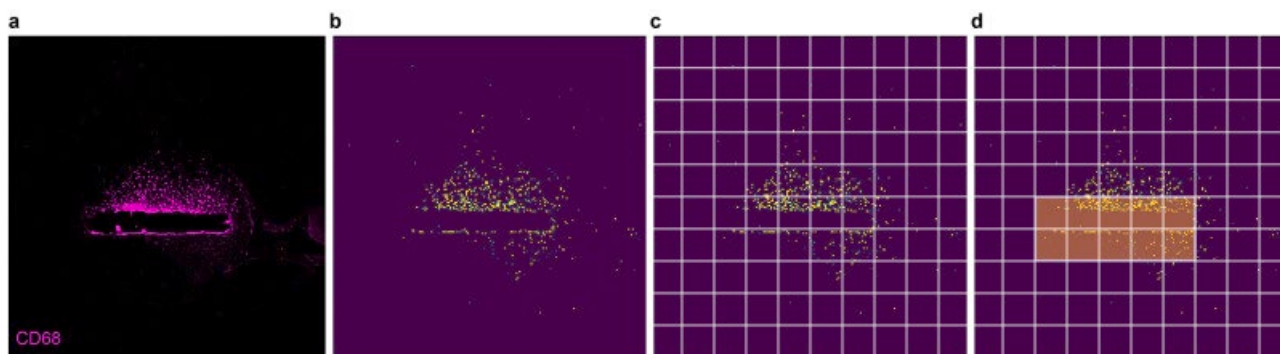
Figure 2.9 Image segmentation. (a) Representative image from a horizontal section of the mice brain implanted with an all-polymeric TNP and stained against CD68. (b) Binary image obtained using a local threshold algorithm on the image in (a). To the pixels whose intensity is above the threshold it is assigned the value 1 (yellow), while to the other pixels it is assigned the value 0 (background). (c) The image in (b) is divided into 10 × 10 quadrants, and the total area of the blobs (formed by adjacent pixels with value 1) is computed for each quadrant. (d) The proximal area (area of the zone adjacent to the probe) is defined as the cumulative area of all the quadrants that are included in a rectangle defined by the extremities of the probe minus the area of the probe itself.

The percentage of the area occupied by blobs was computed as the area occupied by blobs over the proximal area. The average percentage of the proximal area occupied by the blobs for each sample was used as a parameter to compare the experimental groups. Three images for each depth were averaged. The staining for the GFAP (**Figure 2.8**b,c) and the corresponding quantification analysis (**Figure 2.8**d) performed on segmented images showed that the area occupied by the GFAP signal in the zone adjacent to the probe exhibits a decreasing trend over time for all-polymeric TNPs ($p = 0.0178$, two-tailed unpaired t-test) and a stable trend for PI probes ($p = 0.6924$, two-tailed unpaired t-test). Also, the staining for CD68 (**Figure 2.8**b,c), a marker of phagocytic structures in microglia[166], and the corresponding quantification analysis (**Figure 2.8**e) showed that the area occupied by the CD68 signal exhibits a slightly increasing trend over time for all-polymeric TNPs ($p = 0.2897$, two-tailed unpaired t-test), while it remains stable for PI probes ($p = 0.5905$, two-tailed unpaired t-test).

Histological samples of brains implanted with TNPs showed a clustering of the CD68 signal at the level of the electrode (slice 4 in **Figure 2.8**b,c), the only point where the PEDOT:PSS:EG is exposed to the tissue. Following this observation, we performed a second analysis where the segmented images were divided into two parts: the side of the probe with the PEDOT:PSS:EG exposed and the side of the probe with only the PCL exposed (**Figure 2.10**). For each side, the cumulative area occupied by blobs was calculated along the horizontal axis and normalised by the global maximum. The probes were always implanted with the PEDOT:PSS:EG layer exposed to the caudal part of the brain to discriminate the two sides during image analysis. The analysis confirmed that the CD68 signal is highly clustered on the side of the PEDOT:PSS:EG electrodes at both time points (**Figure 2.8**f,g), suggesting an interaction between microglia and PEDOT:PSS:EG.
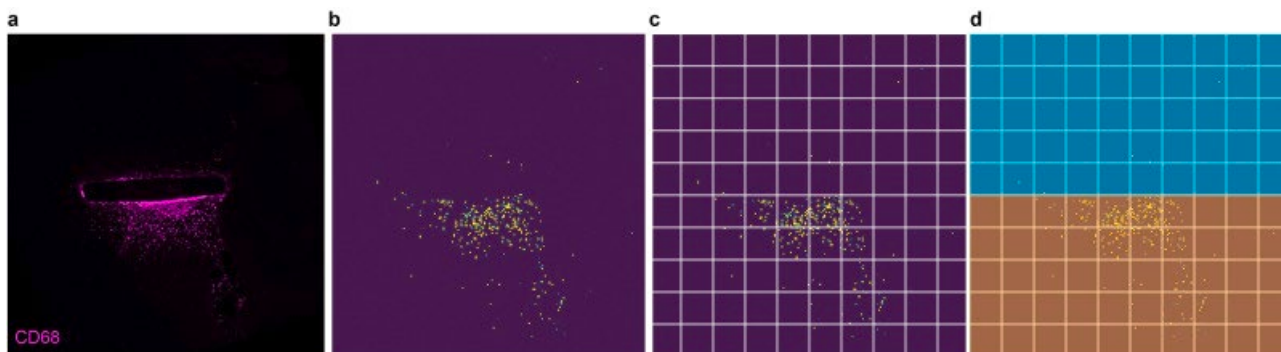
Figure 2.10 Differential image segmentation above and below the probe. (**a**) Representative image from a horizontal section at the electrode level of the mice brain implanted with an all-polymeric TNP and stained against CD68. (**b**) Binary image obtained using a local threshold algorithm on the image in (a). To the pixels whose intensity is above the threshold it is assigned the value 1 (yellow), while to the other pixels it is assigned the value 0 (background). (**c**) The image in (b) is divided into 10 × 10 quadrants, and the total area of the blobs (formed by adjacent pixels with value 1) is computed for each quadrant. (**d**) The image is divided into two parts: the side of the probe with PEDOT:PSS:EG exposed (yellow) and the side of the probe with only the PCL exposed (blue).

Next, we quantified the spatial extent of the GFAP and CD68 signals around the TNP at each cortical depth. Each image (one per depth) was rotated to align the probe vertically (**Figure 2.11**a). Two regions of interest, one on the left and one on the right of the probe, were manually defined as rectangles perpendicular to the probe, spanning from the edge of the probe to the border of the image (**Figure 2.11**b). For each of them, the average intensity along the horizontal axis was computed, starting from the edge of the probe to the border of the image. The average vector of intensities was normalised by dividing each point by the maximum value among the two regions of interest and a normalised intensity plot was generated (**Figure 2.11**c). For each cortical depth, normalised intensity plots from all mice were averaged (6 mice at 1-month post-implantation and 5 mice at 2-months post-implantation) to determine the spatial profile. The spatial profiles of both GFAP (**Figure 2.11**d,e) and CD68 (**Figure 2.11**f,g) resulted uniform along the vertical axis of the probe (cortical depths) at both 1- and 2-months post-implantation (**Figure 2.11**d,f and **Figure 2.11**e,g respectively). In order to quantify the extent of the GFAP and CD68 signals, we measured the distance from the probe at which the average profile among the 4 depths (black lines in **Figure 2.11**d–g) is reduced by 50% (red dots in **Figure 2.11**6d–g). The quantification (**Figure 2.11**h) revealed that the GFAP signal is wider 1-month post-implantation (116.82 and 206.16 μm respectively for the left and the right side of the probe) and it is reduced 2-months post-implantation (96.55 and 95.18 μm respectively for the left and the right side of the probe), although the reduction is not significant (p = 0.3333, two-tailed Mann-Whitney test). This result is in agreement with the previous analysis (**Figure 2.8**d). The CD68 signal is restricted to a small area around the probe (1-month: 85.56 and 62.88 μm; 2-months: 75.60 and 78.00 μm; respectively for the left and the right side of the probe), and it does not change from 1- to 2-months post-implantation (**Figure 2.11**h; p > 0.9999, two-tailed Mann-Whitney test), in agreement with the previous analysis (**Figure 2.8**e).
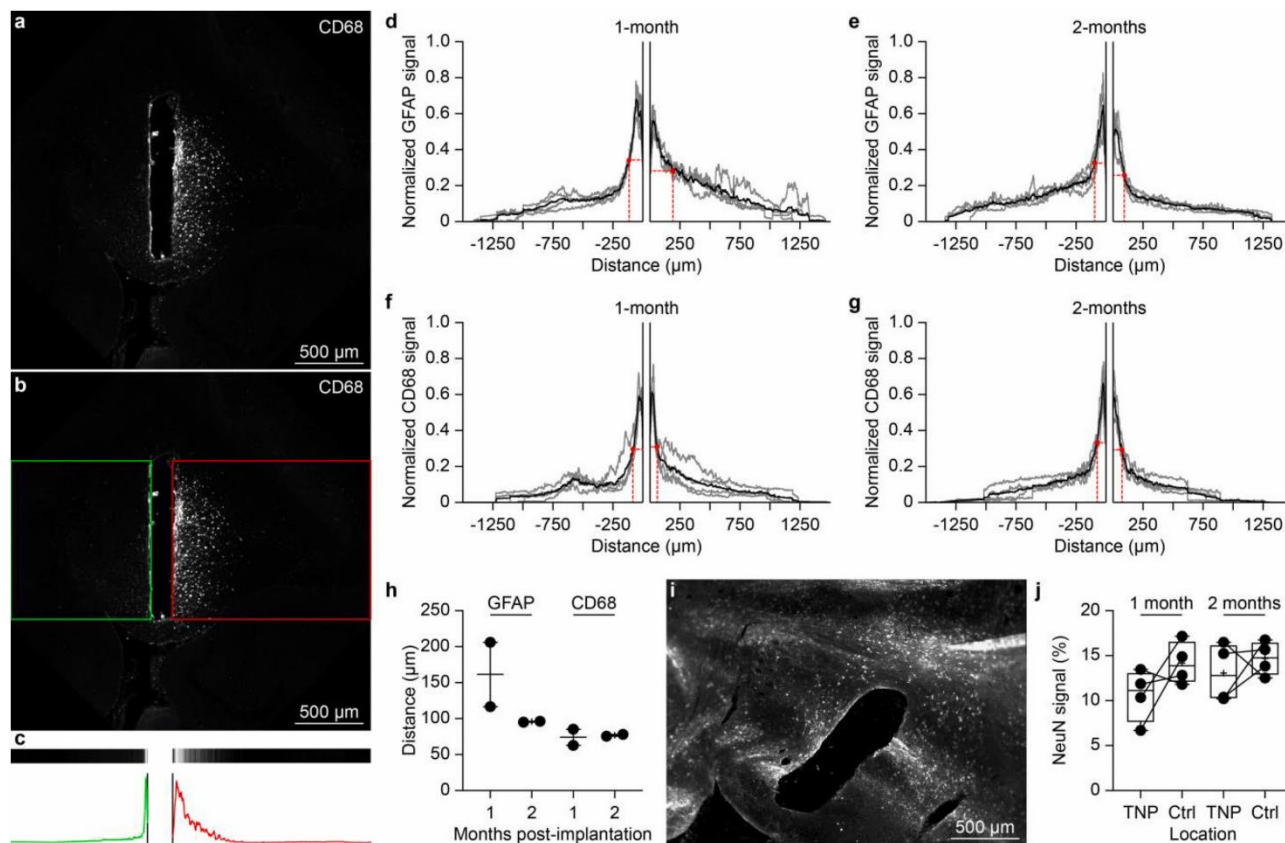
Figure 2.11 Spatial extent of the foreign body reaction. (**a**) Example of CD68 expression in a horizontal slice obtained from the hemisphere implanted with the TNP at 1-month post-implantation. (**b**) Definition of the two regions of interest on the left and on the right of the TNP. (**c**) Average vectors of normalised intensities (top) and normalised intensity plots (bottom). (**d,e**) Normalised intensity plots for GFAP signal 1-month (**d**) and 2-months (**e**) post-implantation. The grey lines correspond to the four cortical depths and the black line is the average. The red dot corresponds to a 50% decrease in the intensity. (**f,g**) Normalised intensity plots for CD68 signal 1-month (**f**) and 2-months (**g**) post-implantation. The grey lines correspond to the four cortical depths and the black line is the average. The red dot corresponds to a 50% decrease in the intensity. (**h**) Quantification of the distance from the TNP at which the intensity plot shows a 50% decrease. (**i**) Example of NeuN expression in a horizontal slice obtained from the hemisphere implanted with the TNP at 1-month post-implantation. (**j**) Quantification of the area occupied by NeuN signal at 1-month and 2-months post-implantation of the TNPs compared to a control (Ctrl) area located far from the TNPs. Each data point corresponds to one cortical depth, average of 3 images per depth.

We also quantified the area occupied by NeuN signal (a marker for neuronal cells) around the TNP at the four cortical depths (**Figure 2.11**i) compared to a control area located far from the TNP. The quantification analysis (average of three sections per cortical depth), performed on one mouse per time point (1- and 2-months post-implantation), showed that the area occupied by the NeuN signal is not statistically different between the two areas (**Figure 2.11**i; 1-month: p = 0.3750, Wilcoxon matched-pairs signed rank test; 2-months: p = 0.6250, Wilcoxon matched-pairs signed rank test).

The clustering of the CD68 signal we observed at the level of the PEDOT:PSS:EG electrode (**Figure 2.8**f,g) encouraged us to further investigate the interaction between phagocytic microglial cells and PEDOT:PSS:EG. To this end, we fabricated TNPs with a PCL substrate coated with PEDOT:PSS:EG labelled with the fluorescent marker FITC [167] and implanted them into the cortex of mice expressing tdTomato in microglia (**Figure 2.12**a). In this experiment, all-polymeric TNPs were not encapsulated to enhance interaction between microglial cells and PEDOT:PSS:EG. High-resolution imaging on clarified brains 1-month (**Figure 2.12**b) and 2-months (**Figure 2.12**c) post-implantation showed colocalization of PEDOT:PSS:EG (in green) and microglial cells (in red). This evidence suggests that the presence of PEDOT:PSS:EG detached from the PCL substrate stimulates phagocytic activity of microglial cells, and that microglia are participating in the clearance of PEDOT:PSS:EG from the implantation site. Horizontal brain sections at 1-month post-implantation also revealed microglial cells (in red) localiz-

ing in the region where PEDOT:PSS:EG (in green) is delaminated or directly in contact with the brain (**Figure 2.12**d). These cells are CD68 positive (in white), the presence of intracellular phagocytic structures. Based on the results discussed above, we hypothesise that implanted TNPs lead to the formation of a less tight glial scar compared to PI probes. As a consequence, microglia have the space needed to access the probe and phagocyte the delaminated PEDOT:PSS:EG flakes.
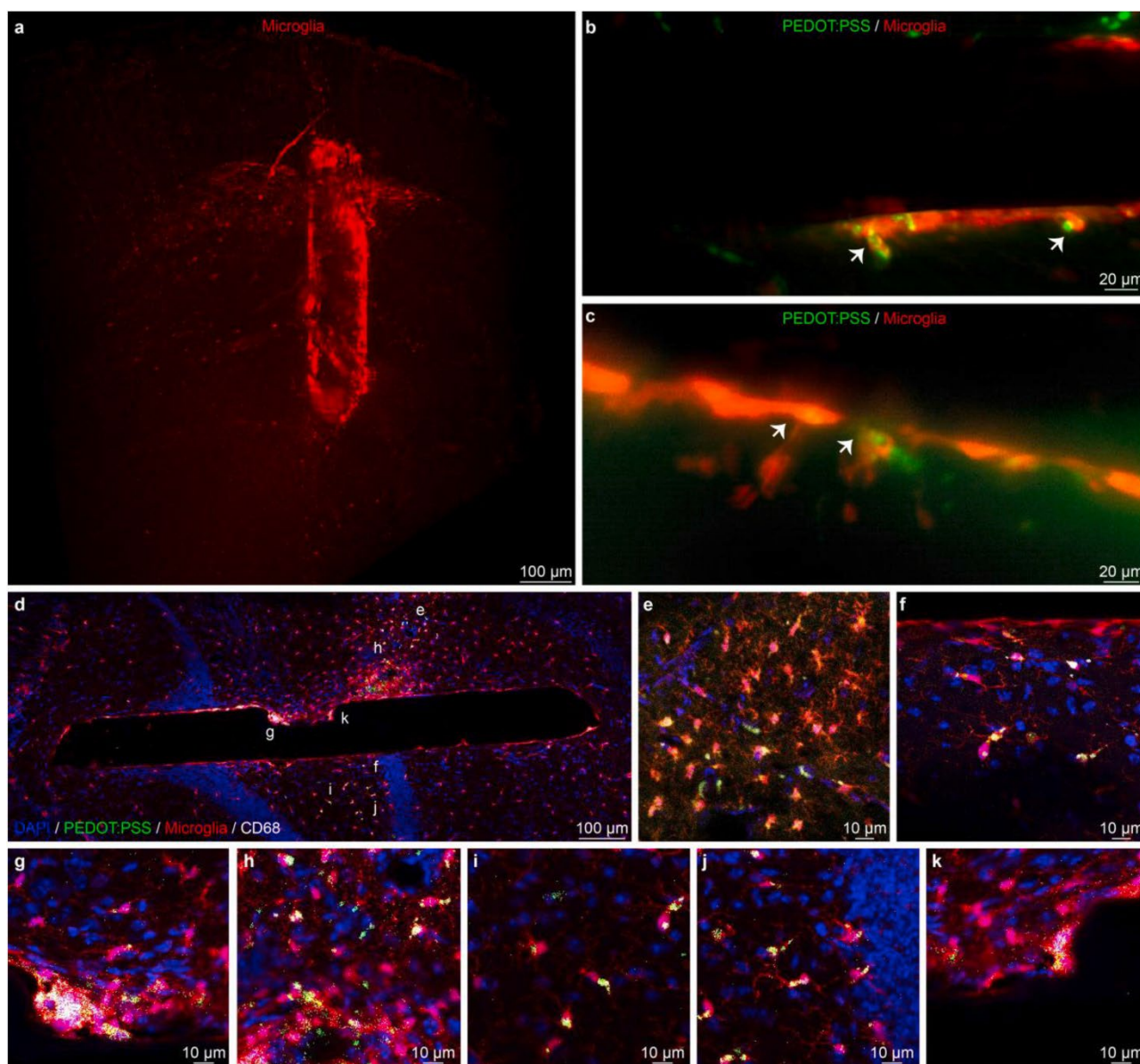
Figure 2.12 Integration with microglia. (**a**) 3D mesoSPIM image of a clarified brain sample with fluorescent microglia (red) implanted with a TNP with FITC-labelled PEDOT:PSS at 1-month post-implantation. (**b,c**), COLM images of the probe surface, showing fluorescent PEDOT:PSS (in green) and microglia (in red) colocalization 1-month (**b**) and 2-months (**c**) post-implantation. Microglia engulf PEDOT:PSS:EG particles which are detaching from the probe (white arrows). (**d**) Horizontal brain section of mouse brain with fluorescent microglia (in red) implanted with a fluorescent TNP (without encapsulation) at 1-month post-implantation. (**e,k**), Various magnifications of the section in (**d**) (corresponding letters) showing phagocytic microglia engulfing PEDOT:PSS:EG (in green). CD68 (in white) is a specific marker for microglial phagocytic structures.

2.2.4 Probe degradation

One of the most exciting features of transient medical devices is their natural ability to disappear in the body, which in turns reduces the long-term foreign body reaction. PCL bulk degradation occurs slowly with a time scale spanning several months or years [35], thus making an in-vivo assessment in

animals extremely challenging. In order to investigate the degradation process of all-polymeric TNPs, we performed in-vitro accelerated degradation tests, by leaving 3 TNPs immersed in PBS at 37 °C and pH 12 and monitoring their weight over time. Scanning electron microscope images showed the appearance of micro- and macro-cracks over time due to hydrolysis (**Figure 2.13**a), and all-polymeric TNPs undergo full degradation in about one year of time at pH 12 (**Figure 2.13**b). A comparison between the days to reach a weight loss of 5% at pH 12 and at pH 7.4 revealed that the test has an acceleration factor of about 2.5. Slow degradation is an appealing feature for TNPs, since it might allow for better tissue remodelling and reduced chronic trauma at the implantation site [39,40,141]. To provide evidence of slow degradation in-vivo of all-polymeric TNPs, we implanted them in the cortex of mice and subsequently performed immunofluorescence assays on horizontal brain slices at a fixed time point. Upon long-term implantation (9 months), the all-polymeric TNPs showed a minor chronic glial scar (**Figure 2.13**c), evaluated with staining for astrocytes against GFAP. The formation of a glial scar should be minimised or avoided for several reasons: it increases the distance between the recording surface of the electrode and neurons, eventually impairing the recording capabilities of the device [168,169], and acts as a barrier for growth factors, ions, and signalling molecules, thus promoting neural apoptosis and impeding axon regeneration [170,171]. In the case of TNPs, the presence of a limited glial scar allows tissue remodelling around the probe, and, as a consequence, neurons (labelled against NeuN in green) are free to relocate within the device, which serves as a support scaffold during the degradation (**Figure 2.13**d). This evidence of the probe slow degradation in-vivo is a promising sign of reduced chronic trauma.
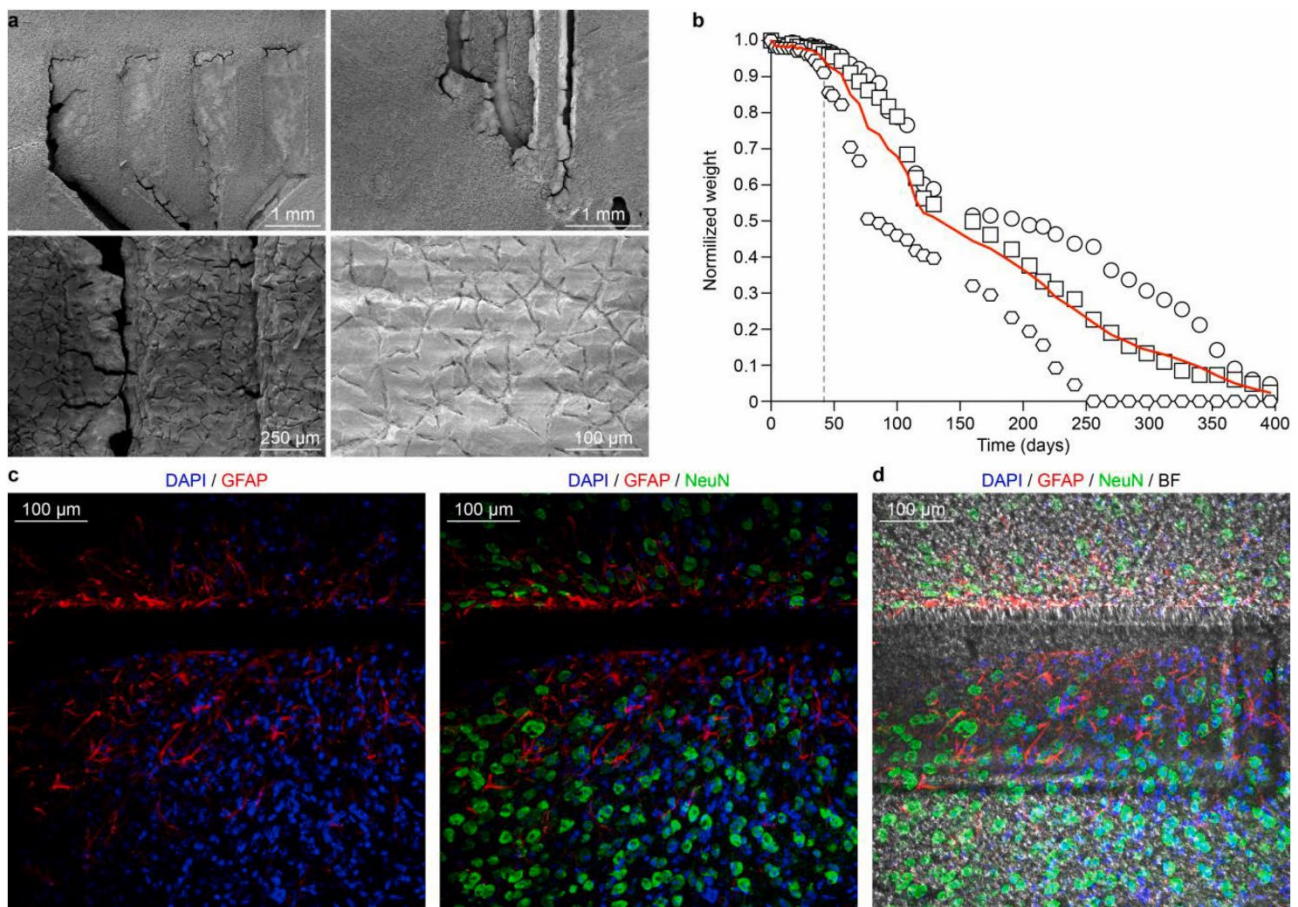
Figure 2.13 Degradation of all-polymeric transient neural probes. (**a**) Scanning electron microscopy images at several magnifications of one all-polymeric TNP obtained 191 days after soaking in PBS at 37 °C and pH 12. (**b**) Plot of the normalised probe weight versus time of 3 TNPs during a degradation test in PBS at 37 °C and pH 12. The red line is the average of the 3 TNPs. The grey dashed line is the time point

(day 42) corresponding to a 5% weight loss. (**c**) Horizontal brain section from a mouse implanted with a TNP in the cortex. 9-months post-implantation staining against GFAP and NeuN. (**d**) The same image in (**c**) with a bright-field overlay to highlight the area occupied by the TNP.

2.3   Discussion

In biomedical engineering and medicine, transient devices are a relatively new concept which has the potential to widen the range of possible applications of implantable medical devices. We explored this new concept with using fully polymer-based devices to exploit their unique characteristics and try to overcome some of the current limitations. So far, transient medical devices showed a short functional lifetime because of the fast degradation of degradable metals in contact with body fluids [134,137].

In this work, we showed the fabrication and characterization of a polymer-based implantable device conceived to disappear after being functional for a few months rather than a few days. A longer device lifetime will allow, for instance, the development of prosthetic devices for mid-term monitoring of the brain activity, either before or after surgery in chronic epileptic patients. Nowadays, clinicians make decisions on localised surgical treatments based on intracranial electroencephalography recordings that are typically lasting for only 1 or 2 weeks in favour of patient compliance. On the other hand, recent publications in this field revealed that intracranial electroencephalography recordings do not stabilize until several weeks after implantation, due to the invasiveness of the procedure and the inflammatory response of the tissue [172,173]. Therefore, an extended chronic monitoring period, together with the possibility to mitigate the inflammatory reaction, would enable a more accurate representation of the spatiotemporal variability of the seizures, translating into a better diagnosis for the patient. Furthermore, a transient device with extended recording capability would allow for continuous monitoring after the surgical procedure, thus providing essential insights into the brain activity during the recovery period and, possibly, into the effects of the following pharmaceutical treatment. Also, the absence of metals in the implanted portion of the device would provide magnetic resonance imaging compatibility [144,174,175], allowing the pairing of the electrophysiological monitoring with structural and functional images, therefore obtaining a clearer picture of the brain activity during the recovery period.

Even though only a few electrodes (approximately 20%) were still operational three months post-implantation, we believe that there is still room for fabrication strategies that can improve the device lifetime, such as enhancing the adhesion between PEDOT:PSS and PCL by using additives or by oxygen plasma treatment. Also, even if a performance comparison with other inorganic and not-transient devices is out of the scope of this study (due to the transient nature of the presented device), the electrochemical characterization of all-polymeric TNPs showed a stable performance within a wide range of frequencies, thus allowing us to perform acute and chronic in-vivo recordings in mice with excellent signal to noise ratio.

Recently, not-transient implantable neural probes reached extreme miniaturisation to reduce chronic foreign body reaction [66,78]. Miniaturisation for the TNP is limited by materials properties and fabrication methods. However, a detailed study of the foreign body reaction revealed that all-polymeric TNPs were responsible for a minimal glial scar around the implant. As a consequence, neurons were able to colonize the slowly degrading PCL layers, hence promoting tissue remodelling: such behaviour is the opposite to what is usually observed with permanent implants of similar sizes, where neurons are depleted from the implantation site [168].

In summary, the in-vivo validation and the degradation study, together with the preliminary evidence of phagocytic microglia engulfing the conductive polymer, demonstrate that the combination of the

transient electronic approach and the usage of polymers is a new promising path to improve the device-tissue interface, extend the durability of implanted transient devices, and increase their possible applications. Although further research is needed to fully understand the fate of microglial cells upon phagocytosis of PEDOT:PSS:EG, these results can drive the conceptualization of new conductive polymers with links could be degradable, for instance, by resident microglia.

2.4 Materials and methods

2.4.1 Fabrication of transient all-polymeric neural probe

Two 4-inch silicon wafers (525-μm thick) were etched (AMS 200, Alcatel) to obtain the positive mould for the substrate layer and the negative mould for the encapsulation layer (both structures are 100-μm thick). Polycaprolactone (PCL, MW 50,000; 25,090, Polyscience) in powder was dissolved in chloroform (C2432, Sigma-Aldrich) at a concentration of 0.25 g ml−1 and was left stirring and heating at 60 °C overnight over a hotplate. The day after, 6 ml of PCL solution were spin-coated on both silicon moulds (positive: 150 rpm for 30 s; negative: 200 rpm for 30 s) pre-treated with chlorotrimethylsilane (92,361, Sigma-Aldrich) to prevent permanent attachment of the PCL layers. The wafers were then left 30 min in the oven at 75 °C to let the chloroform evaporate. After a cool-down period of at least 2 h, the PCL layer from the positive wafer was peeled off, and the design (electrodes, traces and pads) was filled with an aqueous solution of PEDOT:PSS:EG, which is poly(3,4-ethylenedioxythiophene)-poly(styrenesulfonate) (PEDOT:PSS; M122 PH1000, Ossila) mixed with 20 wt% ethylene glycol (EG; 324,558, Sigma-Aldrich), and cured overnight in an oven at 37 °C. The PCL layer from the negative wafer, instead, was peeled off after laser-cutting the openings for the electrodes and pads (Optec MM200-USP). Eventually, the two layers were manually aligned and fused together over a hotplate at 60 °C for a few seconds. A silver-based epoxy (H27D Kit Part A, Epo-Tek) was then applied on the pads and connectors were positioned and immobilised with silicone (DC 734 RTV clear, Dow Corning). Three types of all-polymeric TNPs were fabricated with a different number of electrodes: 4 electrodes (500-μm in diameter; connector 143-56-801, Distrelec), 1 electrode (500-μm in diameter; no connector) and 17 electrodes (700-μm in diameter; connector 61001821821, Wurth Elektronik). Samples with fluorescent PEDOT:PSS:EG were prepared as previously described [19]. Briefly, poly (vinyl alcohol) (PVA, MW 130,000; 563,900, Sigma-Aldrich) was dissolved in deionization water 5 wt%. A composite solution (25 wt%) of PVA and PEDOT:PSS:EG was prepared, deposited on the PCL, and baked (50 °C, 10 min). (3-Glycidyloxypropyl)trimethoxylane (440,167, Sigma-Aldrich) was then deposited by vapour deposition at 90 °C for 45 min. Afterwards, a solution of fluorescein isothiocyanate (FITC) labelled poly-l-lysine (P3543, Sigma-Aldrich) in phosphate buffered saline (PBS; 50 μg ml−1) was drop-casted on the sample and allowed to react for 2 h at room temperature. The sample was then rinsed with PBS (0.1 M), sodium chloride (0.1 M), and deionised water.

2.4.2 Scanning electron microscopy

Images were taken with a Schottky field emission scanning electrons microscope (SU5000, Hitachi) and image post-processing was performed with ImageJ.

2.4.3 Electrochemistry

Electrochemical characterization was performed with a three-electrode potentiostat (Compact Stat, Ivium) at room temperature. Each all-polymeric TNP was immersed in PBS (pH 7.4) together with a silver/silver chloride reference wire and a platinum counter wire. Impedance spectroscopy (IS) was measured between 1 Hz and 1 MHz using an AC voltage of 50 mV.

2.4.4 Resistance measures

Line resistance was measured using a data acquisition and logging digital multimeter system (daq6510, Keithley).

2.4.5 Cytotoxicity test

A test on extract was performed on two all-polymeric TNPs (4-electrodes design) sterilised by UV exposure, with a ratio of the product to extraction vehicle of 3 cm2 ml−1. The extraction vehicle was Eagle's minimum essential medium (11090081, Thermo Fisher Scientific) supplemented with 10% foetal bovine serum (10270106, Thermo Fisher Scientific), 1% penicillin-streptomycin (15070063, Thermo Fisher Scientific), 2 mM L-Glutamine (25030081, Thermo Fisher Scientific) and 2.50 μg ml−1 Amphotericin B (15290026, Thermo Fisher Scientific). The extraction was performed for 24 h at 37 °C and 5% CO2. L929 cells (88102702, Sigma-Aldrich) were plated in a 96-well plate at a sub-confluent density of 7000 cells per well in 100 μl of the same medium. L929 cells were incubated for 24 h at 37 °C and 5% CO2. After incubation, the medium was removed from the cells and replaced with the extract (100 μl per well). After another incubation of 24 h, 50 μl per well of XTT reagent (Cell proliferation kit 11465015001, Sigma-Aldrich) were added and incubated for 4 h at 37 °C and 5% CO2. An aliquot of 100 μl was then transferred from each well into the corresponding wells of a new plate, and the optical density was measured at 450 nm by using a plate reader (FlexStation3, MolecularDevices). Clean medium alone was used as a negative control, whereas medium supplemented with 15% of dimethyl sulfoxide (D2650-5X5ML, Sigma-Aldrich) was used as a positive control.

2.4.6 Accelerated degradation

All-polymeric TNPs were prepared as described above, with the 4-electrode design. After fabrication, samples were weighted to set the initial weight value before starting degradation. Degradation of each sample occurred in 10-ml PBS at 37 °C and was accelerated by pH increase: 100 μl of NaOH (2M NaOH Standard solution, 71,474-1L, Fluka) were added to the solution to reach pH 12. At each time point, samples were first gently dried with a tissue and then let dry completely under vacuum at room temperature for 4 h. Once dry, samples were weighted. Normalised weight for each sample was computed as the ratio between the weight at each time point and the initial value.

2.4.7 Animal handling

All experiments were conducted according to the animal authorizations GE13416 approved by the Département de l'emploi, des affaires sociales et de la santé (DEAS), Direction générale de la santé of the Republique et Canton de Geneve in Switzerland and VD3420 approved by Service de la consommation et des Affaires vétérinaires (SCAV) of the Canton de Vaud in Switzerland. All the experiments were carried out during the day cycle. For the entire duration of the experiment, the health condition was evaluated three times a week, and the bodyweight was controlled once a week. Experiments were performed in adult (>1-month-old) mice. Male and female C57BL/6J mice (Charles River) were kept in a 12 h day/night cycle with access to food and water ad libitum. White light (300 ± 50 lux) was present from 7 a.m. to 7 p.m. and red light (650–720 nm, 80–100 lux) from 7 p.m. to 7 a.m. Homozygous B6.129P2(Cg)-Cx3cr1tm2.1(cre/ERT2)Litt/WganJ mice (Stock No: 021,160, The Jackson Laboratory) and homozygous B6.Cg-Gt(ROSA)26Sortm14(CAG-tdTomato)Hze/J mice (Stock No: 007914, The Jackson Laboratory) were kept in a 12 h day/night cycle with access to food and water ad libitum. White light (300 ± 50 lux) was present from 7 a.m. to 7 p.m. and no light from 7 p.m. to 7 a.m. Homozygous B6.129P2(Cg)-Cx3cr1tm2.1(cre/ERT2)Litt/WganJ mice and homozygous B6.Cg-Gt(ROSA)26Sortm14(CAG-tdTomato)Hze/J mice were

crossed to obtain heterozygous mice bearing a tamoxifen-inducible expression of the tandem dimer Tomato fluorescent in microglia in the brain. Mice were injected with tamoxifen dissolved in corn oil (75 mg kg^{-1}) to induce the expression at postnatal day 35. Surgery was performed between 2 weeks and 1 month after.

2.4.8 Surgical implantation

Mice were anesthetised with isoflurane inhalation (induction 0.8–1.5 l min^{-1}, 4–5%; maintenance 0.8–1.5 l min^{-1}, 1–2%). Analgesia was performed by subcutaneous injection of buprenorphine (0.1 mg kg^{-1}), and a local subcutaneous injection of lidocaine (6 mg kg^{-1}) and bupivacaine (2.5 mg kg^{-1}) with a 1:1 ratio. The depth of anaesthesia was assessed with the pedal reflex, and artificial tears were used to prevent the eyes from drying. The temperature was maintained at 37 °C with a heating pad during both surgical procedures and recording sessions. The skin of the head was shaved and cleaned with betadine. Mice were then placed on a stereotaxic frame, and the skin was opened to expose the skull. A squared craniotomy of approximately (4 × 4 mm) was opened over the visual cortex (identified by stereotaxic coordinates), and the dura mater was removed. UV-sterilised all-polymeric TNPs were inserted in the cortex using a micromanipulator (SM-15R, Narishige). The probes were always implanted with the PEDOT:PSS:EG layer exposed to the caudal part of the brain to clearly discriminate the two sides during image analysis. A reference screw electrode was implanted in the rostral side of the cranium. The craniotomy was closed using dental cement, and an extra layer of dental cement was applied to secure the probe. The mice were left to recover on a heating pad and later returned to their cage.

2.4.9 Acute induction of seizure and monitoring of epileptic activity

Immediately after surgery, mice were removed from the stereotaxic apparatus while still under general anaesthesia, a needle electrode was placed subcutaneously in the dorsal area near the tail as ground, and the four channels of all-polymeric TNPs and the reference electrode were connected to the amplifier (BM623, Biomedica Mangoni). The signals were recorded using the WinAver software (Biomedica Mangoni). The recording was started (bandpass filtered 0.1–2000 Hz and sampling frequency 8192 Hz) and, after a baseline period, 20 µl of pentylenetetrazol (PTZ; 50 mg ml^{-1}, 45 mg kg^{-1}) were delivered via intraperitoneal injection.

2.4.10 Chronic recordings

A first acute recording session was carried out immediately after the implantation to check the functionality of the TNPs at the starting point of the experiment. Chronic recordings were then performed 1- and 2-weeks post-implantation and then every 2 weeks until 12 weeks. The mice were dark-adapted for 2 h before each chronic recording session. Mice were anaesthetised with a mixture of ketamine (87.5 mg kg^{-1}) and xylazine (12.5 mg kg^{-1}). The depth of anaesthesia was assessed with the pedal reflex, and artificial tears were used to prevent the eyes from drying. The temperature was maintained at 37 °C with a heating pad during both surgical procedures and recording sessions. Mice were placed on a stereotaxic apparatus in front of a Ganzfeld flash stimulator (BM6007IL, Biomedica Mangoni) and a needle electrode was placed subcutaneously in the dorsal area near the tail as ground. The four channels of all-polymeric TNPs and the reference electrode were connected to the amplifier (BM623, Biomedica Mangoni). The signals were recorded using the WinAver software (Biomedica Mangoni). First, a baseline recording was obtained for 2.5 min (bandpass filter 0.1–2000 Hz and sampling frequency 8192 Hz). The recording noise was extracted from the baseline recording using a moving average window of 10 points; the mean ± s.d. was calculated for each 500 ms epoch, then the mean

s.d. of all the epochs was averaged to obtain the noise of the whole recording. Channels with a noise level higher than the average plus twice the s.d. of the noise at each time point were considered as non-working channels and excluded from further analysis. Local field potentials (LFPs) were then acquired for 2.5 min (bandpass filter 0.1–100 Hz and sampling frequency 819.2 Hz). After the recordings, a high pass filter at 0.5 Hz was applied, and the periodogram was calculated using the Welch method (window of 4 s) on the whole recording. The area below the curve between 0.5 and 4 Hz frequencies (corresponding to the delta band) was approximated using the composite Simpson's rule. The power of the delta band was then divided by the total power (area below the periodogram) to obtain the relative power of the delta band. Last, visually evoked potentials were recorded (bandpass filter 0.1–200 Hz and sampling frequency 2048 Hz) upon the presentation of 10 consecutive flashes (4 ms, 10 cd s m^{-2}) delivered at 1 Hz of repetition rate. Data were processed and analysed using MATLAB (MathWorks). After each session, the mice were left to recover on a heating pad and later returned to their cage.

2.4.11 Euthanasia

Animals were euthanised with an injection of pentobarbital (150 mg kg^{-1}) under a chemical hood. The chest cavity was opened to expose the beating heart, and a needle was inserted in the left ventricle, while the right atrium was cut to allow complete bleeding. The animal was immediately perfused with PBS followed by a fixative solution of 4% paraformaldehyde (PFA) in PBS. At the end of the procedure, the head of the animal was removed, and the brain collected and placed in 4% PFA overnight for post-fixation.

2.4.12 Histological analysis

Brain samples were cryoprotected in sucrose 30% and frozen in optimal cutting temperature compound. 20 μm thick horizontal sections of the brain were obtained using a cryostat (Histocom, Zug, Switzerland) and placed on microscope slides. The sections were washed in PBS, permeabilised with PBS + Triton 0.1% (Sigma-Aldrich), left for 1 h at room temperature in blocking buffer (Triton 0.1% + 5% normal goat serum), and incubated overnight at 4 °C with primary antibodies for the glial fibrillary acidic protein (GFAP; 1:1000; Z0334, Dako), the cluster of differentiation 68 protein (CD68; 1:400; MCA1957, Biorad) and neural nuclei (NeuN; 1:500; ABN90P, Millipore). The day after, the sections were incubated for 2 h at room temperature with secondary antibodies (1:500; Alexa Fluor 647 and 488, Abcam), counterstained with DAPI (1:300; Sigma-Aldrich) and mounted for imaging with Fluoromount solution (Sigma-Aldrich). Representative images were acquired with a confocal microscope (LSM-880, Zeiss). For image segmentation and quantification, images were acquired using a slide scanner microscope (VS120, Olympus; 20× objective, pixel size 0.34 μm) and analysed in Python, using the scikit-image package (https://scikit-image.org/).

2.4.13 Whole-brain imaging

Brain clarification was performed according to a previously described procedure [176]. Briefly, after overnight post-fixation at 4 °C in PFA 4%, the brain was immersed in hydrogel solution (Acrylamide 40% + VA-044 initiator powder in PBS) at 4 °C for three days. The hydrogel polymerization was induced by keeping the sample at 37 °C for 3 h. Then, the brain was passively clarified in 4% sodium dodecyl sulfate clearing solution (pH 8.5) for four weeks under gentle agitation at 37 °C. The whole clarified brain was transferred to Histodenz solution at pH 7.5 (Sigma-Aldrich). Brains were immersed in a refractive index matching solution (RIMS) containing Histodenz for at least 24 h before being imaged. Brains were glued to a holder and immersed in a 10 × 20 × 45 mm^3 quartz cuvette filled with

RIMS. The cuvette was then placed in a chamber filled with oil with (n = 1.45; Cargille). A custom-made light-sheet microscope optimised for labelled clarified tissue was used to image the implant within the mouse brain (COLM, clarity optimised light-sheet microscope [177]). The sample was illuminated (488 and 554 nm) by two digitally scanned light-sheets coming from opposite directions, and the emitted fluorescence was collected by high numerical aperture objectives (Olympus XLPLN10XSVMP, N.A 0.6) filtered (Brightline HC 525/50, Semrock) and imaged on a digital CMOS camera (Orca-Flash 4.0 LT, Hamamatsu) at a frequency ranging between 5 and 10 frames per second. A self-adaptive positioning of the light sheets across Z-stacks acquisition ensured an optimal image quality over up to 1 cm of tissue. To acquire images of whole samples at lower resolution another custom-made light-sheet microscope was used (mesoSPIM, mesoscale selective plane illumination microscopy [178]). The microscope consists of a dual-sided excitation path using a fibre-coupled multiline laser combiner (405, 488, 561 and 647 nm; Toptica MLE) and a detection path comprising a 42 Olympus MVX-10 zoom macroscope with a 1× objective (Olympus MVPLAPO), a filter wheel (Ludl 96A350), and a CMOS camera (Orca Flash 4.0 V3, Hamamatsu). The excitation paths also contain galvo scanners for light-sheet generation and reduction of shadow artefacts due to absorption of the light-sheet. In addition, the beam waist is scanned using electrically tuneable lenses (EL-16-40-5D-TC-L, Optotune) synchronised with the rolling shutter of the CMOS camera. This axially scanned light-sheet mode leads to a uniform axial resolution across the field-of-view of 5 µm. Image acquisition was made using custom software written in Python. Z-stacks were acquired at 3 µm spacing with a zoom set at 2x resulting in an in-plane pixel size of 7.8 µm (2048 × 2048 pixels). The excitation wavelength was set at 561 nm with an emission 530/40 nm bandpass filter (BrightLine HC, AHF).

2.4.14 Statistical analysis and graphical representation

Statistical analysis and graphical representation were performed with Prism 8 (Graph Pad). The normality test (D'Agostino & Pearson omnibus normality test) was performed in each dataset to justify the use of a parametric or non-parametric test. The box plots always extend from the 25th to 75th percentiles. The line in the middle of the box is plotted at the median. The + is the mean. The whiskers go down to the smallest value and up to the largest. In each figure p-values were represented as: $*p < 0.05$, $**p < 0.01$, $***p < 0.001$, and $****p < 0.0001$.

2.5   Acknowledgements

Chapter 3 Transient neurovascular interface for minimally invasive neural recording and stimulation

The goal addressed in this chapter is the adaptation of the previously presented device to an endovascular delivery and its testing in application-like conditions.

3.1   Introduction

Neurotechnology for neural recording and stimulation opened the door to a deeper understanding of the brain and, at the same time, led to the development of treatments for heavily impairing conditions following traumatic injuries, neurodegenerative diseases, or mental disorders.[179] Although the potential impact of neurotechnology is enormous, its clinical use nowadays is still limited. Many devices require invasive surgery, with related high risks that not always overcome the benefits for the patients. A big step in this direction has been the development of neurovascular interfaces which interact with the neural tissue from within blood vessels. Endovascular procedures are considerably less invasive, are routinely performed and allow for short recovery time.[180] Moreover, neurovascular interfaces do not require craniotomies, reducing the risks associated with the surgical procedure (e.g., susceptibility to seizures). These advantages could increase the chance of patients accepting the treatment.

Neurovascular interfaces developed so far are wires or catheters used as electrodes. Even though these solutions opened the doors to endovascular neural recording and stimulation, their main limitations were the short-term application and the low spatial resolution. The introduction of stent-electrode arrays (e.g., Stentrode) overcame these issues[180], and the advantages of this technology have been recently demonstrated in preclinical and clinical trials for brain-computer-interface[93,117,121,122]. Also, seventeen potential medical targets have been identified where intravascular neuromodulation could replace invasive deep brain stimulation protocols[123]. By accessing the internal cerebral vein or the anterior communicating artery, it would be possible to perform minimally invasive neuromodulation for a wide range of neurological disorders such as Parkinson's, Alzheimer's, essential tremor, depression, and obsessive-compulsive disorders[123]. Furthermore, neurovascular interfaces could be as well applied to the peripheral system for pain relief, motor deficits, bladder control, and stimulation of muscles, among others. However, the main drawback of stent-electrode arrays is the metallic scaffold. A conductive substrate for electrodes makes insulation critical and shortcuts frequent[93]. Also, metallic stents could induce a strong inflammatory response, that could reduce the performances of a neural interface[181–184]. For conventional stent technology, this limitation already led to the development of bioresorbable devices, allowing for a better interaction with the tissue and placement in mechanically solicited areas[185].

These limitations motivated us to develop a transient stent-electrode array based on polymeric materials and built via microfabrication techniques. Reducing the inflammatory response by using a thin and soft scaffold will better preserve the neural interface, providing extended durability and better signal quality[182,186–189]. Moreover, whereas in the case of device failure it would not be easy to replace a metallic stent-electrode array, if not impossible at all, a transient device will leave the possibility for replacement, even if complications occur in the mid- or long-term period. Transient bioelectronics already introduced degradable materials in neurotechnology[190]. Unfortunately, these devices have a short durability, from days to a few weeks, due to the fast degradation rate of the dissolvable metals used for the conductive elements. This limited lifetime prevents their use for mid- and long-term applications[38,137]. Our strategy to overcome this problem is a fully polymeric neural interface, using a slowly biodegradable polymer as a scaffold and a conductive polymer as the active component.

In summary, in this work, we introduce a fully polymeric transient neurovascular interface combining the advantages of transient bioelectronics and stent technology in a single device.

3.2   Results and discussion

3.2.1   Manufacturing of the device

The transient neurovascular interface is a stent-inspired device, whose scaffold consists of poly-ε-caprolactone (PCL): a synthetic polyester approved by the US Food and Drug Administration for several medical applications, such as drug delivery systems, tissue engineering and medical devices[35]. PCL has a long degradation time, from several months to a few years, allowing it to be an insulating and stable scaffold for mid- and long-term applications[35]. Conductive elements are made out of poly(3,4-ethylenedioxythiophene):polystyrene sulfonate (PEDOT:PSS), a conductive biocompatible polymer commonly used in organic photovoltaic cells, and often used as a coating for metallic electrodes in neural interfaces[191–193]. A feature of this device is the absence of metals in electrodes and feedlines, making the device fully polymeric in all components. PEDOT:PSS is here doped with ethylene glycol (EG) for better conductivity, and (3-glycidyloxypropyl)trimethoxysilane (GOPS) for better endurance in aqueous environment[193,194].

Fabrication of the device using replica moulding proved to be facile. Two moulds have been manufactured in SU8 (35-μm thick): one with the engraved pattern of the feedlines (mould for encapsulation in **Figure 3.1**a) and the other with the protruding pattern of the electrodes, feedlines, and pads (mould for substrate in **Figure 3.1**a). After covering the two moulds with a PSS release layer (**Figure 3.1**a, step 1), the PCL solution has been spin-coated on both (**Figure 3.1**a, step 2). After releasing the substrate layer, the PEDOT:PSS-based solution has been dispensed along the engraved pattern for electrodes, feedlines, and pads (**Figure 3.1**a, step 3). For each electrode unit (electrode, feedline, and pad), ≈2 μL of solution would completely fill the pattern. This amount would correspond to a film thickness of ≈1–2 μm, decreasing from the channel wall to the centre (**Figure 3.1**b). After cross-linking of the conductive polymer, thin stainless-steel wires (114 μm diameter) have been attached to the pads using a conductive paste (**Figure 3.1**a, step 4). The openings for the electrodes have been laser cut in the encapsulation layer (**Figure 3.1**a, step 3) and the film has been released (**Figure 3.1**a, step 4). After alignment of the two layers (**Figure 3.1**a, step 5), heating at 60 °C allowed their quick fusion and fixed the wires contacts in between (**Figure 3.1**a, step 6). Finally, the device outline and its characteristic diamond-like holes have been laser cut to allow for easier bending, reduce the amount of material implanted and maintain open sites for molecules exchange from and to the blood flow.
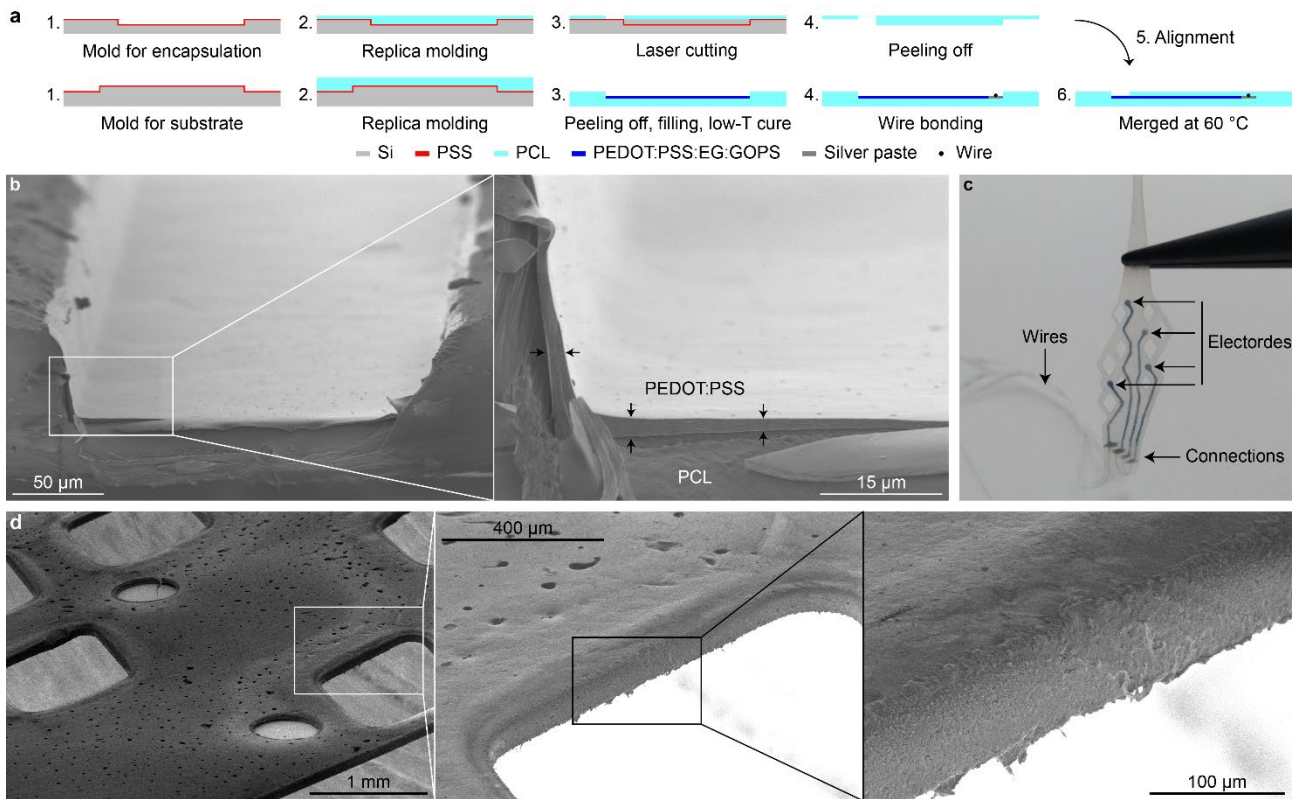
Figure 3.1 Fabrication of a transient endovascular neural interface. **a**) Sketch of the fabrication process. **b**) Scanning electron microscope image showing the cross-section of a feedline filled with the conductive polymer before encapsulation. The conductive polymer layer is indicated in the magnification by the black arrows. **c**) Picture of the transient neurovascular interface after fabrication. **d**) Scanning electron microscope images at different magnifications of the device side view after laser cut.

The device contains four electrodes, with a diameter of 600 μm and a geometrical surface area (GSA) of 0.0019 mm^2 (500 μm opening, not considering superficial roughness). Feedlines are 200 μm wide. The electrodes cover an area of ≈7.6 × 3.6 mm^2 (**Figure 3.1**c). The total length of the device is 44 mm, and its largest width is 7.6 mm. A V-shaped area at the tip is used to smoothen the insertion of the device into the catheter. The total thickness is ≈77 μm, limited by the high viscosity of the PCL-based solution and the depth of the engraved pattern necessary to deposit the PEDOT:PSS-based solution smoothly.

PCL has been recently considered in vascular applications, including grafts and stents. The former usually fabricated via electrospinning, and the latter by printing. Hemocompatibility is affected by the fabrication process since surface roughness strongly correlates to cell adhesion and platelet activation processes[195]. Smooth PCL, compared to electrospun mats, showed better interaction with blood[196]. Also, PCL-based stents fabricated via 3D printing demonstrated good hemocompatibility[197]. For this neurovascular interface, the fabrication via spin-coating resulted in a surface qualitatively similar to casted mats or 3D printed devices rather than electrospun mats (**Figure 3.1**d). However, laser cutting might introduce localized roughness at the edges. Hemocompatibility of polymeric stents made out by laser cutting have been already investigated, showing that, although activation of the coagulation cascade occurred, it was within a safe range of values[198]. Nevertheless, the hemocompatibility of this device remains to be evaluated in a future study.

3.2.2 Electrochemical characterization in static condition

Impedance spectroscopy (**Figure 3.2**a) performed in phosphate buffered solution (PBS) after fabrication revealed a predominantly resistive behaviour of the electrodes, given by the flatness of the magni-

tude plot (**Figure 3.2**a, black) and the phase angle approaching 0° (**Figure 3.2**a, blue) over a wide range of frequencies (10^1–10^5 Hz)[199]. The average (± s.d.) cut-off frequency, corresponding to a phase angle of -45°, was 2.22 ± 1.11 Hz (n = 20 electrodes from N = 5 devices; **Figure 3.2**b) and relevant frequencies in neural recording (1–300 Hz for local field potentials and 300–3000 Hz for extracellular spikes) are above it[200]. At the reference frequency for neural spikes recording (1 kHz), the average (±s.d.) impedance magnitude was 5.50 ± 3.00 kΩ, and the average (±s.d.) impedance phase angle was -0.84 ± 0.55° (n = 20 electrodes from N = 5 devices; **Figure 3.2**c,d). Cyclic voltammetry (**Figure 3.2**e), performed at a scan rate of 50 mV s^{-1} from -0.9 to 0.8 V, indicated a prevalent double-layer capacitance and its integral resulted in a mean total charge storage capacity (CSC) of 42.02 ± 26.89 mC cm^{-2} (n = 20 electrodes from N = 5 devices; **Figure 3.2**f).
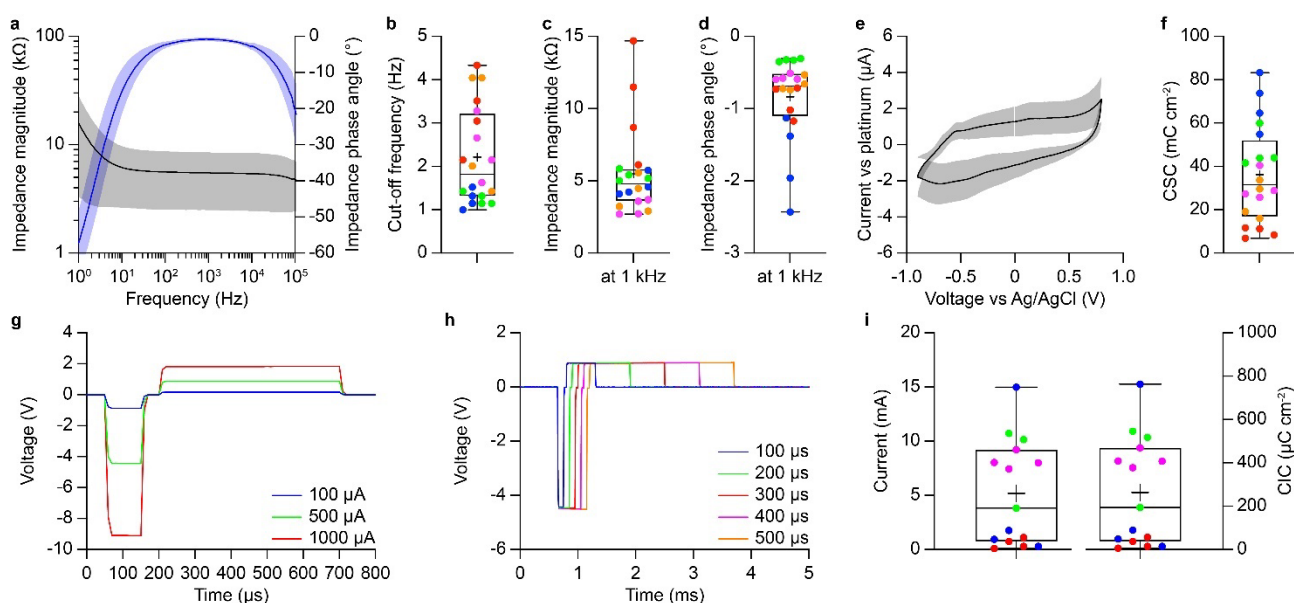
Figure 3.2 Electrochemical characterization. **a**) Average (±s.d.) impedance magnitude (black, left axis) and impedance phase angle (blue, right axis) plots. Solid lines are the averages (n = 20 electrodes from N = 5 devices) and shaded areas are the standard deviations. **b**) Quantification of the cut-off frequency, **c**) the impedance magnitude at 1 kHz and **d**) the impedance phase angle at 1 kHz. Different colours correspond to electrodes from different devices. **e**) Average (±s.d.) cyclic voltammetry plot. The solid line is the average (n = 20 electrodes from N = 5 devices) and the shaded area is the standard deviation. **f**) Quantification of the CSC. Different colours correspond to electrodes from different devices. **g,h**) Representative VTs at **g**) different current amplitudes and **h**) pulse widths. **i**) Box plots of the maximum injectable currents (left axis) and CIC (right axis). Different colours correspond to electrodes from different devices.

It is to be noted that PBS and blood have similar conductivity (respectively 1.6 and 0.7 S m^{-1}) and viscosity (respectively 1 and 4 cP)[123,201–204]. Nevertheless, impedance spectroscopy (**Figure 3.3**a) and cyclic voltammetry (**Figure 3.3**e) performed in PBS have been compared to measures performed in animal blood, to rule out any effect of the medium (n = 4 electrodes from N = 1 device). The cut-off frequency (p = 0. 0.125, Wilcoxon matched-pairs signed rank test; **Figure 3.3**b), the impedance magnitude at 1 kHz (p = 0.125, Wilcoxon matched-pairs signed rank test; **Figure 3.3**c), the impedance phase angle at 1 kHz (p = 0.125, Wilcoxon matched-pairs signed rank test; **Figure 3.3**d) and the CSC (p = 0. 0.125, Wilcoxon matched-pairs signed rank test; **Figure 3.3**f) were not statistically different. However, the cyclic voltammetry plot showed a high anodic peak above 0.5 V, which might be related to Fe^{2+} oxidation to Fe^{3+} or other interactions with biological molecules (i.e., ascorbic and uric acid, cysteine, or melatonin)[205,206].
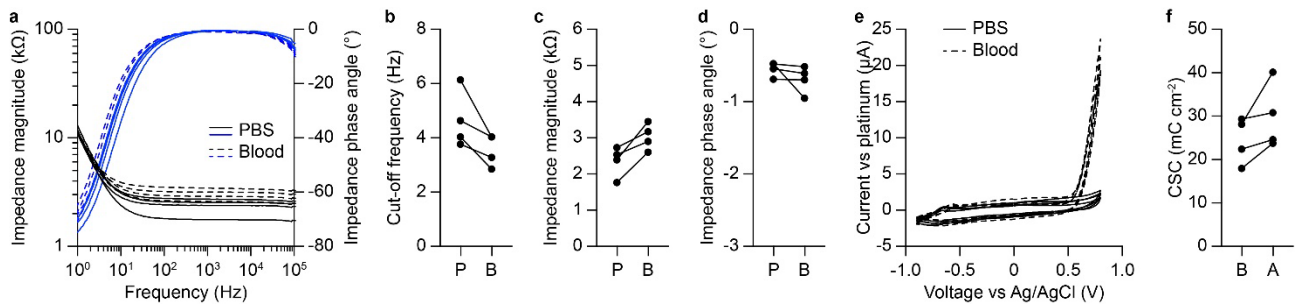
Figure 3.3 Comparison between EIS in PBS and in blood. (**a**) Impedance magnitude (black, left axis) and impedance phase angle (blue, right axis) plots in PBS (solid lines) and animal blood (dashed lines) (n = 4 electrodes from N = 1 device). (**b,c,d**) Quantification of the cut-off frequency (**b**), the impedance magnitude at 1 kHz (**c**) and the impedance phase angle at 1 kHz (**d**) in PBS (P) and animal blood (B). (**e**) Cyclic voltammetry plot in PBS (solid lines) and animal blood dashed lines) (n = 4 electrodes from N = 1 device). (**f**) Quantification of the CSC in PBS (P) and animal blood (B).

To further characterize the device for neural stimulation, voltage transients (VTs) have been investigated, and the charge injection capacity (CIC) has been computed. Each electrode of 4 devices has been stimulated with low-current pulses repeated at 150 Hz until stabilization of the interface polarization was reached. Afterward, the CIC was tested: the injected current has been increased until the most negative (E_{mc}) or the most positive (E_{ma}) maximum polarization exceeded the water window of oxidation and reduction potentials (-0.9 or 0.8 V). All pulses were cathodic first, asymmetric (1:5 cathodic to anodic ratio), charge-balanced with a 50 µs interphase period. VTs showed a rectangular shape with a significant ohmic drop related to the mostly resistive behaviour of the electrodes, visible as well from impedance spectroscopy. This VT waveform is maintained for different injected currents within the maximum limit (**Figure 3.2**g) and different pulse widths (**Figure 3.2**h). Also, the open circuit voltage of the electrode remained constant for stimulations with different pulse widths (from 100 to 500 µs, steps of 100 µs), suggesting no irreversibility in the charge injection[199]. The maximum injectable current has been tested with stimuli of 100 µs duration (cathodic phase). The average (± s.d.) maximum injectable current (always limited by the E_{mc}) was found to be 5.2 ± 4.8 mA (n = 15 electrodes from N = 4 devices) and the respective CIC was 263.6 ± 247.5 mC cm^{-2} (**Figure 3.2**i). Currents used in metallic stent-electrode arrays fall within the range sustainable by the polymeric electrode presented in this article[122].

The electrochemical characterization showed the potential of the transient neurovascular interface for neural recording and stimulation. The low impedance over a wide frequency range is promising for favourable signal-to-noise ratio in recordings[181]. The high CSC (an index of the electrode charge transfer capabilities)[207] and CIC are promising for neurostimulation. It must be noted though that the CSC is usually an overestimation of the charge transfer potential of the electrodes: in fact when stimulating in vivo, at high frequencies and short pulses, only the superficial layers of the bulk PEDOT:PSS film will be active[181].

Next, the device has been tested for prolonged charge injection by exposing the electrodes to 4 million pulses delivered at 200 Hz of repetition rate. The amplitude of the cathodic pulse was set to 500 µA and the duration to 100 µs (50 nC per phase). VTs have been measured at several timepoints during the stimulation protocol: at the start and after 50k, 100k, 200k, 500k, 750k, 1M, 2.5M, and 4M stimuli using the electrochemistry three-electrode setup (**Figure 3.4**a,b). The E_{mc} over pulses was quantified as a parameter for the electrode stability (**Figure 3.4**c). Out of the 12 electrodes tested from 3 devices, in 11 electrodes the E_{mc} remained within the water window limit (**Figure 3.4**c, dashed line), while 1

electrode exceeded this value after 100k pulses. For most electrodes (10 out of 12), the E_{mc} remained stable over the entire protocol of 4M pulses. Electrodes also showed no sign of damage after 4M pulses (**Figure 3.4**d).
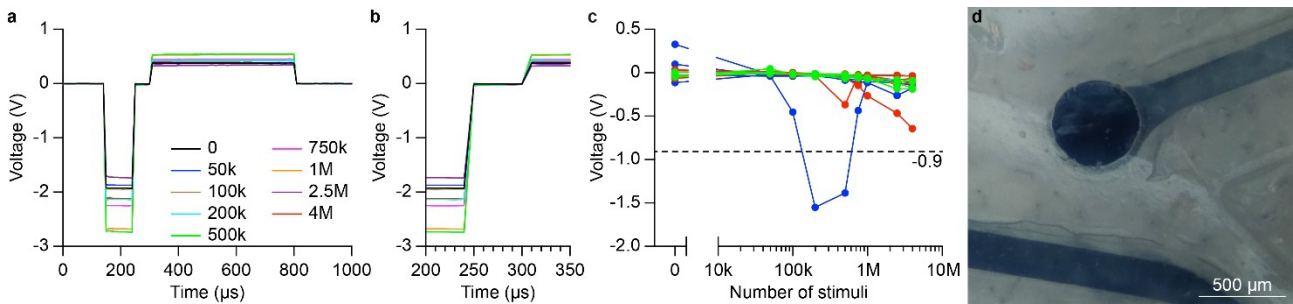
Figure 3.4 Endurance to prolonged stimulation. **a**) VTs during prolonged stimulation at several timepoints. Representative example from 1 electrode. **b**) Magnification of the VTs in (**a**) after the cathodic drop for the quantification of the E_{mc}. **c**) Quantification of the E_{mc} during prolonged stimulation (n = 12 electrodes from N = 3 devices). Each colour highlights electrodes from the same device. **d**) Microscope image of a representative electrode after being exposed to 4M pulses.

Last, we evaluated the insulation resistance in between feedlines to validate the absence of crosstalk between the electrodes. To unambiguously rule out electrode crosstalk, we fabricated fully encapsulated devices (i.e., without electrode openings)[208] and measured the resistance between 3 pairs of neighbouring electrodes, one pair of electrodes per device (**Figure 3.5**a). Resistance measure has been performed in dry condition (i.e., after fabrication) and while the device was immersed in saline solution (0.9% NaCl) at 37 °C for up to 18 days (**Figure 3.5**b). All the measures showed that the electrical resistance remained very high (>10 MΩ) despite immersion in saline solution, and comparable to the values measured in dry condition. PCL is a slow degrading polymer. Therefore, the electrical insulation of the feedlines is expected to last for several weeks.
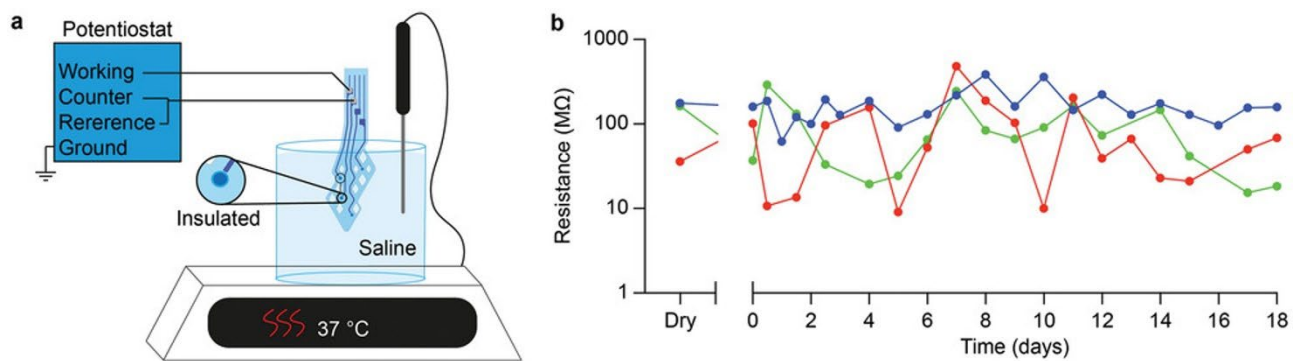
Figure 3.5 Crosstalk analysis. **a**) Sketch of the set-up for the measurement of the resistance between encapsulated electrodes. **b**) Quantification overtime of the resistance between pairs of electrodes (n = 3 pairs from N = 3 devices).

3.2.3 Delivery of the device

We investigated the device compatibility with a standard stent delivery approach (**Figure 3.6**a). The shape of the device has been optimized for a smooth insertion inside the delivery catheter thanks to the V-shaped tip allowing for a gradual bending and adaptation of the device to the cylindrical catheter. The device could be attached to a push wire (0.36-mm diameter) and navigated inside a 5-Fr catheter (1.67-mm outer diameter). During navigation inside the catheter, the device is constrained by the catheter. When deployed, it will tend to restore its original planar configuration with minimal deformation (**Figure 3.6**c). This expansion promises good adherence when deployed inside a blood vessel.

Also, the navigation inside the catheter and the deployment did not affect the mechanical integrity of the device (**Figure 3.6**b,c).
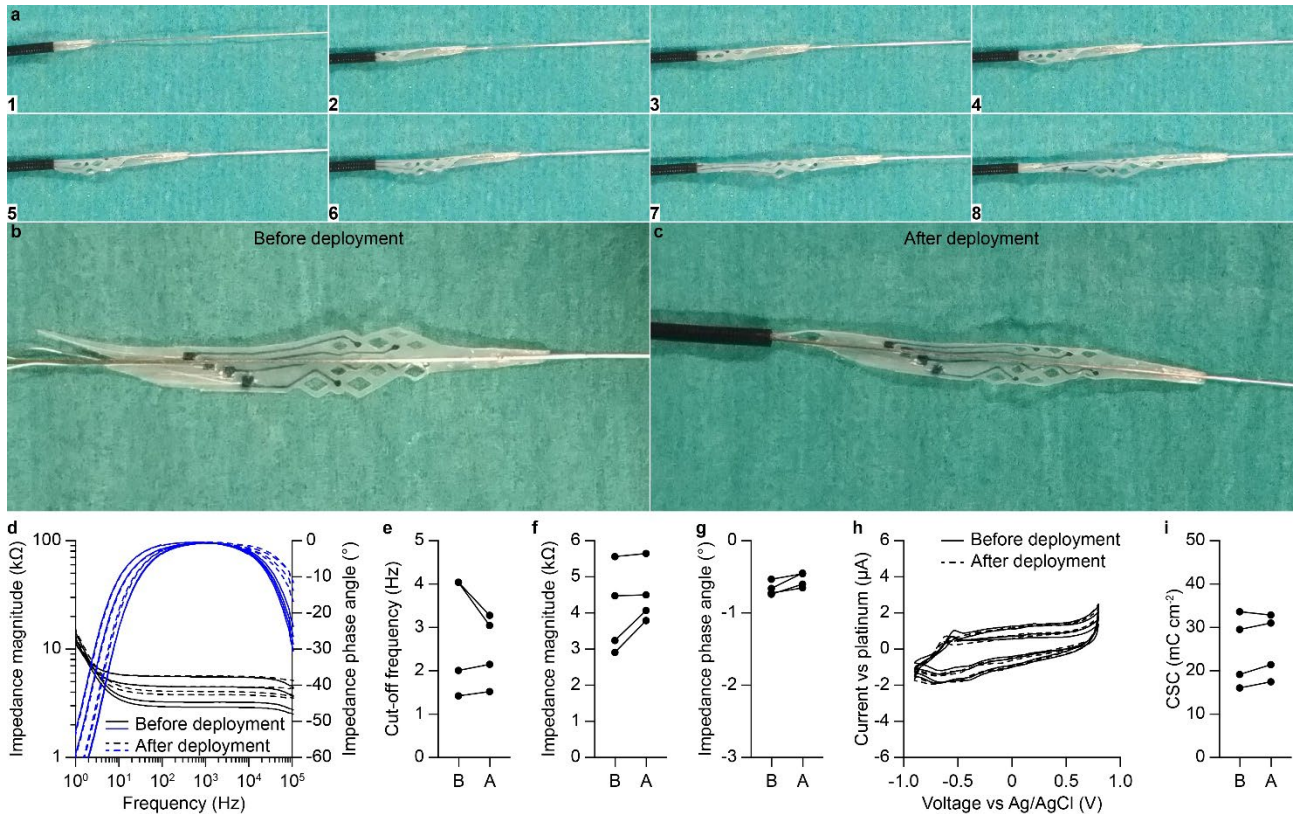
Figure 3.6 Delivery system. **a**) Image sequence of the deployment of the device using a 5-Fr catheter. **b,c**) Comparison of the device **b**) before and **c**) after navigation and deployment. **d**) Impedance magnitude (black, left axis) and impedance phase angle (blue, right axis) plots before (solid lines) and after (dashed lines) deployment of the device using a 5-Fr catheter (n = 4 electrodes from N = 1 device). **e**) Quantification of the cut-off frequency, **f**) the impedance magnitude at 1 kHz and **g**) the impedance phase angle at 1 kHz before (B) and after (A) deployment of the device using a 5-Fr catheter. **h**) Cyclic voltammetry plot before (solid lines) and after (dashed lines) deployment of the device using a 5-Fr catheter (n = 4 electrodes from N = 1 device). **i**) Quantification of the CSC before (B) and after (A) deployment of the device using a 5-Fr catheter.

Impedance spectroscopy (**Figure 3.6**d) and cyclic voltammetry (**Figure 3.6**h) have been performed before and after deployment of the device using a 5-Fr catheter (n = 4 electrodes from N = 1 device). The cut-off frequency (p = 0.625, Wilcoxon matched-pairs signed rank test; **Figure 3.6**e), the impedance magnitude at 1 kHz (p = 0.125, Wilcoxon matched-pairs signed rank test; **Figure 3.6**f), the impedance phase angle at 1 kHz (p = 0.125, Wilcoxon matched-pairs signed rank test; **Figure 3.6**g) and the CSC (p = 0.250, Wilcoxon matched-pairs signed rank test; **Figure 3.6**i) were not statistically different before and after deployment.

3.2.4   Endurance of the device in dynamic condition

Devices has been inserted in a 2-mm channel (made of polydimethylsiloxane) filled with PBS at 37 °C and connected to a peristaltic pump, generating a pulsatile flow inside the channel, to investigate the electrochemical behaviour over time in an environment modelling the vasculature (**Figure 3.7**a). The flow was set at ≈106 mL min^{-1} to simulate the cerebral venous flow of Yucatan pigs (108 mL min^{-1}), which is the envisioned animal model for further in vivo validation of the device[209]. Electrodes have been monitored for 30 days measuring impedance spectroscopy and cyclic voltammetry (n = 12 electrodes from N = 3 devices; respectively **Figure 3.7**b–d). The cut-off frequency could not be measured since the phase angle never reached -45° in the tested range of frequencies (**Figure 3.7**c). The change

in the profile of the phase angle, and the overall higher magnitude plot is not caused by the release of the device from the catheter, but it can be explained by the changes in the geometry of the electrolytic cell, owed to the interposition of the channel volume between the device and the reference and counter electrodes which are left in the bath. Instead of the cut-off frequency, the impedance magnitude at 10 Hz (**Figure 3.7**e) and 1 kHz (**Figure 3.7**f) and the CSC (**Figure 3.7**g) normalized to their respective initial values (day 0) have been used as parameters to assess the electrode endurance. Overall, 10 out of 12 electrodes remained functional for 30 days, while 2 electrodes from one probe stopped functioning: 1 after 21 days and 1 after 30 days (blue empty circles in **Figure 3.7**e–g indicated by E on the y axis).
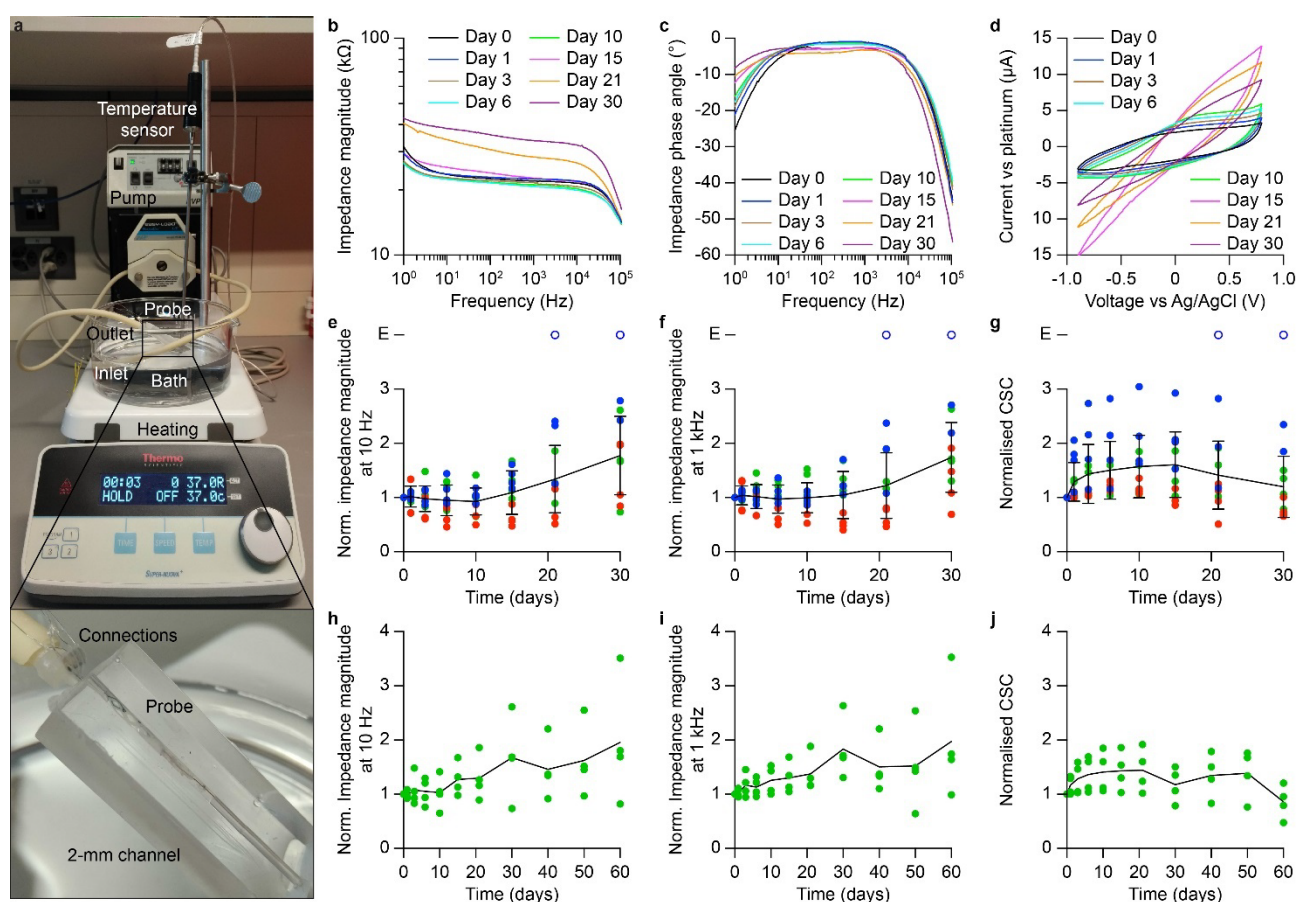
Figure 3.7 Endurance of electrodes to pulsatile flow. a) Picture of the experimental set-up showing: the hot-plate set at 37 °C, the temperature sensor, the beaker containing PBS and the tubes connected to the peristaltic pump and to the channel where the device is deployed. The magnification shows the device deployed in the 2-mm diameter channel. **b**) Average impedance magnitude, **c**) impedance phase angle, and **d**) cyclic voltammetry plots exposed for 30 days to pulsatile flow. **e**) Normalized impedance magnitude at 10 Hz, **f**) normalized impedance magnitude at 1 kHz and **g**) normalized CSC over 30 days. In each plot, different colours correspond to electrodes from different devices. The two empty circles show the two not functional electrodes. E means excluded. The solid line is the average with the standard deviation. **h**) Normalized impedance magnitude at 10 Hz, **i**) normalized impedance magnitude at 1 kHz, and **j**) normalized CSC over 60 days of one of the 3 devices (green). The solid line is the average.

The impedance magnitude plot remained stable for 10 days (**Figure 3.7**b), and it started increasing from day 15. After 30 days, the impedance magnitude increased by 1.78 times and 1.74 times of its original value, respectively, at 10 Hz (**Figure 3.7**e) and 1 kHz (**Figure 3.7**f). The total CSC increased to 1.20 times of its original value (**Figure 3.7**g). The reason why the impedance module increased, and, at the same time, the CSC increased as well is not yet clear. The increase in impedance over time might be attributed to two factors: a deterioration of the electrodes or a tightening of the device-wall interface.

On the other hand, the increase of the CSC might be explained by the swelling of PEDOT:PSS[210–212]. Furthermore, this swelling would cause diffusion of electrolyte within the PEDOT:PSS network and its penetration into those areas covered by the encapsulation layer, increasing the effective GSA of the electrode. The electrolyte leakage is detectable at slow scanning rates (50 mV s^{-1}) but not at high scanning rates since the pore resistance represents an obstacle limiting the access to the area under the encapsulation[199]. Therefore, cyclic voltammetry would be affected by this phenomenon, while impedance measurements at 1 kHz and 10 Hz would not.

For a prolonged investigation, one device has been left inside the pulsatile system for additional 30 days: the impedance module at 10 Hz reached 1.96 times its original value (n = 4, **Figure 3.7**h), the impedance module at 1 kHz reached 1.98 times its original value (n = 4, **Figure 3.7**i) and the CSC decreased to 0.86 times its original value (n = 4, **Figure 3.7**j) at day 60.

These results suggest that the device is still functional after two months, even if signs of electrodes damage appeared in some electrodes after two weeks.

3.2.5 Device apposition to a cylindrical structure

The transient neurovascular interface is designed to expose polymeric electrodes around a cylindrical surface (e.g., facing a vessel wall). Therefore, we deployed the device inside a 2-mm diameter channel built in rigid poly (methyl methacrylate) (PMMA) to evaluate the device apposition once released (**Figure 3.8**a). Apposition has been measured using micro-computed tomography (micro-CT) scans. Once deployed in the channel, the device will naturally try to restore its original planar shape, thus adhering to the wall and remaining constrained in place. The micro-CT scan has been carried out at 10-μm resolution, and both the longitudinal (**Figure 3.8**b) and transversal (**Figure 3.8**c–e) cross-sections of the channel have been analysed. The cross-sections showed a good device apposition against the channel with the lumen almost entirely maintained. Nevertheless, a few gaps between the device and the channel have been observed. On average (±s.d.), gaps were 98.1-μm long (± 42.4 μm, n = 9 for N = 3 cross-sections), sufficiently far from moderate gap values (180 μm) reported in the literature that could potentially affect the hemodynamics within the vessel[213]. The available lumen delimited by the device was on average (± s.d.) 2.57 mm^2 (±0.18 mm^2, n = 9 for N = 3 cross-sections). Compared to the original lumen of 3.14 mm^2, the deployment of the device caused a lumen reduction of 18%. In an ideal scenario of perfect apposition, the lumen reduction would be 15% (device thickness = 77 μm). Both values (18% and 15%) fall far from hemodynamically significant stenosis situations occurring at 50% lumen reduction[214]. It must also be noted that the release in a rigid PMMA block is a worst-case scenario. A more plausible behaviour of the device in situ would be investigated using mock vessels, with mechanical properties closer to the vasculature that would favour a better apposition. Also, even though the device structure is stent inspired, its primary function is not the one of stents (opening a clogged vessel). Therefore, the expansion at the deployment must be sufficient to put the electrodes in contact with the vessel walls, but it will not expand the vessel structure as a stent would do.
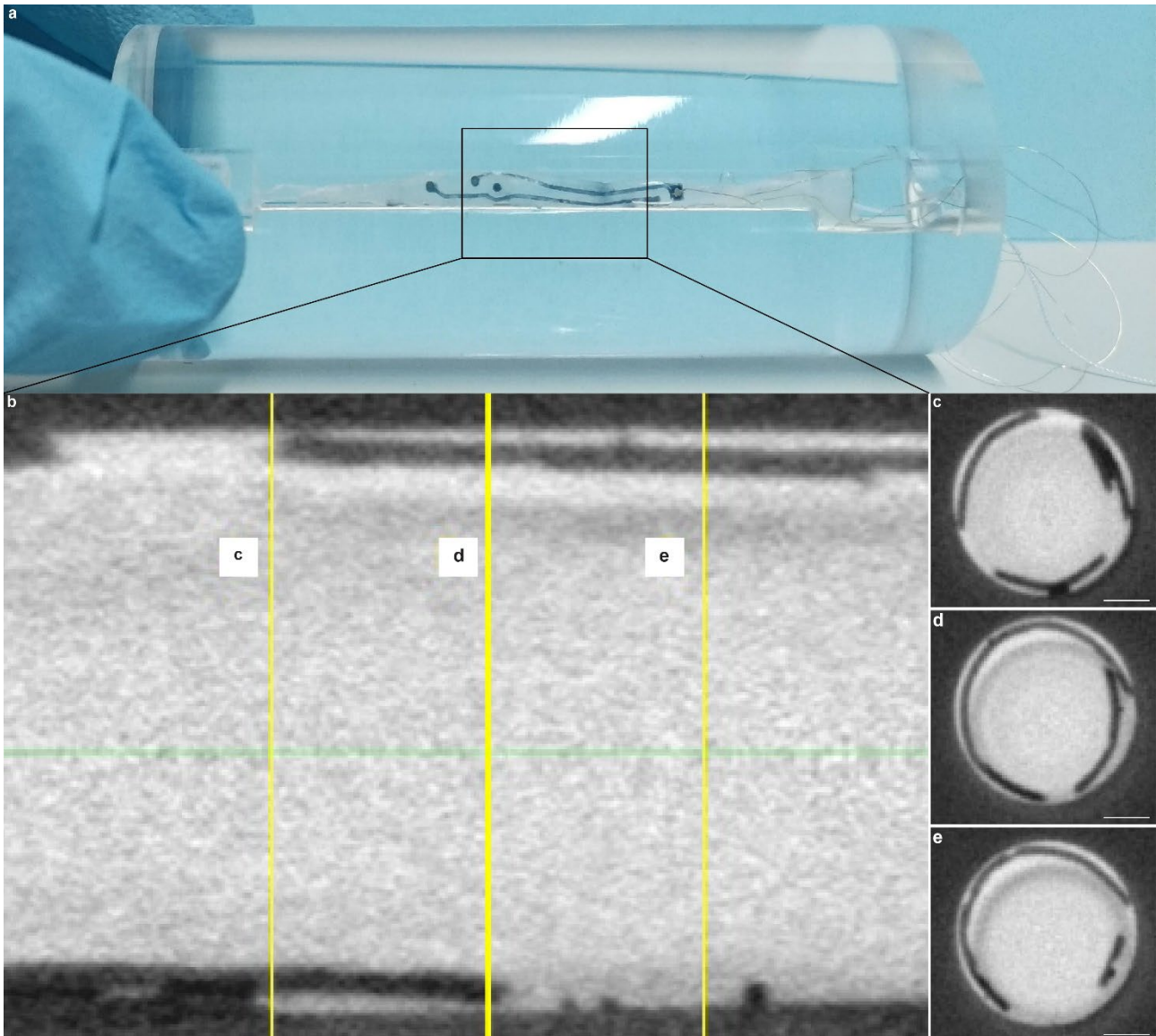
Figure 3.8 Microcomputed tomography of the delivered device. **a**) Picture of the transient neurovascular interface deployed inside a 2-mm sized channel made of PMMA. **b**) Micro-CT image showing the longitudinal cross-section of the device deployed inside the channel. In bright is the contrast agent injected inside the channel. **c–e**) Transversal cross-sections corresponding to the yellow c, d, e, positions in (**b**). The scale bars in panels (**c–e**) are 500 μm.

3.2.6   Degradation study

Last, we tested the degradation profile of the device. An advantage of synthetic degradable polymers is the possibility to tailor their degradation rate. When targeting the vasculature, it is crucial to match the degradation rate to the endothelialisation and remodelling of the blood vessel and avoid chronic recoil and restenosis[30]. A slow degradation is an appealing feature for transient devices since it might allow for better tissue remodelling and reduced chronic trauma at the implantation site[30,39,40,141]. On the other hand, the PCL structure will likely last for several years before full degradation: a time that might largely exceeds the functionality of the PEDOT:PSS electrodes and what is needed to allow endothelialisation and tissue remodelling. Therefore, we considered various blends of PCL and poly (D,L-lactic-co-glycolic acid) (PLGA) by mixing 85:15 PLGA (lactic acid: glycolic acid) with the PCL solution. Mixtures with different ratios of the two compounds have been prepared (80:20 and 70:30 PCL:PLGA) and devices have been fabricated and tested for accelerated in vitro degradation in PBS at 37 °C and pH 12 (**Figure 3.9**a,b). A fast degradation occurred for samples 80:20 and 70:30 since the beginning, while

the pristine PCL started degrading around day 150. The composition 70:30 degraded to half its initial weight around the day 120. As expected, the degradation of the other mixtures is slower: the 80:20 composition degraded to half its initial weight around day 170 and pure PCL around day 260. The acceleration factor at pH 12 is estimated to be 2.5 for PCL (compared to degradation profiles at pH 7), therefore the composition 70:30 is expected to lose half its initial weight after ≈10 months[141]. It must be noted that accelerated ageing only evaluated the PCL degradation by hydrolysis, but PCL is also subjected to enzymatic degradation. Specifically, it has been reported that in vivo PCL undergoes a first degradation by hydrolysis lasting ≈12 months. Then, after its molecular weight is reduced to ≈3000, it is internalized by cells (macrophages, giant cells, and fibroblasts) and degraded by them[35]. Therefore, with accelerated tests, the degradation time might be overestimated.
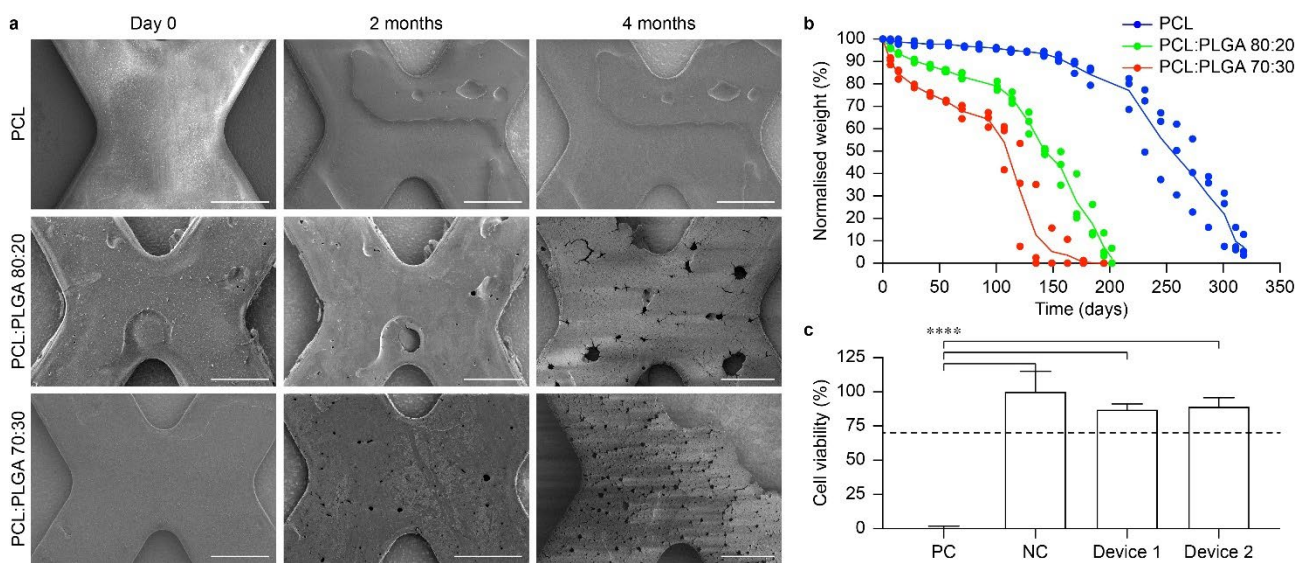
Figure 3.9 Degradation study in PBS at 37°C. a) Scanning electron microscopy images of PCL, PCL:PLGA 80:20, and PCL:PLGA 70:30 samples during degradation. **b**) Normalized weight of PCL (blue), PCL:PLGA 80:20 (green) and PCL:PLGA 70:30 (red) samples during degradation. Solid lines are the averages. **c**) Quantification of in vitro cytotoxicity (mean ± s.d.) for each condition tested: positive control, 0 ± 1.81% (2 samples, 3 replicas per sample); negative control, 100 ± 15% (2 samples, 3 replicas per sample); transient neurovascular interface, 87 ± 4.14% and 89 ± 6.74% (2 devices, 3 replicas per device). One-way ANOVA: F = 108.5 and p < 0.0001. Tukey's multiple comparisons test: positive control versus negative control, p < 0.0001; positive control versus device 1, p < 0.0001; positive control versus device 2, p < 0.0001; negative control versus device 1, p = 0.2891; negative control versus device 2, p = 0.4234; device 1 versus device 2, p = 0.9943.

According to ISO 10993–5: Biological Evaluation of Medical Devices, in vitro cytotoxicity has been evaluated via an extraction test on the murine fibroblastic L929 cells. Notably, in our test, the device did not show any sign of cytotoxicity (**Figure 3.9**c).

3.3   Conclusion

This work aimed at developing a minimally invasive transient neural interface to target the neural tissue from within a blood vessel.

The device has been successfully fabricated with a simple process employing standard cleanroom techniques, which allows for better encapsulation and reproducibility compared to handmade fabrication of metallic stents. Nonetheless, it must be noted that it involved a manual step for the deposition of the PEDOT:PSS-based conductive solution, which could affect the device reproducibility. The advantage of the current PEDOT:PSS deposition system inside grooves is the low amount of conductive polymer needed to fill one electrode unit (≈2 μL). This solution limits substantial waste of material, for

example, such as during spin-coating[215]. Patterning PEDOT:PSS using lithography techniques either by lift-off or using a protective layer would be challenging since the compatibility of these processes with synthetic biodegradable polymers such as PCL is limited by its poor resistance to solvents or temperatures higher than 50 °C[216]. An exciting solution could be using a printing system to automatically move a microinjector along the pattern to deposit the conductive polymer homogeneously. Printing of PEDOT:PSS-based solutions is an open research topic, and a standard protocol is not yet defined. So far, mostly ink-jet printing has been used for patterning PEDOT:PSS on solar cells, low-cost in vitro electrophysiology systems and circuitry design on textiles[151,215–218].

While PCL undergoes slow bulk degradation by hydrolysis and enzymatic reactions, the stability or degradability of pure PEDOT:PSS electrodes in the body is still elusive, regardless of its extensive usage as a coating of metal electrodes in neuroprosthetics[191–193,219,220]. Only a few studies have reported so far chronic performances of PEDOT:PSS in vivo.[156–158,192] Results showed performance drop after a few months of implantation. Given the high complexity of the biological environment, many different factors could contribute to the deterioration and degradation of PEDOT:PSS in vivo. A commonly reported failure mechanism is related to the adhesion of PEDOT:PSS to the substrate, such as metal electrodes[221]. Although bond strength and substrate adhesion can be enhanced using GOPS,[194] in the transient neurovascular interface, the weak adhesion between PEDOT:PSS and polyesters[161] is crucial since PEDOT:PSS might be subjected to water-induced swelling and delamination during the degradation of the PCL scaffold[30]. Moreover, PEDOT has been reported to be susceptible to hydrolysis when exposed to salt aqueous solutions[162] and it can be degraded by high concentration of hydrogen peroxide, which is a physiological oxidant[163,164]. Another study reported that macrophages cultured with PEDOT:PSS generated a significant amount of hydrogen peroxide, that plays a critical role in the regulation of initiation and outcome of cellular phagocytosis[165]. Given the physiological presence of activated macrophages and hydrogen peroxide during inflammation and remodelling processes following device implantation, PEDOT:PSS could possibly be degraded by the combination of hydrolysis, hydrogen peroxide and macrophage uptake. In-depth studies about the fate of PEDOT-based polymers in vivo are required.

The device has been successfully navigated into a standard 5-Fr catheter and deployed inside a 2-mm diameter channel built in a rigid PMMA block. After deployment, the device induced a lumen reduction of only 18%, largely below the threshold to observe hemodynamically significant stenosis (50%). However, the validated delivery system uses a guidewire as a support for the device. The two are attached with glue to ensure effective navigation. Once the device is deployed, it would be ideal to detach the two elements. Possible strategies could involve using temporary glue that would dissolve after deployment or using coil embolization wires. The latter is a guidewire with a detachable coil at the end. The detachment is carried out by applying a current to the guidewire, leading to the rupture of the attachment point. Nevertheless, the Stentrode, built over a stent-retriever consisting of a nitinol stent attached to a metallic shaft, is currently being validated in a clinical trial with its shaft used as support for the wires and, thus, chronically implanted in the superior sagittal sinus through the transverse sinus without adverse effects so far[93,121]. Therefore, unless detachable solutions are found, in vivo validation of the device with the current delivery system could still be considered. Similarly, conductive wires are attached to the device. For the attachment we have used a general-purpose silver paste. However, electrically conductive epoxy pastes are undergoing ISO 10 993 validation with already good preliminary results.

Overall, these results set a good starting point for acute experimentation in vivo. Future work will also focus on the hemocompatibility of the device.

3.4 Materials and methods

3.4.1 Fabrication

Devices were fabricated using a moulding technique. Two master moulds were fabricated: one with protruding pattern of pads, feedlines, and electrodes (substrate mould) and the other one with engraved parts in correspondence of the feedlines (encapsulation mould). The moulds were fabricated by SU8 GM1070 coating (1500 rpm, 35 μm) and patterning on 4-inch Si wafers, using standard photolithography (MLA150, Heidelberg Instruments). After hard baking of the moulds, a release layer (PSS 18 wt% in H2O; 561 223, Sigma Aldrich) was spin coated on both of them and baked at 145 °C for 10 min. Then, PCL (MW 50 000; 25 090, Polyscience, Inc.) was dissolved in chloroform (C2432, Sigma Aldrich) at 30% w/v and spin coated at 800 rpm on both moulds. A soft bake for 30 min at 75 °C removed residual stresses caused by the spin-coating of the viscous solution. Solvent evaporation followed, leaving the wafers under a chemical hood at room temperature for 1 h. Electrode openings were laser cut (Optec MM200-USP) from the encapsulation layer and then both substrate and encapsulation layers were released by immersion in deionized water. The parameters of the laser cutter for the electrode openings were set as follow: speed 200 mm s^{-1}, jump speed 300 mm s^{-1}, laser firing rate 100 kHz/Hz, power 45%, laser ON-delay 85 μs, laser OFF-delay 135 μs, repetitions 40 and mode Galvo. The patterns on the substrate layer were filled with a solution of PEDOT:PSS (M122 PH1000, Ossila) mixed with 20 wt% EG (324 558, Sigma Aldrich) and 1 wt% GOPS (440 167, Sigma Aldrich), before curing overnight in an oven at 37 °C. After washing in deionized water to remove uncross-linked PEDOT:PSS monomers, Teflon coated stainless steel wires (114-μm diameter; Z-790500, Science Products GmbH) were connected to the pads using silver paste (G3692 Acheson Silver DAG 1415, PLANO GmbH). The encapsulation layer was then aligned to the substrate and attached to it by quickly melting the two layers at 60 °C. The outline of the complete device was then laser cut. The parameters of the laser cutter for the outline were set as follow: speed 300 mm s^{-1}, jump speed 300 mm s^{-1}, laser firing rate 100 kHz/Hz, power 35%, laser on delay 85 μs, laser off delay 135 μs, repetitions 30 and mode IFOV.

3.4.2 Electrochemistry

Electrochemical characterization was performed in a three-electrode configuration with a large area platinum counter electrode and a non-current carrying reference electrode (Ag/AgCl; BASMF2056, Sigma). The electrolytic cell was connected to a potentiostat (Compact Stat, Ivium) and electrochemical measurements were taken at room temperature with each device immersed in PBS at pH 7.2. Impedance spectroscopy was carried out between 1 and 10^5 Hz using a 50 mV AC voltage. Cyclic voltammetry curves were obtained by sweeping a cyclic potential at 50 mV s^{-1} scan rate between -0.9 and 0.8 V. For each electrode, the average response over 5 cycles was calculated and the total CSC was computed as the area within the curves. For tests performed in animal blood, blood samples were collected from euthanized C567BL6 mice using a 2-mL syringe and a 23-gauge needle, both pre-coated with Ethylenediaminetetraacetic acid 0.5 m at pH 8 (EDTA; E9884, Sigma). Samples were then transferred into a 2-mL Eppendorf tube containing 9 mg of EDTA per mL of blood. Blood was kept on a shaker at room temperature until use. The experiment was approved by the Département de l'emploi, des affaires sociales et de la santé, Direction générale de la santé of the Republique et Canton de Geneve in Switzerland (authorization GE/70/20).

3.4.3 Electrochemistry under pulsatile flow

A 2-mm diameter channel was fabricated with polydimethylsiloxane (Sylgard 184, Dow Corning) by moulding. The device was inserted in the channel and connected to the tube (Nr.16 MasterFlex L/S PharMed) encased in the rotatory head (7518-10, Masterflex L/S Easy-Load) of a peristaltic pump (Ismatec). The tube and the channel were immersed in PBS (pH 7.2) inside a wide glass beaker placed onto a hotplate (Super-Nuova+, Thermo Scientific) whose temperature probe inside the PBS was set to 37 °C. The pump was set at 500 rpm. Electrochemical measurements of impedance spectroscopy and cyclic voltammetry were performed over time with the device inside the channel, using the beaker as electrolytic cell with a large area platinum counter electrode and a non-current carrying reference electrode (Ag/AgCl; BASMF2056, Sigma) immersed during measurements.

3.4.4 Voltage transients

VTs were performed in the same three-electrode configuration used for electrochemistry, at room temperature with each device immersed in PBS at pH 7.2. The current pulses were asymmetric (1:5 cathodic to anodic ratio), charge-balanced, cathodic first with a 500-µs interphase period. First, electrodes were stabilized with low current pulses (100 or 10 µA, depending on the electrode capacity) at 150 Hz. Stabilization occurred within 6000 pulses and was followed by stimulations at increasing current amplitudes until the E_{mc} or the E_{ma} of the electrode exceeded the water window (–0.9–0.8 V). The E_{mc} and E_{ma} were defined as the voltage value measured after 10 µs from the end of the cathodic or anodic pulse to avoid the ohmic drop. 10 pulses were delivered for each current amplitude and the E_{mc} and E_{ma} values were the average of the repetitions. The maximum injectable current was defined as the maximum current with which the electrodes could be stimulated without their response exceeding the water window limit. The CIC was calculated by multiplying the maximum injectable current by the pulse width (cathodic phase) and dividing the obtained charge by the electrode GSA.

3.4.5 Resistance measures

To measure the resistance, devices were immersed in saline solution (0.9% NaCl) at 37 °C and pH 7.2, and electrode pairs were connected to the potentiostat (Compact Stat, Ivium) and a voltage of 0.5 V was applied to measure the current generated. Resistance values were obtained by dividing the applied voltage by the measured current.

3.4.6 Long-term stimulation

Devices were immersed in saline solution (0.9% NaCl) at room temperature and pH 7.2. Up to 4 M current pulses were delivered using an isolated stimulus generator (STG4002, Multi-Channel Systems) at 200 Hz of repetition rate. During stimulation, and a platinum wire was immersed in the bath as ground electrode. Current pulses were asymmetric (1:5 cathodic to anodic ratio), charge-balanced, cathodic first with a cathodic amplitude of 500 µA, a duration of 100 µs and a 60-µs interphase period. At several timepoints, a measure of VT was performed as described above using the potentiostat (Compact Stat, Ivium) in a three-electrode configuration and applying the same current pulse. The E_{mc} was defined as the voltage value measured after 30 µs from the end of the cathodic pulse to avoid the ohmic drop. For each timepoint, 8 current pulses were delivered and the final E_{mc} value was the average of the repetitions.

3.4.7 Degradation

PCL and PLGA (Resomer RG 858 S; 739979-5G, Sigma) were mixed at various ratios: 100:0, 80:20, and 70:30. The powder mix was dissolved in chloroform (C2432, Sigma-Aldrich) at 45°C and with magnetic stirring at 200 rpm for 2 h. For each composition, 3 samples were prepared. The weight of the samples was recorded after fabrication and kept as a reference. Samples were immersed in 10-mL PBS at pH 12 at 37 °C. At each time point samples were taken out of the solution and dried at room temperature under vacuum for 4 h. Once dry, samples were weighted and, depending on the time point, scanning electron microscopy images were taken.

3.4.8 Delivery system

The top extremity of device was attached to the end of a push wire (STABILIZER 527-300E, 0.36 mm diameter, Cordis) using super glue (Supergel, UHU). The push wire with the device attached was then immersed in deionized water, and the target catheter (5Fr, Navien™ A+ 058, Intracranial Support Catheter, OD 1.7 mm) was filled with deionized water. This wetting is used to improve insertion and navigation of the device inside the catheter. The device attached to the push wire was then pushed inside the catheter and navigated until exiting after ≈1m of navigation.

3.4.9 Microtomography imaging

A channel was created in PMMA with a 2-mm diameter. The device was deployed inside the channel. To avoid metallic artifacts generated by the push wire, the attachment site was cut after deployment. To improve the device visibility within the channel, the channel was filled with a contrast agent (Iopamiro 300 mg mL^{-1}, Bracco) mixed with NaCl solution at 30% v/v. Imaging was performed at 10-µm resolution with a 5-mm field of view (Qunatum CT Lab GX, Rigaku microCT Technology and Perkin Elmer software).

3.4.10 Scanning electron microscopy

Images were taken with a Schottky field emission scanning electron microscope (SU5000, Hitachi) at 1 kV access voltage and 10% of maximum spot intensity.

3.4.11 Cytotoxicity test

A test on extract was performed with devices sterilized by UV exposure, with a ratio of the product to extraction vehicle of 3 cm^2 mL^{-1}. The extraction vehicle was Eagle's minimum essential medium (11 090 081, Thermo Fisher Scientific) supplemented with 10% fetal bovine serum (10 270 106, Thermo Fisher Scientific), 1% penicillin-streptomycin (15 070 063, Thermo Fisher Scientific), 2 mm L-Glutamine (25 030 081, Thermo Fisher Scientific), and 2.50 µg mL^{-1} Amphotericin B (15 290 026, Gibco-Thermo Fisher Scientific). The extraction was performed for 24 h at 37 °C and 5% CO2. L929 cells (88 102 702, Sigma) were plated in a 96 well plate at a sub-confluent density of 7000 cells per well in 100 µL of the same medium. L929 cells were incubated for 24 h at 37 °C and 5% CO2. After incubation, the medium was removed from the cells and replaced with the extract (100 µL per well). After another incubation of 24 h, 50 µL per well of XTT reagent (Cell proliferation kit 11 465 015 001, Sigma) were added and incubated for 4 h at 37 °C and 5% CO2. An aliquot of 100 µL was then transferred from each well into the corresponding wells of a new plate, and the optical density was measured at 450 nm by using a plate reader (FlexStation3, MolecularDevices). Clean medium alone was used as a negative control, whereas medium supplemented with 15% of dimethyl sulfoxide (D2650-5×5ML, Sigma) was used as a positive control. Each condition was tested in triplicates.

3.4.12 Statistical analysis and graphical representation

Statistical analysis and graphical representation were performed with Prism (Graph Pad). Normality test was performed in each dataset to justify the use of a parametric or non-parametric test. The box plots always extend from the 25th to 75th percentiles. The line in the middle of the box is plotted at the median. The + is the mean. The whiskers go down to the smallest value and up to the largest. In each figure p-values were represented as: * $p < 0.05$, ** $p < 0.01$, *** $p < 0.001$, and **** $p < 0.0001$.

3.5   Acknowledgements

Chapter 4 Flow driven robotic navigation of microengineered endovascular probes

The goal addressed in this chapter is the investigation of a new navigation method for endovascular probes and catheters, to reduce risks related to techniques currently used and to widen the number of vascular targets that can be reached (e.g., microvasculature).

4.1   Introduction

The cardiovascular system oxygenates the entire body through an exquisitely interconnected fluid network, potentially providing physicians and scientists minimally invasive access to any target tissue. Taking advantage of this opportunity, the diagnosis and treatment of prominent abnormalities and diseases in the brain such as tumours, aneurysms, stroke, and arteriovenous malformations have been routinely accomplished using catheterization techniques[222–226]. Recent work has also demonstrated long-term recording and stimulation of brain dynamics using endovascular stent electrode arrays[93,122]. However, the majority of the brain is still inaccessible because the existing tools are bulky and navigating through the minuscule and tortuous cerebral vasculature without causing tissue damage is extremely challenging. While technological progress in microengineering has introduced a variety of microdevices that can perform optical, thermal, electrical and chemical interrogation and modulation of the nervous system[84,227–233], conventional navigation techniques are incapable of transporting miniaturized tethered devices deep into the microvasculature primarily due to mechanical limitations. The invention of a methodology that provides rapid and safe passage for microdevices regardless of the complexity of the trajectory may become instrumental for translational medicine and neuroscience research.

Advancement of conventional catheters relies on manual adjustment of the curvature of their distal tip. To automate the navigation process, robotics research has introduced continuum devices with active control over body deformation through cable-driven mechanisms, concentric tube systems or devices that possess tuneable mechanical properties such as shape-memory and variable stiffness[234–240]. Seminal work has demonstrated the feasibility of using external magnetic fields to remotely control the pose of elastic magnetic rods[126,241–250]. However, navigating gently through increasingly intricate vascular networks, while avoiding lesions, requires the development of microscopic probes (μ-probes) as small as blood cells with extraordinary flexibility. This is particularly important for neurological interventions in which accessing distal and tortuous vessels prohibitively increases the operation time and risk of intraoperative tissue damage. The bending stiffness of a rectangular beam scales cubically with the thickness of the material and, thus, reducing the dimensions of even high-modulus slender structures dramatically increases their flexibility. Furthermore, friction forces progressively increase with the distance, making it harder to push structures forward inside small vessels. As a result, state-of-the-art navigation techniques are not suitable for the advancement and steering of miniaturized endovascular devices.

Here, we introduce a robotic navigation strategy that relies solely on the ability of the blood flow to transport devices in vessels with arbitrary tortuosity. The method is based on the exploitation of elastohydrodynamic coupling between flexible structures and the surrounding fluid. Harnessing viscous stresses and pressure for propulsion while controlling the heading with spatially homogenous magnetic fields nullifies the need for proximal pushing. This strategy allows autonomous flow-driven transportation of μ-probes along three-dimensional (3D) trajectories close to the speed of flow (**Figure 4.1**a). The torque exerted on the magnetic head bends the distal end of the device, which in turn interacts with the flow in such a way that the structure is conveyed to the chosen trajectory. The torque required to effectively steer the μ-probe scales favourable with vessel size and can be provided by a magnetic head as small as 40 μm under magnetic field strength, **B**, as low as 5 mT. The persistent presence of flow ensures safe advancement of the μ-probe until the next bifurcation without external intervention and with minimal contact with the walls, promoting autonomous passage through unknown or highly structured channels. In addition, in order to significantly reduce the size of the elec-

tromechanical µ-probes, we abandoned the conventional two-step navigation paradigm that is based on the use of a flexible guidewire for the advancement of the functional catheter. Instead, we designed and engineered endovascular microrobotic devices with cross-sectional area as small as $25 \times 4 \, \mu m^2$ that travel effortlessly in the vessels as if they were untethered while taking full advantage of the electrical and fluidic tethers. The physical principles of the navigation strategy have been systematically explored inside microfluidic devices with relevance to clinical challenges and using an experimentally validated computational model, which together led to the development of a repertoire of design and wireless control strategies. Finally, we demonstrate the feasibility of operating (multiple) microengineered µ-probes at the target locations for making physical measurements in custom-made biomimetic phantoms and ex vivo local injection of chemicals inside the vasculature of a rabbit ear.
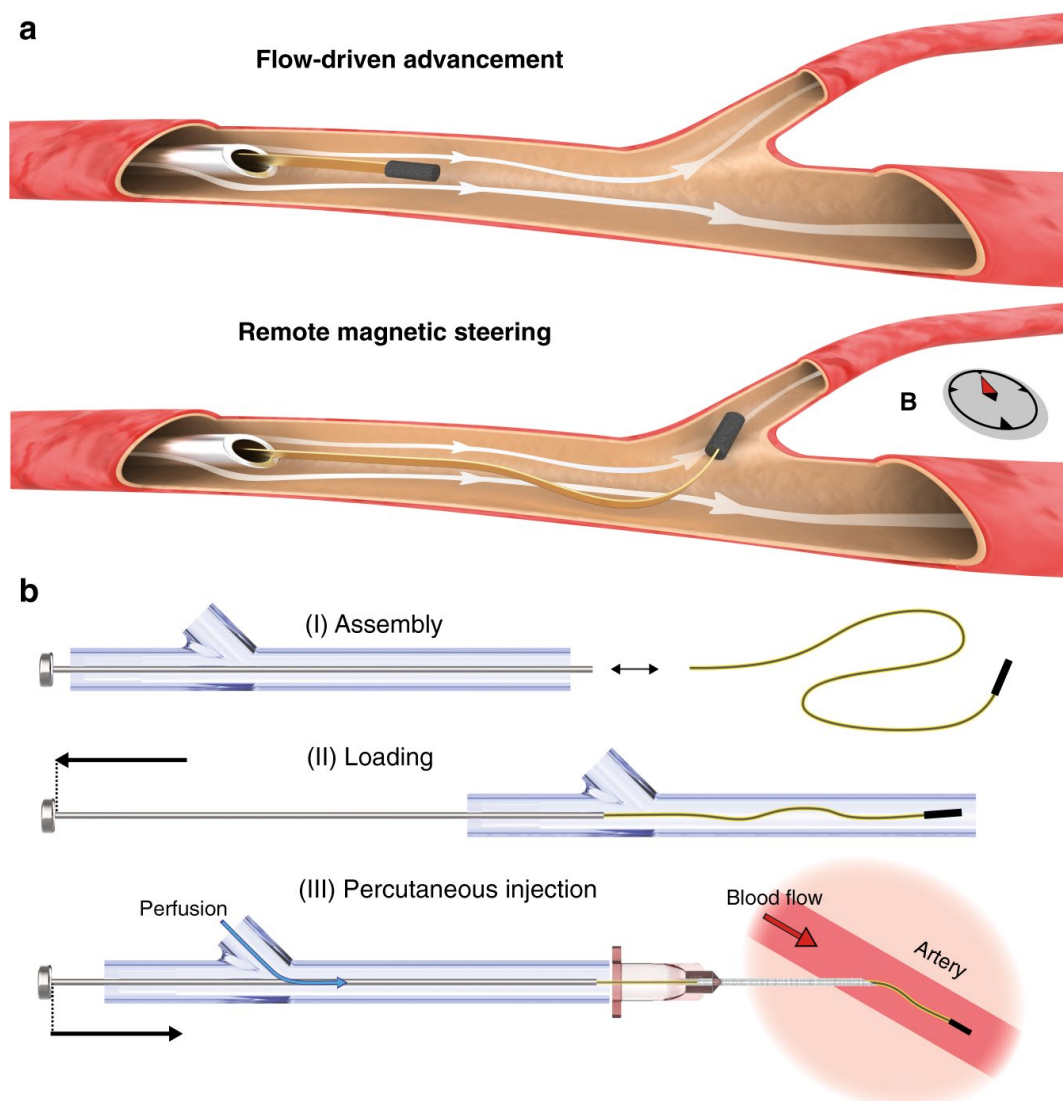
Figure 4.1 Flow-driven deployment and advancement of endovascular µ-probes. (**a**) Ultra-flexible µ-probes are transported inside vessels by the hydrodynamic forces (top). Controlled rotation of the magnetic head using external magnetic fields steers the device into the target vessel (bottom). The small size of the µ-probe allows direct release into the vessels with standard hypodermic needles. (**b**) Effective deployment of the µ-probes using a proper cannulation system that overcomes mechanical instabilities. Perfusion with a physiological solution during delivery keeps the structure under tension until the flow in the artery takes over. Drawings are not to scale.

4.2   Results

4.2.1   Microfabrication of the μ-probes

To ensure effortlessly navigation driven only by the flow and directed by small amplitude magnetic fields, polyimide (PI) was chosen as flexible and biocompatible material to build the device. Through spin coating technique it is possible to reach the small thickness required, such as 4 μm. The width of the stripes was laser cut to reach values in the range of 25-300 μm depending on the target vessel size. The length of the probes varied around 7 cm, within the limits of the 4-inch Si wafer used as microfabrication substrate. A 100 nm-thick layer of Au was sputtered along the length of the probe to help in optical visualization and mimic the presence of electrical circuitry on the device in the navigation tests.

By using standard microfabrication processes, different sensors have been patterned on the μ-probes. The thickness of the device was maintained by patterning the circuitry over a 3 μm thick PI and encapsulating it with a 1 μm-thick layer of PI. The simplest design was a single oval electrode (0.065 mm^2 area) intended for endovascular neural recording, stimulation or local cauterization. The electrode and trace were in sputtered gold; 100nm of IrOx was added on the electrode to reduce the impedance and increase the charge storage capacity. Preliminary tests (not reported here) showed that these electrodes inserted in a tortuous channel are operational even under bending due to high curvatures (1.4 mm radius).

Next, a temperature sensor was fabricated on the PI stripes. To ensure high dependability on temperature, the gold used so far was replaced by platinum. However, the sensor itself requires a high resistance to increase the sensitivity. For this reason, the deposition of the sensors (25 nm Pt) was separated from the deposition of the traces (300 nm Pt) connecting the sensor to the external control unit. Probably due to the high aspect-ratio of the probes ($\simeq$ 7 cm by 30 μm) and poor adhesion of the Pt to the PI, lift-off patterning guaranteed only a limited fabrication yield, while dry-etching proved to be a more reliable process. First 275 nm of Pt were sputtered (over a Ti adhesion layer) to produce the traces after etching through a photoresist mask, and then 25 nm of Pt were similarly added on the traces (to reach the final thickness of 300 nm) and continued beyond them to draw the high-resistance serpentine representing the sensor. This probe's design was then adapted to host an additional serpentine to create a flow sensor depicted in **Figure 4.14** and characterized in section **4.2.7**.

4.2.2   Design and operation of a μ-probe-insertion device

Unlike conventional endovascular catheters[251], ultra-flexible and ultra-lightweight filaments cannot simply be pushed into a stream because axial compressive loads will no longer be effectively transmitted due to bending of the μ-probe. For this purpose, we developed a hydromechanical insertion system that seamlessly couples with the vasculature and keeps the μ-probe under tension during the entire operation. The proximal extremity of the μ-probe was attached to a rigid rod that slid across a sealing gasket at the rear end of a custom-made syringe barrel, and the motion of the rod was controlled by a linear positioner. Gentle pulling of the rod ensured proper loading of the μ-probe into the barrel. Saline solution was pumped inside the system through an intake, applying tensile stress to the relaxed filament. Percutaneous cannulation in conjunction with controlled perfusion was performed for the fast and versatile deployment of the μ-probe (**Figure 4.1**b, **Figure 4.2**). The axial movement of the rod determined the portion of the μ-probe that was released into the target vessel. The hydrodynamic pulling forces ensured smooth passage of μ-probes into the cannula in the absence of pushing forces.

Upon introduction of the μ-probe into the vessel, viscous stresses applied by the physiological blood stream dominate the propulsion and the perfusion may be terminated.
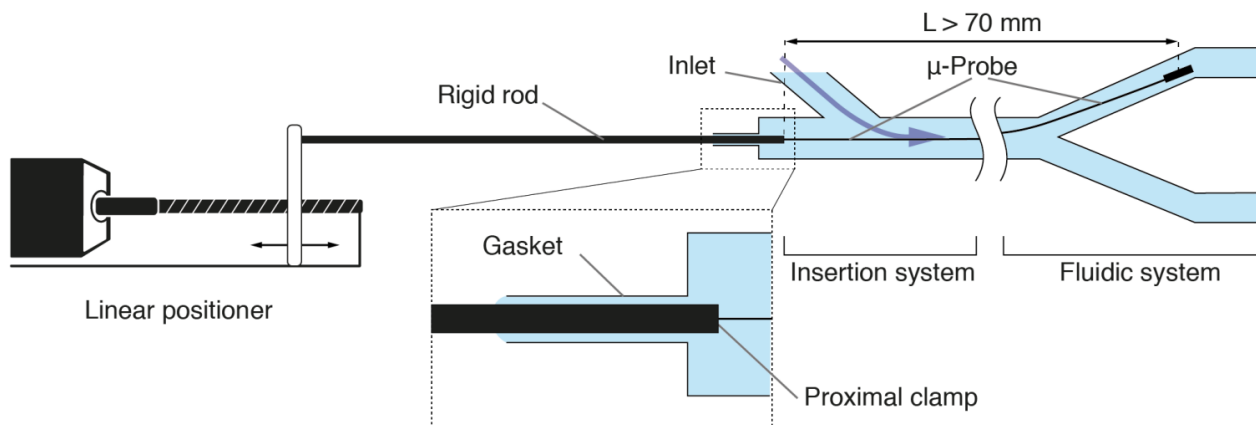
Figure 4.2 Insertion system. The μ-probe is proximally coupled to a rigid rod and its position controlled by the movement of the rod. The main purpose of the rigid rod is to provide a rigid coupling across the gasket between the linear positioner and the flexible μ-probe, and to control the release rate of the μ-probe that is being pulled by the flow. The μ-probes used in this study were longer than 70 mm. Drawings are not to scale.

4.2.3 Fluid-structure interactions in ultra-flexible μ-probes

We first studied the deformation and passive deployment of the μ-probe in a nonuniform viscous flow with curved streamlines. Flexible electronic devices fabricated by depositing conductive elements on thin polymer substrates offer a versatile route for the development of smart μ-probes. We manufactured 4-μm-thick polyimide (PI) ribbons with 200-μm width as generic structures for the study of fluid-body interactions under the influence of flow. Coating the complete surface of the ribbon with a 100-nm-thick gold film exaggerates the stiffness of functional μ-probes with patterned electrical circuits. As a result, we guarantee that the navigation results are representative for all electronic μ-probes presented in this work. Cylindrical magnetic heads with varying sizes, diameter from 40 to 350 μm, were fabricated from a hard-magnetic elastomer composite using a moulding process. The experiments were performed inside biomimetic vascular networks made from photopolymer or elastomer using 3D printing and sacrificial moulding, respectively. A Newtonian fluid matching the viscosity of blood was pumped into the channels. We regulated the average fluid velocity, $\bar{u}$, according to the size of the vessels to stay in the physiologically relevant regime.

We realized a tortuous fluidic scenario to replicate challenging vascular trajectories as shown in **Figure 4.3**a. As soon as the μ-probe was fed into the channel using the insertion device, fluid flow started to pull on the structure and kept it under tension at all times. The μ-probe was fed by moving the plunger forward and the filament perfectly followed the central streamline in the linear portion of the channel. The viscous stresses bent and transported the μ-probe through each high-curvature turn to the target location. For the chosen geometric and flow parameters, curvature up to 0.8 mm^{-1} and $\bar{u}$ = 20 cm s^{-1}, the maximal attainable velocity of the μ-probe (i.e., the maximum velocity at which we can feed the μ-probe without generating mechanical instabilities) was 2.8 cm s^{-1}, which corresponded to 0.15 $\bar{u}$ ([Supplementary Movie 1](#)). Intuitively, faster advancement can be achieved at higher fluid velocity due to the increase in viscous stresses on the μ-probe. Likewise, straighter channels allow faster deployment, pushing the maximum attainable deployment speed closer to the flow velocity. To demonstrate the instrumental role of the viscous stresses in the advancement process, we temporarily turned off the pump and kept pushing the μ-probe. The structure immediately lost tension along with

hydrodynamic lift upon removal of the flow. With further pushing, the contact between the walls of the channel and the magnetic head generated mechanical instabilities such as buckling (**Figure 4.3**b, Supplementary Movie 2). The structure unfolded and regained its straight configuration as soon as the pump was turned on, regardless of the deformed shape of the µ-probe.
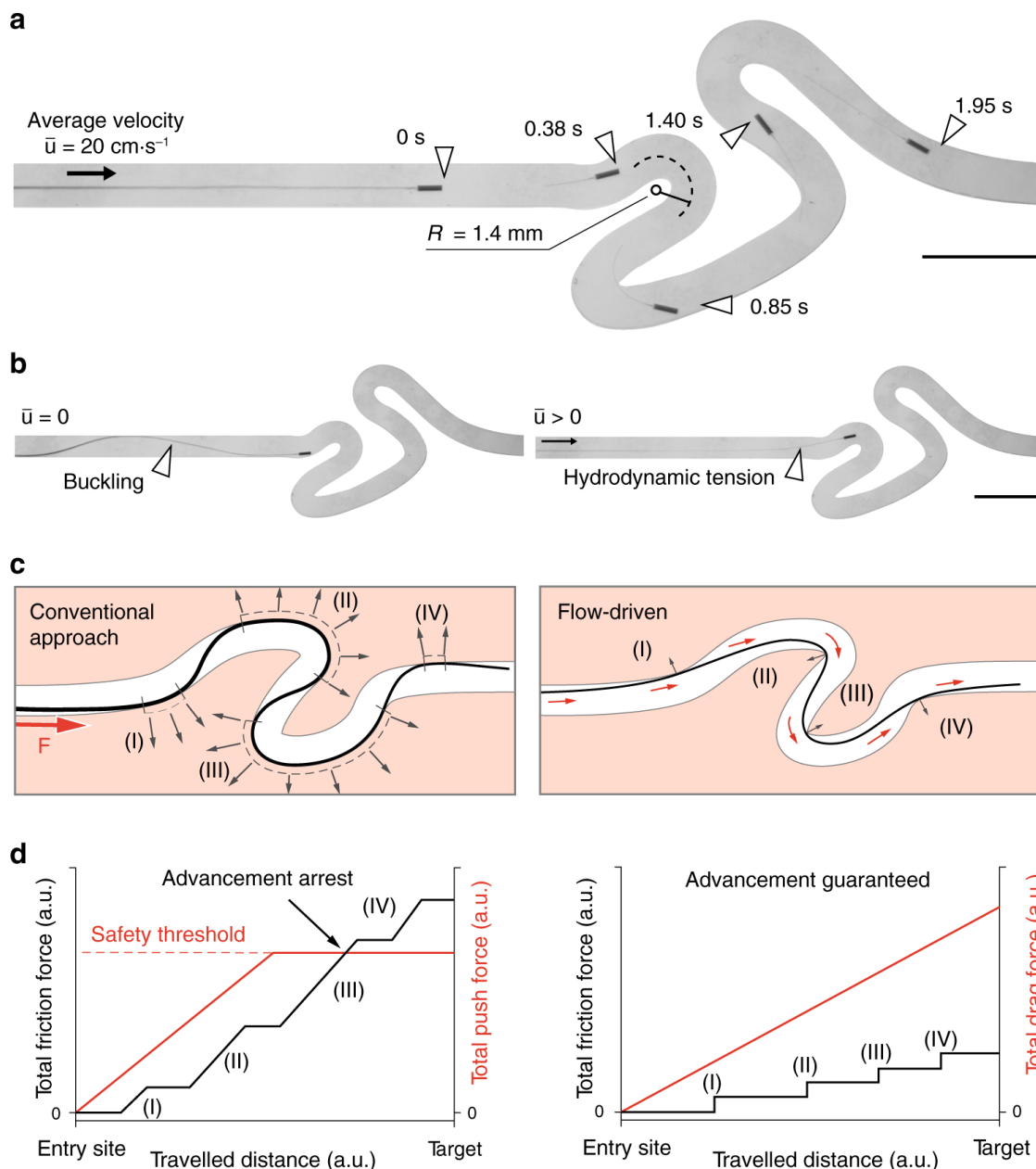
Figure 4.3 Characterization of the flow-driven autonomous advancement of µ-probes. (**a**) Slender µ-probes are transported by the flow inside tortuous channels with high curvature at a forward average velocity of 2.8 cm s^{-1}. The average flow velocity is given by $\bar{u}$ and R denotes the radius of curvature. R in the second and third turns are 1.2 and 1.8 mm, respectively. (**b**) In the absence of flow, pushing the µ-probe forward generates mechanical instabilities and the advancement ceases (left). Upon introduction of the flow, the µ-probe re-engages with it and continues to advance inside the channel. (**c**) A comparison between the conventional catheter advancement approach and fluid-driven transport introduced in this work. The conventional approach relies on a finite proximal force, F, and the contact pressure exerted on the outward wall (grey arrows) to transmit forces distally (left). Our approach relies instead on the tensile forces applied by the viscous stresses along the entire structure (right). Small red arrows represent drag forces. Drawings and forces not to scale. (**d**) In conventional navigation paradigm, friction forces increase with the length of the filament. The externally applied push force must be increased accordingly to be able to maintain the advancement. However, input forces above a safety threshold may result in vessel perforation or dissection. Ultimately, when the friction exceeds the push force, the intervention reaches its limit. On the other hand, in our approach, the continuous presence of hydrodynamic forces maintains tension on the structure and warrants a positive difference between the drag force and the friction, regardless of the travelled distance. Plots are conceptual. Scale bars are 5 mm.

The sustained tension on the µ-probe provided by the viscous stresses differentiate the proposed deployment system from conventional strategies. Standard push-based endovascular devices rely on the outward wall contact to be able to transmit the axial force along the structure in non-linear trajectories (**Figure 4.3**c, left). The result is an important increase in friction and normal forces on the walls that would ultimately overcome the proximal insertion force and lead to advancement arrest or potentially to blood vessel wall perforation. Oppositely, in flow-driven navigation, the contact points are limited to the inward wall of the curve due to the experienced tensile regime (**Figure 4.3**c, right). The discrete contact regions, in combination with the distributed drag force, allows maintaining a ratio larger than one between the total drag force and friction force along the entire trajectory and therefore ensuring uninterrupted advancement (**Figure 4.3**d). The tip of the µ-probe followed almost identical trajectories while it was being pulled forward by the flow or pulled back by the insertion device (**Figure 4.4**). One important consideration for the retraction process is the friction at corners with high curvature. The structure must be ultra-flexible yet inextensible for effective and safe retraction through tortuous paths. Since the position of the µ-probe depends on the flow along its length, the µ-probe is not always aligned with the local streamlines. For example, when the flow has curved streamlines, the filament does not align with the flow, but rather it crosses the streamlines. A similar behaviour was reported on biological filaments forming in curved microfluidic channels[252].
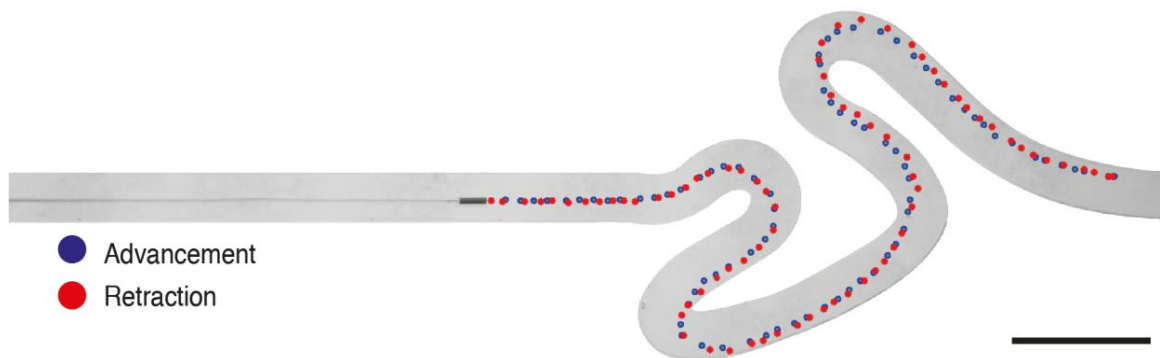
Figure 4.4 Visualization of the tip trajectories during advancement and retraction of a µ-probe. The tip of the µ-probe follows a very similar path during advancement (blue dots) and retraction (red dots). Scale bar is 5 mm.

We developed a computational model to gain more insight on the navigation mechanism and for rapid testing of robotic control strategies (see <u>Supplementary Note 1</u> for details). The stationary pose of the µ-probe in the channel was obtained by solving a lumped model of the discretized structure while probing the fluid velocities at each node of the structure at each iteration. The simulations were based on the same channel geometry used for the navigation experiment shown in **Figure 4.5**a, along with the measured value of the flow rate ($\bar{u}$ =20 cm s^{-1}) and Young's modulus of the filament (E = 3 GPa).
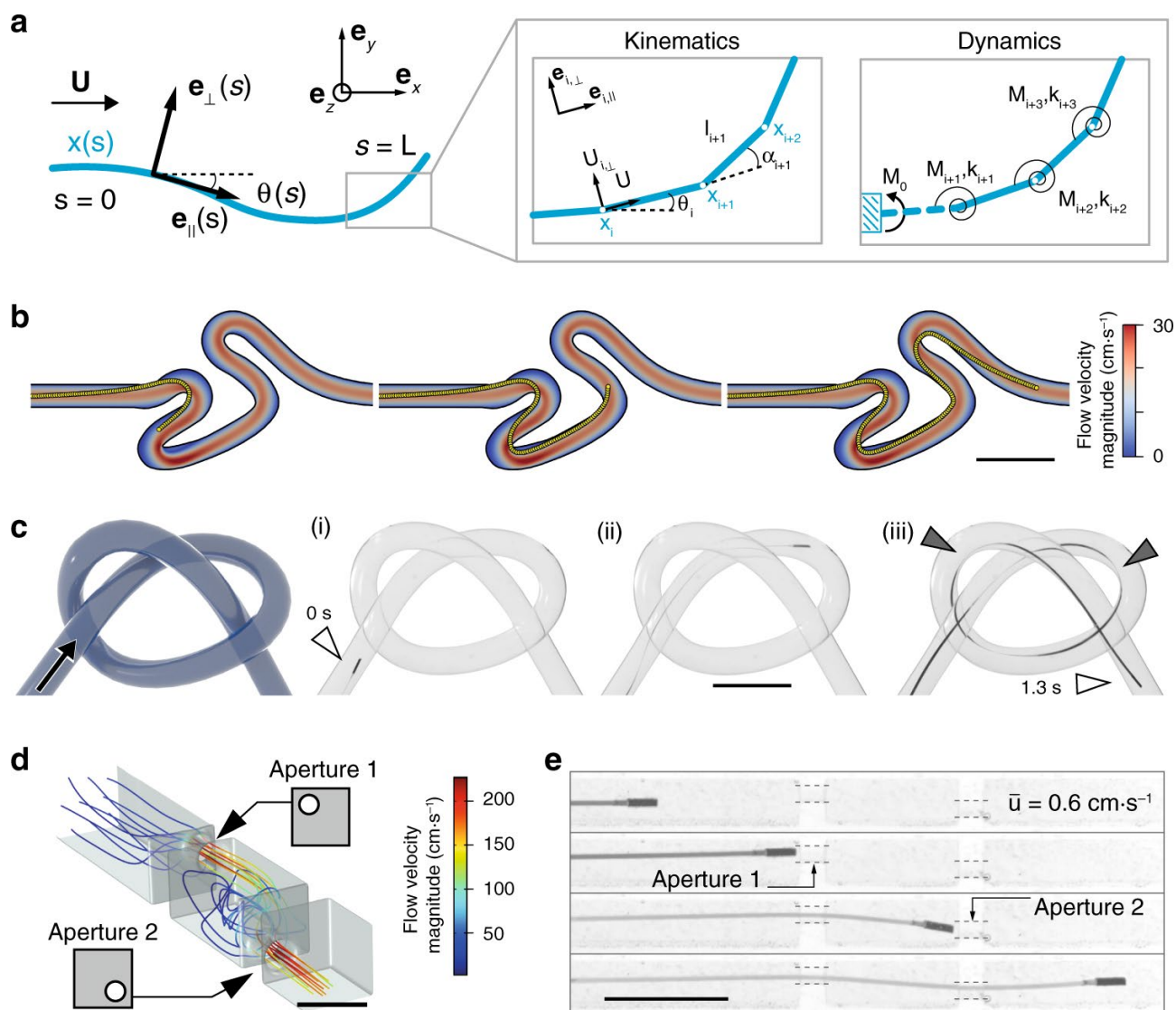
Figure 4.5 Simulation of the µ-probe dynamics and adaptive navigation. (**a**) The µ-probe deforming in two-dimensional space is described by the centreline coordinate s and a material reference frame characterized by {e⊥, e||}. The fluid velocity is denoted by **U**. Discretized model of the µ-probe is shown on the right. This model is used to calculate the velocities and forces. Deformation is calculated iteratively at each node from the resultant torque, M and spring coefficient, k. (**b**) Simulations showing the advancement of the µ-probe in the same tortuous channel shown in **Figure 4.3**a and Supplementary Movie 1. (**c**) Schematic illustration of a 3D channel with the knot shape and time-lapse images of the µ-probe (i–iii) advancing through a channel with the same geometry. The µ-probe successfully reached the target location in 1.3 s with a forward velocity of 4 cm s⁻¹. Grey arrows indicate points of contact with the wall. (**d**) CFD simulation of the flow in a channel with extreme occlusions. The main channel has 2 mm × 2 mm cross-sectional area and 750-µm-diameter holes were placed on two walls in the top-left and bottom-right corner, respectively. Scale bar is 2 mm (**e**) Snapshots from the advancement of the µ-probe inside the structured channel simulated in (**d**), finding its way through the holes even at very low flow velocity ($\bar{u} = 0.6$ cm s⁻¹). Scale bars in b, c and e are 5 mm.

To reproduce the advancement of the filament inside the channel, we iteratively added material at the tip and solved the equations for the full structure. This strategy resulted in a much shorter simulation time compared to translating the whole µ-probe as it requires significantly fewer iterations for convergence. Furthermore, this formulation was less prone to mechanical instabilities. A penalty algorithm was implemented in order to account for contact between the walls of the channel and the µ-probe. A force normal to the channel that depended quadratically on the penetration depth was applied on each node of the filament that violated the non-penetration condition. Snapshots of numerical simulations are given in **Figure 4.5**b and an animation of the overall motion is shown in Supplementary Movie 3. While the contact points with the channel walls were predicted correctly, the simulated shape of the µ-probe showed deviations due to the simplifications of the model (**Figure 4.6**).
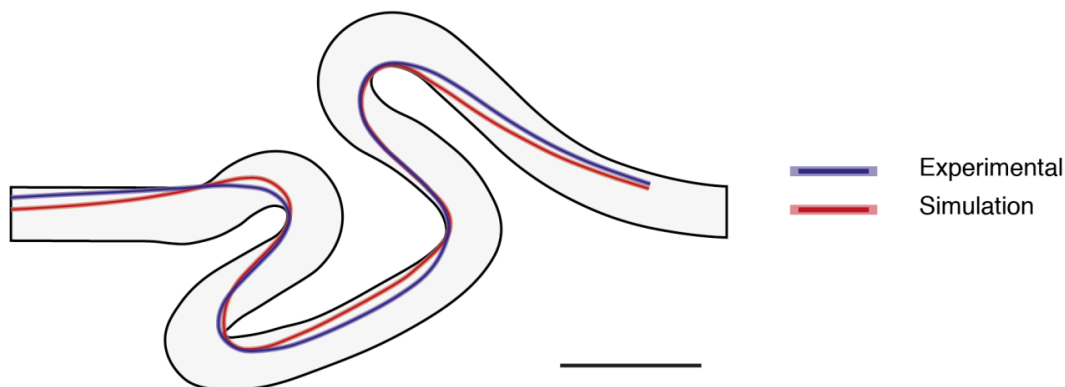
Figure 4.6 Comparative analysis of empirical and numerical results. Comparison between the steady-state shape of the μ-probe in experimental (blue) and simulation (red). Scale bar is 5 mm.

4.2.4 Adaptive transport of μ-probes in complex vessel phantoms

Using elasto-hydrodynamic coupling for propulsion enables enticing opportunities for μ-probes navigating inside highly curved, structured, or dynamically changing environments. We explored whether the elastic body could continuously morph in accordance with the geometry of the channels by testing the devices in a phantom with a braided channel forming a 3D knot with curvature as high as 0.25 mm^{-1} (**Figure 4.5**c). The μ-probe completed the track in 1.3 s at a deployment velocity of 4 cm s^{-1} under the control of the fluid flow with $\bar{u}$ =30 cm s^{-1}. Grey arrows indicate contact points between the channel wall and the μ-probe.

The rapid pursuit of streamlines without any external manipulation set the ground to test whether the μ-probes can pass through occlusions mimicking extreme vascular stenoses. We fabricated a channel with two internal occluding walls where the only passage was provided through two circular windows with a diameter twice as large as the size of the magnetic head. Computational fluid dynamics (CFD) simulations visualized the 3D streamlines inside the channel and quantified the distribution of flow velocity (**Figure 4.5**d). The μ-probe autonomously navigated through both apertures while the kinematics of the motion followed the flow field imposed by the occlusions (**Figure 4.5**e, <u>Supplementary Movie 4</u>). Shakes on the μ-probe head were visible in between the walls for $\bar{u}$ larger than 0.6 cm s^{-1} as a manifestation of unsteady flow created by abrupt changes in channel geometry. The μ-probe moved as fast as 2.8 cm s^{-1} at $\bar{u}$ = 20 cm s^{-1}.

4.2.5 Magnetic actuation of the tip for controlled bending of the μ-probe

While the translational motion of the μ-probe is controlled by the drag forces, the selection of a specific path requires the application of external torque. We observed that the transversal tip position of the μ-probe, y_{tip}, right before entering a bifurcation is a reliable indicator for the direction the μ-probe is going to take (**Figure 4.7**a). We hypothesized that by rotating the head of the μ-probe and positioning the tip at the correct location with respect to the stagnation streamline (white dashed line), we could harness the current in this new position (brown streamlines) to have the μ-probe pulled into the downstream vessel. The μ-probe would then be transported to the next bifurcation autonomously in the absence of external manipulation and the same protocol would be applied to select a new trajectory. We decided to use magnetic actuation to apply torque due to the ease of generating uniform magnetic fields, scalability arguments, and medical compatibility.
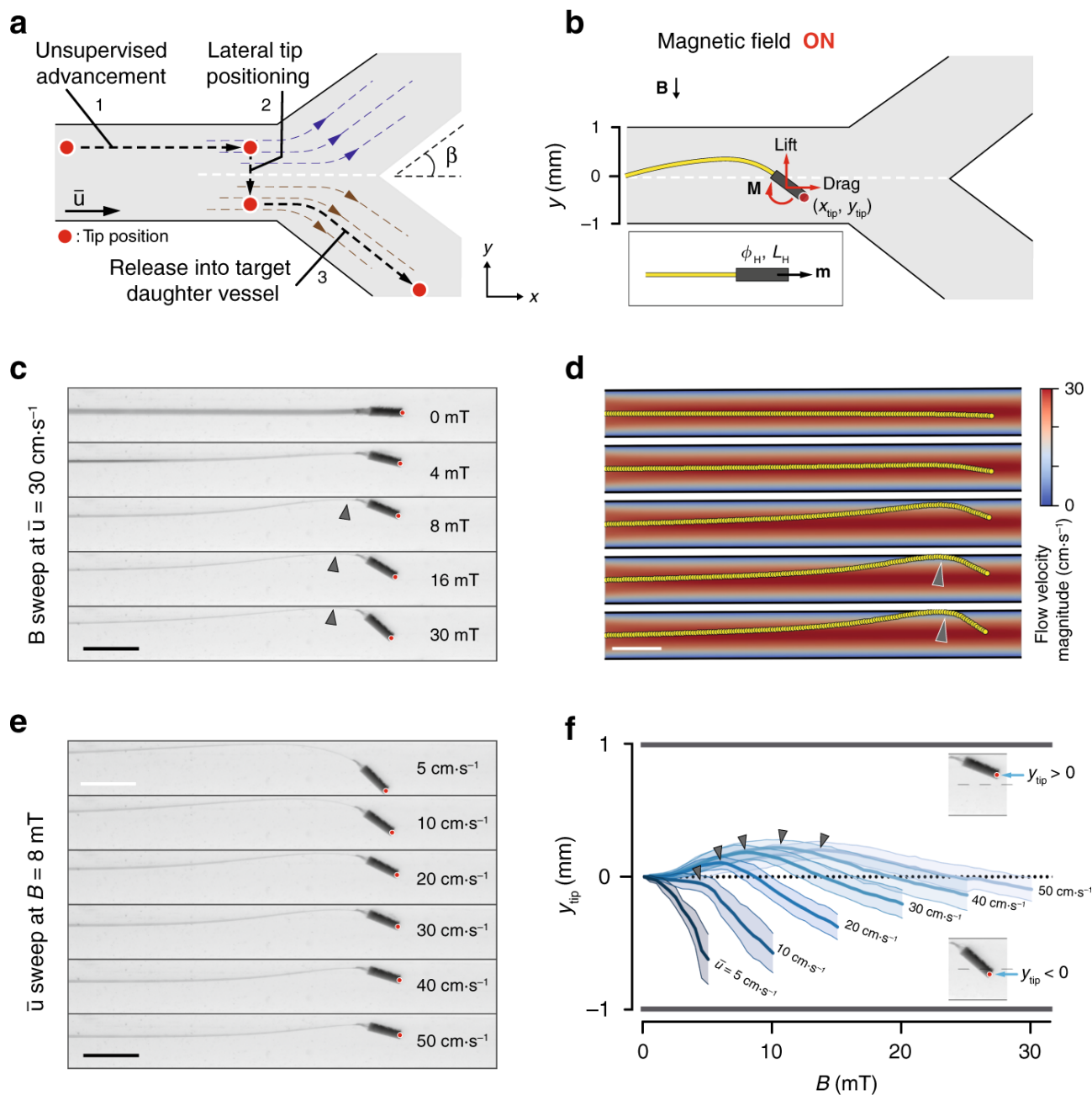
Figure 4.7 Magnetic tip steering for controlling the μ-probe position. (**a**) Conceptual description of our proposed strategy to navigate the μ-probe into the target daughter vessel. Upon reaching a bifurcation, the μ-probe tip is laterally moved from the current stream (blue dashed lines) into the target stream (brown dashed lines) with the application of magnetic torque. The μ-probe is pulled into the stream with further release of the structure. Black dashed line shows the trajectory of the tip passing through the stagnation streamline (white dashed line) and β denotes the bifurcation angle. (**b**) The transversal position of the tip, y_{tip}, is controlled by the magnetic actuation of the head that has length L_H, diameter $Ø_H$, and magnetisation **m**. Upon application of the magnetic field, **B**, the torque, **M**, exerted on the head rotates the head and bends the filament leading to an increase in both lift and drag forces. Red dot indicates the tip position. (**c**) The equilibrium shape of the μ-probe with increasing magnetic field at constant flow velocity ($\bar{u}$ = 30 cm s⁻¹). Red dot indicates the tip position. d Simulations of the μ-probe deformation under varying magnetic torque and constant flow velocity match the empirical results shown in (c). (**e**) The equilibrium shape of the μ-probe with increasing flow velocity at constant magnetic field (**B** = 8 mT). Red dot indicates the tip position. (**f**) The evolution of y_{tip} in response to the fluid velocity and magnetic field sweeps. Darker lines represent the average and lighter areas represent the average ± standard deviation. Each measurement was repeated three times for both magnetic field directions and for three different μ-probes (n = 18). Grey arrows indicate contact with the channel wall. Scale bars are 2 mm.

We systematically studied the effects of the magneto-elasto-hydrodynamic coupling on y_{tip} to develop a robust strategy for navigating μ-probes. We fabricated a representative μ-probe with a cylindrical magnetic head ($Ø_H$ = 350 μm and L_H = 1 mm) and used this prototype for the following characterization experiments, unless stated otherwise. Upon application of the magnetic field, the head rotated in order

to align with the direction of the field, which changed the distribution of hydrodynamic forces and elastic stresses, leading to a new equilibrium configuration (**Figure 4.7**b, <u>Supplementary Movie 5</u>). In the first set of trials, the µ-probe was placed in the middle of a channel at $\bar{u}$ = 30 cm s⁻¹ and subjected to varying magnetic fields (**Figure 4.7**c). At low **B**, the lift force acting on the structure moved the entire µ-probe to the upper half of the channel in the opposite direction of the field. This steering mechanism closely mimics the motion of wakeboards and reaction ferries. At **B** larger than 8 mT, the µ-probe started to contact the upper wall (grey arrow), which constrained the lift-induced upwards motion of the structure and served as a support point to further bend the distal end towards the direction of the magnetic field. At higher **B**, magnetic head rotated further, which resulted in the entry of the µ-probe tip into the bottom half of the channel. We recapitulated the µ-probe deformation under hydrodynamic forces and magnetic torque using numerical simulations (**Figure 4.7**d). The effect of magnetic actuation was incorporated into the computational model by discretizing the flexible head and applying magnetic moment at the corresponding nodes. We tuned the magnetization value to match the equilibrium shape at a certain **B** and $\bar{u}$, and used the same calibrated value for the following simulations.

Next, we performed a velocity sweep at **B** = 8 mT. With increasing $\bar{u}$, the contribution of the hydrodynamic forces to the final shape also increased, resulting in a straightening of the µ-probe. As a result, the tip eventually moved from the bottom to the upper half of the channel (**Figure 4.7**e). The overlay of the equilibrium µ-probe shapes under varying $\bar{u}$ and **B** summarized the competing effects of hydrodynamic forces and magnetic torque on y_{tip} and the steady-state shape of the µ-probe (**Figure 4.8**).
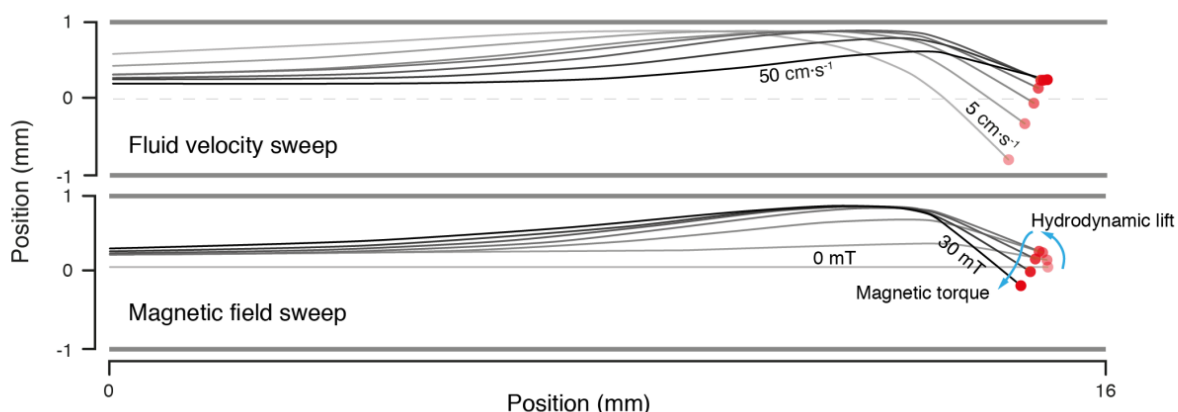
Figure 4.8 The influence of magnetic field and flow velocity on the equilibrium. Skeleton overlays of a µ-probe subjected to varying flow velocity (top) and magnetic torque (bottom). The magnetic field strength was set to 8 mT for the velocity sweep and the flow velocity was kept at 30 cm s⁻¹ for the magnetic field sweep. Red dots indicate the position of the tip.

To better visualize the effects of **B** and $\bar{u}$ on the µ-probe shape, we plotted y_{tip} for different conditions and observed a change in heading for $\bar{u}$ larger than 10 cm s⁻¹ (**Figure 4.7**f). This effect was the result of the µ-probe touching the upper channel wall, which blocked the lift-induced upward motion. Grey arrows denote the moment at which the µ-probe contacted the wall. The characterization experiments were repeated with magnetic heads of different sizes and geometries. Intuitively, longer and/or thicker heads could harness more lift force and require lower magnetic torque for actuation. However, longer magnetic heads did not fully exploit lift force because of the boundary conditions imposed by the geometry of the vessel (**Figure 4.9**).
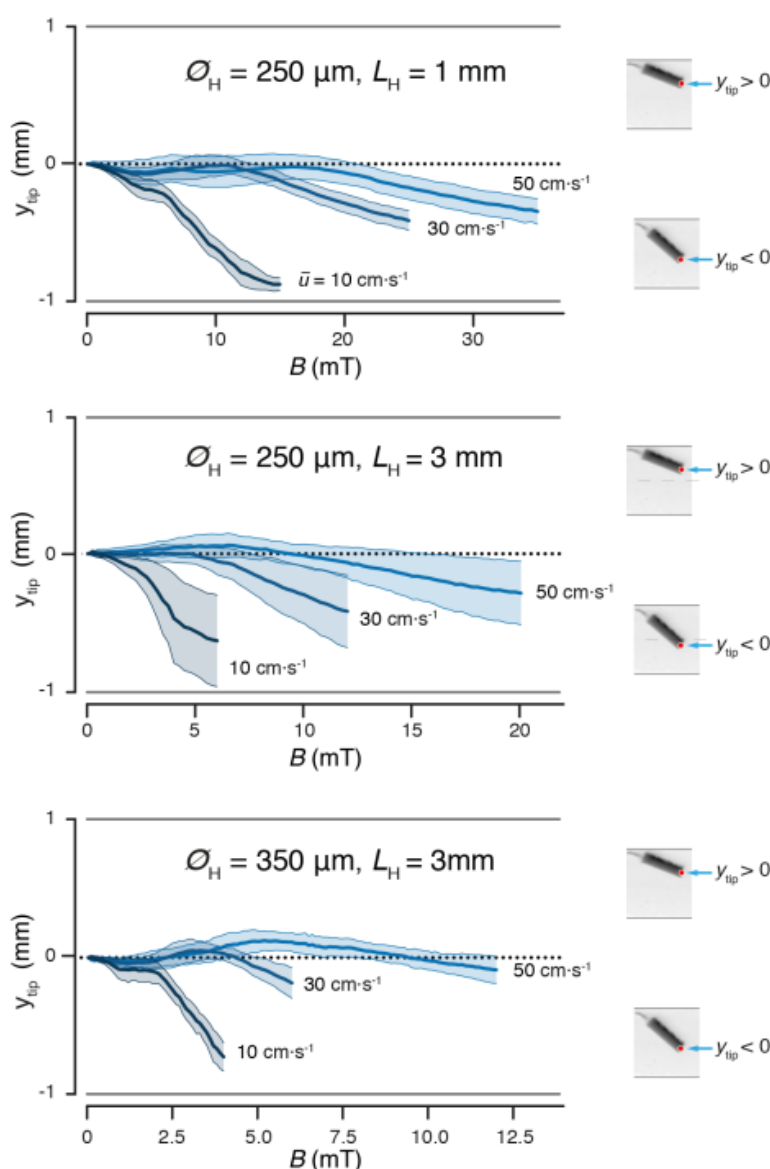
Figure 4.9 The influence of magnetic head geometry on the equilibrium pose. The displacement of the tip for three different magnetic head geometries at varying magnetic fields and flow velocities. Darker lines represent the average and lighter areas represent the ± standard deviation.

4.2.6 Controlled navigation of µ-probes in fluidic networks

After establishing a method for effective tip positioning under flow, we tested the success of steering in the presence of bifurcations. The µ-probe was fed into a channel that splits into two symmetrical daughter vessels with $\beta = 40°$ and $\bar{u} = 30$ cm s^{-1}. We discovered two distinct navigation strategies for selecting daughter vessels. In controlled-lift (CL), the rotation of the head drifts the structure towards the selected streamline by hydrodynamic lift (**Figure 4.10**a, Supplementary Movie 6). Navigation based on CL is particularly appealing for situations where contact with the walls must be minimized, magnetic torque is limited, or fluid velocity is relatively high. On the other hand, in controlled-heading (CH), magnetic torque imposes the head pose while working against hydrodynamic forces (**Figure 4.10**b, Supplementary Movie 7). CH was generally accompanied with the µ-probe contacting the channel wall, even though the success of the navigation did not rely on this hinge mechanism. While we set the velocity of the linear positioner to 4 mm s^{-1}, the navigation strategies worked at velocities as high

as 0.2 $\bar{u}$. We recapitulated the transport of the μ-probe with the computational model by iteratively moving the whole structure forward along the longitudinal axis. The simulation results matched major empirical observations—CL was achieved by exploiting lift to reach the target streamline and enter the daughter vessel at relatively low **B** (**Figure 4.10**c). CH was successfully executed at higher **B** while the simulated μ-probe contacted the walls at similar locations (**Figure 4.10**d, Supplementary Movie 8).
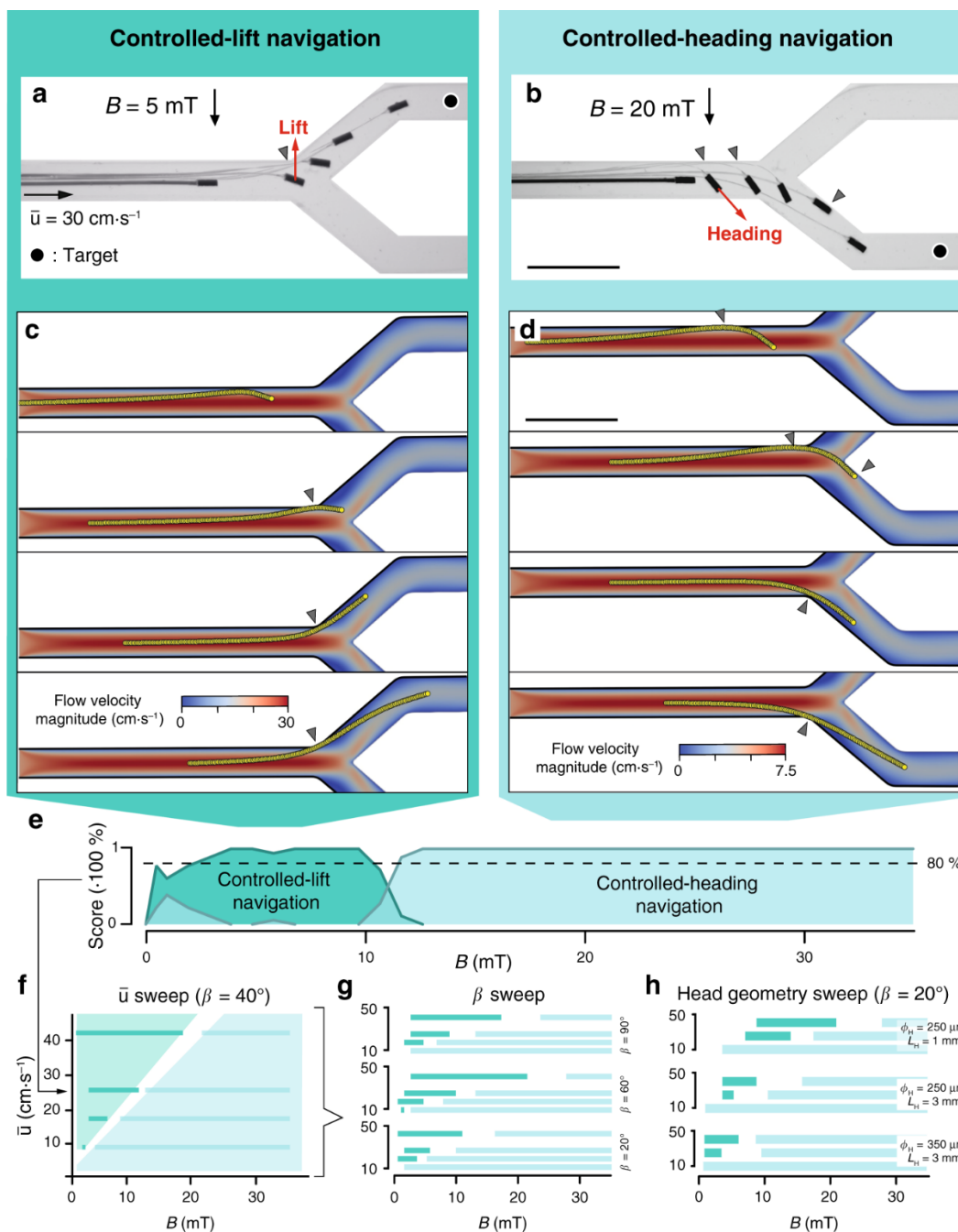
Figure 4.10 Navigation strategies to deploy μ-probes at target locations in the vasculature. (**a**), (**b**) Overlay of time-lapse images showing controlled transport of μ-probes to the target location (black dot) using (**a**) CL and (**b**) CH navigation. At lower **B**, CL navigation exploits the lift force emerging from the elastohydrodynamic coupling between the flow and the flexible structure. Lift force drifts the entire device into the upper daughter vessel (left). At higher **B**, the stronger magnetic torque enables setting of a course along which the μ-probe is transported by the flow (right). (**c**), (**d**) Simulations showing the successful navigation of the structure adopting (**c**) CL or (**d**) CH methods. (**e**) A score plot quantifying the statistics of the success rate for each navigation strategy at different **B** and constant flow velocity ($\bar{u}$ = 26 cm s^{-1}). The μ-probe was placed in the middle of a 2 mm × 2 mm channel bifurcating at an angle β = 40°. Navigation tests were repeated three times for both daughter arteries with three different μ-probes (n = 18). (**f**) Phase diagram illustrating the most favourable navigation strategy for given $\bar{u}$ and **B**. The values are binarized at an 80% confidence. (**g**) Effects of β on the success of each navigation strategy. (**h**) The influence of the magnetic head geometry on the navigation score. Scale bars are 5 mm.

After recording the results of several navigation trials at different magnetic fields, we were able to discriminate two separate regimes favouring navigation based on CL and CH. **Figure 4.10**e shows a representative plot of the dominant navigation strategies for varying **B** at $\bar{u}$ = 26 cm s^{-1} and β = 40°. We created a phase diagram by repeating this characterization process at different flow rates (**Figure 4.10**f). In the phase diagram, every line corresponds to a plot that is in the form of **Figure 4.10**, binarized with an 80% confidence. Next, we generated concatenated diagrams by stacking phase plots for different β (**Figure 4.10**g) and head geometry (**Figure 4.10**h). All results showed that the CL regime is predominant with increasing $\bar{u}$, while CH navigation had a better success rate at bifurcating angles above β = 40° for a given velocity. Increasing the aspect ratio of the magnetic head in μ-probe design promoted CH over CL due to the restricted space for the motion of the head. Decreasing the cross-sectional area of the channel from 2 × 2 mm^2 to 1 × 1 mm^2 completely precluded navigating the μ-probe using the CL method with the chosen design and mechanical properties. Decreasing the magnetic head size and/or the bending stiffness of the μ-probe will allow navigation using the CL method in sub-mm vessels.

So far, we only showed navigation inside channels residing on a plane for detailed characterization of the deformation and motion of the μ-probe. The magnetic steering was easily extended to 3D for a complex channel geometry that was provided to the user prior to the operation (**Figure 4.11**). Alternatively, teleoperated 3D navigation was performed using the visual feedback provided by two cameras observing the workspace from orthogonal views.
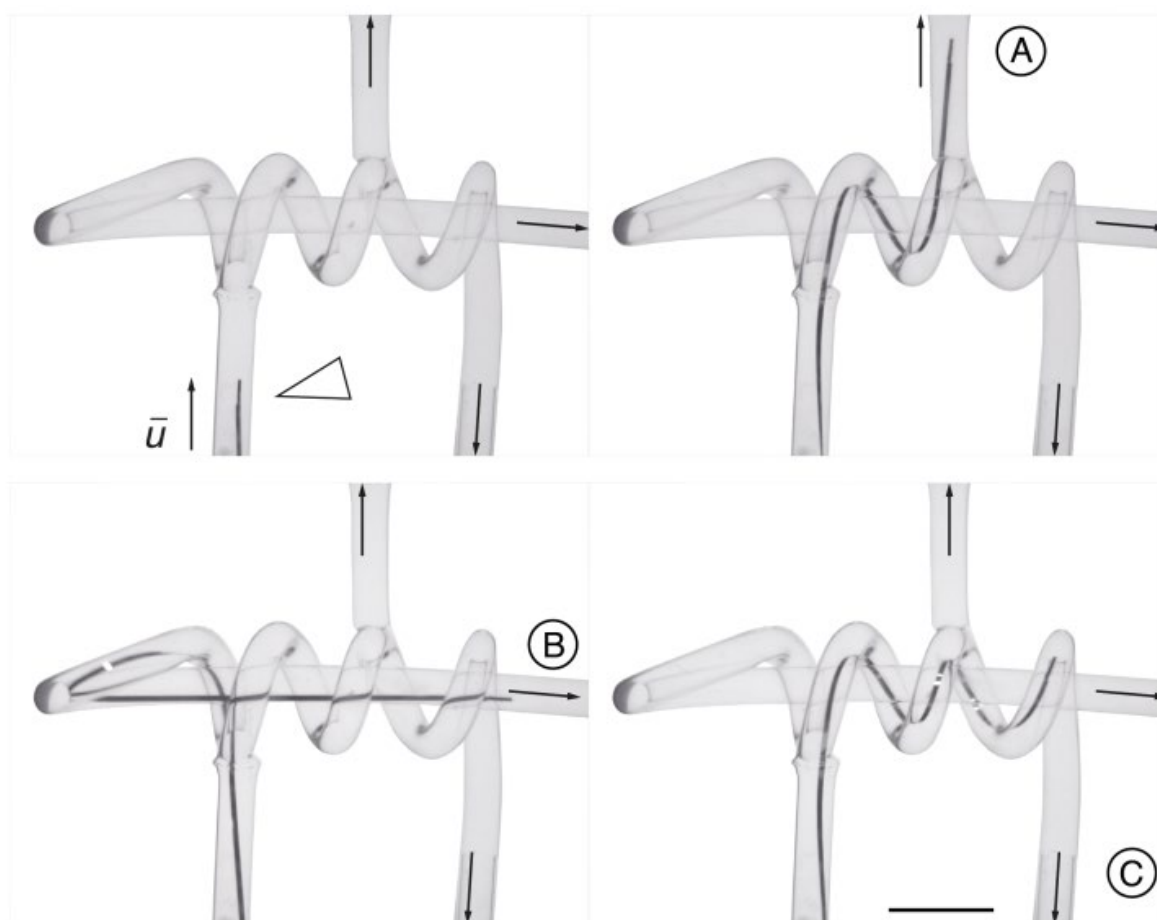
Figure 4.11 Controlled navigation in a 3D channel. The channel is looped around itself and has two vertically diverging bifurcations. The µ-probe successfully reached all 3 target locations (A, B and C) under the guidance of magnetic actuation. The µ-probe was transported at a velocity of 2 cm s^{-1} at $\bar{u}$ = 30 cm s^{-1}. Scale bar is 5 mm.

Controlled application of magnetic torque only when the µ-probe approaches bifurcations would suffice for reaching target locations. On the other hand, our method may fail when the flow in the chosen branch has significantly lower velocity compared to the alternative route. Fortunately, magnetic continuum devices provide a rich repertoire of actuation modes that can generate propulsion inside stationary fluids[253–255]. By actuating the head with time-varying magnetic fields, we facilitated entry into hydrodynamically unfavourable vessels (Supplementary Note 2). Notably, we can navigate µ-probes in tight vessels that are slightly larger than the magnetic head. To demonstrate this feature, we released µ-probes with 250 µm head into a 300 µm channel. The structure barely bent under magnetic actuation due to the confined space, yet the µ-probe successfully navigated through bifurcations (**Figure 4.12**a-c, Supplementary Movie 9). With further miniaturization (**Figure 4.12**d,e), navigation inside microfluidic channels as small as 100 µm in width became feasible. We successfully transported µ-probes with a size of 25 µm × 4 µm and a 40-µm diameter magnetic head in < 2 s (**Figure 4.12**f,g).
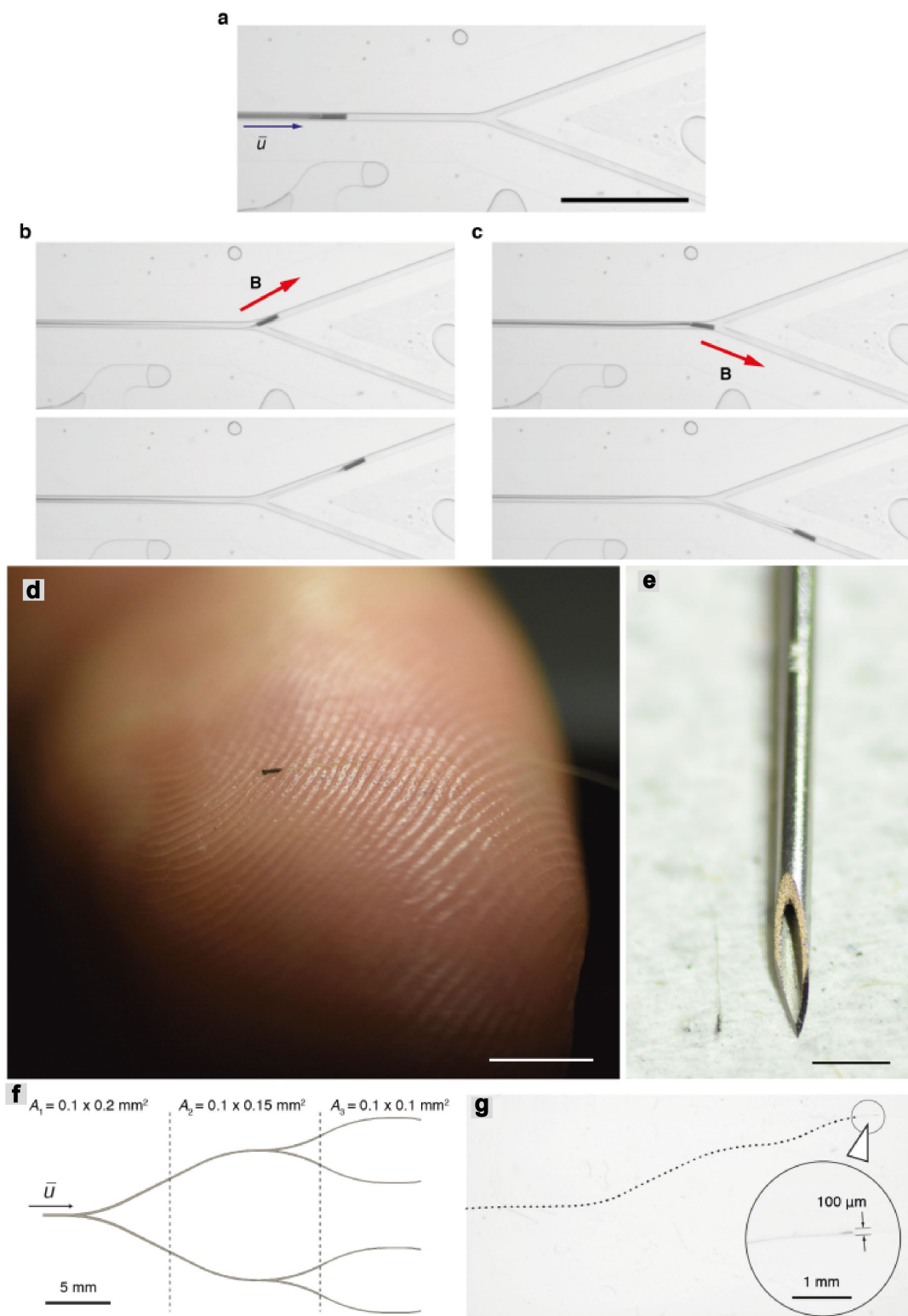
Figure 4.12 Flow-driven navigation in narrow channels. Channel size (300 µm) is comparable to the diameter of the magnetic head diameter (250 µm) at $\bar{u}$ = 0.5 cm s^{-1}. (**a**) A µ-probe is deployed into a channel branching into daughter vessels with 20° angle. Scale bar is 5 mm. (**b**) The magnetic head is steered towards the top channel (top) and released to advance further in the top channel under the control of flow (bottom). (**c**) The same control strategy is applied to steer the µ-probe into the bottom daughter vessel. (**d**) Picture of a 25 µm-wide ultraflexible µ-probe on a human finger and (**e**) with a 21 G hypodermic needle (0.8 mm diameter). Scale bars are 2 mm. (**f**) Schematic of the microfluidic channel showing the dimensions of each branch. All channels are 100 µm in height. Upon entry the µ-probe is transported by the fluid and steered with magnetic actuation to reach the target locations shown in (**g**). Inset in (g) shows the 25 µm-wide µ-probe and the 40 µm-diameter magnetic head inside the 100 µm x 100 µm channel.

Using μ-probes within a similar size range, we may reach distal microvasculature in the body, a feature that is currently impossible to achieve. Finally, our navigation strategy is compatible with the deployment of multiple μ-probes. We iteratively steered four μ-probes to pre-determined target locations in a phantom with three bifurcations (**Figure 4.13**). The profile of the flow around the existing μ-probes autonomously creates alternative paths for the incoming μ-probes. Thus, the number of μ-probes that can be simultaneously deployed is only limited by the relative size of the μ-probe with respect to the vessel diameter.
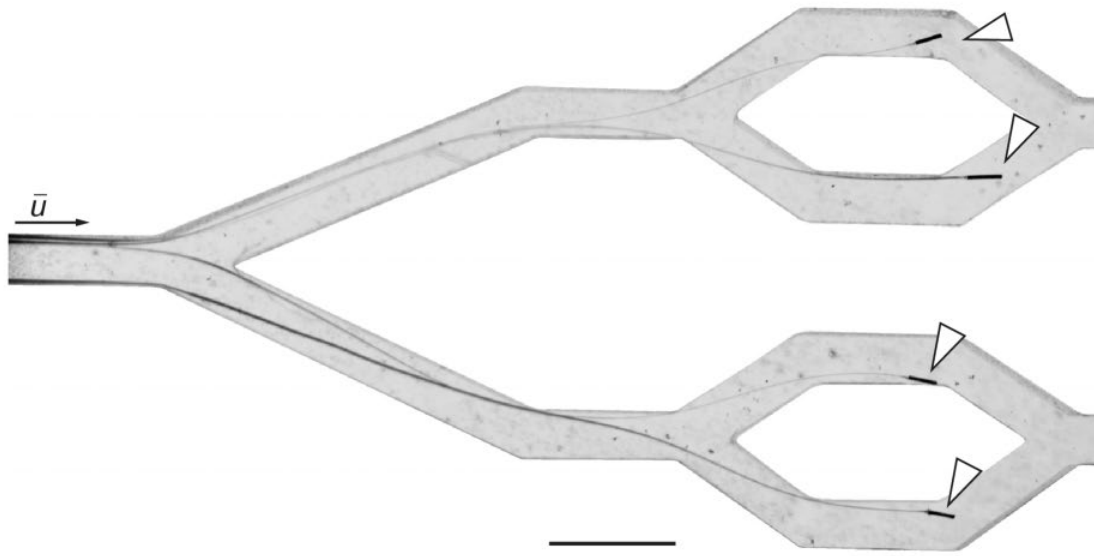
Figure 4.13 Simultaneous deployment of multiple μ-probes. Adaptive and autonomous flow-driven transportation ensures safe passage of the slender structures despite the partial occlusions created by the presence of other μ-probes. Scale bar is 5 mm.

4.2.7 Local characterization of flow using electronic μ-probes

After establishing the navigation strategy, we explored whether we could dynamically record physiological parameters such as electric potential, temperature, or flow characteristics using μ-probes. PI substrate was used to fabricate the main chassis while titanium and platinum strips were deposited to form electrodes and electrical circuits, respectively. As a proof of concept, we engineered a μ-probe that uses convective heat transfer to measure the characteristics of local fluid flow. Upon injection of current into the heater circuit, the generated heat is transferred to the sensor circuit at a rate determined by the velocity profile of the fluid. The fabricated electronic μ-probes consisted of a $0.1\,\text{mm} \times 2\,\text{mm}$ heating element and a $200\,\mu\text{m} \times 500\,\mu\text{m}$ sensor component, positioned $50\,\mu\text{m}$ apart from each other (**Figure 4.14**a). Conventional flow sensors that are based on heat transfer operate either in continuous mode or pulsed mode[256–259]. In continuous mode, the change in the sensor resistance with the flow is monitored. As a result, this measurement requires high signal-to-noise ratio (SNR), making it challenging to be implemented on miniaturized devices. Our flow sensors were operated in pulsed mode, by measuring the time-of-flight (TOF) between the injection of current to the heater and the detection of peak resistance at the sensor. This method requires a high sampling rate, which does not pose a trade-off with miniaturization.
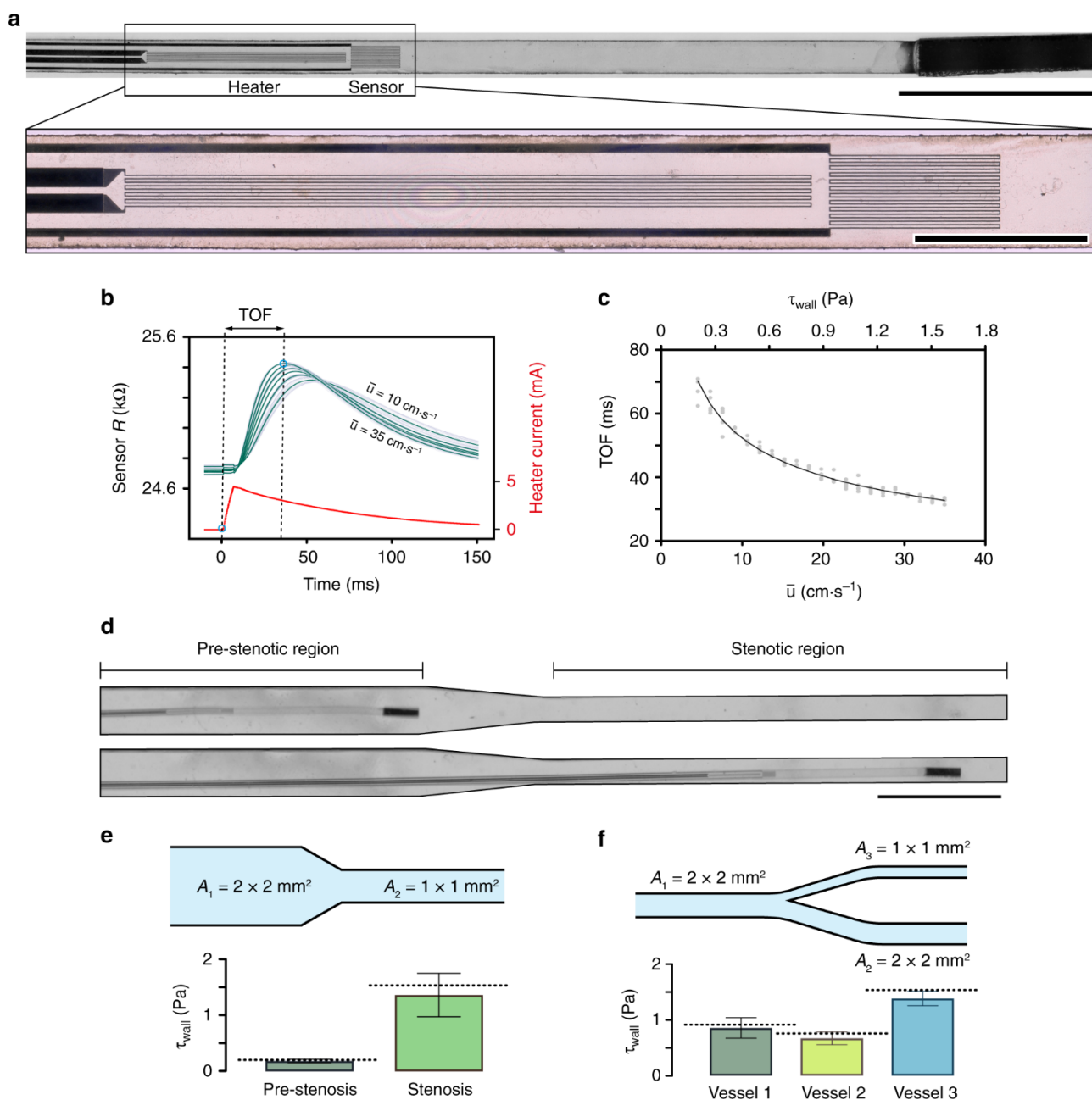
Figure 4.14 Development and navigation of microengineered thermal flow sensors. (**a**) Picture of the flow sensing μ-probe showing the heater and sensor elements along with the magnetic head. Scale bar is 1 mm. Inset shows the details of the heater and the sensor circuits placed 50 μm apart from each other. Scale bar is 500 μm. (**b**) Temporal variation in the resistance of the sensor is recorded and compared with the input signal to measure the TOF of the heat pulse. Dark lines represent the average of 30 consecutive measurements that are shown in light curves. The TOF is measured for varying $\bar{u}$ in a 2 mm × 2 mm channel. (**c**) Calibration curve of TOF with respect to $\bar{u}$ and the τ_{wall} in a 2 mm × 2 mm channel. Black curve represents the average of 6 different tests. (**d**) Representative images showing the μ-probe at a pre-stenotic region and inside the stenosis. The cross-sectional area decreases 4 times inside the stenotic region. Scale bar is 5 mm. (**e**) Wall shear stress measurements taken in the stenotic model shown in (d), after calibration with the curve shown in (c). The histograms are an average of 8 different trials with 30 measurements made at each trial. The dashed lines show the analytical calculations; error bars represent the average ± standard deviation. (**f**) Wall shear stress measurements taken in a bifurcating channel at three different locations (black bullets), after calibration using the curve shown in (c). Histograms represent 10 different trials with 30 measurements at each trial.

The input to the heater was a 10-ms current pulse with 4 mA peak value, and the sensor resistance was recorded at 5 kHz sampling rate (**Figure 4.14**b). A single temporal readout was acquired within 150 ms under physiologically relevant fluidic regimes. The speed of sensing allowed real-time interrogation of the flow during navigation. We performed a series of measurements at the wall of a channel

with 2×2 mm² cross-sectional area at varying fluid velocities. The data showed an exponential decrease in the TOF with increasing $\bar{u}$ (**Figure 4.14**c). However, the extracted calibration curve gave inaccurate results in channels with different cross-sectional area. The measurements were strongly influenced by the position of the μ-probe as a manifestation of the parabolic flow profile. Notably, the small ratio between the thermal over the flow boundary layer thickness dictates that the convection of generated heat is governed by the velocity gradient on the surface of the μ-probe. As a result, we calibrated the TOF with respect to the wall shear stress, τ_{wall}, which captures the effects of channel geometry on the thermal convection. The wall shear stress was computed from the fully developed flow profile, which was extracted using the Fourier sum approach[260] (see <u>Supplementary Note 3</u>). Finite element method (FEM) simulations quantitatively showed that the measurements were indeed highly local around the sensor unit (i.e., thermal boundary layer much smaller than flow boundary layer). Thus, the heat convection was dictated by the flow profile and hence the τ_{wall} (see <u>Supplementary Note 4</u>).

To validate the calibration curve at different channel geometries and flow conditions, we made on the fly measurements of τ_{wall} while being navigated within structured channels. The μ-probe was deployed into a stenotic region where the cross-sectional area of the channel was reduced from 2×2 mm² to 1×1 mm² (**Figure 4.14**d). Empirical data recorded at the pre-stenotic and stenotic regions varied only by 2.1% and 13.9% from the analytically calculated values (**Figure 4.14**e and **Table 1).**

Dimensions (mm x mm) $w \cdot h$	Average velocity $\bar{u}$ (cm·s⁻¹)			Wall shear stress τ_{wall} (Pa)			
	Calculated	Measured	Error	Calculated	Measured	Error	
Pre-stenosis 2 x 2	4.3	4.2	2.3%	0.191	0.187	2.1%	**Stenosis**
Stenosis 1 x 1	17.3 (4x)	29.8 (7x)	72.3%	1.530 (8x)	1.317 (7x)	13.9%	
Vessel 1 2 x 2	20.4	18.9	7.4%	0.901	0.860	4.6%	**Bifurcation**
Vessel 2 2 x 2	16.7 (0.8x)	15.0 (0.8x)	10.2%	0.738 (0.8x)	0.675 (0.8x)	8.5%	
Vessel 3 1 x 1	17.3 (0.8x)	31.2 (1.7x)	80.3%	1.526 (1.7x)	1.388 (x1.6)	9.0%	

Table 1 Flow velocity and shear stress measurements. Comparison between the analytical and empirical values of flow velocity and wall shear stress under different conditions. Flow velocity and shear stress were calculated from the input flow velocity and measured using the microfabricated flow sensor. Number in parenthesis corresponds to the incremental factor with respect to the levels in the pre-stenosis or vessel 1.

The relative increase in τ_{wall} was approximately eightfold as expected from the relation $\tau_{wall} \propto (\bar{u} \, h^{-1})$ where h is the height of the channel. As a final demonstration, we verified that magnetic actuation and bending of the filament did not interfere with the flow measurements. The μ-probe was navigated in a channel with two branches that had a different cross-sectional area (**Figure 4.14**f and **Figure 4.15**a).

The µ-probe was successfully positioned at both branches, and the shear stress measurements were close to the calculated values with 4.6%, 8.5%, and 9.0% error, respectively (**Table 1**). The repeated measurements performed at different locations and with three different µ-probes showed reliable measurement and manufacturing (**Figure 4.15**b).
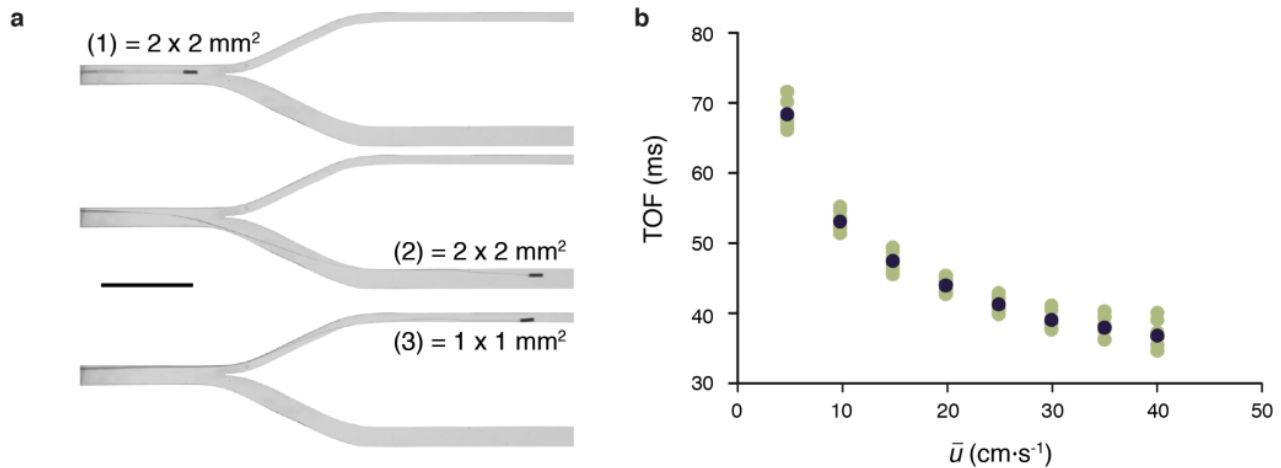
Figure 4.15 Characterization of the flow sensor. (**a**) Pictures of the experimental channel where flow measurements were taken. The mother vessel bifurcates into two daughter vessels with different cross-sectional area. Thus, the fluid velocities are expected to be different. Scale bar is 10 mm. (**b**) The repeatability of the measurements was verified in a 2 mm x 2 mm channel using three different µ-probes and by performing three independent trials with each µ-probe (n = 9). Mean value is marked with black dots.

4.2.8   Ex vivo demonstration using µ-probes and microscopic catheters (µ-catheters)

To test the feasibility of the navigation of the µ-probes under physiological conditions, we performed ex vivo tests on perfused rabbit ears (**Figure 4.16**a). The favourable transparency of the tissue allows standard camera imaging of µ-probes without requiring advanced medical angiography systems. Moreover, the subcutaneous position of the vessels enables the percutaneous insertion of the µ-probes with our hypodermic insertion device. We first injected a blue ink into the central artery to map the arterial system (**Figure 4.16**b). Four target locations were chosen (denoted by capital letters) and three layers of bifurcations were marked (i, ii, and iii). The ear was perfused with a saline solution at a constant flow rate between 30–90 µl s^{-1}. A µ-probe with $\varnothing_H$ = 150 µm and L_H = 3 mm and 4 µm × 250 µm body cross-section successfully reached all target locations through CH navigation under 3 s with an average advancement velocity of 1 cm s^{-1} (**Figure 4.16**c, Supplementary Movie 10). So far, to navigate inside biomimetic phantoms, we applied a magnetic field that is perpendicular to the orientation of the main artery and tuned the strength of the magnetic field to guide the tip to the chosen daughter artery. Here, we applied a magnetic field with constant field strength and dynamically tuned its orientation to align the µ-probe head along the direction of the chosen daughter artery. We anticipate that this strategy will be easier to implement in clinics. The µ-probe entered all the physically fitting vessels, with no apparent friction arising from vessel walls and without causing any perforation. In fact, ex vivo tests revealed excellent lubrication capabilities compared to in vitro experiments.
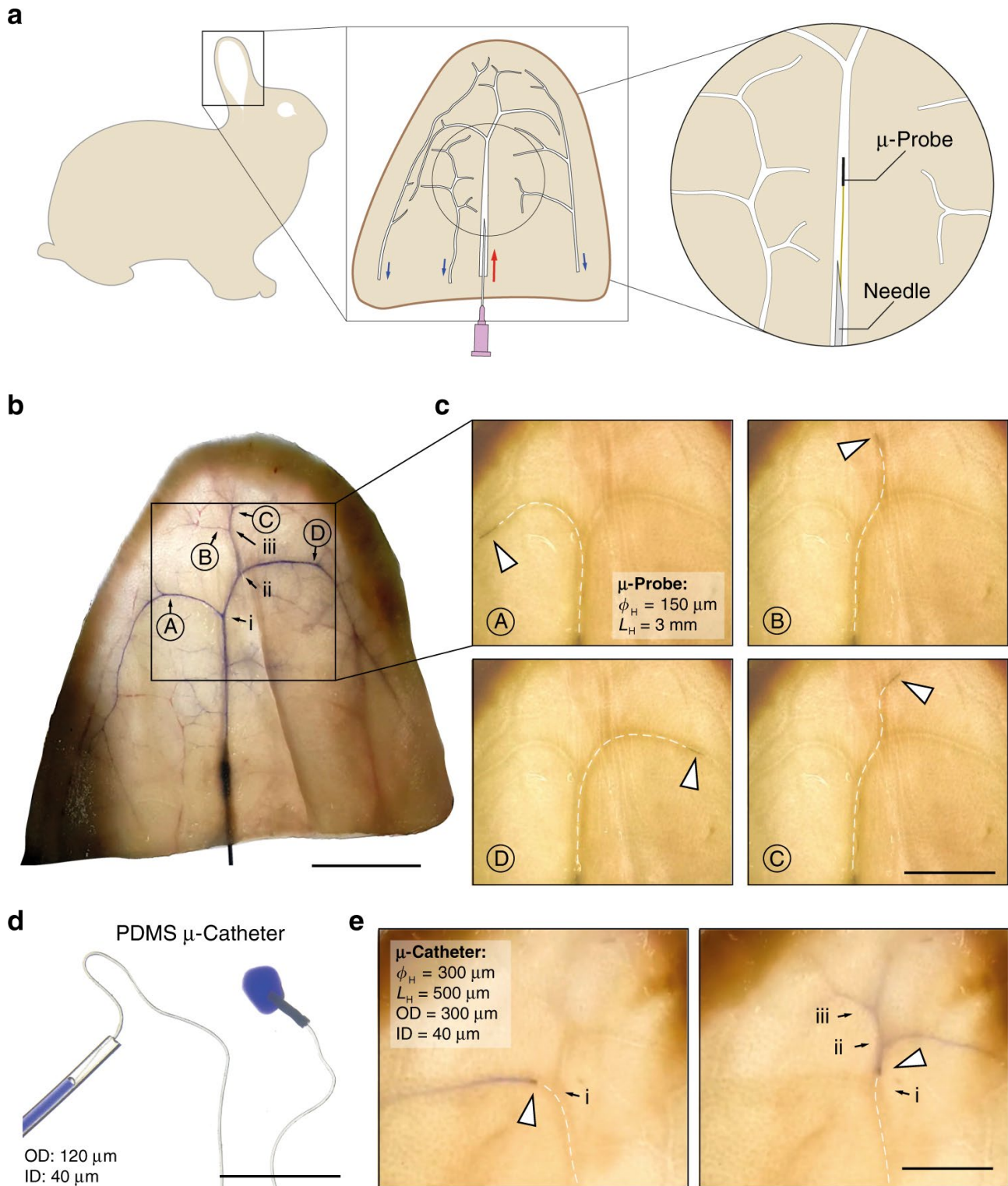
Figure 4.16 Navigation and operation of µ-probes in perfused ex vivo rabbit ears. (**a**) Schematic representation of the vascular system in the rabbit ear. Red arrow marks the central artery ramification and blue arrows indicate the venous system. (**b**) Ink-perfused ear at the proximal central artery, highlighting the main arterial branches. Bifurcation is marked with roman letters (i, ii, and iii) while the targets locations are marked with capital letters (A, B, C, and D). Scale bar is 20 mm. (**c**) A µ-probe with 150-µm diameter and 3-mm long magnetic head was proximally inserted into the vasculature using the perfusion-based insertion system at a flow velocity between 0.5 and 1.5 cm s⁻¹. White dashed lines outline the µ-probe for clarity. Scale bar is 10 mm. (**d**) A picture of the magnetic µ-catheter tube. A blue ink is injected through the µ-catheter. Scale bar is 5 mm. (**e**) Positioning of the µ-catheter head at target locations and localized injection of the ink. A total of 9 rabbit ears were used. Scale bar is 10 mm.

Slender filaments in different forms and material composition may further extend the capabilities of the proposed concept of flow-driven navigation. Conventional catheters are manufactured as tubes

that enable injection of contrast agents and embolization agents or even allow the collection of blood clots. Motivated by these capabilities, we fabricated elastomer microtubes using a thermal polymerization technique. A tubular magnetic head was glued to the distal end of the flexible tube to complete the μ-catheter. This protocol allows fabricating Polydimethylsiloxane (PDMS) μ-catheters with an outer diameter as small as 120 μm and several cm-long (**Figure 4.16**d). Upon perfusion through the insertion system, the hydrodynamic forces transported the flexible μ-catheter inside the vessels of the rabbit ear, and magnetic steering allowed the device to navigate through bifurcations. To demonstrate the potential for endovascular embolization or targeted drug delivery, we temporarily stopped the perfusion and injected a blue dye at various locations within the vascular network (**Figure 4.16**e and Supplementary Movie 11). The diameter of the vessels, where the dye injection was performed, were estimated from the evacuation speed of the dye upon re-activation of the perfused flow. Assuming equal flow distribution at the first two bifurcations and no other prior bifurcation, we estimated the diameter of the artery at the point D to be 300 μm. Experimental observation corroborated with this estimation; the μ-probe in **Figure 4.16**c got stuck at point D, indicating a vessel diameter in the order of the largest feature of the μ-probe, which was 250 μm.

4.2.9 Translation of the technology to in vivo applications

By actuating the head of the μ-probes with uniform magnetic fields that are relatively weak and vary slowly, we provided a technology that can be directly translated to in vivo studies. Human-sized magnetic control systems such as Stereotaxis Niobe and Aeon Phocus are capable of generating magnetic fields with the required strength, complexity, and speed[242,261]. On the other hand, interventional neuroradiologists usually perform endovascular operations using the visual feedback provided by a fluoroscope. To this end, we verified the visibility (i.e., radiopacity) of the magnetic head inside an ex vivo rabbit head and an anthropomorphic head phantom using two different fluoroscopes that are regularly used in the operating room (**Figure 4.17**). We could track magnetic structures as small as 75 μm while more advanced systems can resolve even smaller structures. The image quality can be further enhanced with the incorporation of radiocontrast agents such as iodine and barium into the magnetic head. Thanks to the minimal external control required by our navigation strategy, it would be possible to drastically reduce X-ray exposure. Another potential concern is the magnitude of forces applied to the vessel walls during the advancement and retraction of the μ-probe. We built an analytical model by approximating the configuration as a belt friction system[262] and developed a series of experimental platforms that can report traction forces on the μ-probe during navigation inside the phantoms (Supplementary Note 5). The results showed that the normal and tangential forces are on the order of 10^{-4} N while the forces recorded with conventional endovascular catheters are on the order of 10^{0} N[263,264].
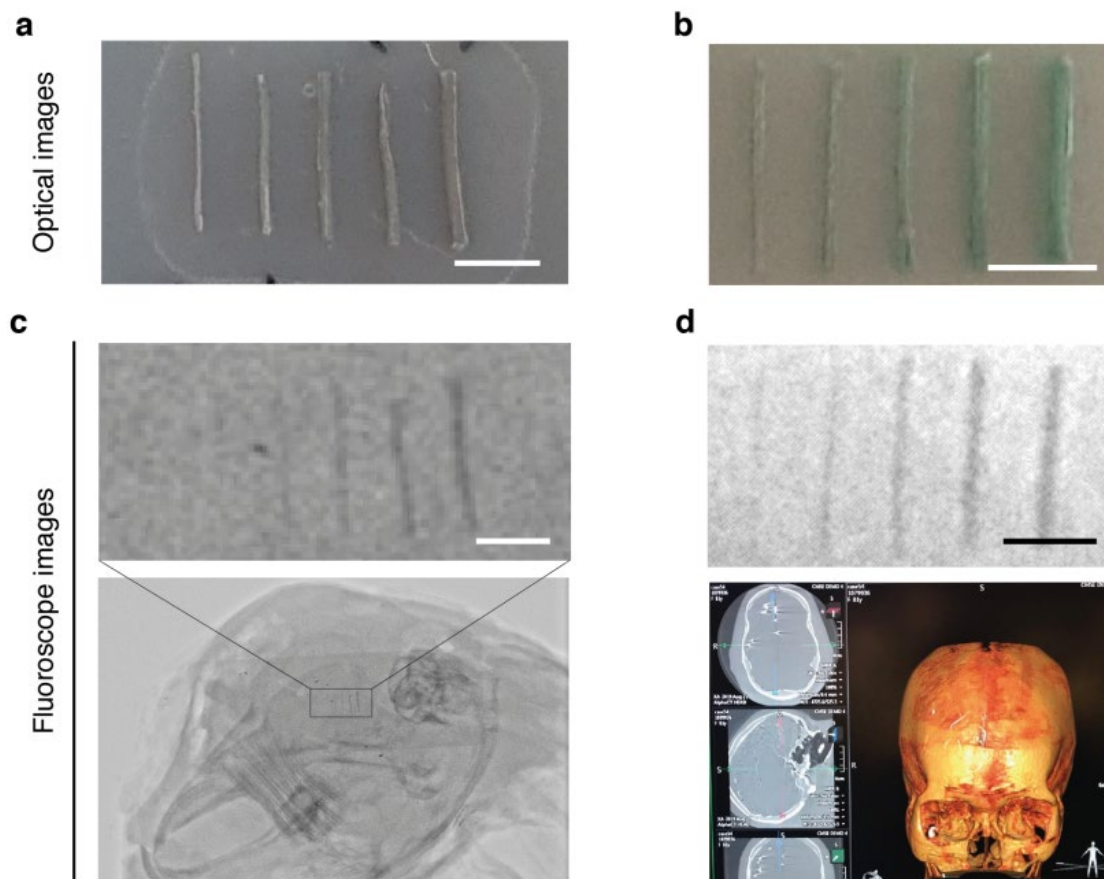
Figure 4.17 Imaging of μ-probes using two different fluoroscopes in realistic environments. (**a**,**b**) Optical images of the samples under test. The composite consists of PDMS:NdFeB microparticles that was mixed at a 1:1 volume ratio. The diameter of the magnetic samples varied between 150 μm and 350 μm. (**c**) Fluoroscope images (Canon Alphenix Sky+, 200 μm resolution) of the magnetic structures (top) placed in an ex vivo rabbit head (bottom). (**d**) Fluoroscope images (Canon Alphenix Core+, 76 μm resolution) of the magnetic structures (top) inside an anthropomorphic head phantom (bottom). Scale bars are 5 mm.

In both in vitro and ex vivo experiments, we were perfusing the vessels with a saline solution, and the same perfusion system was coupled to the insertion device for the deployment of the μ-probe. In in vivo trials, the injection device must engage to the existing cardiovascular pumping system through proper cannulation. We devised a deployment system for subcutaneous insertion of the μ-probes using standard flexible cannulas (**Figure 4.18**). Analogous to the previous version of the insertion system shown in **Figure 4.1**b, the system comprises of a rigid rod for controlling the deployment of the μ-probe, a commercially available Y-shape adapter for perfusion, and a flexible cannula for the injection. The flow was provided by an IV-bag instead of the peristaltic pump. The hydrostatic pressure was sufficient to provide a gentle flow that drags the μ-probe into the vessel.
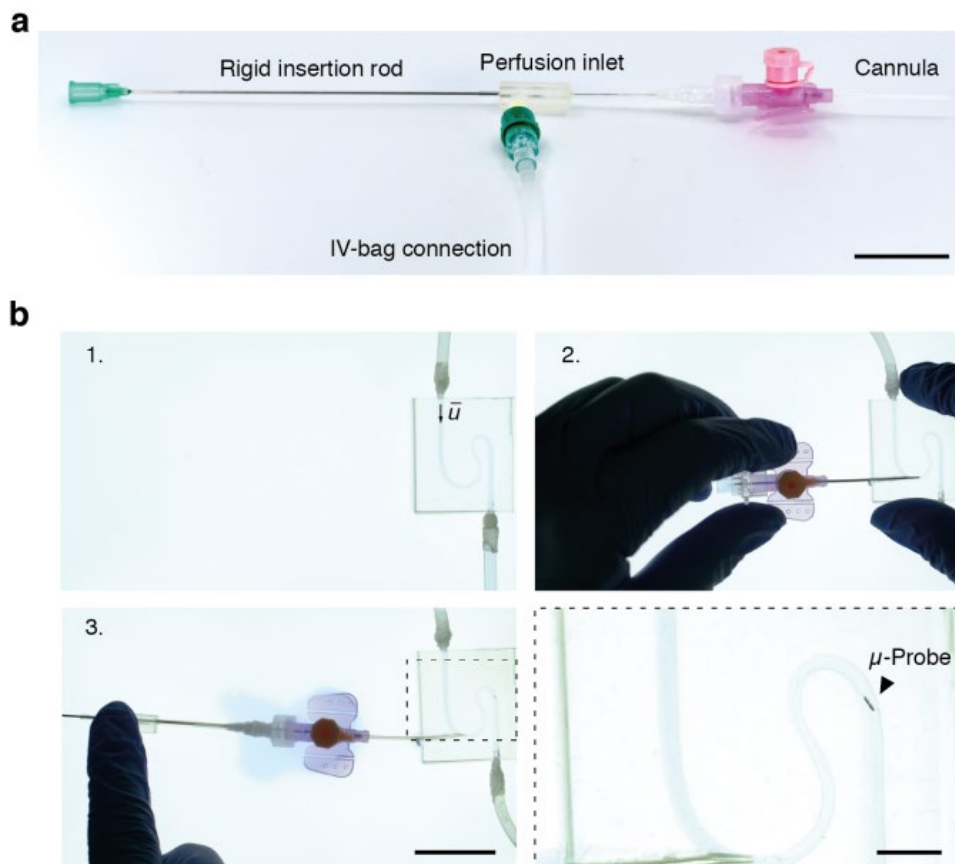
Figure 4.18 Flow-driven deployment using off-the-shelf equipment. (**a**) A standard cannula was connected to the insertion device that is perfused by a standard pressurized IV-bag. (**b**) Snapshots of a cannulation process of a PDMS phantom. Scale bars are 30 mm and 5 mm (inset).

We have also developed a hybrid toolkit that combines our technology with commercially available catheters and guidewires. Here, the μ-probe was attached to the tip of a 300 μm guidewire that moves inside a 3F (French) catheter (**Figure 4.19**). Proximal perfusion through a 5 mL syringe or a pressurized IV-bag was again sufficient to provide the drag forces to keep the μ-probe in tension. The main advantage of this modification is the compatibility of the technique with standard surgical protocols.
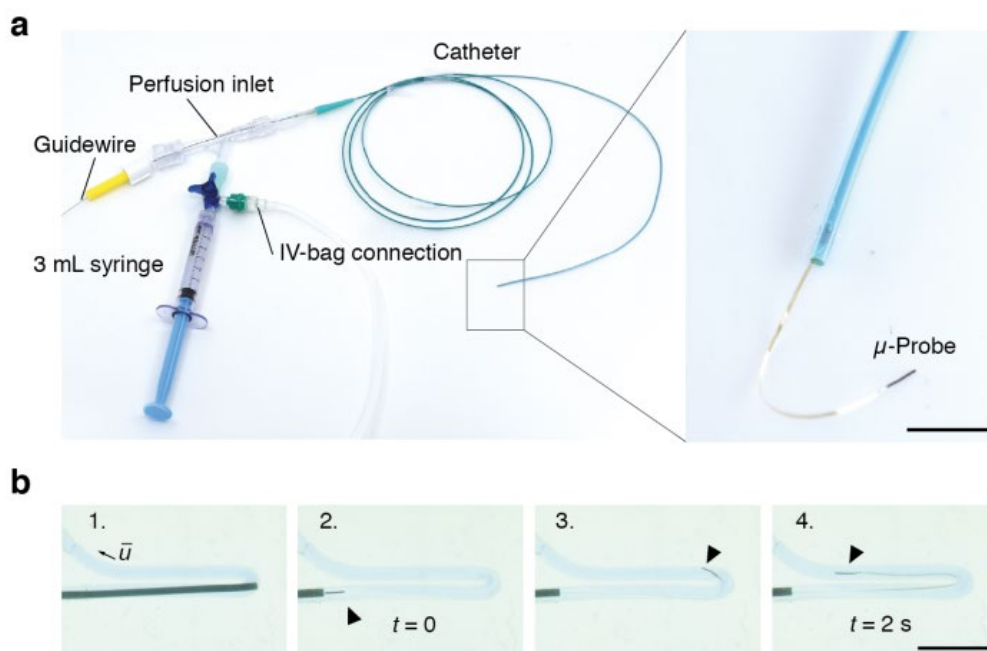
Figure 4.19 Flow-driven deployment using commercially available endovascular catheter. (**a**) A 3 F catheter is connected to a perfusion syringe and a pressurized IV-bag. The μ-probe (Ø150 μm x 2 mm magnetic head) is glued to the guidewire and pulled into the catheter. Upon introduction of perfusion, pushing the guidewire allows the μ-probe to exit the catheter (right). (**b**) Demonstration of the hybrid catheter/μ-probe device. Once the catheter reaches places that it cannot advance (e.g., a high curvature turn), it can deploy the μ-probe that can effortlessly advance with the flow and reach the target location. Scale bars is 5 mm.

As a final remark, clot formation during navigation in blood vessels is a critical risk factor. We evaluated the anticoagulant properties of our μ-probes using fresh human blood. The μ-probes induced neither platelet activation nor platelet aggregation, revealing that the polymers that the chosen polymers do not induce thrombus formation in their original finishing (**Figure 4.20**). The surface properties of the μ-probes may be modified if needed using an additional bioinspired omniphobic surface coating, that was previously shown to drastically enhance anti-fouling and anti-coagulation properties of medical devices[265].
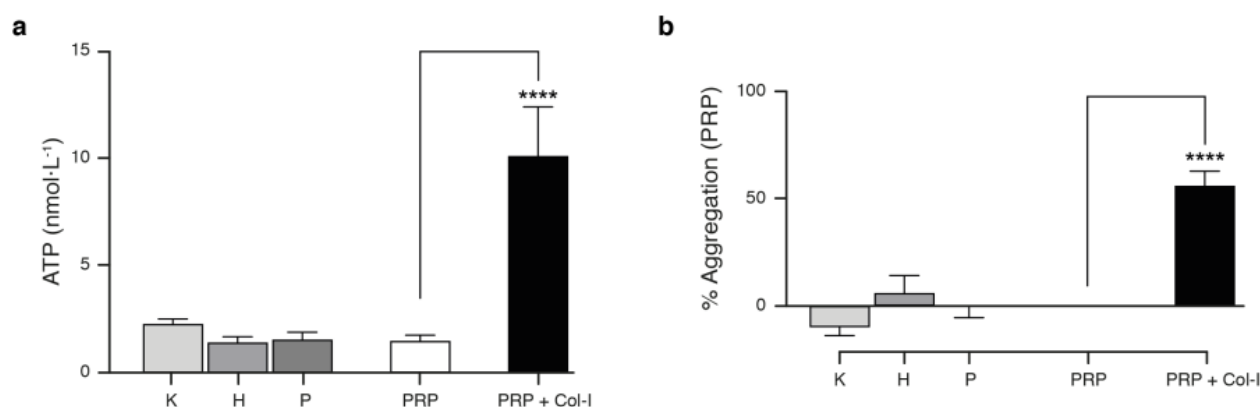
Figure 4.20 Hemocompatibility assay on fresh human blood under high shear stress condition. Three different samples were tested, Kapton film (K: 0.004 x 0.2 x 10 mm³), magnetic head with silica-coated magnetic particles (H: Ø0.3 mm x 1 mm), and whole μ-probe (P: K + H). Negative and positive control are platelet rich plasma (PRP – non-activated platelets) and PRP exposed to collagen type-I (PRP+Col-I – activated platelets). (**a**) ATP release from platelets was measured using luciferin-luciferase reaction. (**b**) Platelet aggregation was measured using absorbance (595 nm). The aggregation % was defined by the transmission of light through non-activated PRP, represented as 0 % aggregation, and through platelet-poor plasma (PPP) as 100 % aggregation. Both techniques have been vastly used in the platelet field to investigate the thrombogenicity of different materials and devices. Values were compared with the non-activated platelet, (***P < 0.001, PRP) by one-way ANOVA followed by Dunnett's post hoc test (SEM, duplicate average from four independent experiments).

4.3 Discussion

The ability to reach very peripheral vessels or to access those that are currently too small to be catheterized may allow endovascular specialists to penetrate the so-called perforating arteries, thereby giving access to therapeutic options in structures such as the brain stem, the retinal arteries or the basal ganglia. Such access might open new therapeutic options to treat deep-seated or very peripheral tumours inside the brain and target thromboembolic diseases. The technology we have developed may open new perspectives in the work up and management of neurological disorders such as epileptic seizures. Moreover, the concept of transporting multiple µ-probes with the flow will allow easier penetration in the depths of arteriovenous malformations. Other delicate structures that could benefit from enhanced atraumatic peripheral navigation are the spinal arteries that are known to be fragile and dangerous to catheterize. Aside from clinical potential, we foresee a clear path on long-term recording and stimulation of neural tissues through arterial access. Seminal work has shown that these tasks can be performed in cerebral veins using large stent-shaped electrodes[93,122]. The ability to simultaneously deploy multiple leads will enable 3D mapping of activity and spatiotemporally controlled activation at multiple sites. Optogenetics emerged as a versatile technique to address numerous scientific questions in neuroscience[233,266,267], however, state-of-the-art stimulation devices are bulky and invasive. With our technology, for the first time, we showed that accessing deep brain regions through the endovascular path is technically feasible. This will enable surgery-free optogenetic stimulation using designer µ-probes.

The µ-probes were fabricated using conventional clean-room technology, thus, they can be produced in large numbers and decorated with sophisticated electronic circuits[268]. While thin-film techniques manufacture electronic µ-probes with high fidelity, the space provided by silicon wafers is currently imposing a limit in the total length of the devices. Alternative manufacturing techniques such as thermal drawing[269,270] and 3D printing[271] enable production of metre-long smart fibres and electronic devices. The navigation paradigm is not dependent on the material choice. We can tune the bending stiffness of microfabricated devices by changing their design so that flow-driven navigation would work. We demonstrated this versatility by manufacturing devices from a wide range of stiffnesses, PDMS (Young's modulus: 10 MPa) and Kapton (Young's modulus: 4 GPa). Devices can be fabricated from medical-grade polymers that are used to manufacture commercially available catheters such as polyurethane and polyethylene. The design paradigm can also be adapted to hydrogels such as gelatin and N-isopropylacrylamide (NIPAAm), opening up the floor for biodegradable electronic devices[272] and programmable soft micromachines[273].

4.4 Materials and methods

4.4.1 Experimental platform

The experimental setup consists of an electromagnetic manipulation system, a linear positioner, and a fluid circuit (**Figure 4.21**). The 3-axis nested Helmholtz coil system was designed following the instructions provided elsewhere[274]. Homogenous magnetic fields are generated within a volumetric space of $94 \times 53 \times 22$ mm³ with a maximum **B** of 50, 60, and 85 mT, respectively. The current flowing through the coils is provided by three sets of power supplies (S8VK 480 W, Omron and SM 52-AR-60, Delta Elektronika) and servo controllers (Syren25 and Syren50, Dimension Engineering), which are modulated using an analog/digital I/O PCi Express board (Model 826, Sensoray). The off-the-shelf motorized stepper-motor linear positioner controls the forward and backward motion of the connect-

ing rod and, as a result, the position of the μ-probes. Teleoperation of μ-probes was performed using a 3D mouse (3DConnexion) and keyboard. The fluid flow was provided by a peristaltic pump (LP-BT100-2J, Drifton). The oscillations in pressure were dampened using a Windkessel element. A solution of 42.5 wt% of glycerol (Sigma-Aldrich) in deionized water was used as a blood analogue. Visualization of the μ-probes inside the phantoms was performed using CMOS camera (acA4024-29uc, Basler). We built an illumination system from smartphone backlights.
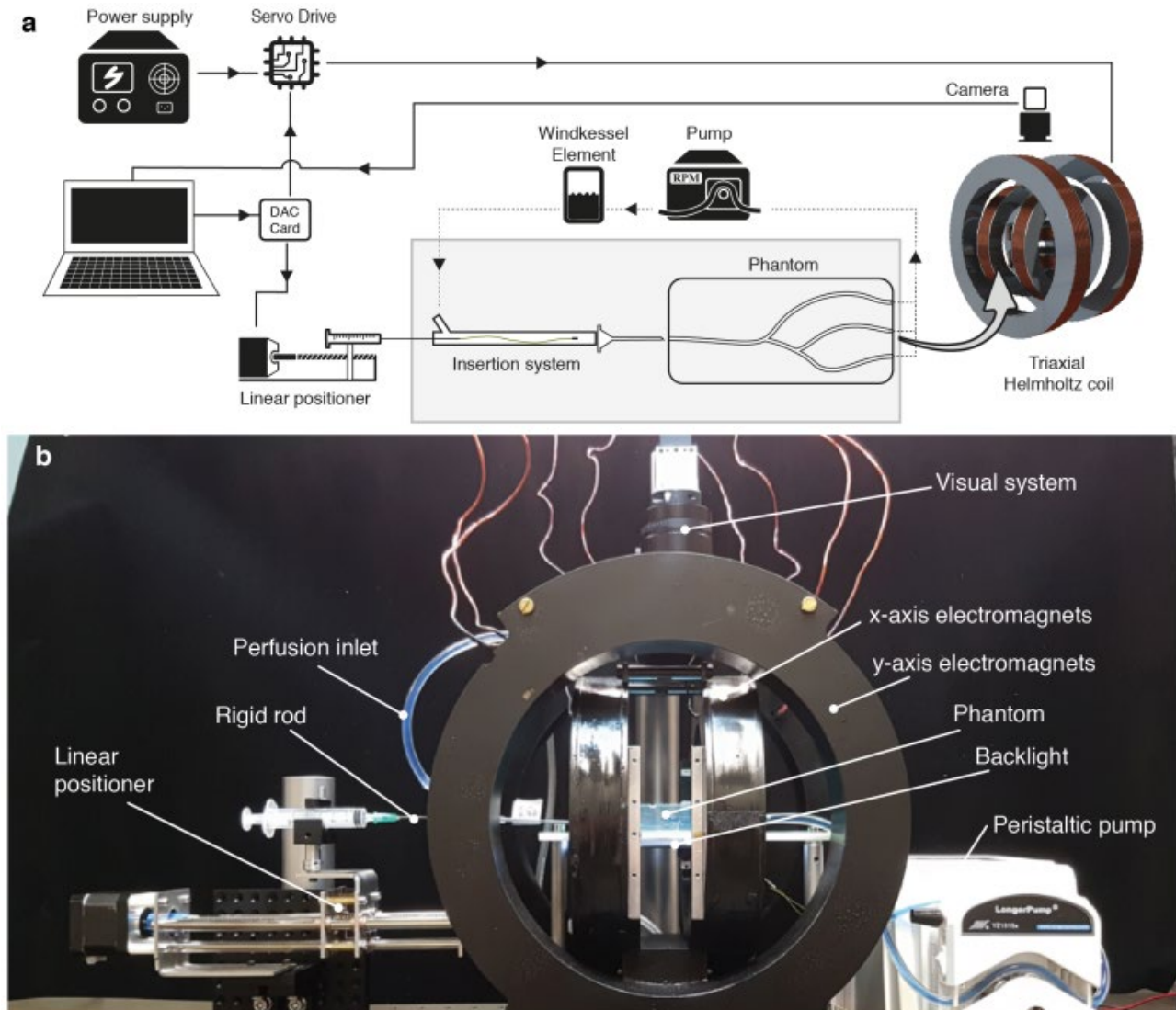
Figure 4.21 Experimental platform. (**a**) Digital to Analog Converter (DAC) card allows real-time communication between the computer and the hardware. The servo drives adjust the current provided by the power supplies to the coils. The linear positioner allows controllable release of the μprobe through the rigid rod of the insertion system. Windkessel system is placed between the peristaltic pump and the perfusion-based insertion system to dampen the flow oscillations from the pump. Visual feedback for teleoperation is provided by a CMOS camera. Drawings are not to scale. (**b**) Picture of the experimental platform.

4.4.2 Fabrication of biomimetic phantoms

Phantoms were fabricated using two different techniques. The first method allows fine control over the design of complex channels that reside on a single plane. Devices drawn with CAD software (Autodesk Fusion360) were printed using a 3D stereolithography printer (Formlabs 2) from a transparent resin (Clear resin, Formlabs). The surface of the printed piece was coated with a UV-glue (NOA81, Thorlabs) to optimize optical transparency. A second method that is based on a recently published report[275] was developed for fabricating 3D phantoms. A sacrificial negative mould was fabricated from

1.75-mm diameter water-soluble poly vinyl alcohol (PVA) filaments used in extrusion 3D printing. The PVA filament can be manually shaped using the thermoplastic properties of the material. The filament was heated above the glass temperature with a heat gun prior to shaping. Increased temperatures allow the bonding of filaments and the formation of bifurcations. The PVA mould was then casted inside PDMS (Sylgard 184, Dow-Corning) scaffold prepared at a 10:1 mass ratio (prepolymer: curing agent) and partially cured at room temperature overnight. A final curing step in the oven at 65 °C for 2 h ensured complete polymerization without deforming the PVA mould. The PVA mould was dissolved in water in a sonicating bath (CPX3800H-E, Bransonic) at 60 °C for a few days. Off-the-shelf pen ink was injected into the channels to enhance optical contrast between fluidic channels and the background.

4.4.3   Computational model

The filament was discretized in n elements of lengths li as shown in **Figure 4.5**a. The fluid velocity at each node was projected onto a local coordinate system. The Stokes hypothesis does not hold for the whole range of Reynolds numbers encountered in the experiments (Re~0.01–1000). Therefore, viscous forces at each node, $F^i_\perp$ and $F^i_{//}$ are calculated from the normal and tangential components of the velocity at that node, $U^i_\perp$ and $U^i_{//}$, using an extended resistive force theory[276] that takes inertial effects into account. The proximal tip of the μ-probe was clamped while the distal tip was kept free. A lumped model for the discretized filament was derived from the pure bending beam equation. Each node has a torsional stiffness $k_i = (EI) (l_i)^{-1}$ where E is the elastic modulus and I is the area moment of inertia. We determined the relative bending angle at each node from the total torque generated by elastic, magnetic, and viscous stresses. An iterative method[277] was implemented to solve the lumped model for large macroscopic deformations. We refer the reader to Supplementary Note 1 for the details of the formulation.

Two-dimensional (2D) CFD simulations of the flow inside the vessels were performed using an open-source software (OpenFOAM). The CAD design of the phantoms was used to extract the boundaries of the vessels. The cartesian2DMesh module of cfMesh was used to create the two-dimensional meshes of the channels with boundary layer elements. The initialisation of the flow was done using potentialFoam and the incompressible steady-state laminar Navier-Stokes equations were solved with simpleFoam. 3D CFD and FEM simulations were performed using COMSOL Multiphysics software.

4.4.4   Fabrication of electronic μ-probes

The flow sensor has been fabricated by standard microfabrication techniques. A silicon (Si) wafer, 4-inch, has been primed by oxygen (O_2) plasma for 5 min. A thin layer of polyimide (PI, PI2611 Hitachi Chemical DuPont MicroSystems GmbH, 3 μm) has been spin-coated at 4000 RPM for 30 s. Curing of the polymer required an initial soft bake at 75 °C and at 115 °C for 3 min for each temperature, followed by a gradual hard bake. (3 °C min^{-1} temperature ramp from room temperature to 200 °C under normal atmosphere, 1 h bake at 200 °C under N_2 atmosphere, 3 °C min^{-1} temperature ramp to 300 °C and bake for 1 h under N_2 atmosphere and temperature decrease to 200 °C; room temperature restoration under normal atmosphere). After the PI surface activation by argon plasma, a titanium/platinum (Ti/Pt 10 nm/275 nm) adhesion/conductive layer was sputtered (Alliance Concept AC450). Patterning of the traces has been performed by spin-coating of positive photoresist (AZ9260, 8 μm), baking at 110 °C for 240 s, rehydrating at room temperature for 20 min followed by UV exposure (Heidelberg Instruments MLA150, 405 nm and 340 mJ cm^{-2}) and development (AZ400K for 360 s). Pt excess was removed by chlorine dry etching (Corial 210IL). Photoresist residuals have been removed by slow O_2 plasma for 1

min (Corial 210IL) and dipping for 5 min inside a Remover 1165 solution at 60 °C. To add the two serpentines, serving as temperature sensor and heater, another 25 nm-thick layer of platinum has been sputtered over the wafer, after surface activation by argon plasma (Alliance Concept AC450). To define the serpentines shapes a positive photoresist mask has been spin-coated (AZ1512, 2 μm) over the thin platinum layer, soft baked at 110 °C for 90 s, patterned by UV exposure (Heidelberg Instruments MLA150, 405 nm and 104 mJ cm^{-2}) and developed (AZ 726 MIF developer for 45 s). Excess platinum was then dry etched with chlorine (Corial 210IL). To remove photoresist residual, O_2 plasma has been used for 1 min, the wafer has then been dipped in a Remover 1165 solution at 60 °C for 5 min. Before encapsulation of the device, an adhesion promoter (VM652) has been spin-coated. Encapsulating PI (PI2610 Hitachi Chemical DuPont MicroSystems GmbH, 1 μm) has been then deposited at 4000 RPM and cured by soft and hard bake (same process as above). Opening of the contacts has been done using a positive photoresist mask (AZ1512, 2 μm exposed by Heidelberg Instruments MLA150, 405 nm and 104 mJ cm^{-2} and developed by AZ 726 MIF developer for 45 s) and PI etching by O_2 plasma (Corial 210IL). Final stripping of photoresist residuals has been carried out by dipping the wafer in a Remover 1165 solution at 60 °C for 5 min. The borders of the μ-probe have been then laser cut (Optec MM200-USP) to 300 μm x 65 mm rectangles and detachment from the wafer has been done manually.

Generic μ-probes for fluid-structure interactions studies have been prepared by spin-coating on a 4-inch Si wafer a 4 μm-thick layer of PI (PI2610 Hitachi Chemical DuPont MicroSystems GmbH) and baking with the same process as above. A positive photoresist (AZ1512, 2 μm exposed by Heidelberg Instruments MLA150, 405 nm and 104 mJ cm^{-2} and developed by AZ 726 MIF developer for 45 s) has been used as mask for sputtering (Alliance Concept AC450) a 100 nm-thick layer of gold in stripes of 250 μm-width and 9 cm-length, followed by lift-off in acetone. The μ-probes borders have been then laser cut (Optec MM200-USP) and detachment from the wafer has been done manually. Finally, generic μ-probes without gold, have been fabricated as the latter without the gold deposition and laser cutting stripes of different widths varying from 25 μm to 300 μm.

The magnetic head for all μ-probes was fabricated from a composite of PDMS and Neodymium Boron Iron (NdFeB) microparticles with an average diameter of 5 μm (Magnequench, Germany), mixed at a mass fraction of 1:1. The structures were cured at 65 °C in the oven in a custom-made mould. The size of the cylindrical magnetic heads varied from 40 to 350 μm in diameter and from 100 μm to 3 mm in length. Magnetization was performed using an impulse magnetizer (Magnet-Physik) at a field strength of 3500 kA m^{-1}. The magnetic head was attached to the distal end of the Kapton ribbon using epoxy and manual positioners (Thorlabs). The electrical measurements were performed using a sensitive dual-channel source measure unit (Keysight B2902A).

4.4.5 Fabrication of μ-catheters

Microfluidic μ-probes were fabricated by following a simplified version of a previously described protocol[278]. In brief, a 40-μm-diameter tungsten wire (Goodfellow) was immersed in PDMS (10:1 ratio) and heated with the electrical current at a density of 320 A mm^{-2}. Thermal dissipation provided by Joule's heating ensured local polymerization around the wire. The thickness of the PDMS μ-catheter was determined by the time of polymerization. The wire coated with the polymerized PDMS was then immersed in an acetone bath and vigorously agitated to remove uncured PDMS. After completing curing in an oven at 65 °C for 2 h, the tungsten wire was first gently and mechanically disengaged from the PDMS coat using tweezers. Next, to apply a distributed load, the PDMS μ-catheter was sandwiched between two sheets of PDMS and the tungsten wire was gently pulled out while applying pressure on

the PDMS sheets. A tubular magnetic head was bonded to the distal end of the μ-catheter using PDMS as a glue and a tungsten wire to prevent clogging.

4.4.6   Ex vivo experiments

Navigation experiments were performed with ex vivo Rex rabbit (weight between 2.8 and 3.5 kg, age ~4 months) ears immediately following their delivery. The ears were perfused with phosphate-buffered saline (PBS) solution 1X (Sigma Aldrich) in the central artery shortly after excision. The μ-probes were introduced into the central ear artery using the insertion device and a 21 G hypodermic needle. A 3×10^{-3} w/v% of Pluronic-F127 solution (Sigma Aldrich) was added to the PBS solution to avoid adhesion of the PDMS tubes to the barrel of the insertion system. Mean perfusion flow was maintained at a rate of $90\,\mu l\,s^{-1}$. A total of nine ears were used throughout the experiments. The ears were obtained from a local farm (La Ferme Aebischer, 1595 Faoug, Switzerland).

4.4.7   Platelet aggregation and activation

Fresh human blood samples were collected from the Health Point at EPFL. Platelet-rich plasma (PRP, 300 μL) was added to the wells containing the devices, and the plate was agitated for 15 min, 1200 RPM at room temperature. Platelet aggregation was measured using a plate reader (595 nm – PerkinElmer, Victor X3). For the platelet activation test, the ATP release from activated platelets was measured using luciferin-luciferase reaction, as previously described[279]. In brief, Luciferin-luciferase ATP reaction buffer (ATP mix) was prepared using $200\,\mu g\,mL^{-1}$ of luciferin, $40\,\mu g\,mL^{-1}$ of luciferase, $2.4\,mg\,mL^{-1}$ of bovine serum albumin, and $2.4\,mg\,mL^{-1}$ $MgSO_4$. 100 μL ATP mix were added into the well containing the samples previously agitated for 15 min, 1200 RPM at room temperature before measuring platelet aggregation using absorbance. Four independent experiments were performed for both tests using blood from four different donors ($2.75 \times 10^5\,\mu L^{-1}$ to $3.66 \times 10^5\,\mu L^{-1}$ – PRP concentration among donors). Collagen-I ($10\,\mu g\,mL^{-1}$) was used as positive control and PRP incubated with PBS was used as negative control. All protocols were approved by the Swiss ethics committee (project-ID 2017-00732).

4.4.8   Fluoroscope images

X-ray images of the magnetic structures were taken using two different fluoroscopes, Canon Alphenix Sky+ with 200-μm resolution and Canon Alphenix Core+ with 76-μm resolution, inside an ex vivo rabbit head or an anthropomorphic head phantom.

4.5   Acknowledgements

Chapter 5   Locomotion of sensor-integrated soft robotic devices inside sub-millimetre arteries with impaired flow conditions

The goal addressed in this chapter is the adaptation of the previously presented endovascular navigation system to locations where the blood flow is absent and flow-driven navigation is impaired.

Supplementary Information (SI) and videos are available online at this link. Only part of the SI is reported in this thesis for sake of length and relevance to the main objective of this work.

5.1   Introduction

Interventional cardiology and neuroradiology have revolutionized medicine by offering minimally invasive endovascular procedures to treat various life-threatening conditions such as stroke, arteriovenous malformations, aneurysms, atherosclerosis, and cancer[223,224,280–283]. In the majority of these procedures, the physician manually steers a guidewire to the target site with the aid of a fluoroscope, a real-time X-ray imaging system. The guidewire serves as a guide during the placement and removal of the larger tube-shaped catheter. Steering guidewires and endovascular devices using robotic actuation promise to improve the speed, safety, and efficacy of interventions[238,240,244,246–250,284–293]. Integration of electronic devices on endovascular instruments such as force, temperature, pressure, and flow sensors[294–296] facilitated the development of intelligent machines that are capable of navigating the cardiovascular system autonomously[297]. Sensor-integrated catheters have been miniaturized to millimeter[298–301] and even micrometre scale[302] using microengineering methods. Despite these technological advances, catheterization of tortuous small vessels using the conventional push-based navigation technique is still tedious, time-consuming, and can damage the vasculature. As a result, a significant portion of the human vasculature remains clinically inaccessible to tethered diagnostic and therapeutic tools.

We have recently discovered a navigation method that exploits hydrokinetic energy to transport ultraflexible microfabricated electromechanical devices without the aid of a guidewire[127]. The devices were designed to have a cross-sectional profile that drastically increased their compliance, allowing the coupling between their motion and the dynamics of the blood flow inside tortuous vessels. The ribbon shape also affords the incorporation of onboard flow sensors using conventional cleanroom techniques. Homogenous magnetic fields are applied at vasculature bifurcations to tilt the magnetic head and generate lift forces, to facilitate the entry of the tip into the target lumen. The dependence on the hydrodynamic force, however, prohibits the use of this technology in situations where blood flow is impaired, namely in obstructed arteries. The obstruction could be caused by embolism, thrombosis, and traumatic injury, all of which would require endovascular monitoring and interventions.

Here, we present a wireless actuation methodology to transport ultraflexible sensor-integrated robots throughout the microvasculature without the aid of physiological flow. Recent work has shown that small pieces of magnetic elastomer sheets could be actuated using time-varying homogeneous magnetic fields to generate undulatory motion or inchworm-like gait within closed channels[253,303,304]. The idea of magnetically actuating and steering endovascular instruments precedes the use of guidewires, and magnetic navigation was extensively explored by the para-operation device (POD) catheters, although at much larger scales[305–307]. Inspired by these studies, we postulated that the thrust generated by an undulating magnetic head could pull an ultraflexible tether inside vessels with the impaired flow (hypoperfusion) or no flow. The soft robotic device consists of a flexible polyimide ribbon that carries onboard sensors, and a head made of a magnetorheological elastomer (**Figure 5.1**a). We systematically explored the geometric design and magnetization of the head as well as the waveform of the actuation signal to optimize the navigation performance.
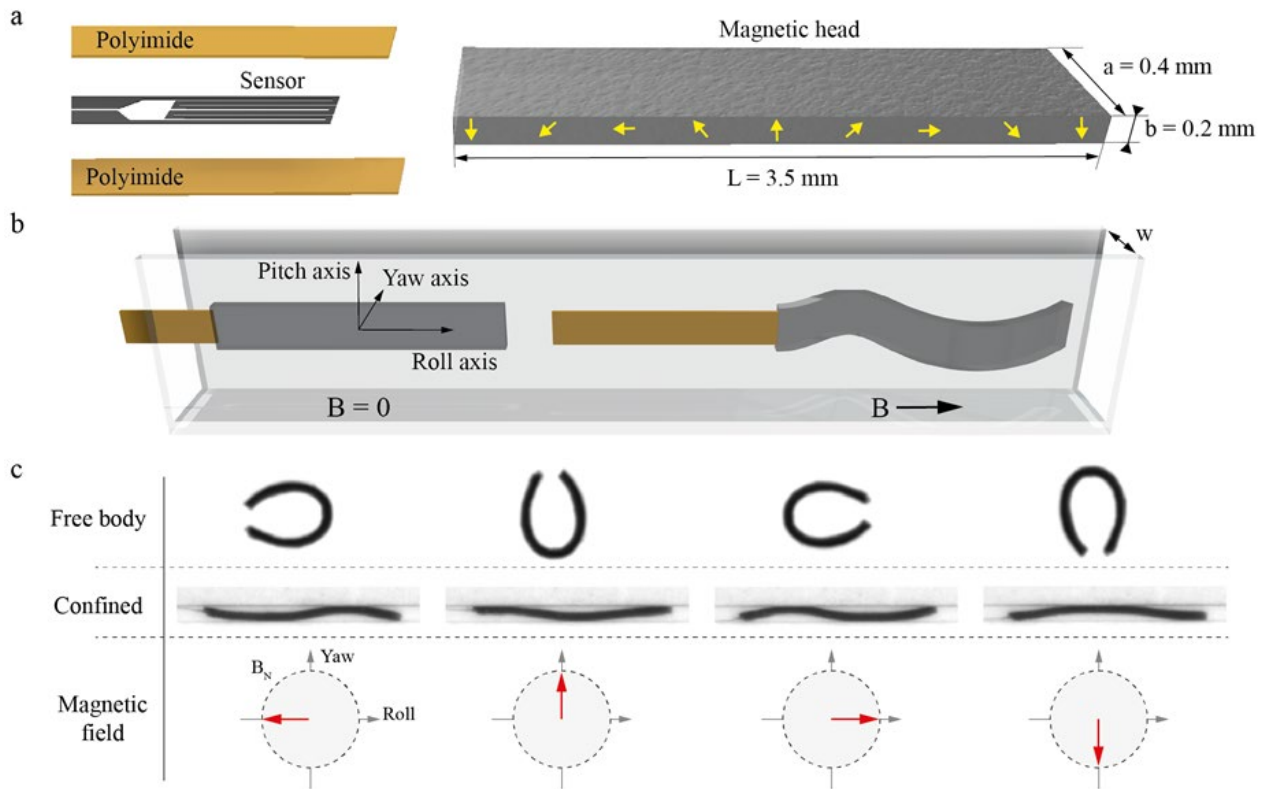
Figure 5.1 Development of the sensor-integrated soft robotic device. (**a**) Illustration showing the individual components of the device; the polymer tether (250 µm × 3 µm cross-section) with embedded flow sensor and the ferromagnetic head. Yellow arrows indicate the alignment of the magnetic dipoles. (**b**) (Left) Illustration showing the roll, pitch, and yaw axes of the device inside a rectangular channel. (Right) Upon application of the actuation field, B_N, the head bends and contacts the channel walls. (**c**) The shape of an untethered magnetic head along with the shape the same head takes when it is attached to the tether and inserted into a 0.3 mm-wide rectangular channel. The rotating uniform magnetic field is applied on the Roll–Yaw plane.

5.2   Results and discussion

The first prototype consists of a ribbon-shaped head with an axially symmetric harmonic magnetization profile. The device was inserted into a channel phantom such that the Roll axis was parallel to the longitudinal axis of the channel (**Figure 5.1**b). A rotating circular magnetic field of nominal magnitude B_N and frequency f imposes periodic spatiotemporal torques on the internal magnetic dipoles. This periodic magnetic field generates undulations of the head, which effectively pull the tether inside the saline-filled rectangular channels (**Figure 5.1**c).

A robust kinematic performance was achieved when the magnetic field was rotated on the plane where the Yaw and Roll axes reside—hereon referred to as the "actuation plane". It is generally accepted that undulatory motion follows the following pattern: higher actuation frequencies generate higher forward velocity provided that the magnetic field is strong enough to dictate the deformation of the head. We performed a parametric sweep of the magnetic field (from 5 mT up to 40 mT) and the actuation frequency (from 1 Hz up to 30 Hz) within the capabilities of the electromagnetic system. The highest forward velocity was recorded at f = 20 Hz and B_N = 25 mT (**Figure 5.2**a). The channel width, w, is also expected to play an important role in the crawling of the head. The forward velocity of the devices monotonically increased with increasing w up to a certain threshold, reaching a maximum value of 2.46 mm s^{-1}. The velocity was able to increase because the head could attain larger amplitude strokes during each actuation cycle (**Figure 5.2**b). Increasing w further led to a reduction in velocity because the structures struggled to contact the walls.
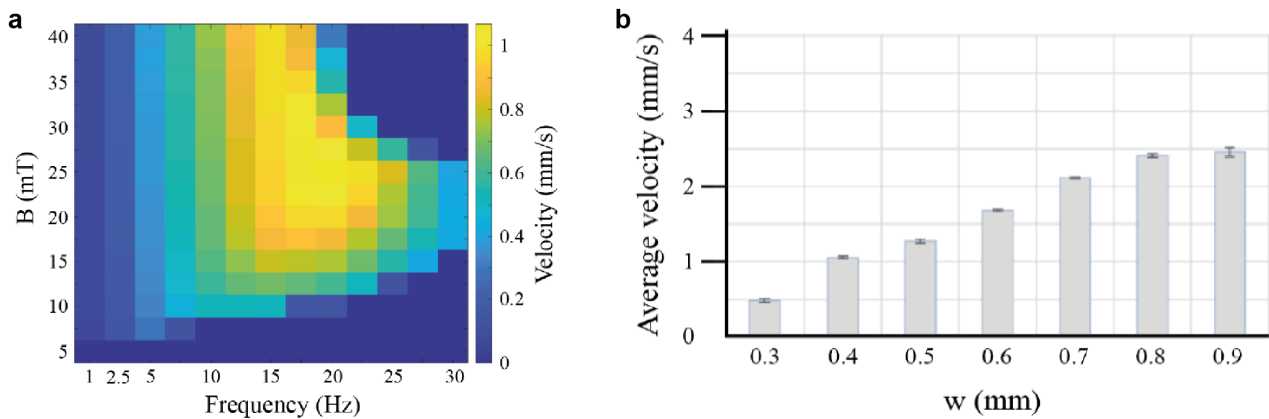
Figure 5.2 Velocity - *B/w* analysis. The effect of the magnetic field amplitude and the actuation frequency on the average velocity of the robot in a 300 µm-wide flat channel.

Blood vessels have nominally circular profiles; thus, tests performed inside rectangular channels may not be representative of cardiovascular interventions. Indeed, the device could not reliably move forward inside phantoms with a circular cross-sectional profile. Unlike rectangular channels, round channels do not restrain the device from rolling, and as a result, mechanical instabilities generated by torsion led to erratic twists (**Figure 5.3**a). Notably, the distal tip of the head twists around the roll axis, and this undesirable deformation propagates backward (**Figure 5.3**b and Movie S1, Supporting Information). As a result, the magnetic dipoles gradually drift away from the actuation plane, which generates torsion, and ultimately disrupts the overall motion. This observation is consistent with the results of a recent article wherein untethered magnetic devices were reported to display erratic motion inside circular channels[304]. This issue could be addressed by rotating the untethered devices like a screw or rolling them like a wheel. However, these modes of locomotion are not suitable for tethered devices as a continuous rotation of the head can cause twisting or wrapping of the tether and is mechanically limited by the construction.
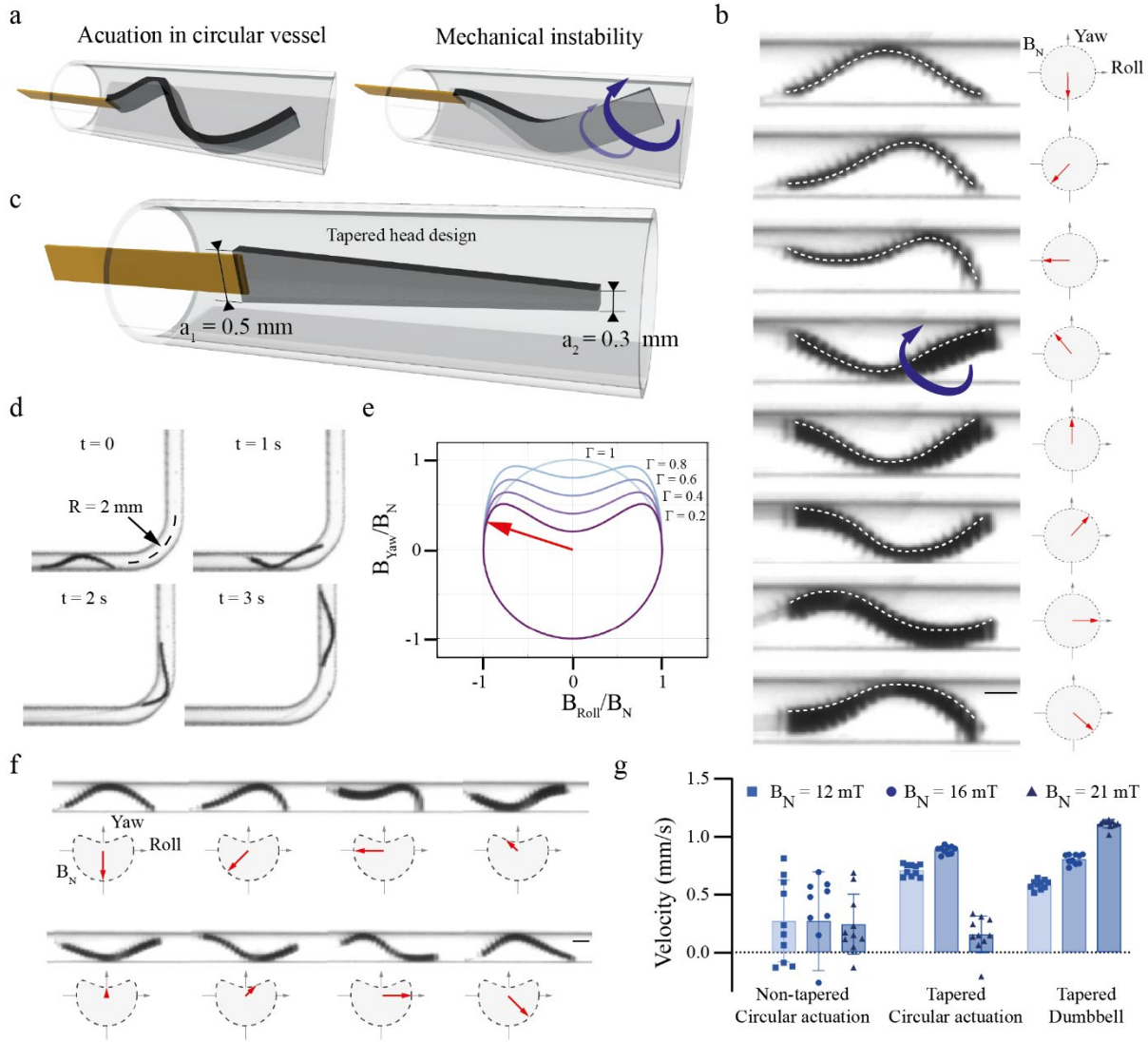
Figure 5.3 Robust crawling inside channels with a circular profile. (**a**) A mechanical instability is generated when the magnetic head twists, which is accompanied by the loss of contact with the channel wall. (**b**) Snapshots from the actuation of the rectangular magnetic head inside a circular channel. (**c**) Illustration showing a width-tapered magnetic head inside a circular channel. (**d**) Snapshots of the device crawling through a 1 mm-diameter channel with a 90°-turn. (**e**) Shape of the dumbbell magnetic control function at different Γ values. (**f**) Snapshots over an actuation cycle showing beneficiary effects of the tapered head design on the stabilization of the pose. The channel diameter is 1 mm. (**g**) Bar plot highlighting the synergistic effects of using a tapered magnetic head and the dumbbell waveform on the forward velocity of locomotion. Scale bars are 500 μm.

We propose two complementary upgrades to avoid mechanical instabilities during actuation and generate propulsive undulations over the course of navigation. First, we postulated that the twisting of the elastic head could be constrained at the distal tip by decreasing the torsional rigidity at this region. The angle of twist, θ, scales inversely with the torsional stiffness as follows.

$$\theta = \frac{TL}{GJ}$$

Equation 1

where G is the shear modulus of the material, J is the polar moment of inertia (the product GJ/L can be interpreted as the torsional stiffness), T is the applied torque, and L is the ribbon's length. For the rectangular geometry of the magnetic head, the torsional constant in **Equation 1** is given by:

$$J = a_R b_R^3 \left[\frac{1}{3} - 0.21 * \frac{b_R}{a_R} \left(1 - \frac{b_R^4}{12 a_R^4} \right) \right]$$

Equation 2

where a_R and b_R denote the width and the thickness of the ribbon, respectively[308]. We designed the head as a linearly decreasing taper that confines the twist at the tip, therefore, protecting the rest of the head from the out-of-axis deformation. This intuition can be supported by modal analysis. When calculating the first normal vibration mode of ribbons, tapering the ribbon shifts the nodal point toward the distal tip (Supplementary Note 1)[309]. It is also found that the relative torsion magnitude, at a given axial position, is decreased with increased taper angle.

To further clarify the role of the taper, we made a mesoscale demonstration where we rotated one end of magnetic elastomer structures by 180° while keeping the other end clamped (**Figure 5.4**a). While the half-torsion point was situated exactly in the middle between the two ends of the structure with a rectangular shape, repeating the same procedure with a tapered structure resulted in the appearance of the half-torsion point closer to the tapered end. Following this insight, we fabricated a magnetic head with an isosceles trapezoid shape, where the proximal base a_1 is larger than the distal base a_2. The taper index is defined as $= \frac{a_2 - a_1}{a_1}$, and we fixed this value at $\delta = -0.4$ (**Figure 5.3**c), which we found empirically to be an optimal trade-off between torsional-response and magnetic volume. Smaller δ values would improve stability but also decrease the magnetic volume at the tip. We found that tapering the width of the head substantially improved the mechanical stability of the structure, and as a result, facilitated progressive navigation. We tested the manoeuvrability of the devices in many different channels, with 90° turns at various radii R, and found that navigation is guaranteed for $0.5 < R < 5$ mm (**Figure 5.3**d). At radii smaller than 0.5 mm, the advancement often failed due to insufficient contact with the channel walls.

The diameter is expected to change in obstructed arteries. We tested whether the magnetic head could advance in a channel with a varying diameter. To this end, we fabricated an hourglass-shaped glass capillary using thermal pulling. The inner diameter of the channel decreases from 0.9 to 0.6 mm in the middle of the stenotic region (**Figure 5.4**b). Once actuated with as field of $B_N = 15$ mT and $f = 5$ Hz, the device managed to navigate the whole channel. The forward velocity decreased by 60% inside the stenotic area. A constant forward velocity could be maintained by adapting the actuation signal to the channel size. We have also studied the effect of fluid viscosity on the forward velocity, as the instrument would eventually be used inside blood vessels. We performed tests in a solution of 42% glycerol in water (w/w) to mimic the viscosity of blood[310,311]. The device moved with the same forward velocity as in water at different actuation frequencies (i.e., up to 20 Hz), revealing that interactions between the viscous fluid and the structure were negligible in this range.
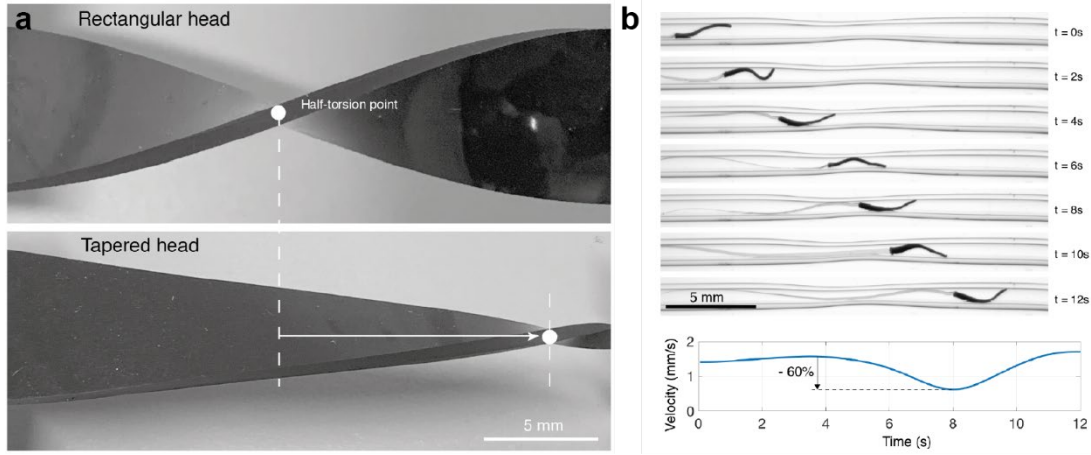
Figure 5.4 Tapered design and its crawling. (**a**) Macroscale demonstration of the beneficial effects of a taper design on the position of the half-torsion point. The structure is twisted 180 degrees from the right side while the left tapered side was clamped. δ = - 0.8. (**b**) Crawling inside structured channel. Top, a glass capillary with inner diameter 0.9 mm presents a stenosis with a 0.6 mm inner diameter. The microrobotic device is actuated at B = 15 mT and f = 5 Hz. Bottom, velocity variation across the stenosis.

So far, we tried to resolve the negative impact of the magnetic twist by modifying the structural design of the head. A complimentary solution lies in the control of the actuation signal. There exists a time period during each actuation cycle where the magnetic dipoles at the distal end of the head are aligned in the opposite direction of the actuation signal. We aimed to mitigate the torsion induced by this transient antiparallel alignment of the distal magnetic dipoles with respect to the rotating magnetic field. To this end, we modified the control signal in a way that lower torque was applied on the distal magnetic dipoles during this time period. The new magnetic waveform, which we call the dumbbell actuation signal, presents a cusp Γ that indents the previous circular trajectory along the yaw axis (**Figure 5.3**e). The dumbbell actuation signal is parameterized as follows.

$$B_{Roll}(t) = B_N \left(\frac{4t-T}{T}\right), B_{Yaw}(t) = B_N \left(\left(\frac{4t-T}{T}\right)^2 + \Gamma\right) \left|\sqrt{1-\left(\frac{4t-T}{T}\right)^2}\right| \text{ for } t = [0,\frac{T}{2}]$$

$$B_{Roll}(t) = B_N \cos\left(2\pi\frac{t-\frac{T}{2}}{T}\right), B_{Yaw}(t) = -B_N \sin\left(2\pi\frac{t-\frac{T}{2}}{T}\right) \text{ for } t = [\frac{T}{2}, T]$$

Equation 3

In **Equation 3**, $\Gamma \in [0,1]$. When Γ =0, the curve indents downwards and crosses the origin, leading to a zero-field stationary condition. When Γ =1 , the actuation signal is imposed circularly. Through trial and error, we recorded the best performance at Γ = 0.4. In the presence of the dumbbell control, the tip was less subjected to torsion, and the head appeared to be maintained at the correct pose during the whole actuation cycle (**Figure 5.3**f). A systematic characterization of the device motion at different f, Γ and B_N showed the synergistic effects of the two proposed upgrades (**Figure 5.3**g). Devices with the tapered head design reached forward velocities as high as 1.26 mm s^{-1} at B_N = 21 mT and f = 1 Hz under the dumbbell actuation signal ([Movie S2, Supporting Information](#)). The results were repeatable over several devices and trials (**Figure 5.5**a,b). The contribution of the dumbbell actuation paradigm was obvious at higher magnetic fields, where the head lost stability under a rotating magnetic field with a circular profile. Locomotion at higher magnetic fields is not only useful to reach higher speeds, but also instrumental to cope with scenarios that require larger thrust. For example, relatively high

friction forces arise from prolonged navigation in tortuous channels or moving against gravity (**Figure 5.5**c). A 30%-increase in the magnetic field amplitude resulted in a 20% increase in velocity (**Figure 5.5**d). Unless specified, the following experiments were performed adopting a tapered magnetic head and an actuating dumbbell waveform (δ = −0.4 and Γ = 0.4).
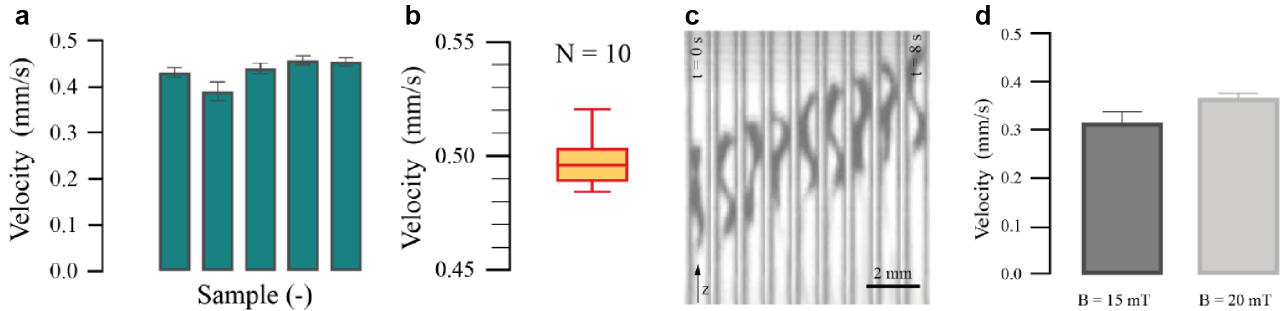
Figure 5.5 Reproducibility and influence of friction and magnetic field magnitude. Repeatability (**a**) and confidence (**b**) tests using a tapered design and the dumbbell magnetic control signal (B_N = 15 mT, f = 1 Hz, Γ = 0.4). Velocity was averaged over 10 trials. (**c**) Effect of gravity on the advancement velocity of a robot actuated at B_N = 15 mT, f = 1 Hz, Γ = 0.4. Snapshots of a robot moving vertically inside a 0.8 mm-diameter glass capillary. (**d**) Increasing the magnitude of the magnetic field increases the forward velocity.

So far, we have demonstrated that the magnetic head can be used as a remotely controlled propulsion system to transport an ultraflexible tether through round-sectioned channels with curvilinear shapes. Next, we asked whether we could steer the devices in the presence of bifurcating channels. Control on heading was implemented by generating an offset in the Centre of Rotation (C_{Rot}) on the actuation plane, i.e., C_{Rot} = (dB_{Roll}, dB_{Yaw}) (**Figure 5.6**a). As a result, the tip of the head maintains its stable undulatory motion while leaning toward the selected daughter vessel. As an important remark, the orientation of Γ must be actively maintained parallel to R at all times.
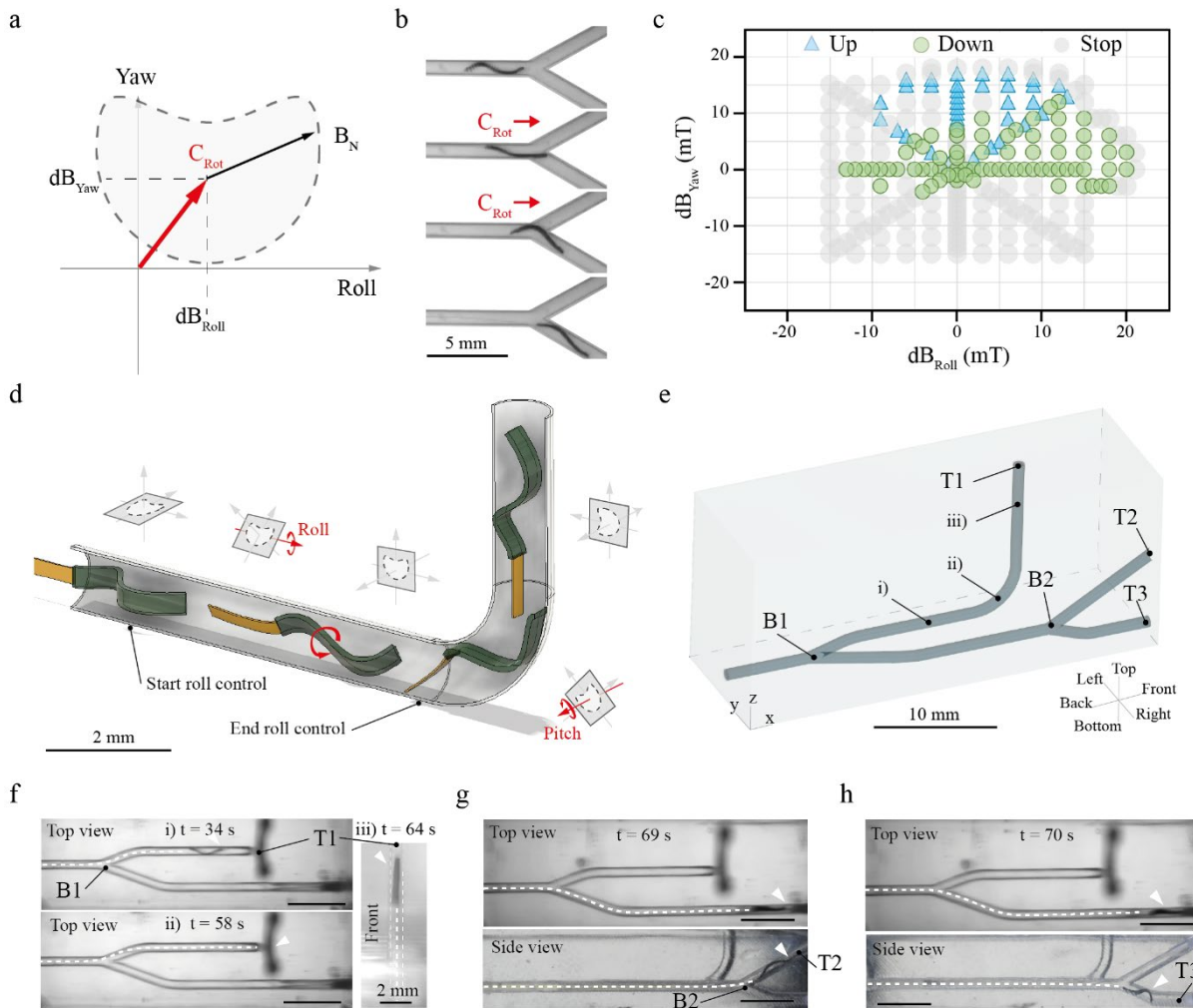
Figure 5.6 Open-loop control of automated 3D navigation. (**a**) An offset in C_{Rot} is used to steer the device at bifurcations. b) Snapshots showing the steering of the device into the lower channel by applying an offset in C_{Rot}. (**c**) A plot of C_{Rot} offset values leading to upward (blue triangles) and downward (green circles) motion. Gray circles correspond to impaired locomotion. The control parameters are B_N = 15 mT, Γ = 0.2, and f = 1 Hz. (**d**) Schematic representation of the 3D steering strategy where the head is rolled before a turn that involves moving upwards or downwards. (**e**) Schematic showing the 3D map of the phantom with two bifurcations, B1 and B2, and the three target points T1, T2, and T3. Snapshots from a successful automated navigation attempt that resulted in reaching all three target points are shown in (**f–h**). The control parameters are B_N = [10–20] mT, f = 1 Hz and Γ = 0.2. Scale bars are 5 mm.

We studied the effects of the dumbbell offset control on the efficacy of crawling in a biomimetic phantom (**Figure 5.6**b and Movie S3, Supporting Information). The bifurcation consisted of two symmetric daughter channels diverting at 30° from the incident mother channel. Favourable C_{Rot} values for upward and downward steering are summarized in **Figure 5.6**c. The region at which we could reliably control the heading was confined to the first quadrant, and equally populated by parameters that would guide the device to the top or the bottom channel. Notably, negative dB_{Yaw} values precluded passage through the bifurcation. This restriction was due to the modified shape of the dumbbell (Γ = 0.2, B_N = 15 mT, f = 1 Hz), which made the entire waveform fall in the lower quadrants, even at slightly negative dB_{Yaw} values. A closer look at the kinematics revealed that the full undulatory motion was lost because the head showed a strong forward motion followed by a weak backward motion, which severely compromised the advancement (Figure S8, Supporting Information).

The bending stiffness scales cubically with the thickness, and the thickness of our devices is 10 times smaller than their width. As a result of the 10^4-fold higher flexibility around the Pitch axis, bending around the Yaw axis is extremely unfavourable. Therefore, while navigating inside 3D curvilinear ves-

sels, roll correction must be implemented through the magnetic torque. The idea is to put the device in a configuration so that steering at a bifurcation would require bending around the favourable Pitch axis (**Figure 5.6**d). At the entry of each turn, the Yaw axis is parallel to R and the roll axis is tangential to the channel. Roll correction involves rotating the actuation plane around the roll axis. To be able to dynamically correct for orientation while the device is crawling, the correction must be imposed gradually and over several actuation cycles. Otherwise, the magnetic dipoles may reside outside the actuation plane, which would disrupt the undulatory motion. The device must be steered in both directions, therefore, the largest possible rotation for realignment is $\mp 90°$.

Empowered with a robust navigation strategy, we explored the possibility of automating the procedure using an open-loop controller. We fabricated a phantom that contained two bifurcations in the x–y and x–z planes, with channels pointing in all three cartesian axes **Figure 5.6**e). We used the 3D geometry of the phantom to plan a trajectory. The actuation frequency and the field amplitude were maintained the same, and the controller determined when to change the waveform of the magnetic signal for steering the device based on prior velocity measurements. First, the device was guided across bifurcation B1 using control parameters chosen from the plot shown in **Figure 5.6**c. After the S-shape turn, the Yaw axis, which had been lying in the x-y plane (**Figure 5.6**f(i)), was gradually rotated upwards (+90° degree roll) to prepare for the vertical turn leading to target T1. During the navigation across the full length of the turn, the Yaw axis was concomitantly rotated +90° around the Pitch axis and maintained parallel to R all along (**Figure 5.6**f(ii)). These two manoeuvres are illustrated in **Figure 5.6**d. During ascension in the vertical channel, f and B_N were increased to counteract the gravity and friction forces generated from the contact between the tether and the channel walls (**Figure 5.6**f(iii)). After pulling back the device to the starting point, it was steered to the right daughter channel at B1. To perform the vertical bifurcation B2, the head was gradually rolled to align the yaw axis to the z-axis. Navigation across B2 into the upper (**Figure 5.6**g) and the lower (**Figure 5.6**h) channels were completed using the parameter values from **Figure 5.6**c.

We have previously shown that ultraflexible sensor-integrated soft robotic devices could be transported by the fluid flow[127]. We modified the experimental platform to incorporate the equipment required to implement flow-driven advancement including a peristaltic pump, a Windkessel unit, and flow sensors (**Figure 5.7**a). As a first step, we verified that multimode locomotion was feasible by navigating the devices inside a microfluidic phantom with nonuniform flow conditions (**Figure 5.7**b). The navigation started with flow-driven advancement in the main channel, and the phantom contained three bifurcations along the trajectory. The main channel diverged into two daughter channels, both with physiological perfusion rate (blue channels). The device was guided to either daughter channel using static uniform magnetic fields (**Figure 5.7**c and [Movie S4, Supporting Information](#)), as described elsewhere[127]. The daughter channel with physiological flow split into two other channels where the fluid in the upper channel was completely blocked (red channels). Entry into the obstructed channel was performed by directing the head into that channel and subsequently activating the rotating uniform magnetic field. Further advancement inside the obstructed channel was accomplished with the dumbbell control, and navigation through the last bifurcation was performed by generating an offset in C_{Rot}.
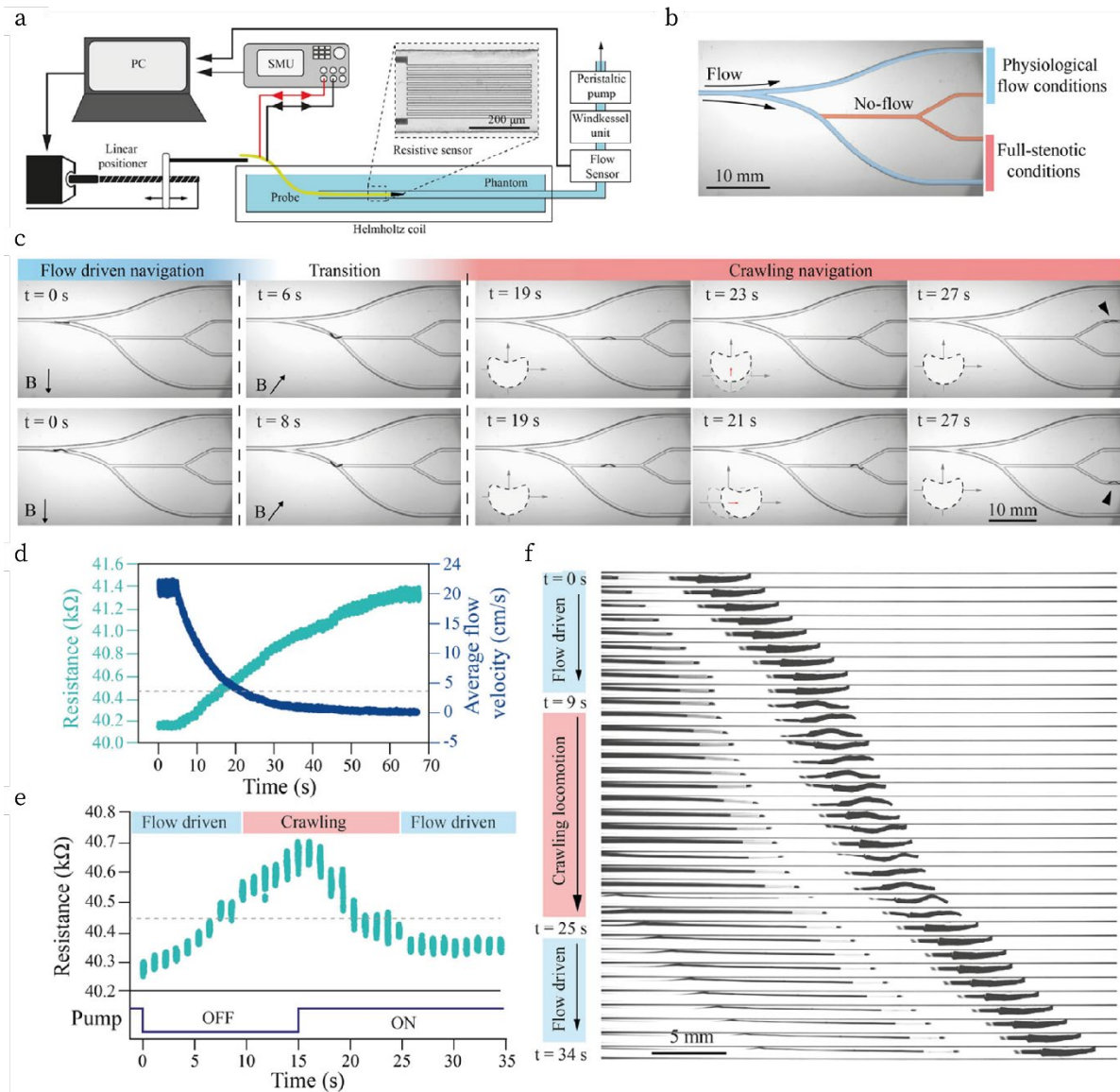
Figure 5.7 Closed-loop feedback control for multimodal locomotion. (**a**) Experimental setup for operating the onboard sensor and setting the flow conditions inside the microfluidic channel. Inset shows a picture of the electronic sensor micro-engineered on the tether of the device. (**b**) An image of the phantom used for demonstrating multimodal locomotion. Channels that are painted blue have physiological flow conditions, while channels that are painted red are fully obstructed, i.e., flow velocity is zero. (**c**) Static magnetic fields are used for steering during flow-driven navigation in perfusing channels and to position the head inside the obstructed channels. Application of the rotating magnetic field instantiates crawling locomotion which realizes motion and steering in the absence of flow. (**d**) Calibration of a hot-wire resistive senor with respect to the average flow velocity. Gray dashed line indicates the threshold for switching locomotion modes. (**e**) Resistance measured by the onboard sensor informs the controller about the flow conditions, and this information is used by the controller to autonomously switch between crawling and flow-driven locomotion. (**f**) Snapshot from an experiment where the transition from flow-driven to crawling and back to flow-driven advancement is coordinated autonomously by the robot.

Next, we investigated whether the control system could automatically switch between flow-driven advancement and crawling, depending on the flow conditions. To this end, we engineered devices with an onboard flow sensor. The flow sensor was designed in a hot wire configuration to record the change in electrical resistance upon changes in the flow conditions (**Figure 5.7**d). That is to say, a reduction in the flow rate translated into a self-heating phenomenon, increasing the resistance of the circuit. To avoid overheating, the sensor was operated in a pulsed mode at 1 Hz actuation frequency (50% duty cycle) and an acquisition rate of 1 kHz. The device was inserted in a straight circular-profile channel, and the flow rate was modulated in such a way that the device was challenged to autonomously decide when to switch between flow-driven mode and crawling mode (**Figure 5.7**e). The light red area illustrates the temporal window in which the device activated crawling locomotion as a

response to the removal of flow assistance, i.e., the average flow velocity was reduced below $4\,\text{cm}\,\text{s}^{-1}$. The sequential images in **Figure 5.7**f show an initial advancement under physiological flow followed by the autonomous activation of the crawling locomotion ($t = 9\,\text{s}$). Upon reestablishment of the favourable hydrodynamic conditions ($t = 25\,\text{s}$), the sensor informed the controller to switch back to the flow-driven advancement mode. To guarantee that the oscillating field does not interfere with the sensor, we compared the measurements at different actuation frequencies (**Figure 5.8**a) and found no statistical difference ($p < 0.05$) between the groups.
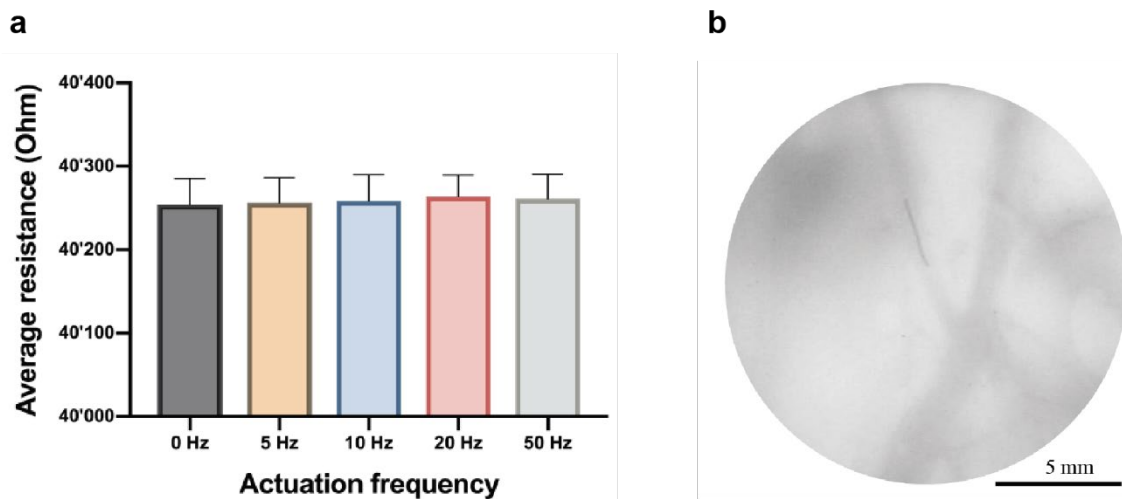
Figure 5.8 Electromagnetic interference and X-ray visibility. (**a**) The average resistance was recorded without the magnetic head and in the presence of an oscillating spatially homogeneous magnetic field ($B = 20$ mT) at different frequencies. No statistical difference was found between the groups (t-test, two-tailed, $p < 0.05$). (**b**) X-ray image of the robot inside a 0.8 mm coronary of an ex vivo swine heart.

The in-vitro tests were done using a nested Helmholtz electromagnetic control system. However, this system was not compatible with the fluoroscope due to size constraints. To address this issue, we developed a simpler magnetic control system that consisted of a motorized rotating shaft holding a permanent magnet (**Figure 5.9**a). We first tested whether this system was capable of driving undulatory motion by actuating a magnetic head inside a glass capillary. We placed the control magnet behind the magnetic head to test whether the motion was generated due to body deformation or magnetic field gradients, and verified that the head moved away from the magnet with undulations (Movie S5, Supporting Information). Next, we confirmed that the arteries inside the ex vivo porcine heart as well as the head of our device could be visualized using the fluoroscope (**Figure 5.8**b). Application of a rotating magnetic field initiated crawling motion inside a 1 mm diameter coronary artery (**Figure 5.9**b).
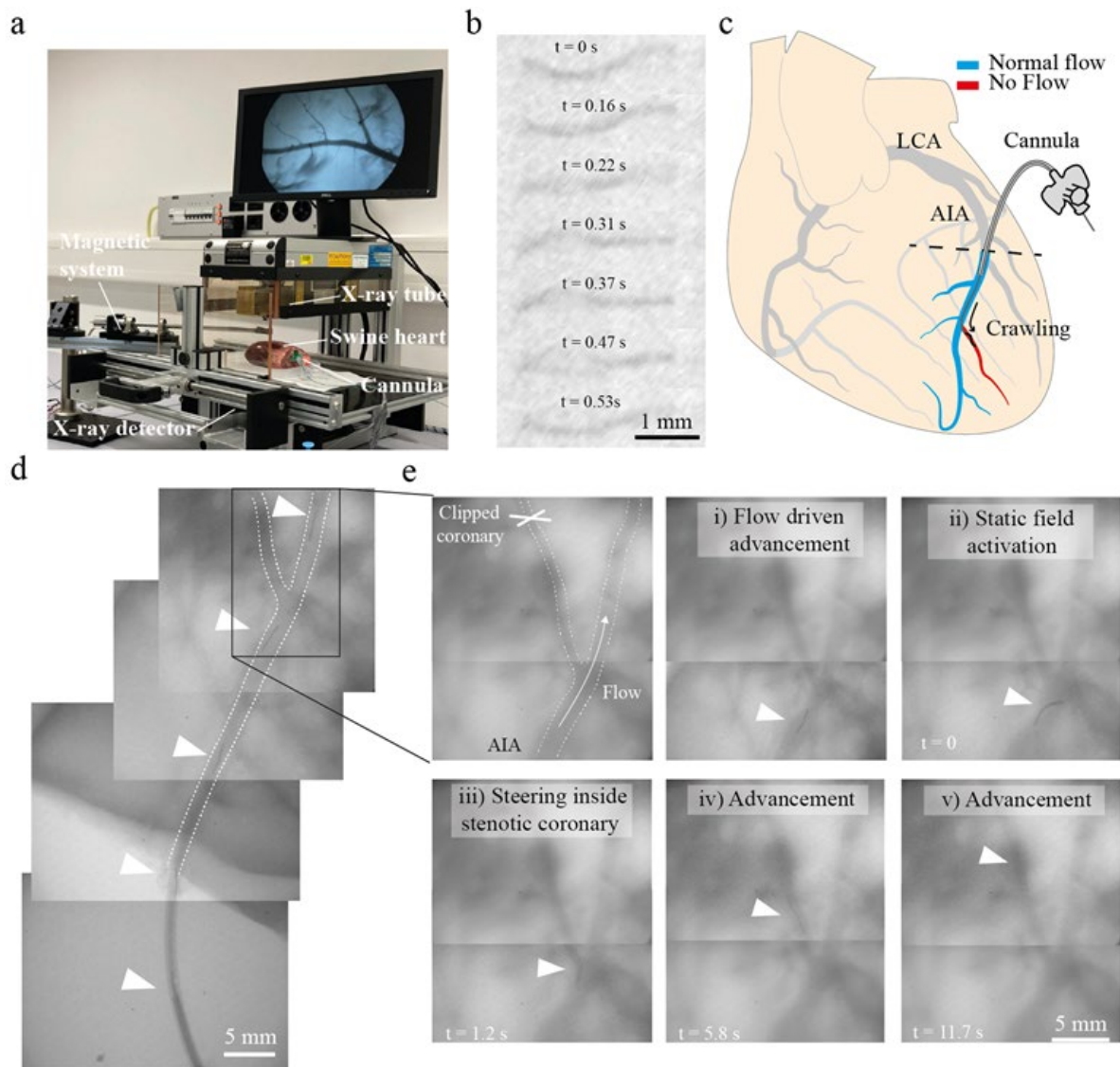
Figure 5.9 Fluoroscopy assisted multimodal navigation inside ex vivo porcine coronaries. (**a**) High-definition fluoroscope imaging system and the magnetic control system that consists of a rotating permanent magnet. (**b**) X-ray images of a device crawling inside a coronary. (**c**) Schematic representation of the porcine heart highlighting the arteries and the flow conditions. (**d**) Flow-driven injection of the device into the coronary artery through a medical cannula. (**e**) X-ray image showing the diverging coronary that was clipped to induce full obstruction. Application of the rotating magnetic field instantiated entry and navigation inside this obstructed coronary.

We aimed to repeat the in vitro multimodal locomotion paradigm inside the coronary tree of porcine ex vivo coronaries with the impaired flow (red coronary, **Figure 5.9**c). The experiment started with the perfusion of the anterior interventricular artery (AIA) branch of the left coronary artery (LCA) using a flexible cannula (Figure S11, Supporting Information). A high-concentration contrast agent was injected and maintained inside the arterial walls for at least 2 h to label all the arteries. After ejection from the cannula, the device was kept under fluidic tension and inserted inside the AIA at a perfusion rate of 0.05 mL s^{-1}. Flow-driven navigation failed in steering the device inside the obstructed artery because the distal portion was clipped with haemostat forceps, which recapitulated the hypoperfusion conditions presented by obstructed vessels (**Figure 5.9**d). We activated the control magnet to actuate the head, and the resulting undulatory motion induced by the rotating field allowed the head to crawl inside the obstructed branch (**Figure 5.9**e). To verify again that the locomotion was indeed caused by undulatory motion and was not simply due to magnetic pull, we sequentially stopped the rotation of the magnet, which repeatedly resulted in a complete cessation of motion (Figure S12, Supporting In-

[formation](#)). Reactivation of the rotating magnetic field re-established crawling motion until reaching the distal portion of the artery.

5.3   Conclusions

Taken together, these results highlight the importance of the geometry and mechanics of the device, and the waveform of the magnetic actuation signal for locomotion in structured environments. There is no formal methodology for the design of the presented prototypes. We explored two major strategies, changing the shape of the magnetic head and applying a rotating magnetic field, primarily through intuition and trial and error. The time-varying large deflection of ferromagnetic soft continuum robots can be computed using analytical solutions and finite element modeling[312–314]. Physical interactions with the vessel wall and fluid–structure interactions may be considered in these models, as demonstrated for the modelling of soft robotic systems actuated by artificial muscles[315]. A full simulation of robot motion would reveal design and actuation parameters for optimizing the locomotion performance for any given vessel anatomy and flow conditions.

Harnessing hydrokinetic energy and contact forces open up the possibility to navigate ultraflexible robotic devices inside extreme microvasculature. Our results showed that the control performance highly depends on when and how these external factors are considered in the kinematics of the problem. In the clinical setting, the interventionalist would need to discriminate between normally perfusing and hypoperfusing vessels to choose the proper advancement mode. However, it would be challenging to measure the flow rate from fluoroscope images during operation or to make pre-operative predictions; therefore, integrating flow sensors is instrumental to implementing a multimode advancement scheme. Using onboard sensory information to assist endovascular interventions is an unconventional strategy. The complete reliance on the capabilities of the surgeon is currently necessary partly due to the lack of instrumentation. The majority of the existing catheters and guidewires are mechanical instruments that do not carry electronic components. We microfabricated devices using manufacturing processes compatible with the engineering of flow sensors to enable real-time data acquisition. Carrying onboard flow and pressure sensors has paramount importance to perform a complete assessment of the physiological state of the cardiovascular system[316]. Fast and accurate measurement of the pressure and absolute flow within the coronary arteries, for example, is instrumental for the cardiologist to decide whether a stent must be deployed in a stenotic area. In this regard, our soft robotic devices can serve a unique function, probing the peripheral cerebrovascular arteries for the diagnosis of vascular conditions.

As a step forward, we described materials and methods that empower the robotic devices with the capability to autonomously switch between flow-driven and crawling-based motion. Solving the navigation problem for microfabricated electromechanical devices advances the robotics research field from teleoperated interventions to machine intelligence. With the incorporation of other electronics such as pressure and chemical sensors, the device could be programmed to reach regions with pathologic conditions without external supervision.

5.4   Materials and methods

5.4.1   Experimental setup

The electromagnetic system was designed following the instructions reported elsewhere[274]. Briefly, a 3-axis nested Helmholtz coil generated the homogeneous magnetic fields within a space of

$22 \times 53 \times 94$ mm^3. The three pairs of coils measured 114, 198, and 299 mm and were capable of generating a magnetic field of 85, 60, and 50 mT. The current was supplied and modulated by three sets of power supplies (S8VK 480 W, Omron, and SM 52-AR-60, Delta Elektronika) and servo controllers (Syren25 and Syren50, Dimension Engineering). An analog/digital I/O PCi Express board (Model 826 Sensoray) interfaced with the software (programmed in MATLAB, Mathworks) and the hardware. The pulsatile flow was generated by a peristaltic pump (LP-BT100-2J, Drifton). Movies were recorded using a complementary metal oxide semiconductor (CMOS) camera (acA4024-29uc, Basler). The microfluidic phantoms were fabricated by Protolabs (France) from ABS material according to CAD drawings. Alternatively, microvasculature phantoms can be fabricated using a 3D printer (Ultimaker) by sacrificial negative molding in silicone with water-soluble polyvinyl-alcohol extrusion materials[127,317]. The electrical measurements were performed using a source meter (B2902A, Keysight).

5.4.2   Fabrication of the magnetic head

The magnetic structures were fabricated by blade casting a mixture of silicon polymer (EcoFlex 00-10) and neodymium iron boron (NdFeB) microparticles (5 µm, Magnequench, Germany) at a 1:1 mass ratio[304]. The slurry was filled into a well formed with 200 µm-thick spacers and cured overnight at room temperature. The structures were cut with a flat razor blade and wrapped around a glass capillary (1 mm-diameter) such that the two ends would connect, completing a full circle. The structures were then magnetized using an impulse magnetizer (Magnet-Physik). The structures were then glued to the polyimide tether using an instant glue (Loctite 401).

5.4.3   Fabrication of the flow sensor

The details of the fabrication process for the sensor-integrated tether were reported elsewhere[127] (See also Errore. L'origine riferimento non è stata trovata.). Briefly, devices have been prepared by spin-coating on a 4-inch Si wafer a 4 µm thick layer of PI (PI2610 Hitachi Chemical DuPont MicroSystems GmbH). A positive photoresist (AZ1512, 2 µm exposed by Heidelberg Instruments MLA150, 405 nm, and 104 mJ cm^{-2} and developed by AZ 726 MIF) has been used as a mask for sputtering (Alliance Concept AC450) a 100 nm-thick layer of gold in stripes of 250 µm width and 9 cm length, followed by lift-off in acetone. The borders have been then laser cut (Optec MM200-USP) and detachment from the wafer has been done manually. The fabrication of the flow sensors involves the sputtering of titanium and platinum layers serving for adhesion and electrical conduction, respectively. To add the two serpentines, designated as temperature sensor and heater, another 25 nm thick layer of platinum has been sputtered over the wafer, after surface activation by argon plasma (Alliance Concept AC450). The shapes of the traces and serpentines were defined using spin-coating and removal of positive photoresists (AZ9260, 8 µm, and AZ1512, 2 µm). The electrical circuits were sandwiched between PI layers.

5.4.4   Ex vivo experiments

Swine hearts were obtained from a local farm (LaFerme Aebischer, 1595 Faoug, Switzerland). The AIA was perfused using a flexible cannula (18 G Vasofix, B. Braun) and an intravenous (IV) bag. X-ray imaging was performed using a benchtop fluoroscope (Labscope, Glenbrook technologies) and a radiopaque contrast agent (Iopamiro 370, Bracco, Switzerland). After mapping the coronary tree, the diverging artery was clipped with hemostat forceps to recapitulate vessel obstruction. The magnetic system was composed of a 1 cm^3 NdFeB magnet assembled at the tip of a rotating shaft. The shaft was rotated by a DC motor (EC-i30, Maxon motor) and controlled by a servo driver (ESCON 36/3 EC, Maxon motor).

5.5 Acknowledgements

Chapter 6   Conclusion
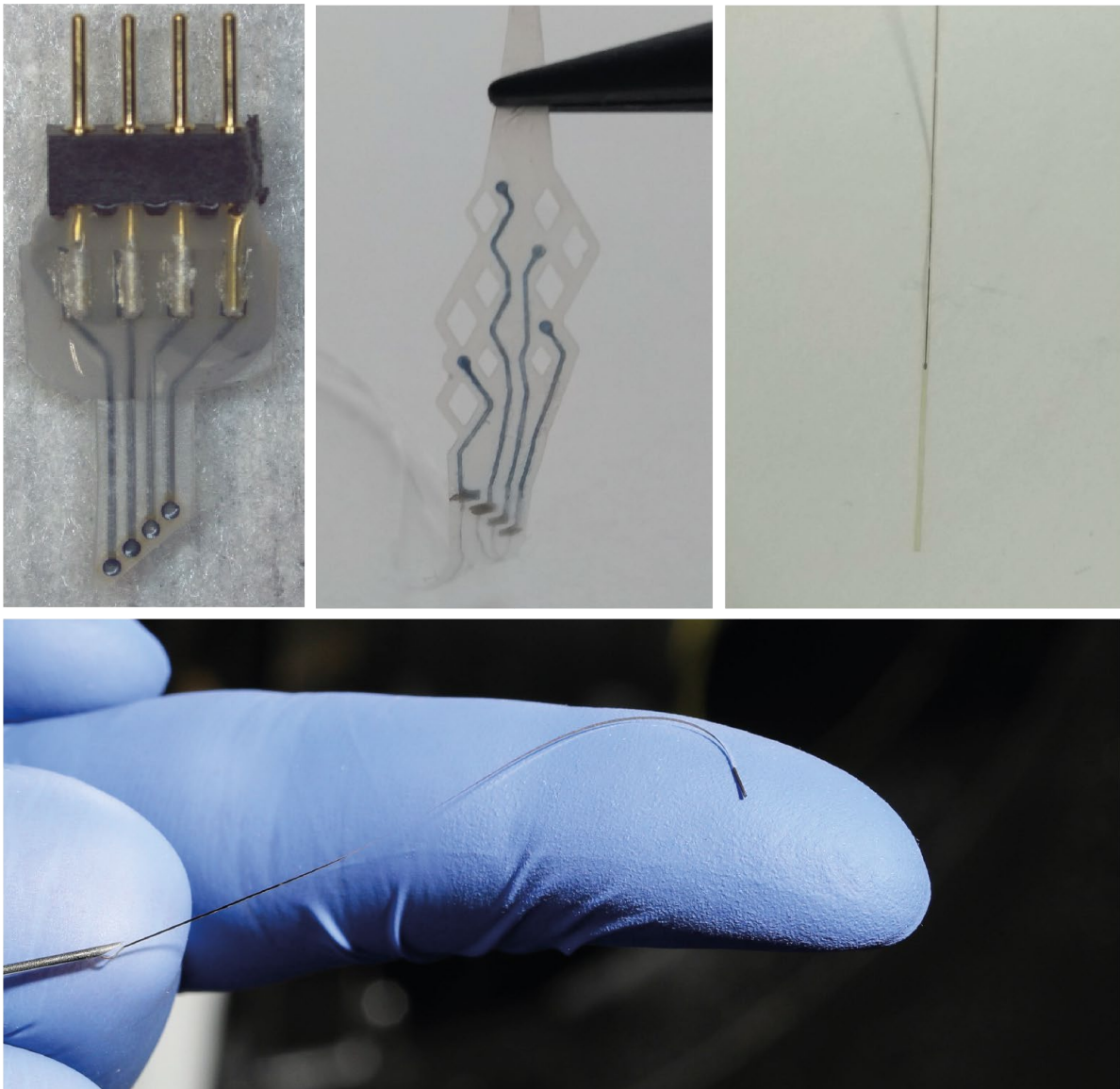
6.1   Achieved results

The development of novel neural interfaces that meet a trade-off between invasiveness, risks and benefits for the patients is crucial for the development of effective neurotechnologies. This thesis represents a new step towards this direction. By combining an endovascular approach with transient materials, a novel paradigm is introduced in the field of minimally invasive interfaces.

To achieve this goal, first the materials constituting the device were selected and tested. As a biodegradable scaffold, PCL has been chosen to ensure a slow degradation rate of the device, promoting physiological tissue remodelling and eliminating the need for removal surgeries and risks of chronic foreign body reactions. The electrodes have been fabricated in the conductive polymer PEDOT:PSS:EG, without any metal component, creating an all-polymeric device. Degradable metals that would have made the device entirely biodegradable cannot withstand the operational lifetime offered by PCL and thus would have restricted the number of possible applications. Choosing a non-degradable metal, such as Pt or Au, would have been difficult to implement given the poor compatibility of PCL with microfabrication techniques needed for such metals, and would have probably offered poorer electrochemical properties compared to those obtained with PEDOT:PSS:EG only. A fabrication procedure has been tailored to obtain the all-polymeric neural probe and, after its electrochemical characterization, its potential in neural recording has been successfully tested in acute and chronic experiments in mice. Results showed low noise values (< 10 µV) and ability to record VEPs until 12 weeks after implantation, although the number of functional electrodes strongly decreased over time. Degradation of the PCL scaffold allowed for a less tight fibrotic scar and decreased astrocytes activation compared to a non-degradable implant of a similar size. In addition, device colonization by neurons and astrocytes was found in studies at 9 months after implantation. A specific interaction between microglia and PEDOT:PSS:EG was also noticed and might be worth further investigations to understand the in vivo fate of the conductive polymer.

These promising results led to the decision to further minimize the device biological footprint by reshaping it to allow an endovascular implantation, far enough not to damage the tissue of interest, and close enough to still collect relevant signals or stimulate neural activity, depending on the application. This meant thinning the device and increasing the electrode stability with the addition of GOPS to the PEDOT:PSS:EG mixture. Moreover, the overall shape was designed to fit inside a 5Fr catheter and to be delivered in a vessel of 2 mm diameter. This could allow future in vivo testing in the superior sagittal sinus of miniature pigs. The new electrodes have been electrochemically characterized in both standard PBS and blood showing low impedance and high CSC in both conditions. To understand how these properties might be impacted by the flow of the blood, the device was inserted in a 2 mm diameter channel and exposed to pulsed PBS for up to 2 months: impedance increased but remained below 100 kΩ and the average CSC changed only slightly. Investigating the potential use of the device for neurostimulation, prolonged current pulsing has been carried out and electrodes didn't show damage after 4 million pulses. A delivery system has also been proposed using a 5Fr catheter able to deploy the device in a 2 mm diameter channel. Adhesion to the tube walls was also evaluated through micro-CT and the resulting gaps and lumen size were within safety limits.

One of the biggest limitations of the endovascular approach for neural interfaces is the vasculature complexity, difficult or impossible to overcome with current catheter technologies. For this, an alternative (non-degradable) device designed for a novel navigation system has been developed. The µ-probe has a thickness of 4 µm and width of 200 µm. Sandwiched between two layers of PI, the device hosts oval electrodes for neural recording or stimulation, or serpentines for temperature and flow monitor-

ing. Given its dimensions and materials, this device can autonomously navigate blood vessels just by the dragging forces of physiological pulsatile flow, even through knot-like curvatures. By attaching a cylindrical magnetic head of 40 – 350 μm diameter at its tip, it is possible to control the direction of the probe navigation by applying small magnetic fields (5 - 30 mT). With the smallest magnetic heads, it is possible to navigate vessels as small as 300 μm in diameter. In bigger channels it is possible to deliver multiple probes at the same time, allowing for example the mapping of measurable properties (i.e., neural activity, temperature, flow velocity) in a specific area. Using the same navigation systems, PDMS microtubes of 150 μm diameter can be delivered in the arteries of explanted rabbit ears and solutions can be injected through them. Fluoroscopic monitoring can also be done thanks to the radiopacity of the magnetic heads.

To overcome the problem of impaired navigation in the absence of flow, such as in obstructed arteries related to embolism, thrombosis, or traumatic injury, an alternative navigation mode has been proposed. A thrust can be induced in a tapered magnetic head of μ-probes to propel the movement of the ultra-flexible tethers inside channels of radius between 0.5 and 5 mm, even in fluids with physiological viscosity and in vertically aligned channels. Thanks to the electronics microfabricated on the device, it was possible to monitor the velocity of the flow in the channel and switch between the crawling navigation and the flow-driven mode depending on the need. Finally, a proof-of-concept test demonstrated this navigation approach inside porcine ex vivo coronaries.

Overall, the obtained results are promising for the development of minimally invasive and endovascular neural interfaces and devices. However, further optimization is inevitably needed to address the limitations highlighted in the next section and move forward to preclinical studies.

6.2 Current limitations

Developing truly minimally invasive devices with effective performance and minimal risks for the patients is indeed a challenging task. Multiple limitations can be found in the results of this thesis, leaving room for future modifications.

Although the in vivo studies of **Chapter 2** highlighted a promising tissue integration at 9 months, longer time points are necessary to have a clearer picture of the degradation profile of the device. In particular, specific attention must be paid to the fate of the conductive polymer in vivo as only few studies did chronic experiments with various PEDOT-based coatings and no detailed analysis has been done regarding its possible biodistribution, execration or degradation. For example, it might be interesting to investigate the role of reactive oxygen species generated during inflammation caused by the penetration of the tissue by a foreign body. As mentioned in sections **2.2.2** and **3.3**, PEDOT is susceptible to H_2O_2 at very high concentrations: local conditions during inflammation might reach values higher than physiological status which could affect its stability.

In vivo studies also didn't determine the actual durability of the PCL scaffold. Bench-side aging tests can give only an estimation for now. Although the quality of the signals obtained after 12 weeks from implantation was good, the percentage of viable electrodes at the end was below 20%. In an attempt to solve this problem, stabilizing GOPS has been added in the endovascular design of the device in **Chapter 3** and preliminary tests of EIS and CV under pulsatile PBS flow revealed a potential success of this strategy. However, validation and durability studies in vivo are completely missing for this probe. This is mainly due to the complexity of the set-up and the limitations still present in the delivery system.

More devices need to be tested before and after delivery to ensure the survival of the electrodes and connections after the navigation and deployment. In addition, the attachment of the device to the guidewire used as a shaft is presently achieved using super-glue, negating the possibility to retrieve the shaft after deployment.

A constrain shared by both devices is the manual deposition of the PEDOT-based conductive polymers, which could affect reproducibility and lead to user-dependent results. Moreover, both of them require wires for powering and data communication. This could potentially compromise the stability and safety of the devices. The contact between the PEDOT-based pads and the wires is achieved through small amounts of silver paste with low adhesion strength that could cause unreliable measurements in case of movements, especially for the percutaneous wiring of the penetrating probe. Wires inside the vessels, together with the delivery shaft, could instead be prone to fracture, leakage and be home for infections or induce thrombus.

By using an endovascular approach, despite the notable extension of the vascular network, there are limitations in the number of reachable targets, in both terms of presence of vessels and of complex vasculature obstacles. Compared to minimally invasive tissue penetrating devices, the distance between the neurons and the electrodes inside the blood vessel can affect the selectivity: it would be challenging to distinguish neuronal populations or single neurons from endovascular recordings or stimulate only certain fibres within a proximal nerve. However, for applications where a high selectivity is not needed, endovascular devices still represent a competing alternative.

Finally, in vivo studies are also missing for the μ-probes and μ-catheters described in **Chapter 4** and **Chapter 5**, for reasons similar to those of the transient endovascular device. In this case though, a higher complexity is represented by the need of magnetic coils in the operating room and the possible noise caused to and by the other machines present there.

Moreover, this system is only applicable to the arterial system and doesn't work in vessels with diameters bigger than 2 mm. There are still challenges related to the microfabrication of the probes: the obtainable length of the stripe is limited at the wafer diameter; hollow catheters with thin rectangular cross-sections in Kapton haven't been successfully fabricated yet. Finally, tensile rupture as failure mode of the device still needs to be tested.

6.3 Suggested future developments and outlook

The devices presented in this thesis are proof-of-concepts for minimally invasive neural interfaces and endovascular devices that, although promising, need further optimization to reach a complete validation.

Understanding the degradation or clearance pathway of PEDOT and PEDOT-based films, such as the electrodes and traces of these devices, is of primary importance for an eventual clinical translation. For this both in vitro cell culture and in vivo chronic tests should be done. For the former, a proper cell line must be chosen: reactions induced by PEDOT to microglia or macrophages, cells dedicated to the clearance of foreign bodies, could provide relevant information in this sense. In vivo testing should also consider an animal model that can ensure time points for longer than a year, given that noticeable preliminary results were only obtained after 9 months. The challenge in both these tests is labelling the PEDOT to clearly monitor it under fluoresce microscopy and for quantitative analysis. The pristine PEDOT molecule lacks available functional groups for fluorescent tags. To solve this problem, it could be possible to polymerize EDOT derivatives containing attachment sites such as the commercially

available EDOT-MeOH (hydroxymethyl EDOT) and then proceed to functionalization through EDC-NHS chemistry[318]. Moreover, in the projects reported here, PEDOT has always been used together with PSS and ethylene glycol: the latter induces rearrangements in the polymer structure improving the stacking of the PEDOT and the dispersion of the PSS, enhancing the overall conductivity[148]. Potential effect of this dopant to the degradation of the polymer should be investigated. In the case of potential toxicity issues (even with the small amount used to make the device, i.e. $\simeq 8$ μl), other configurations with smaller segments of the PEDOT backbone interrupted by hydrolysable or enzymatically cleavable molecules could be investigated, at the price however of the conductivity.

Not only the fate of PEDOT should be investigated, but also the actual degradation time of the PCL scaffold must be determined. This must be long enough to allow safe tissue remodelling but possibly not too different from the electrodes lifetime if a longer therapy is required for which a subsequent device is needed in the same location. Given the slow degradation rate of PCL, in vivo animal model should be maintainable for at least 1 year. Also in this case, the PCL would need to be fluorescent to be detected over time, for example by addition of dye moieties inside its chain[319].

Especially regarding the endovascular device, it is important to verify that the device integrates in the endothelium of the vessel and that its degradation in such a dynamic environment doesn't cause thrombogenic debris. It would be interesting to design a specific lab testing environment to achieve this, simultaneously reducing the overall number of animals needed for the device validation and improving the control of the failure modes.

Always within the context of safety of an endovascular device, it is important to test the hemocompatibility of the constituting materials and fabrication methods in terms of platelets aggregation and activation, similar to what has been done in section **4.2.9**. By exposing the device to platelet-rich plasma, aggregation of platelets could be detected by absorbance changes at 595 nm (yellow-orange band). Release of adenosine triphosphate by the platelets is then monitored by luminescent reaction with luciferin and luciferase molecules. In addition, SEM images could clarify possible cellular attachment to the device.

To enhance the bio-acceptability of the transient devices, anti-inflammatory and anti-coagulant drugs could be embedded directly inside the PCL scaffold and slowly be released during degradation. Taking inspiration from drug-eluting stents (DES), even anti-proliferative drugs could be used, such as pactitaxel or serolimus, to reduce risks of in-stent stenosis.

Regarding the fabrication, a possible strategy to replace the manual deposition of the PEDOT-solution could be to exploit 3D printing systems for its automatic patterning and injection into the engraved traces and electrodes. Alternatively, although more material would be wasted, a detachable mask (like a polyethylene terephthalate or polyimide thin foil) could be temporarily attached to a flat PCL substrate and the PEDOT solution could be spin-coated or laminated over it. After a semi-curing step, the mask could be removed and curing of the remaining pattern could be completed. This could potentially help in standardizing the process and improve the achievable minimum size for traces and electrodes as well.

A future design of the endovascular neural interface would have a wireless system for power and data transmission. Biodegradable wireless neurostimulators exploiting inductive coupling for example have already been developed, as seen in section **1.2.1**. The challenge here would consist in miniaturizing it, so that it can fit inside the blood vessel and do not affect the blood flow, maintaining as well good performances at blood vasculature depths. In addition, it would be interesting as well to investi-

gate the possibility of integrating different types of sensors on the device, such as pressure or flow sensors, without being limited to only measuring or inducing neural activity.

An improvement to the delivery system could replace the super-glue used so far to attach the device to the delivery shaft, with biocompatible and biodegradable adhesives. This would provide only a temporary attachment and consequent possibility to retrieve the shaft, leaving only the device in place.

Furthermore, radiopaque markers should be added to monitor the advancement of the device in the vessels during the fluoroscopically guided implantation procedure. This could be done for example with degradable tungsten microparticles embedded in the PCL scaffold (provided the safety of the quantity needed to make the device visible).

Finally, on the road to clinical translation, an effective, non-damaging sterilization method must be chosen. One example could be ethylene oxide sterilization, which is already used for PCL and other degradable polyesters, although it's known that toxic residues might be generated during the process[320].

6.4 Applications

Together with the magnetically driven probes, the transient devices proposed in this thesis represent new tools in the physician toolbox for new ways to diagnose and treat patients.

With the microengineered, magnetically navigated, endovascular probes it is possible to reach microvasculature never explored before. For instance, it could be possible to do neural recording/stimulation, temperature and flow control in deep locations such as the brain stem, retinal arteries and basal ganglia, without opening the skull.

The transient neural probe of **Chapter 2**, in a penetrating configuration or placed superficially over the brain, can be exploited in combination with its endovascular version for mapping epileptic foci or tumours before resection surgery. Using compliant materials inducing only a mild immune response could guarantee good quality and reliable signals for an extended period of time compared to current practice (2-3 weeks[321,322]), before device degradation. In this way a more comprehensive map could be drawn both in terms of seizure frequency (useful in case of neuromodulation therapies) and in terms of validation of the specific location. The latter is especially important for patients with seizures occurring with low frequency (< 1 / week), for whom seizure induction is normally considered. However, the actual utility of neural monitoring for longer time hasn't been scientifically proven yet, as the chance of infection development and technical complications could increase with current technologies[321]. Thanks to the degradability of the electrode scaffold, after the monitoring is concluded or technical problems occur, the surgery for device removal is not needed anymore, reducing the overall risks of the procedure.

The concept of a transient, yet durable, neural interface can also be applied to preliminarily test neurostimulation therapies, such as Deep Brain Stimulation therapies. Making a device that is operational for longer than 3 months, could allow for a patient to familiarize with a neurostimulation device, understand if the therapy could be successful (e.g., reduced pharmacological need in the case of neurostimulation for depression, increased patient autonomy in the case of brain stimulation for essential tremor) or if the device needs to be repositioned. The endovascular probe can also be adapted to be deployed in deep brain vessels in close contact to areas such as nucleus accumbens and the ventral capsule, normally stimulated for treating treatment resistant depression, obsessive-compulsive disor-

ders, addiction, obesity and anorexia mentosa[123]. After the trial period is concluded, then the physician and the patient could decide whether to continue with the therapy or not, and the device safely degrades without need for removal. This would make the physician and the patients more confident in trying innovative therapies. At the same time, the transiency of the device can induce a reduced foreign body reaction, compared to non-degradable materials, reducing the overall risks of the device and increasing the number of targetable patients.

Besides brain vasculature, the transient endovascular neural interface could be applied for neural recording or neurostimulation of the peripheral nervous system. For instance, it could be used in preliminary trials of neurostimulators for pain relief. Examples of vessels that could be targeted are the ulnar and radial arteries (diameter $\simeq$ 2 mm) for upper limbs[323–325]; axillary (diameter $\simeq$ 6 mm[326]) and circumflex humeral arteries (diameter $\simeq$ 3 mm, posterior[327,328], diameter $\simeq$ 2 mm, anterior[328]) for the shoulders; femoral, internal/external iliac and inferior gluteal arteries (diameter $\simeq$ 1 cm[329], $\simeq$ 1 cm[329] and $\simeq$ 2 mm[330,331], respectively) and their branches for lower limbs. The device lasting for longer than 3 months, it could be possible to assess if the relief is achieved, and it can be quantified in terms of less need of drugs and overall pain reduction overtime. If then patient and physician are satisfied by the treatment, a permanent implant might be considered or again the transient device to keep the possibility to stop the therapy without needing to remove the implant.

The endovascular neurostimulator could also be used for temporary support of motor rehabilitation of stroke and paralysis patients, although muscular selectivity might be challenging.

Together with the transiency of the device and its therapy, the simple implantation procedure, that does not require any craniotomy, stereotactic guides or deep cuts to reach the nerves, could make the physician and patient more confident in applying such technology. This would not only widen the patients' access to innovative treatments, but also increase the information about the nervous system and the efficacy of neurotechnology-based therapies. Despite the long way to go and the plenty of optimizations necessary, this might represent a good moment to start discussing with clinicians and patients and consider their opinions in the future developments of the devices. These alternative and minimally invasive devices can hopefully one day be a useful tool in bringing neural engineering researchers closer to clinicians and accelerate clinical translation of efficient devices addressing neurodegenerative disorders.

Acknowledgements

First of all, I'd like to thank my supervisor, professor Diego Ghezzi, who led me through these 4 years of PhD, tried to teach me to be synthetic and not to address too many things at the same time, and shared both the excitements and the frustrations of research.

I'm grateful to the members of the jury committee for taking the time to read and evaluate my thesis and my presentation: professor Róisín Owens, professor Silvestro Micera, professor Rylie Green and professor Carlotta Guiducci.

I would like to thank also the great collaborators I had the chance to work with: Olivier Brina, Dr. Philippe Reymond and Dr. Paolo Machi, who dedicated their time to help me with their expertise in the validation of the delivery system of my device; professor Rosa Chiara Paolicelli and Katia Monsorno, who applied their knowledge of the microglia to help us better analyze our results and for the countless experiments exploring unanswered questions on PEDOT; professor Selman Sakar and Lucio Pancaldi, PhD, who warmly welcomed me in their robotic project and shared the love and struggles of the endovascular approach. Working with you really enriched my experience and highlighted once again the need of synergistic collaborations in research.

I want to thank all the students that joined me in the PhD journey, and especially little Ele, for being the very first! And never giving up on challenges; Samuel, for your determination in making our ideas a reality; Filippo, for enduring the hardest difficulties with exceptional outcome; Yasmine, for mastering the platelets, your impressive courage and ability to manage multiple exams, projects, life and job interviews at the same time; Daniela & Stefania, for your energy and for sharing with me the last efforts.

My deepest gratitude to Michael and the "cleanroom guys", supporting "LNE girls" and working with us every step of the way: Jeremy, for the support with our automatic dispensing system; Valerian for bringing some smiley light-heartedness in the CR and endure the challenges of the serpentines fabrication with me; Anthony, for all the above and beyond, for all the calls and messages (to threaten the machines that do not work and instantly work when you reply..), for all the sweat, early-morning chats and late-evening motivation for the gym. I couldn't have done it without you.

It's true that during a PhD it's just you and your project, staring at each other in a race to the last one to laugh, but at CB you're lucky enough to have very friendly neighbours. I want to sincerely thank Rob-erto from the Fondation Campus Biotech, for his familiar affection and his extraordinary ability to say something precious every time he speaks, for his contagious passion for philosophy, art and linguistics and for reminding to poke the science bubble from time to time. I want to thank the LSBI people for never making you feel truly alone, at any time of the day and night, and sharing common phases of the PhD: to Outman, for your endless passion, creativity and energy that will definitely lead you to accom-plish great things; to Vale, for your generosity, kindness, availability, determination and extraordinary swimming ability; to the Neurosoft team, for being the living inspiration making neurotech researchers believe that one day their ideas might find a clinical application.

Going every day to the lab wouldn't have been the same without knowing the amazing people you get to work with at LNE: Laura, you taught me how to beautifully paint with PEDOT and set the key seeds of my project, I couldn't ask for a better teacher and dog-lover; Charles, an energy bomb with a mind-blowing CV, thank you for the very initial brainstorms on polymers rolling and delivery techniques; Vivien, the official artist of LNE and master of Moscow mules and Neuron; Naig, thanks for sustaining our social gathering efforts, for sharing your cultural passions with us from time to time and for being a reference example of a very successful PhD; Paola, thank you for "all the fish" (including *octopuses*), showing us what becoming a bouldering pro looks like and for being part of the crazy Turin adventure; Marta, thanks for your genuine passion for science and for disclosing the secret life of giant rabbits at lunch breaks; Elodie, you're the official Wonder Mum of LNE, always busy taking care of everything and pushing to do more to follow your passion, and being the coolest parent at the same time; Fred, thank you so much for all the respiration exercises, mediation clues, massages and for overall trying to lift our shoulders off of stress; Golenaz, thanks for demonstrating what truly means "attention to detail" and all the good cakes; Gian Luca, master of students, for your precious and passionate knowledge of electronic circuits; Franklin, for the company in the office, showing how to be a computer-tech pro and making nanowires dance; Jake, for the affection, letting me watch the stars with the VR and the English proof reading; Sandrine, your joy and enthusiasm are contagious. Even though you only briefly passed through LNE, I'm grateful I had the chance to meet you, laugh with you and learn from you: Giulia, Enrico, Marina, Luca.

I'm so happy I could share the last 2 years with Dani, wonderful office mate: thanks for your patience with my accent and my out-of-the-blue vocabulary questions, for following me in my sport activities and for showing me others, for the support and push when I needed them. I'm glad I got to be your punchball.

Outside the lab, I was lucky enough to meet and enjoy quality time at the beach, at home, restaurants, swimming pool, movies, rivers, tennis courts and so on, with a wonderful international family of friends: Sammy, Soumya, Zuzza, Luca, Nicolas, Roberto, Tommaso, Ricardo and Cipo. You were always there for support, making the day brighter and constant reminder that there's more to life than the PhD.

I want to sincerely thank the people of Innovation Forum and Innovation Forum Lausanne. Their activities were one of the greatest parts of my PhD and one of those I enjoyed the most. Thank you to all the members for all the efforts and successes we accomplished: Bea, Cate, Claudia, Andrea, Michele, Alvaro, Davide, Daniel, Alessia, Francesco, Nicolò, Luca, Paris, Aleks, Armand, Gloria, Giammarco, Iwan, Hugo, Gianmarco, Alessandro, Anna & Sophia.

An essential part of this journey was Ele. There are not good enough words in any vocabulary to describe what we shared during these years. You were there every step of the way, you were my left arm, the gaze and thought that don't need words to be understood, you supported me, pushed me, stopped me; we drank, worked, led, shopped, sang, laughed, cried, trained, danced, ran and climbed together. I cannot have hoped for a better partner in crime.

Finally, I would like to thank my family. First my parents, without whose unlimited support and love I would have never made it this far, not even thought about it. Thank you for your patience with me. Thanks to Chiara, for teaching me how to ride chaos and always strive for more. Thanks to Stella for always being there. Last and foremost, the love of my life, my comfort zone, my shelter, my fuel, my cane, my reason why, my fan n°1, my favourite singer, my spoil, my turbo, my peace, my Amo, my Gian.

References

1. Shim, J.-S., Rogers, J. A. & Kang, S.-K. Physically transient electronic materials and devices. *Materials Science and Engineering: R: Reports* **145**, 100624 (2021).

2. Li, W. *et al.* Biodegradable Materials and Green Processing for Green Electronics. *Adv. Mater.* **32**, 2001591 (2020).

3. World Economic Forum. *A new circular vision for electronics.* (2019).

4. Lee, G., Choi, Y. S., Yoon, H.-J. & Rogers, J. A. Advances in Physicochemically Stimuli-Responsive Materials for On-Demand Transient Electronic Systems. *Matter* **3**, 1031–1052 (2020).

5. Peng, X., Dong, K., Wu, Z., Wang, J. & Wang, Z. L. A review on emerging biodegradable polymers for environmentally benign transient electronic skins. *J Mater Sci* **56**, 16765–16789 (2021).

6. Hwang, S.-W. *et al.* A Physically Transient Form of Silicon Electronics, With Integrated Sensors, Actuators and Power Supply. *Science* **337**, 1640–1644 (2012).

7. Lee, M. H. *et al.* A Biodegradable Secondary Battery and its Biodegradation Mechanism for Eco-Friendly Energy-Storage Systems. *Adv. Mater.* 2004902 (2021) doi:10.1002/adma.202004902.

8. Su, Z. *et al.* Robust, high-barrier, and fully recyclable cellulose-based plastic replacement enabled by a dynamic imine polymer. *J. Mater. Chem. A* **8**, 14082–14090 (2020).

9. Han, W. B., Lee, J. H., Shin, J. & Hwang, S. Advanced Materials and Systems for Biodegradable, Transient Electronics. *Adv. Mater.* **32**, 2002211 (2020).

10. Li, C. *et al.* Design of biodegradable, implantable devices towards clinical translation. *Nat Rev Mater* **5**, 61–81 (2020).

11. Li, R., Wang, L. & Yin, L. Materials and Devices for Biodegradable and Soft Biomedical Electronics. *Materials* **11**, 2108 (2018).

12.   Lu, D. *et al.* Bioresorbable, Wireless, Passive Sensors as Temporary Implants for Monitoring Regional Body Temperature. *Adv. Healthcare Mater.* **9**, 2000942 (2020).

13.   Yang, Q. *et al.* Materials, Mechanics Designs, and Bioresorbable Multisensor Platforms for Pressure Monitoring in the Intracranial Space. *Adv. Funct. Mater.* **30**, 1910718 (2020).

14.   Won, S. M. *et al.* Natural Wax for Transient Electronics. *Adv. Funct. Mater.* **28**, 1801819 (2018).

15.   Lee, J. *et al.* Flexible, sticky, and biodegradable wireless device for drug delivery to brain tumors. *Nat Commun* **10**, 5205 (2019).

16.   Nguyen, T. D. & Curry, E. J. Biodegradable Piezoelectric Sensor. 4.

17.   Guo, Q. *et al.* A Bioresorbable Magnetically Coupled System for Low-Frequency Wireless Power Transfer. *Adv. Funct. Mater.* **29**, 1905451 (2019).

18.   Koo, J. *et al.* Wireless bioresorbable electronic system enables sustained nonpharmacological neuroregenerative therapy. *Nat Med* **24**, 1830–1836 (2018).

19.   Yu, K. J. *et al.* Bioresorbable silicon electronics for transient spatiotemporal mapping of electrical activity from the cerebral cortex. *Nature Mater* **15**, 782–791 (2016).

20.   Bai, W. *et al.* Bioresorbable photonic devices for the spectroscopic characterization of physiological status and neural activity. *Nat Biomed Eng* **3**, 644–654 (2019).

21.   Peng, X. *et al.* A breathable, biodegradable, antibacterial, and self-powered electronic skin based on all-nanofiber triboelectric nanogenerators. *Sci. Adv.* **6**, eaba9624 (2020).

22.   Li, H. *et al.* Fully Bioabsorbable Capacitor as an Energy Storage Unit for Implantable Medical Electronics. *Adv. Sci.* **6**, 1801625 (2019).

23.   Sheng, H. *et al.* A thin, deformable, high-performance supercapacitor implant that can be biodegraded and bioabsorbed within an animal body. *Sci. Adv.* **7**, eabe3097 (2021).

24.   Lee, H. *et al.* Facile fabrication of a fully biodegradable and stretchable serpentine-shaped wire supercapacitor. *Chemical Engineering Journal* **366**, 62–71 (2019).

25.   Xu, K. *et al.* Bioresorbable Electrode Array for Electrophysiological and Pressure Signal Recording in the Brain. *Adv. Healthcare Mater.* **8**, 1801649 (2019).

26. Li, R. *et al.* A flexible and physically transient electrochemical sensor for real-time wireless nitric oxide monitoring. *Nat Commun* **11**, 3207 (2020).

27. Boutry, C. M. *et al.* Biodegradable and flexible arterial-pulse sensor for the wireless monitoring of blood flow. *Nat Biomed Eng* **3**, 47–57 (2019).

28. Fu, R. *et al.* Implantable and Biodegradable Poly(l-lactic acid) Fibers for Optical Neural Interfaces. 8 (2018).

29. Tran, H. *et al.* Stretchable and Fully Degradable Semiconductors for Transient Electronics. *ACS Central Science* 8 (2019).

30. Ferlauto, L. *et al.* All-polymeric transient neural probe for prolonged in-vivo electrophysiological recordings. *Biomaterials* **274**, 120889 (2021).

31. Park, J. *et al.* Wireless pressure sensor integrated with a 3D printed polymer stent for smart health monitoring. *Sensors and Actuators B: Chemical* **280**, 201–209 (2019).

32. She, D., Tsang, M. & Allen, M. Biodegradable batteries with immobilized electrolyte for transient MEMS. *Biomed Microdevices* **21**, 17 (2019).

33. Fanelli, A. *et al.* Transient Neurovascular Interface for Minimally Invasive Neural Recording and Stimulation. *Adv. Mater. Technol.* 2100176 (2021) doi:10.1002/admt.202100176.

34. Teodorescu, M., Bercea, M. & Morariu, S. Biomaterials of PVA and PVP in medical and pharmaceutical applications: Perspectives and challenges. *Biotechnology Advances* **37**, 109–131 (2019).

35. Woodruff, M. A. & Hutmacher, D. W. The return of a forgotten polymer—Polycaprolactone in the 21st century. *Progress in Polymer Science* **35**, 1217–1256 (2010).

36. Choi, Y. S. *et al.* Biodegradable Polyanhydrides as Encapsulation Layers for Transient Electronics. *Adv. Funct. Mater.* **30**, 2000941 (2020).

37. Choi, Y. S. *et al.* Stretchable, dynamic covalent polymers for soft, long-lived bioresorbable electronic stimulators designed to facilitate neuromuscular regeneration. *Nat Commun* **11**, 5990 (2020).

38. Kang, S.-K. *et al.* Bioresorbable silicon electronic sensors for the brain. *Nature* **530**, 71–76 (2016).

39.   Su, Y. *et al.* Zinc-Based Biomaterials for Regeneration and Therapy. *Trends in Biotechnology* **37**, 428–441 (2019).

40.   Shin, J. *et al.* Bioresorbable pressure sensors protected with thermally grown silicon dioxide for the monitoring of chronic diseases and healing processes. *Nat Biomed Eng* **3**, 37–46 (2019).

41.   Namgung, S. D. *et al.* Tyrosine-Rich Peptide Insulator for Rapidly Dissolving Transient Electronics. *Adv. Mater. Technol.* 2000516 (2020) doi:10.1002/admt.202000516.

42.   da Silva, A. C. & Córdoba de Torresi, S. I. Advances in Conducting, Biodegradable and Biocompatible Copolymers for Biomedical Applications. *Front. Mater.* **6**, 98 (2019).

43.   Implants that vanish. *Nat Biomed Eng* **3**, 585–585 (2019).

44.   Anderson, J. M., Rodriguez, A. & Chang, D. T. Foreign body reaction to biomaterials. *Seminars in Immunology* **20**, 86–100 (2008).

45.   Bernstein, J. E., Kashyap, S., Ray, K. & Ananda, A. Infections in Deep Brain Stimulator Surgery. *Cureus* (2019) doi:10.7759/cureus.5440.

46.   Conen, A. *et al.* Management of neurosurgical implant-associated infections. *Swiss Med Wkly* (2020) doi:10.4414/smw.2020.20208.

47.   Provenzano, D. A., Falowski, S. M., Xia, Y. & Doth, A. H. Spinal Cord Stimulation Infection Rate and Incremental Annual Expenditures: Results From a United States Payer Database. *Neuromodulation: Technology at the Neural Interface* **22**, 302–310 (2019).

48.   Abode-Iyamah, K. O. *et al.* Deep brain stimulation hardware–related infections: 10-year experience at a single institution. *Journal of Neurosurgery* **130**, 629–638 (2019).

49.   Frizon, L. A. *et al.* Outcomes following deep brain stimulation lead revision or reimplantation for Parkinson's disease. *Journal of Neurosurgery* **130**, 1841–1846 (2019).

50.   Israeli-Korn, S. D. *et al.* Decreasing battery life in subthalamic deep brain stimulation for Parkinson's disease with repeated replacements: Just a matter of energy delivered? *Brain Stimulation* **12**, 845–850 (2019).

51.   De Santis, M. & Cacciotti, I. Wireless implantable and biodegradable sensors for postsurgery monitoring: current status and future perspectives. *Nanotechnology* **31**, 252001 (2020).

52. Lu, D. *et al.* Bioresorbable Wireless Sensors as Temporary Implants for In Vivo Measurements of Pressure. *Adv. Funct. Mater.* **30**, 2003754 (2020).

53. Selvarajan, S., Kim, A. & Song, S. H. Biodegradable Piezoelectric Transducer for Powering Transient Implants. *IEEE Access* **8**, 68219–68225 (2020).

54. Huang, X. *et al.* A Fully Biodegradable Battery for Self-Powered Transient Implants. *Small* **14**, 1800994 (2018).

55. Wang, L. *et al.* A fully biodegradable and self-electrified device for neuroregenerative medicine. *Sci. Adv.* **6**, eabc6686 (2020).

56. Le Roux, P. Chapter 15 Intracranial Pressure Monitoring and Management. *Translational Research in Traumatic Brain Injury* 20 (2016).

57. Anyanwu, C. & Motamedi, G. Diagnosis and Surgical Treatment of Drug-Resistant Epilepsy. *Brain Sciences* **8**, 49 (2018).

58. Yin, L. *et al.* Materials, Designs, and Operational Characteristics for Fully Biodegradable Primary Batteries. *Adv. Mater.* **26**, 3879–3884 (2014).

59. Li, J., Long, Y., Yang, F. & Wang, X. Degradable piezoelectric biomaterials for wearable and implantable bioelectronics. *Current Opinion in Solid State and Materials Science* **24**, 100806 (2020).

60. Jiang, W. *et al.* Fully Bioabsorbable Natural-Materials-Based Triboelectric Nanogenerators. *Adv. Mater.* **30**, 1801895 (2018).

61. Curry, E. J. *et al.* Biodegradable nanofiber-based piezoelectric transducer. *Proc Natl Acad Sci USA* **117**, 214–220 (2020).

62. Chao, S., Ouyang, H., Jiang, D., Fan, Y. & Li, Z. Triboelectric nanogenerator based on degradable materials. *EcoMat* **3**, (2021).

63. Vachicouras, N. *et al.* Microstructured thin-film electrode technology enables proof of concept of scalable, soft auditory brainstem implants. *Sci. Transl. Med.* **11**, eaax9487 (2019).

64. Ferlauto, L. *et al.* Design and validation of a foldable and photovoltaic wide-field epiretinal prosthesis. *Nat Commun* **9**, 992 (2018).

65. Schiavone, G. & Lacour, S. P. Conformable bioelectronic interfaces: Mapping the road ahead. *Sci. Transl. Med.* **11**, eaaw5858 (2019).

66. Yang, X. *et al.* Bioinspired neuron-like electronics. *Nat. Mater.* **18**, 510–517 (2019).

67. Kim, D., Yang, S.-H., Sung, J., Lee, S. & Son, B. Significance of Intracranial Pressure Monitoring after Early Decompressive Craniectomy in Patients with Severe Traumatic Brain Injury. *J Korean Neurosurg Soc* **55**, 26 (2014).

68. Jinnouchi, H. *et al.* Fully bioresorbable vascular scaffolds: lessons learned and future directions. *Nat Rev Cardiol* **16**, 286–304 (2019).

69. Castel-Lacanal, E. Sites of electrical stimulation used in neurology. *Annals of Physical and Rehabilitation Medicine* **58**, 201–207 (2015).

70. Javeed, S., Faraji, A. H., Dy, C., Ray, W. Z. & MacEwan, M. R. Application of electrical stimulation for peripheral nerve regeneration: Stimulation parameters and future horizons. *Interdisciplinary Neurosurgery* **24**, 101117 (2021).

71. Gilmore, C. A. *et al.* Percutaneous 60-day peripheral nerve stimulation implant provides sustained relief of chronic pain following amputation: 12-month follow-up of a randomized, double-blind, placebo-controlled trial. *Reg Anesth Pain Med* **45**, 44–51 (2020).

72. Teo, C. The Concept of Minimally Invasive Neurosurgery. *Neurosurgery Clinics of North America* **21**, 583–584 (2010).

73. Larson, P. S. Minimally Invasive Surgery for Movement Disorders. *Neurosurgery Clinics of North America* **21**, 691–698 (2010).

74. Pei, F. & Tian, B. Nanoelectronics for Minimally Invasive Cellular Recordings. *Advanced Functional Materials* **30**, 1906210 (2020).

75. Veronica, A., Li, Y. & Hsing, I. Minimally Invasive & Long-lasting Neural Probes from a Materials Perspective. *Electroanalysis* **31**, 586–602 (2019).

76. Hong, J.-W., Yoon, C., Jo, K., Won, J. H. & Park, S. Recent advances in recording and modulation technologies for next-generation neural interfaces. *iScience* **24**, 103550 (2021).

77. Zhao, Z. *et al.* Parallel, minimally-invasive implantation of ultra-flexible neural electrode arrays. *J. Neural Eng.* **16**, 035001 (2019).

78. Luan, L. *et al.* Ultraflexible nanoelectronic probes form reliable, glial scar–free neural integration. *Sci. Adv.* **3**, e1601966 (2017).

79. Xie, C. *et al.* Three-dimensional macroporous nanoelectronic networks as minimally invasive brain probes. *Nature Mater* **14**, 1286–1292 (2015).

80. Guan, S. *et al.* Elastocapillary self-assembled neurotassels for stable neural activity recordings. *Science Advances* **5**, eaav2842.

81. Gao, L. *et al.* Free-Standing Nanofilm Electrode Arrays for Long-Term Stable Neural Interfacings. *Advanced Materials* **34**, 2107343 (2022).

82. Vitale, F. *et al.* Fluidic Microactuation of Flexible Electrodes for Neural Recording. *Nano Lett.* **18**, 326–335 (2018).

83. Liu, J. Syringe-injectable electronics. *NATURE NANOTECHNOLOGY* **10**, 9 (2015).

84. Fu, T.-M. *et al.* Stable long-term chronic brain mapping at the single-neuron level. *Nat Methods* **13**, 875–882 (2016).

85. Ho, E. *et al.* The Layer 7 Cortical Interface: A Scalable and Minimally Invasive Brain–Computer Interface Platform. *bioRxiv* 2022.01.02.474656 (2022) doi:10.1101/2022.01.02.474656.

86. Viveros, R. D. *et al.* Advanced One- and Two-Dimensional Mesh Designs for Injectable Electronics. *Nano Lett.* **19**, 4180–4187 (2019).

87. Benfenati, F. & Lanzani, G. Clinical translation of nanoparticles for neural stimulation. *Nat Rev Mater* **6**, 1–4 (2021).

88. Paladino, J., Mrak, G., Miklić, P., Jednacak, H. & Mihaljević, D. The Keyhole Concept in Aneurysm Surgery - A Comparative Study: Keyhole versus Standard Craniotomy. *Minim Invasive Neurosurg* **48**, 251–258 (2005).

89. Fortuny, E. *et al.* Minimally Invasive Endoscopy Versus Craniotomy for Acute Subdural Hematomas: A Retrospective Matched Cohort Study. *Neurosurgery* **66**, nyz310_842 (2019).

90.   Reisch, R. & Perneczky, A. Ten-year Experience with the Supraorbital Subfrontal Approach through an Eyebrow Skin Incision. *Operative Neurosurgery* **57**, ONS-242-ONS-255 (2005).

91.   Hariz, M. I. Complications of deep brain stimulation surgery. *Mov Disord.* **17**, S162–S166 (2002).

92.   Lan, Q. *et al.* International expert consensus statement about methods and indications for key-hole microneurosurgery from International Society on Minimally Invasive Neurosurgery. *Neurosurg Rev* **44**, 1–17 (2021).

93.   Oxley, T. J. *et al.* Minimally invasive endovascular stent-electrode array for high-fidelity, chronic recordings of cortical neural activity. *Nat Biotechnol* **34**, 320–327 (2016).

94.   Leuthardt, E. C., Moran, D. W. & Mullen, T. R. Defining Surgical Terminology and Risk for Brain Computer Interface Technologies. *Front. Neurosci.* **15**, 599549 (2021).

95.   Krauss, J. K. *et al.* Technology of deep brain stimulation: current status and future directions. *Nat Rev Neurol* **17**, 75–87 (2021).

96.   Doshi, P. K., Rai, N. & Das, D. Surgical and Hardware Complications of Deep Brain Stimulation—A Single Surgeon Experience of 519 Cases Over 20 Years. *Neuromodulation: Technology at the Neural Interface* S1094715922000071 (2022) doi:10.1111/ner.13360.

97.   Rajah, G., Saber, H., Singh, R. & Rangel-Castilla, L. Endovascular delivery of leads and stentrodes and their applications to deep brain stimulation and neuromodulation: a review. *Neurosurgical Focus* **45**, E19 (2018).

98.   Birnie, D. H. *et al.* Risk Factors for Infections Involving Cardiac Implanted Electronic Devices. *Journal of the American College of Cardiology* **74**, 2845–2854 (2019).

99.   Tarakji, K. G. *et al.* Antibacterial Envelope to Prevent Cardiac Implantable Device Infection. *N Engl J Med* **380**, 1895–1905 (2019).

100.   Dai, M. *et al.* Trends of Cardiovascular Implantable Electronic Device Infection in 3 Decades. *JACC: Clinical Electrophysiology* **5**, 1071–1080 (2019).

101.   Reddy K.V., C., Sanzgiri, P., Thanki, F. & Suratkal, V. Coronary stent infection: Interesting cases with varied presentation. *Journal of Cardiology Cases* **19**, 5–8 (2019).

102.   Medtronic. What is balloon angioplasty and stenting? https://www.medtronic.com/us-en/patients/treatments-therapies/heart-surgery-cad/balloon-angioplasty-stenting-what-is-it.html.

103.   Raza, S. A. *et al.* Endovascular Neuromodulation: Safety Profile and Future Directions. *Front. Neurol.* **11**, 351 (2020).

104.   Morice, M.-C., Hayashi, E. B. & Guagliumi, G. A Randomized Comparison of a Sirolimus-Eluting Stent with a Standard Stent for Coronary Revascularization. *The New England Journal of Medicine* 8 (2002).

105.   Stone, G. W., O'Shaughnessy, C. & Greenberg, J. A Polymer-Based, Paclitaxel-Eluting Stent in Patients with Coronary Artery Disease. *The New England Journal of Medicine* 11 (2004).

106.   Moses, J. W., Holmes, D. R. & Williams, D. O. Sirolimus-Eluting Stents versus Standard Stents in Patients with Stenosis in a Native Coronary Artery. *The New England Journal of Medicine* 9 (2003).

107.   Soldozy, S. *et al.* A systematic review of endovascular stent-electrode arrays, a minimally invasive approach to brain-machine interfaces. *Neurosurgical Focus* **49**, E3 (2020).

108.   Gerboni, G. STENT-BASED ENDOVASCULAR BRAIN INTERFACE: CHARACTERISATION OF RECORDING AND STIMULATING PROPERTIES. 268.

109.   Llinás, R. R., Walton, K. D., Nakao, M., Hunter, I. & Anquetil, P. A. Neuro-vascular central nervous recording/stimulating system: Using nanotechnology probes. *J Nanopart Res* **7**, 111–127 (2005).

110.   Watanabe, H., Takahashi, H., Nakao, M., Walton, K. & Llinás, R. R. Intravascular neural interface with nanowire electrode. *Electron. Comm. Jpn.* **92**, 29–37 (2009).

111.   Bower, M. R. *et al.* Intravenous recording of intracranial, broadband EEG. *Journal of Neuroscience Methods* **214**, 21–26 (2013).

112.   He, B. D., Ebrahimi, M., Palafox, L. & Srinivasan, L. Signal quality of endovascular electroencephalography. *J. Neural Eng.* **13**, 016016 (2016).

113.   Chen, J. C. *et al. Wireless endovascular nerve stimulation with a millimeter-sized magnetoelectric implant.* http://biorxiv.org/lookup/doi/10.1101/2021.07.06.450036 (2021) doi:10.1101/2021.07.06.450036.

114.   Opie, N. L. *et al.* Chronic impedance spectroscopy of an endovascular stent-electrode array. *J. Neural Eng.* **13**, 046020 (2016).

115.   Opie, N. L. *et al.* Micro-CT and Histological Evaluation of an Neural Interface Implanted Within a Blood Vessel. *IEEE Trans. Biomed. Eng.* **64**, 928–934 (2017).

116.   Gerboni, G. *et al.* Visual evoked potentials determine chronic signal quality in a stent-electrode endovascular neural interface. *Biomed. Phys. Eng. Express* **4**, 055018 (2018).

117.   John, S. E. *et al.* Signal quality of simultaneously recorded endovascular, subdural and epidural signals are comparable. *Sci Rep* **8**, 8427 (2018).

118.   Forsyth, I. A. *et al.* Evaluation of a minimally invasive endovascular neural interface for decoding motor activity. in *2019 9th International IEEE/EMBS Conference on Neural Engineering (NER)* 750–753 (IEEE, 2019). doi:10.1109/NER.2019.8717000.

119.   Yoo, P. E. *et al.* Feasibility of identifying the ideal locations for motor intention decoding using unimodal and multimodal classification at 7T-fMRI. *Sci Rep* **8**, 15556 (2018).

120.   Opie, N. L., Ronayne, S. M., Rind, G. S., Yoo, P. E. & Oxley, T. J. Mechanical suitability of an endovascular braincomputer interface. in *2020 8th International Winter Conference on Brain-Computer Interface (BCI)* 1–6 (IEEE, 2020). doi:10.1109/BCI48061.2020.9061643.

121.   Oxley, T. J. *et al.* Motor neuroprosthesis implanted with neurointerventional surgery improves capacity for activities of daily living tasks in severe paralysis: first in-human experience. *J NeuroIntervent Surg* **13**, 102–108 (2021).

122.   Opie, N. L. *et al.* Focal stimulation of the sheep motor cortex with a chronically implanted minimally invasive electrode array mounted on an endovascular stent. *Nat Biomed Eng* **2**, 907–914 (2018).

123.   Teplitzky, B. A., Connolly, A. T., Bajwa, J. A. & Johnson, M. D. Computational modeling of an endovascular approach to deep brain stimulation. *J. Neural Eng.* **11**, 026011 (2014).

124.   Fukui, T., Takanashi, S. & Hosoda, Y. Coronary Endarterectomy and Stent Removal in Patients With In-Stent restenosis. *The Annals of Thoracic Surgery* **79**, 558–563 (2005).

125. Nishigawa, K., Fukui, T. & Takanashi, S. Off-pump coronary endarterectomy with stent removal for in-stent restenosis in the left anterior descending artery. *Interact CardioVasc Thorac Surg* **21**, 594–597 (2015).

126. Hwang, J., Kim, J. & Choi, H. A review of magnetic actuation systems and magnetically actuated guidewire- and catheter-based microrobots for vascular interventions. *Intel Serv Robotics* **13**, 1–14 (2020).

127. Pancaldi, L. *et al.* Flow driven robotic navigation of microengineered endovascular probes. *Nat Commun* **11**, 6356 (2020).

128. Lei, T. *et al.* Biocompatible and totally disintegrable semiconducting polymer for ultrathin and ultralightweight transient electronics. 6.

129. Salvatore, G. A. *et al.* Biodegradable and Highly Deformable Temperature Sensors for the Internet of Things. *Adv. Funct. Mater.* **27**, 1702390 (2017).

130. Dagdeviren, C. *et al.* Transient, Biocompatible Electronics and Energy Harvesters Based on ZnO. *Small* **9**, 3398–3404 (2013).

131. Lee, G. *et al.* Fully Biodegradable Microsupercapacitor for Power Storage in Transient Electronics. *Adv. Energy Mater.* **7**, 1700157 (2017).

132. Tao, H. *et al.* Silk-based resorbable electronic devices for remotely controlled therapy and in vivo infection abatement. *Proc Natl Acad Sci USA* **111**, 17385–17389 (2014).

133. Lu, L. *et al.* Biodegradable Monocrystalline Silicon Photovoltaic Microcells as Power Supplies for Transient Biomedical Implants. *Adv. Energy Mater.* **8**, 1703035 (2018).

134. Hwang, S.-W. *et al.* Biodegradable Elastomers and Silicon Nanomembranes/Nanoribbons for Stretchable, Transient Electronics, and Biosensors. *Nano Lett.* **15**, 2801–2808 (2015).

135. Brenckle, M. A. *et al.* Modulated Degradation of Transient Electronic Devices through Multilayer Silk Fibroin Pockets. *ACS Appl. Mater. Interfaces* **7**, 19870–19875 (2015).

136. Hwang, S.-W. *et al.* High-Performance Biodegradable/Transient Electronics on Biodegradable Polymers. *Adv. Mater.* **26**, 3905–3911 (2014).

137. Li, R., Wang, L., Kong, D. & Yin, L. Recent progress on biodegradable materials and transient electronics. *Bioactive Materials* **3**, 322–333 (2018).

138. Pranti, A. S., Schander, A., Bödecker, A. & Lang, W. PEDOT: PSS coating on gold microelectrodes with excellent stability and high charge injection capacity for chronic neural interfaces. *Sensors and Actuators B: Chemical* **275**, 382–393 (2018).

139. Nyitray, C. E. *et al.* Polycaprolactone Thin-Film Micro- and Nanoporous Cell-Encapsulation Devices. *ACS Nano* **9**, 5675–5682 (2015).

140. Schlesinger, E., Ciaccio, N. & Desai, T. A. Polycaprolactone thin-film drug delivery systems: Empirical and predictive models for device design. *Materials Science and Engineering: C* **57**, 232–239 (2015).

141. Sharma, U. *et al.* The development of bioresorbable composite polymeric implants with high mechanical strength. *Nature Mater* **17**, 96–103 (2018).

142. Cellot, G. *et al.* PEDOT:PSS Interfaces Support the Development of Neuronal Synaptic Networks with Reduced Neuroglia Response In vitro. *Front. Neurosci.* **9**, (2016).

143. Koutsouras, D. A. *et al.* PEDOT:PSS microelectrode arrays for hippocampal cell culture electrophysiological recordings. *MRS Communications* **7**, 259–265 (2017).

144. Cuttaz, E. *et al.* Conductive elastomer composites for fully polymeric, flexible bioelectronics. *Biomater. Sci.* **7**, 1372–1385 (2019).

145. Liu, Y. *et al.* Soft and elastic hydrogel-based microelectronics for localized low-voltage neuromodulation. *Nat Biomed Eng* **3**, 58–68 (2019).

146. Ferlauto, L. *et al.* Development and Characterization of PEDOT:PSS/Alginate Soft Microelectrodes for Application in Neuroprosthetics. *Front. Neurosci.* **12**, 648 (2018).

147. Feig, V. R., Tran, H. & Bao, Z. Biodegradable Polymeric Materials in Degradable Electronic Devices. *ACS Cent. Sci.* **4**, 337–348 (2018).

148. Effect of incorporation of ethylene glycol into PEDOT:PSS on electron phonon coupling and conductivity. *Journal of Applied Physics* **117**, 215501 (2015).

149.   Wei, Q., Mukaida, M., Naitoh, Y. & Ishida, T. Morphological Change and Mobility Enhancement in PEDOT:PSS by Adding Co-solvents. *Advanced Materials* **25**, 2831–2836 (2013).

150.   Blau, A. *et al.* Flexible, all-polymer microelectrode arrays for the capture of cardiac and neuronal signals. *Biomaterials* **32**, 1778–1786 (2011).

151.   Garma, L. D., Ferrari, L. M., Scognamiglio, P., Greco, F. & Santoro, F. Inkjet-printed PEDOT:PSS multi-electrode arrays for low-cost *in vitro* electrophysiology. *Lab Chip* **19**, 3776–3786 (2019).

152.   Liu, Y. *et al.* Morphing electronics enable neuromodulation in growing tissue. *Nat Biotechnol* **38**, 1031–1036 (2020).

153.   Lüttjohann, A., Fabene, P. F. & van Luijtelaar, G. A revised Racine's scale for PTZ-induced seizures in rats. *Physiology & Behavior* **98**, 579–586 (2009).

154.   Javadian, N., Rahimi, N., Javadi-Paydar, M., Doustimotlagh, A. H. & Dehpour, A. R. The modulatory effect of nitric oxide in pro- and anti-convulsive effects of vasopressin in PTZ-induced seizures threshold in mice. *Epilepsy Research* **126**, 134–140 (2016).

155.   Yonekawa, W. D., Kupferberg, H. J. & Woodbury, D. M. Relationship between pentylenetetrazol-induced seizures and brain pentylenetetrazol levels in mice. *J Pharmacol Exp Ther* **214**, 589–593 (1980).

156.   Schander, A. *et al.* Design and fabrication of novel multi-channel floating neural probes for intracortical chronic recording. *Sensors and Actuators A: Physical* **247**, 125–135 (2016).

157.   Charkhkar, H. *et al.* Chronic intracortical neural recordings using microelectrode arrays coated with PEDOT–TFB. *Acta Biomaterialia* **32**, 57–67 (2016).

158.   Ludwig, K. A., Uram, J. D., Yang, J., Martin, D. C. & Kipke, D. R. Chronic neural recordings using silicon microelectrode arrays electrochemically deposited with a poly(3,4-ethylenedioxythiophene) (PEDOT) film. *J. Neural Eng.* **3**, 59–70 (2006).

159.   Schander, A. *et al.* A Flexible 202-Channel Epidural ECoG Array With PEDOT: PSS Coated Electrodes for Chronic Recording of the Visual Cortex. *IEEE Sensors Journal* **19**, 820–825 (2019).

160.   Fanelli, A. *et al.* Degradable endovascular neural interface for minimally invasive neural recording and stimulation. 2021.03.24.436737 (2021) doi:10.1101/2021.03.24.436737.

161. Gong, F., Meng, C., He, J. & Dong, X. Fabrication of highly conductive and multifunctional polyester fabrics by spray-coating with PEDOT:PSS solutions. *Progress in Organic Coatings* **121**, 89–96 (2018).

162. Sethumadhavan, V., Zuber, K., Bassell, C., Teasdale, P. R. & Evans, D. Hydrolysis of doped conducting polymers. *Commun Chem* **3**, 1–9 (2020).

163. Thaning, E. M., Asplund, M. L. M., Nyberg, T. A., Inganäs, O. W. & von Holst, H. Stability of poly(3,4-ethylene dioxythiophene) materials intended for implants. *Journal of Biomedical Materials Research Part B: Applied Biomaterials* **93B**, 407–415 (2010).

164. Chen, T., Lin, Y., Bi, X. & Gu, Y. Conductive poly(3,4-ethylenedioxythiophene) is effectively degradable by hydrogen peroxide with iron (II) chloride. *Materials Chemistry and Physics* **242**, 122509 (2020).

165. Gong, H. *et al.* Stimulation of immune systems by conjugated polymers and their potential as an alternative vaccine adjuvant. *Nanoscale* **7**, 19282–19292 (2015).

166. Fu, R., Shen, Q., Xu, P., Luo, J. J. & Tang, Y. Phagocytosis of Microglia in the Central Nervous System Diseases. *Mol Neurobiol* **49**, 1422–1434 (2014).

167. Strakosas, X. *et al.* A facile biofunctionalisation route for solution processable conducting polymer devices. *Journal of Materials Chemistry B* **2**, 2537–2545 (2014).

168. Jorfi, M., Skousen, J. L., Weder, C. & Capadona, J. R. Progress towards biocompatible intracortical microelectrodes for neural interfacing applications. *J. Neural Eng.* **12**, 011001 (2014).

169. Scaini, D. & Ballerini, L. Nanomaterials at the neural interface. *Current Opinion in Neurobiology* **50**, 50–55 (2018).

170. Wellman, S. M. & Kozai, T. D. Y. Understanding the Inflammatory Tissue Reaction to Brain Implants To Improve Neurochemical Sensing Performance. *ACS Chem. Neurosci.* **8**, 2578–2582 (2017).

171. Cregg, J. M. *et al.* Functional regeneration beyond the glial scar. *Experimental Neurology* **253**, 197–207 (2014).

172. Ung, H. *et al.* Intracranial EEG fluctuates over months after implanting electrodes in human brain. *J. Neural Eng.* **14**, 056011 (2017).

173. Ung, H. *et al.* Temporal behavior of seizures and interictal bursts in prolonged intracranial recordings from epileptic canines. *Epilepsia* **57**, 1949–1957 (2016).

174. Li, P., Du, D., Guo, L., Guo, Y. & Ouyang, J. Stretchable and conductive polymer films for high-performance electromagnetic interference shielding. *Journal of Materials Chemistry C* **4**, 6525–6532 (2016).

175. Wang, Y. & Jing, X. Intrinsically conducting polymers for electromagnetic interference shielding. *Polymers for Advanced Technologies* **16**, 344–351 (2005).

176. Lee, E. *et al.* ACT-PRESTO: Rapid and consistent tissue clearing and labeling method for 3-dimensional (3D) imaging. *Sci Rep* **6**, 18631 (2016).

177. Asboth, L. *et al.* Cortico–reticulo–spinal circuit reorganization enables functional recovery after severe spinal cord contusion. *Nat Neurosci* **21**, 576–588 (2018).

178. Voigt, F. F. *et al.* The mesoSPIM initiative: open-source light-sheet microscopes for imaging cleared tissue. *Nat Methods* **16**, 1105–1108 (2019).

179. Personalized Neuroprosthetics. https://www.science.org/doi/10.1126/scitranslmed.3005968?url_ver=Z39.88-2003&rfr_id=ori:rid:crossref.org&rfr_dat=cr_pub%20%200pubmed.

180. Fan, J. Z., Lopez-Rivera, V. & Sheth, S. A. Over the Horizon: The Present and Future of Endovascular Neural Recording and Stimulation. *Front. Neurosci.* **14**, 432 (2020).

181. Boehler, C., Carli, S., Fadiga, L., Stieglitz, T. & Asplund, M. Tutorial: guidelines for standardized performance tests for electrodes intended for neural interfaces and bioelectronics. *Nat Protoc* **15**, 3557–3578 (2020).

182. Kozai, T. D. Y., Jaquins-Gerstl, A. S., Vazquez, A. L., Michael, A. C. & Cui, X. T. Brain Tissue Responses to Neural Implants Impact Signal Sensitivity and Intervention Strategies. *ACS Chem. Neurosci.* **6**, 48–67 (2015).

183. Polikov, V. S., Tresco, P. A. & Reichert, W. M. Response of brain tissue to chronically implanted neural electrodes. *Journal of Neuroscience Methods* **148**, 1–18 (2005).

184. Prodanov, D. & Delbeke, J. Mechanical and Biological Interactions of Implants with the Brain and Their Impact on Implant Design. *Front. Neurosci.* **10**, (2016).

185. McMahon, S. *et al.* Bio-resorbable polymer stents: a review of material progress and prospects. *Progress in Polymer Science* **83**, 79–96 (2018).

186. Gulino, M., Kim, D., Pané, S., Santos, S. D. & Pêgo, A. P. Tissue Response to Neural Implants: The Use of Model Systems Toward New Design Solutions of Implantable Microelectrodes. *Front. Neurosci.* **13**, 689 (2019).

187. Biran, R., Martin, D. C. & Tresco, P. A. Neuronal cell loss accompanies the brain tissue response to chronically implanted silicon microelectrode arrays. *Experimental Neurology* **195**, 115–126 (2005).

188. Saxena, T. *et al.* The impact of chronic blood–brain barrier breach on intracortical electrode function. *Biomaterials* **34**, 4703–4713 (2013).

189. Biran, R., Martin, D. C. & Tresco, P. A. The brain tissue response to implanted silicon microelectrode arrays is increased when the device is tethered to the skull. *J. Biomed. Mater. Res.* **82A**, 169–178 (2007).

190. Hwang, S.-W. *et al.* A Physically Transient Form of Silicon Electronics. *Science* **337**, 1640–1644 (2012).

191. Bodart, C. *et al.* Electropolymerized Poly(3,4-ethylenedioxythiophene) (PEDOT) Coatings for Implantable Deep-Brain-Stimulating Microelectrodes. *ACS Appl. Mater. Interfaces* **11**, 17226–17233 (2019).

192. Schander, A. *et al.* In-vitro evaluation of the long-term stability of PEDOT:PSS coated microelectrodes for chronic recording and electrical stimulation of neurons. in *2016 38th Annual International Conference of the IEEE Engineering in Medicine and Biology Society (EMBC)* 6174–6177 (IEEE, 2016). doi:10.1109/EMBC.2016.7592138.

193. Khodagholy, D. *et al.* Highly Conformable Conducting Polymer Electrodes for In Vivo Recordings. *Adv. Mater.* **23**, H268–H272 (2011).

194. Håkansson, A. *et al.* Effect of (3-glycidyloxypropyl)trimethoxysilane (GOPS) on the electrical properties of PEDOT:PSS films. *J. Polym. Sci. Part B: Polym. Phys.* **55**, 814–820 (2017).

195. Sarode, D. N. & Roy, S. In Vitro models for thrombogenicity testing of blood-recirculating medical devices. *Expert Review of Medical Devices* **16**, 603–616 (2019).

196. Dong, X. *et al.* Construction of a bilayered vascular graft with smooth internal surface for improved hemocompatibility and endothelial cell monolayer formation. *Biomaterials* **181**, 1–14 (2018).

197. Qiu, T., Jiang, W., Yan, P., Jiao, L. & Wang, X. Development of 3D-Printed Sulfated Chitosan Modified Bioresorbable Stents for Coronary Artery Disease. *Frontiers in Bioengineering and Biotechnology* **8**, (2020).

198. Szymonowicz, M., Rybak, Z., Witkiewicz, W., Pezowicz, C. & Filipiak, J. In vitro hemocompatibility studies of (poly(L-lactide) and poly(L-lactide-co-glycolide) as materials for bioresorbable stents manufacture. *Acta of bioengineering and biomechanics / Wrocław University of Technology* **16**, 131–9 (2014).

199. Cogan, S. F. Neural Stimulation and Recording Electrodes. *Annu. Rev. Biomed. Eng.* **10**, 275–309 (2008).

200. Aqrawe, Z., Montgomery, J., Travas-Sejdic, J. & Svirskis, D. Conducting polymers for neuronal microelectrode array recording and stimulation. *Sensors and Actuators B: Chemical* **257**, 753–765 (2018).

201. Tzirtzilakis, E. E. A mathematical model for blood flow in magnetic field. *Physics of Fluids* **17**, 077103 (2005).

202. Brown, P. H., Balbo, A., Zhao, H., Ebel, C. & Schuck, P. Density Contrast Sedimentation Velocity for the Determination of Protein Partial-Specific Volumes. *PLOS ONE* **6**, e26221 (2011).

203. Abdalla, S., Al-ameer, S. S. & Al-Magaishi, S. H. Electrical properties with relaxation through human blood. *Biomicrofluidics* **4**, 034101 (2010).

204. Connes, P. *et al.* The role of blood rheology in sickle cell disease. *Blood Reviews* **30**, 111–118 (2016).

205.   Chevion, S. & Chevion, M. Antioxidant Status and Human Health: Use of Cyclic Voltammetry for the Evaluation of the Antioxidant Capacity of Plasma and of Edible Plants. *Annals of the New York Academy of Sciences* **899**, 308–325 (2000).

206.   Wang, H.-W. *et al.* Cyclic Voltammetry in Biological Samples: A Systematic Review of Methods and Techniques Applicable to Clinical Settings. *Signals* **2**, 138–158 (2021).

207.   Schiavone, G. *et al.* Guidelines to Study and Develop Soft Electrode Systems for Neural Stimulation. *Neuron* **108**, 238–258 (2020).

208.   Porto Cruz, M. F. *et al.* Can Crosstalk Compromise the Recording of High-Frequency Neural Signals? in *2019 9th International IEEE/EMBS Conference on Neural Engineering (NER)* 924–927 (2019). doi:10.1109/NER.2019.8717009.

209.   Habib, C. A. *et al.* MR imaging of the yucatan pig head and neck vasculature: Cerebral Venous Drainage System in Swine. *J. Magn. Reson. Imaging* **38**, 641–649 (2013).

210.   Lu, B. *et al.* Pure PEDOT:PSS hydrogels. *Nat Commun* **10**, 1043 (2019).

211.   Bießmann, L. *et al.* Monitoring the Swelling Behavior of PEDOT:PSS Electrodes under High Humidity Conditions. *ACS Appl. Mater. Interfaces* **10**, 9865–9872 (2018).

212.   Modarresi, M., Mehandzhiyski, A., Fahlman, M., Tybrandt, K. & Zozoulenko, I. Microscopic Understanding of the Granular Structure and the Swelling of PEDOT:PSS. 12 (2020).

213.   Chen, W. X. *et al.* Haemodynamic effects of incomplete stent apposition in curved coronary arteries. *Journal of Biomechanics* **63**, 164–173 (2017).

214.   Thiriet, M., Delfour, M. & Garon, A. Vascular Stenosis: An Introduction. in *PanVascular Medicine* (ed. Lanzer, P.) 781–868 (Springer Berlin Heidelberg, 2015). doi:10.1007/978-3-642-37078-6_32.

215.   Teo, M. Y. *et al.* Direct Patterning of Highly Conductive PEDOT:PSS/Ionic Liquid Hydrogel via Microreactive Inkjet Printing. *ACS Appl. Mater. Interfaces* **11**, 37069–37076 (2019).

216.   Charlot, B. *et al.* Micropatterning PEDOT:PSS layers. *Microsyst Technol* **19**, 895–903 (2013).

217.   Eom, S. H. *et al.* Polymer solar cells based on inkjet-printed PEDOT:PSS layer. *Organic Electronics* **10**, 536–542 (2009).

218. Guo, Y. *et al.* PEDOT:PSS "Wires" Printed on Textile for Wearable Electronics. *ACS Appl. Mater. Interfaces* **8**, 26998–27005 (2016).

219. Someya, T., Bao, Z. & Malliaras, G. G. The rise of plastic bioelectronics. *Nature* **540**, 379–385 (2016).

220. Khodagholy, D. *et al.* NeuroGrid: recording action potentials from the surface of the brain. *Nat Neurosci* **18**, 310–315 (2015).

221. Dijk, G., Rutz, A. L. & Malliaras, G. G. Stability of PEDOT:PSS-Coated Gold Electrodes in Cell Culture Conditions. *Advanced Materials Technologies* **5**, 1900662 (2020).

222. Hu, J. *et al.* Advances in Biomaterials and Technologies for Vascular Embolization. *Advanced Materials* **31**, 1901071 (2019).

223. Crowley, R. W., Ducruet, A. F., McDougall, C. G. & Albuquerque, F. C. Endovascular advances for brain arteriovenous malformations. *Neurosurgery* **74 Suppl 1**, S74-82 (2014).

224. Zhu, Y. *et al.* Endovascular Metal Devices for the Treatment of Cerebrovascular Diseases. *Advanced Materials* **31**, 1805452 (2019).

225. Flow-Diverter Stent for the Endovascular Treatment of Intracranial Aneurysms | Stroke. https://www.ahajournals.org/doi/full/10.1161/STROKEAHA.110.589911.

226. Brain arteriovenous malformation treatment using a combination of Onyx and a new detachable tip microcatheter, SONIC: short-term results - PubMed. https://pubmed.ncbi.nlm.nih.gov/20190210/.

227. Won, S. M., Song, E., Reeder, J. T. & Rogers, J. A. Emerging Modalities and Implantable Technologies for Neuromodulation. *Cell* **181**, 115–135 (2020).

228. Rivnay, J., Wang, H., Fenno, L., Deisseroth, K. & Malliaras, G. G. Next-generation probes, particles, and proteins for neural interfacing. *Sci. Adv.* **3**, e1601649 (2017).

229. Chen, R., Canales, A. & Anikeeva, P. Neural recording and modulation technologies. *Nat Rev Mater* **2**, 1–16 (2017).

230. Obidin, N., Tasnim, F. & Dagdeviren, C. The Future of Neuroimplantable Devices: A Materials Science and Regulatory Perspective. *Advanced Materials* **32**, 1901482 (2020).

231. Lacour, S. P., Courtine, G. & Guck, J. Materials and technologies for soft implantable neuroprostheses. *Nat Rev Mater* **1**, 1–14 (2016).

232. Won, S. M. *et al.* Recent Advances in Materials, Devices, and Systems for Neural Interfaces. *Advanced Materials* **30**, 1800534 (2018).

233. Montgomery, K. L. *et al.* Wirelessly powered, fully internal optogenetics for brain, spinal and peripheral circuits in mice. *Nat Methods* **12**, 969–974 (2015).

234. Webster, R. J. & Jones, B. A. Design and Kinematic Modeling of Constant Curvature Continuum Robots: A Review. *The International Journal of Robotics Research* **29**, 1661–1683 (2010).

235. Mahvash, M. & Dupont, P. E. Stiffness Control of Surgical Continuum Manipulators. *IEEE Transactions on Robotics* **27**, 334–345 (2011).

236. Camarillo, D. B., Carlson, C. R. & Salisbury, J. K. Configuration Tracking for Continuum Manipulators With Coupled Tendon Drive. *IEEE Transactions on Robotics* **25**, 798–808 (2009).

237. Rucker, D. C., Webster, R. J., Chirikjian, G. S. & Cowan, N. J. Equilibrium Conformations of Concentric-tube Continuum Robots. *The International Journal of Robotics Research* **29**, 1263–1280 (2010).

238. Rafii-Tari, H., Payne, C. J. & Yang, G.-Z. Current and Emerging Robot-Assisted Endovascular Catheterization Technologies: A Review. *Ann Biomed Eng* **42**, 697–715 (2014).

239. Runciman, M., Darzi, A. & Mylonas, G. P. Soft Robotics in Minimally Invasive Surgery. *Soft Robotics* **6**, 423–443 (2019).

240. Burgner-Kahrs, J., Rucker, D. C. & Choset, H. Continuum Robots for Medical Applications: A Survey. *IEEE Transactions on Robotics* **31**, 1261–1280 (2015).

241. Tillander, H. Magnetic Guidance of a Catheter with Articulated Steel Tip. *Acta Radiologica* **35**, 62–64 (1951).

242. Armacost, M. P. *et al.* Accurate and Reproducible Target Navigation with the Stereotaxis Niobe® Magnetic Navigation System. *Journal of Cardiovascular Electrophysiology* **18**, S26–S31 (2007).

243. Ernst, S. *et al.* Initial Experience With Remote Catheter Ablation Using a Novel Magnetic Navigation System. *Circulation* **109**, 1472–1475 (2004).

244.   Krings, T. *et al.* Magnetic versus manual guidewire manipulation in neuroradiology: in vitro results. *Neuroradiology* **48**, 394–401 (2006).

245.   Edelmann, J., Petruska, A. J. & Nelson, B. J. Magnetic control of continuum devices. *The International Journal of Robotics Research* **36**, 68–85 (2017).

246.   Kratchman, L. B., Bruns, T. L., Abbott, J. J. & Webster, R. J. Guiding Elastic Rods With a Robot-Manipulated Magnet for Medical Applications. *IEEE Transactions on Robotics* **33**, 227–233 (2017).

247.   Kim, Y., Parada, G. A., Liu, S. & Zhao, X. Ferromagnetic soft continuum robots. *Science Robotics* **4**, eaax7329 (2019).

248.   Jeon, S. *et al.* A Magnetically Controlled Soft Microrobot Steering a Guidewire in a Three-Dimensional Phantom Vascular Network. *Soft Robotics* **6**, 54–68 (2019).

249.   Chautems, C. *et al.* Magnetic Continuum Device with Variable Stiffness for Minimally Invasive Surgery. *Advanced Intelligent Systems* **2**, 1900086 (2020).

250.   Azizi, A., Tremblay, C. C., Gagné, K. & Martel, S. Using the fringe field of a clinical MRI scanner enables robotic navigation of tethered instruments in deeper vascular regions. *Sci. Robot.* **4**, eaax7342 (2019).

251.   Bassett, E. K. *et al.* Design of a mechanical clutch-based needle-insertion device. *Proceedings of the National Academy of Sciences* **106**, 5540–5545 (2009).

252.   Autrusson, N., Guglielmini, L., Lecuyer, S., Rusconi, R. & Stone, H. A. The shape of an elastic filament in a two-dimensional corner flow. *Physics of Fluids* **23**, 063602 (2011).

253.   Hu, W., Lum, G. Z., Mastrangeli, M. & Sitti, M. Small-scale soft-bodied robot with multimodal locomotion. *Nature* **554**, 81–85 (2018).

254.   Lum, G. Z. *et al.* Shape-programmable magnetic soft matter. *Proceedings of the National Academy of Sciences* **113**, E6007–E6015 (2016).

255.   Ren, Z., Hu, W., Dong, X. & Sitti, M. Multi-functional soft-bodied jellyfish-like swimming. *Nat Commun* **10**, 2703 (2019).

256.   Ejeian, F. *et al.* Design and applications of MEMS flow sensors: A review. *Sensors and Actuators A: Physical* **295**, 483–502 (2019).

257. Kuo, J. T. W., Yu, L. & Meng, E. Micromachined Thermal Flow Sensors—A Review. *Microm-achines* **3**, 550–573 (2012).

258. Mahvi, A. J., El Fil, B. & Garimella, S. Accurate and inexpensive thermal time-of-flight sensor for measuring refrigerant flow in minichannels. *International Journal of Heat and Mass Transfer* **132**, 184–193 (2019).

259. Mistry, K. K. & Mahapatra, A. Design and simulation of a thermo transfer type MEMS based micro flow sensor for arterial blood flow measurement. *Microsyst Technol* **18**, 683–692 (2012).

260. Henrik Bruus. *Theoretical Microfluidics*. (OUP Oxford, 2008).

261. Chautems, C. & Nelson, B. J. The tethered magnet: Force and 5-DOF pose control for cardiac ablation. in *2017 IEEE International Conference on Robotics and Automation (ICRA)* 4837–4842 (2017). doi:10.1109/ICRA.2017.7989562.

262. Lubarda, V. A. The Mechanics of Belt Friction Revisited. *International Journal of Mechanical Engineering Education* **42**, 97–112 (2014).

263. Rafii-Tari, H. *et al.* Objective Assessment of Endovascular Navigation Skills with Force Sensing. *Ann Biomed Eng* **45**, 1315–1327 (2017).

264. Mokin, M. *et al.* Assessment of distal access catheter performance during neuroendovascular procedures: measuring force in three-dimensional patient specific phantoms. *Journal of NeuroInterventional Surgery* **11**, 619–622 (2019).

265. Leslie, D. C. *et al.* A bioinspired omniphobic surface coating on medical devices prevents thrombosis and biofouling. *Nat Biotechnol* **32**, 1134–1140 (2014).

266. Mickle, A. D. *et al.* A wireless closed-loop system for optogenetic peripheral neuromodulation. *Nature* **565**, 361–365 (2019).

267. Park, S. I. *et al.* Soft, stretchable, fully implantable miniaturized optoelectronic systems for wireless optogenetics. *Nat Biotechnol* **33**, 1280–1286 (2015).

268. Jeong, J.-W. *et al.* Wireless Optofluidic Systems for Programmable In Vivo Pharmacology and Optogenetics. *Cell* **162**, 662–674 (2015).

269. Qu, Y. *et al.* Superelastic Multimaterial Electronic and Photonic Fibers and Devices via Thermal Drawing. *Advanced Materials* **30**, 1707251 (2018).

270. Loke, G., Yan, W., Khudiyev, T., Noel, G. & Fink, Y. Recent Progress and Perspectives of Thermally Drawn Multimaterial Fiber Electronics. *Advanced Materials* **32**, 1904911 (2020).

271. Adams, J. J. *et al.* Conformal Printing of Electrically Small Antennas on Three-Dimensional Surfaces. *Advanced Materials* **23**, 1335–1340 (2011).

272. Baumgartner, M. *et al.* Resilient yet entirely degradable gelatin-based biogels for soft robots and electronics. *Nat. Mater.* **19**, 1102–1109 (2020).

273. Huang, H.-W. *et al.* Adaptive locomotion of artificial microswimmers. *Science Advances* **5**, eaau1532.

274. Abbott, J. J. Parametric design of tri-axial nested Helmholtz coils. *Review of Scientific Instruments* **86**, 054701 (2015).

275. Kaneko, N. *et al.* Manufacture of patient-specific vascular replicas for endovascular simulation using fast, low-cost method. *Sci Rep* **6**, 39168 (2016).

276. Kunhappan, D., Harthong, B., Chareyre, B., Balarac, G. & Dumont, P. J. J. Numerical modeling of high aspect ratio flexible fibers in inertial flows. *Physics of Fluids* **29**, 093302 (2017).

277. Campanile, L. F. & Hasse, A. A simple and effective solution of the elastica problem. *Proceedings of the Institution of Mechanical Engineers, Part C: Journal of Mechanical Engineering Science* **222**, 2513–2516 (2008).

278. Xi, W. *et al.* Soft tubular microfluidics for 2D and 3D applications. *Proceedings of the National Academy of Sciences* **114**, 10590–10595 (2017).

279. Martins Lima, A. *et al.* An optimized and validated 384-well plate assay to test platelet function in a high-throughput screening format. *Platelets* **30**, 563–571 (2019).

280. DeVries, J. T., White, C. J., Cunningham, M. C. & Ramee, S. R. Catheter-based therapy for acute ischemic stroke: A national unmet need. *Catheterization and Cardiovascular Interventions* **72**, 705–709 (2008).

281.   Lubicz, B. *et al.* Flow-Diverter Stent for the Endovascular Treatment of Intracranial Aneurysms. *Stroke* **41**, 2247–2253 (2010).

282.   Holmes, D. R. & Williams, D. O. Catheter-Based Treatment of Coronary Artery Disease. *Circulation: Cardiovascular Interventions* **1**, 60–73 (2008).

283.   D'Amico, R. S. *et al.* Super selective intra-arterial cerebral infusion of modern chemotherapeutics after blood–brain barrier disruption: where are we now, and where we are going. *J Neurooncol* **147**, 261–278 (2020).

284.   Mattmann, M. *et al.* Thermoset Shape Memory Polymer Variable Stiffness 4D Robotic Catheters. *Advanced Science* **9**, 2103277 (2022).

285.   Edelmann, J., Petruska, A. J. & Nelson, B. J. Estimation-Based Control of a Magnetic Endoscope without Device Localization. *J. Med. Robot. Res.* **03**, 1850002 (2018).

286.   Gunduz, S., Albadawi, H. & Oklu, R. Robotic Devices for Minimally Invasive Endovascular Interventions: A New Dawn for Interventional Radiology. *Advanced Intelligent Systems* **3**, 2170021 (2021).

287.   Dupont, P. E., Lock, J., Itkowitz, B. & Butler, E. Design and Control of Concentric-Tube Robots. *IEEE Transactions on Robotics* **26**, 209–225 (2010).

288.   Heunis, C., Sikorski, J. & Misra, S. Flexible Instruments for Endovascular Interventions: Improved Magnetic Steering, Actuation, and Image-Guided Surgical Instruments. *IEEE Robotics Automation Magazine* **25**, 71–82 (2018).

289.   Abbott, J. J., Diller, E. & Petruska, A. J. Magnetic Methods in Robotics. *Annual Review of Control, Robotics, and Autonomous Systems* **3**, 57–90 (2020).

290.   Yin, X., Guo, S., Hirata, H. & Ishihara, H. Design and experimental evaluation of a teleoperated haptic robot–assisted catheter operating system. *Journal of Intelligent Material Systems and Structures* **27**, 3–16 (2016).

291.   Fu, Y., Liu, H., Huang, W., Wang, S. & Liang, Z. Steerable catheters in minimally invasive vascular surgery. *The International Journal of Medical Robotics and Computer Assisted Surgery* **5**, 381–391 (2009).

292.   Kanagaratnam, P. *et al.* Experience of robotic catheter ablation in humans using a novel remotely steerable catheter sheath. *J Interv Card Electrophysiol* **21**, 19–26 (2008).

293.   Gopesh, T. *et al.* Soft robotic steerable microcatheter for the endovascular treatment of cerebral disorders. *Science Robotics* **6**, eabf0601 (2021).

294.   Kim, D.-H. *et al.* Materials for multifunctional balloon catheters with capabilities in cardiac electrophysiological mapping and ablation therapy. *Nature Mater* **10**, 316–323 (2011).

295.   Kim, D.-H. *et al.* Electronic sensor and actuator webs for large-area complex geometry cardiac mapping and therapy. *Proceedings of the National Academy of Sciences* **109**, 19910–19915 (2012).

296.   Han, M. *et al.* Catheter-integrated soft multilayer electronic arrays for multiplexed sensing and actuation during cardiac surgery. *Nat Biomed Eng* **4**, 997–1009 (2020).

297.   Fagogenis, G. *et al.* Autonomous robotic intracardiac catheter navigation using haptic vision. *Science Robotics* **4**, eaaw1977 (2019).

298.   Li, C., Ahn, C. H., Shutter, L. A. & Narayan, R. K. Toward real-time continuous brain glucose and oxygen monitoring with a smart catheter. *Biosensors and Bioelectronics* **25**, 173–178 (2009).

299.   Li, C. *et al.* Smart catheter flow sensor for real-time continuous regional cerebral blood flow monitoring. *Appl. Phys. Lett.* **99**, 233705 (2011).

300.   Chatzipirpiridis, G. *et al.* Miniaturized magnetic force sensor on a catheter tip. in *2015 Transducers - 2015 18th International Conference on Solid-State Sensors, Actuators and Microsystems (TRANSDUCERS)* 1727–1730 (2015). doi:10.1109/TRANSDUCERS.2015.7181278.

301.   Moonla, C. *et al.* An integrated microcatheter-based dual-analyte sensor system for simultaneous, real-time measurement of propofol and fentanyl. *Talanta* **218**, 121205 (2020).

302.   Rivkin, B. *et al.* Electronically integrated microcatheters based on self-assembling polymer films. *Science Advances* **7**, eabl5408.

303.   Pham, L. N., Steiner, J. A., Leang, K. K. & Abbott, J. J. Soft Endoluminal Robots Propelled by Rotating Magnetic Dipole Fields. *IEEE Transactions on Medical Robotics and Bionics* **2**, 598–607 (2020).

304.   Ren, Z. *et al.* Soft-bodied adaptive multimodal locomotion strategies in fluid-filled confined spaces. *Science Advances* **7**, eabh2022.

305.   Frei, E. H. *et al.* The POD and its applications. *Med Res Eng* **5**, 11–18 (1966).

306.   Molcho, J., Karny, H. Z., Frei, E. H. & Askenasy, H. M. Selective Cerebral Catheterization. *IEEE Transactions on Biomedical Engineering* **BME-17**, 134–140 (1970).

307.   Hilai, S. K., Jost Michelsen, W., Driller, J. & Leonard, E. Magnetically Guided Devices for Vascular Exploration and Treatment. *Radiology* **113**, 529–540 (1974).

308.   Young, W. & Roark, R. *Roark's formulas for stress and strain, 6th ed.* (McGraw Hill, 1989).

309.   Thomas, J. Vibration Characteristics of Tapered Cantilever Beams. (1968).

310.   Cheng, N.-S. Formula for the Viscosity of a Glycerol–Water Mixture. *Ind. Eng. Chem. Res.* **47**, 3285–3288 (2008).

311.   Volk, A. & Kähler, C. J. Density model for aqueous glycerol solutions. *Exp Fluids* **59**, 75 (2018).

312.   Wang, L., Kim, Y., Guo, C. F. & Zhao, X. Hard-magnetic elastica. *Journal of the Mechanics and Physics of Solids* **142**, 104045 (2020).

313.   Zhao, R., Kim, Y., Chester, S. A., Sharma, P. & Zhao, X. Mechanics of hard-magnetic soft materials. *Journal of the Mechanics and Physics of Solids* **124**, 244–263 (2019).

314.   Yan, D., Pezzulla, M., Cruveiller, L., Abbasi, A. & Reis, P. M. Magneto-active elastic shells with tunable buckling strength. *Nat Commun* **12**, 2831 (2021).

315.   Zhang, X., Chan, F. K., Parthasarathy, T. & Gazzola, M. Modeling and simulation of complex dynamic musculoskeletal architectures. *Nat Commun* **10**, 4825 (2019).

316.   Tonino, P. A. L. *et al.* Fractional Flow Reserve versus Angiography for Guiding Percutaneous Coronary Intervention. *New England Journal of Medicine* **360**, 213–224 (2009).

317.   Poupart, O. *et al.* Pulsatile Flow-Induced Fatigue-Resistant Photopolymerizable Hydrogels for the Treatment of Intracranial Aneurysms. *Frontiers in Bioengineering and Biotechnology* **8**, (2021).

318.   Fenoy, G. E., Azzaroni, O., Knoll, W. & Marmisollé, W. A. Functionalization Strategies of PEDOT and PEDOT:PSS Films for Organic Bioelectronics Applications. *Chemosensors* **9**, 212 (2021).

319.   Huang, S., Wang, K., Wang, S., Wang, Y. & Wang, M. Highly Fluorescent Polycaprolactones with Tunable Light Emission Wavelengths across Visible to NIR Spectral Window. *Advanced Materials Interfaces* **3**, 1600259 (2016).

320. Tipnis, N. P. & Burgess, D. J. Sterilization of implantable polymer-based medical devices: A review. *International Journal of Pharmaceutics* **544**, 455–460 (2018).

321. Shah, A. & Mittal, S. Invasive electroencephalography monitoring: Indications and presurgical planning. *Ann Indian Acad Neurol* **17**, 89 (2014).

322. Duun-Henriksen, J. *et al.* A new era in electroencephalographic monitoring? Subscalp devices for ultra–long-term recordings. *Epilepsia* **61**, 1805–1817 (2020).

323. Ashraf, T. *et al.* Size of radial and ulnar artery in local population. *J Pak Med Assoc* **60**, 817–819 (2010).

324. Beniwal, S., Bhargava, K. & Kausik, S. K. Size of distal radial and distal ulnar arteries in adults of southern Rajasthan and their implications for percutaneous coronary interventions. *Indian Heart J* **66**, 506–509 (2014).

325. Riekkinen, H. V., Karkola, K. O. & Kankainen, A. The radial artery is larger than the ulnar. *The Annals of Thoracic Surgery* **75**, 882–884 (2003).

326. Tayal, R. *et al.* CT Angiography Analysis of Axillary Artery Diameter versus Common Femoral Artery Diameter: Implications for Axillary Approach for Transcatheter Aortic Valve Replacement in Patients with Hostile Aortoiliac Segment and Advanced Lung Disease. *Int J Vasc Med* **2016**, 3610705 (2016).

327. van de Pol, D. *et al.* Ultrasound assessment of the posterior circumflex humeral artery in elite volleyball players: Aneurysm prevalence, anatomy, branching pattern and vessel characteristics. *Eur Radiol* **27**, 889–898 (2017).

328. Fontes, E. B., Precht, B. L. C., Andrade, R. C. L., Fernandes, R. M. P. & Cisne, R. Relaciones de las Arterias Circunflejas Humerales y sus Variaciones. *International Journal of Morphology* **33**, 1171–1175 (2015).

329. Lorbeer, R. *et al.* Reference values of vessel diameters, stenosis prevalence, and arterial variations of the lower limb arteries in a male population sample using contrast-enhanced MR angiography. *PLoS One* **13**, e0197559 (2018).

330. Hamdi, M. & Gagnon, A. R. CHAPTER 28 - Gluteus flap. in *Flaps and Reconstructive Surgery* (eds. Wei, F.-C. & Mardini, S.) 377–395 (W.B. Saunders, 2009). doi:10.1016/B978-0-7216-0519-7.00028-9.

331. Vigato, E. *et al.* Radiological anatomy of the perforators of the gluteal region: The "radiosome" based anatomy. *Microsurgery* **38**, 76–84 (2018).

Curriculum Vitae

Adele **Fanelli**

🏠 Avenue de Jurigoz 5
1006 Lausanne,
Switzerland

📱 (+41) 77 988 01 75

✉ delefan@hotmail.it
🔗 https://www.linkedin.com/in/adele-fanelli-641939130/

Nationality: Italian **Date of birth**: 06.07.1993.

Academic Education

April 2018 - present Lausanne, Switzerland	**PhD in Biotechnology and Bioengineering (Neural Engineering)** *École Polytechnique Fédérale de Lausanne (EPFL)* At Medtronic Chair in Neuroengineering, principal investigator Diego Ghezzi, PhD Campus Biotech, Geneva, Switzerland *Thesis:* "Development of a transient and minimally invasive neural interface" *Peer-reviewed publications*: 5 journal articles
Sept. 2015 – Oct. 2017 Turin, Italy	**M.Sc. in Biomedical Engineering (Bionanotechnologies and Tissue Engineering)** *Politecnico di Torino* *Thesis*: "Design and fabrication of microneedles for transdermal delivery of growth factors for chronic wound healing" *Final Grade*: 110/110 cum laude
Sept. 2016 – Feb. 2017 Vienna, Austria	**Exchange student (Erasmus+ Program)** *University of Applied Sciences Technikum Wien*
Sept. 2012 – July 2015 Turin, Italy	**B.Sc. in Biomedical Engineering** *Politecnico di Torino* *Thesis*: "Analysis of cell-penetrating peptides with Modeller and Visual Molecular Dynamics" *Final Grade*: 106/110

Working Experiences

April 2018 - present Geneva, Switzerland	**PhD Student** *Medtronic Chair in Neuroengineering, EPFL, Campus Biotech* • Design, conduct and report results of research projects • Worked on biodegradable polyesters, conductive polymers, microfabrication and electrochemical characterization • Involvement in research collaborations with physicians and technicians of the University Hospital of Geneva and professors and researcher from EPFL and University of Lausanne • Supervision of 3 Master Thesis Students, 5 Master Semester Project Students
Feb. 2017 – Aug. 2017 Boston, MA, USA	**Research Trainee** *Khademhosseini Lab, Harvard-MIT Health Science & Technology (HST)* *Project i)*: • Founded by National Institutes of Health (NIH) • Design, fabrication, and characterization of microneedle patches for drug delivery and angiogenesis • Tissue penetration testing, drug-model and VEGF release profile determination, VEGF delivery efficacy in vitro assessment Project ii): • Founded by MilliporeSigma • 3D printing of cell-laden scaffolds for muscle tissue regeneration • Characterization of different formulations of a hydrogel in terms of swelling, mechanical properties, biocompatibility, printability and bio-printability

Skills and Competences

Laboratory practice	Cleanroom procedures, photolithography, electrochemical tests, UV-Vis spectroscopy, scanning electron microscopy
	Cell culture procedures (adherent cells), cell proliferation, viability and migration assays, immunostaining, fluorescence microscopy, histology assays
	ELISA
Software	Word, LATEX, Power Point, Adobe Illustrator
	Excel, Prism, Origin
	AutoCAD, Solidworks, Comsol, Simulink
	Matlab, C, Python
	Modeller, Visual Molecular Dynamics
Languages	*Italian*: Native *English*: Full professional proficiency (C1, Cambridge Certificate in Advanced English, 2012) *French*: Intermediate proficiency
Driving license	B license

Organisational and Social Skills

From working environment	• planning of efficient, priority-based working schedules • coordination of projects with other professional figures • organization of work of supervised students, stimulating and supporting them • organize and carry out scientific discussions with my supervisors and collaborators • coordination of practice sessions and projects in the context of teaching assistant duties
From extra-curricular activities	• worked as associate, vice-president and co-president of Innovation Forum Lausanne, a PhD students and postdocs association aimed at promoting entrepreneurship among researchers • organization of internal meetings, tasks setting, assignment and status check • organization of > 10 events in 4 years for scientific divulgation (topics decisions, speakers' identification and contact, budget analysis, fundraising, logistics, marketing material preparation and strategy development) • organization of meetings with partners and sponsors • design and organization of an accelerator program for early-stage scientific start-ups • coordination between the local team of Innovation Forum Lausanne and the global team of Innovation Forum based in UK

Volunteering

Nov. 2018 – present Lausanne, Switzerland	**Associate, Vice-president and co-President** *Innovation Forum Lausanne (IFL), https://lausanne.inno-forum.org/* *Local branch of: https://inno-forum.org/*

Peer-reviewed publications

2022	**Locomotion of sensor-integrated soft robotic devices inside sub-millimetre arteries with impaired flow conditions** L. Pancaldi, L. Noseda, A. Dolev, **A. Fanelli**, D. Ghezzi, A. J. Petruska, M. S. Sakar. *Advanced Intelligent Systems* https://doi.org/10.1002/aisy.202100247

2021	**Transient neurovascular interface for minimally invasive neural recording and stimulation**
	A. Fanelli, L. Ferlauto, E. G. Zollinger, O. Brina, P. Reymond, P. Machi, D. Ghezzi. *Advanced Materials Technologies* https://doi.org/10.1002/admt.202100176
2021	**Transient electronics: new opportunities for implantable neurotechnology**
	A Fanelli, D Ghezzi. *Current Opinion in Biotechnology*, https://doi.org/10.1016/j.copbio.2021.08.011
2021	**All-polymeric transient neural probe for prolonged in-vivo electrophysiological recordings**
	L. Ferlauto, P. Vagni, **A. Fanelli**, E. G. Zollinger, K. Monsorno, R. C. Paolicelli, D. Ghezzi. *Biomaterials*, https://doi.org/10.1016/j.biomaterials.2021.120889
2020	**Flow driven robotic navigation of microengineered endovascular probes**
	L. Pancaldi, P. Dirix, **A. Fanelli**, A. Martins Lima, N. Stergiopulos, P. J. Mosimann, D. Ghezzi & M. S. Sakar, *Nature Communications*, https://doi.org/10.1038/s41467-020-20195-z

Conferences

2022	**Materials Research Society (MRS), Spring meeting & exhibit**
	Accepted Poster (not peer-reviewed): "Development of a transient and minimally invasive neural interface"
2022	**Gordon Research Conference (GRC) on Neuroelectronic Interfaces**
	Accepted Poster (not peer-reviewed): "Development of a transient and minimally invasive neural interface"
2022	**Gordon Research Seminar (GRS) on Neuroelectronic Interfaces**
	Accepted Poster (not peer-reviewed): "Development of a transient and minimally invasive neural interface"
2021	**International IEEE/EMBS Conference on Neural Engineering (NER)**
	Accepted Poster (peer-reviewed): "Bioresorbable endovascular neural interface for neural stimulation and recording"
2020	**Materials Research Society (MRS), Spring meeting & exhibit**
	Accepted Poster (not peer-reviewed): "Bioresorbable endovascular neural interface for neural stimulation and recording"
2018	**NanoBioTech-Montreux Conference**
	Accepted Poster (not peer-reviewed): "Bioresorbable endovascular neural interface for neural stimulation and recording". Received **Poster Award for Promising Research**.

Awards

October 2018	**Poster Award for Promising Research** at NanoBioTech-Montreux Conference
December 2017	**Prize "Antonio e Margherita Poletto"**
	Prize awarded to students with best academic results and Master Thesis living in "Collegio Universitario di Torino Renato Einaudi" during a.y. 2016-2017.

Hobbies and Interests

Professional	Neurotechnology, Tissue engineering, Regenerative medicine, Drug delivery systems, Lab-on-a-chip, Organ-on-chip
Extra-curricular	Sport, Entrepreneurial and start-up world, Event organization, Cooking, and Travelling.